Form and Function Relationships Governing Complex Muscle-Soft Tissue Interactions Revealed with 3D Modeling: Applications to Aging

---

A

Dissertation

Presented to

the faculty of the School of Engineering and Applied Science

University of Virginia

---

in partial fulfillment

of the requirements for the degree

Doctor of Philosophy

by

Katherine Read Knaus

May 2021

APPROVAL SHEET

This

Dissertation

is submitted in partial fulfillment of the requirements
for the degree of

Doctor of Philosophy

Author: Katie Read Knaus

This Dissertation has been read and approved by the examing committee:

Advisor: Silvia Blemker

Committee Member: George Christ

Committee Member: Jeffrey Holmes

Committee Member: Jason Kerrigan

Committee Member: Darryl Thelen

Accepted for the School of Engineering and Applied Science:

Craig H. Benson, School of Engineering and Applied Science

May 2021

Form and Function Relationships Governing Complex Muscle-Soft Tissue Interactions Revealed with 3D Modeling: Applications to Aging

Katie Read Knaus

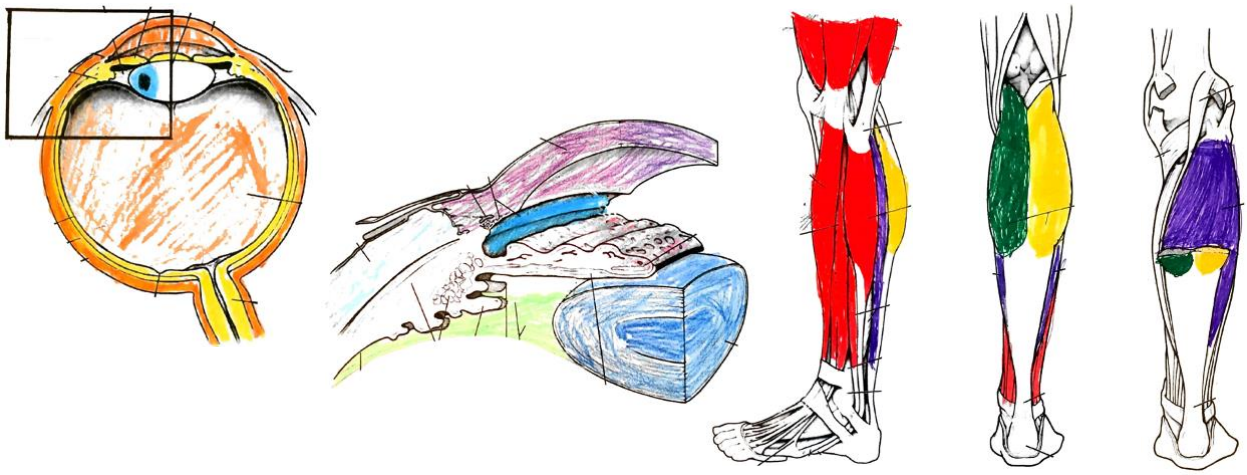

- Carter Knaus

Abstract

The universal experience of aging presents many clinical problems rooted in muscle dysfunction. Muscles actuate movement required for daily life and understanding muscle function prior to the onset of age-related changes is critical in addressing these problems. Muscle function depends on both its fiber architecture (the arrangement of its cells) and its interaction with elastic connective tissues. When muscles have complex architectures and connective tissue interfaces it is difficult to intuit the full relationship between structure and function. As a result, questions about how age-related structural changes alter movement remain unanswered. Physics-based computational modeling allows us to represent complex three-dimensional (3D) muscle and connective tissue in order to relate tissue morphology and material properties to biomechanical function. In my dissertation, I have developed finite element models to investigate unique examples of architecturally complex muscle-driven systems that experience significant mechanical dysfunction with age.

I first studied the eye to examine muscle-related vision impairment. The human eye is capable of accommodation, where optical range is adapted for distant and near vision, however, this ability progressively declines with age. Accommodation relies on deformation of the lens surfaces which occurs as tension on the lens is modified during contraction of the ciliary muscle. With tri-sectioned fiber architecture, the ciliary muscle pulls against outer layers of the eye while interfacing with lens through a network of fibers. This complex mechanism is difficult to probe experimentally, so the biomechanics of this process are still unclear. I have developed a model of the eye's accommodative mechanism to reveal how action of the multi-section ciliary muscle deforms the lens. I then used this model to predict how age-related changes in mechanical properties of different tissues reduce accommodative capacity.

Next, I focused on mobility by investigating the complex triceps surae group which generates plantarflexion power at the ankle during walking. Reduction of this power is the most universal hallmark of elderly gait impairment. I compared imaged-based measurements of triceps surae muscles and Achilles tendons with walking kinetics of young and older adults to understand structure-function changes with

age. To elucidate how anatomic variability impacts the mechanics of the Achilles tendon, I created models with different twisted morphologies to predict effects on loading during walking. Finally, I created a model of the soleus, the largest of the triceps surae, to reveal how the morphology and material properties of the interdigitating connective tissue structures within this muscle influence architecture changes in its multiple compartments as it lengthens.

This dissertation advances our knowledge of muscle-driven production of movement by illuminating relationships between the form and function of these complex tissues, thus progressing understanding of vision and mobility impairments that occur with aging.

Keywords: muscle, finite element modeling, biomechanics, aging, soft tissue mechanics

Acknowledgements

I don't think in a few pages I can express my gratitude to everyone who made this possible and find the words to say how much I mean it. However, this is me trying to do just that.

To Silvia, my advisor, role model, friend – I will forever & always be grateful that you found a place for me in your lab and shared your contagious passion for muscle modeling. Your unwavering support and encouragement have helped me to achieve more than my wildest dreams. I cannot tell you the moment I knew that I would be getting a PhD, but I think you knew long before me. I am so glad that you talked me into this and were such an outstanding role model along the way. Working with you, I not only learned how to produce high quality research but also how to maintain the delicate balance between research and life or how to make it work when the balance isn't perfect. Thank you for mentoring me!

I am very fortunate to have been able to work with and learn from some incredible people during the seven years of my graduate studies. I want to say a special thank you to the members of my committee. To George Christ, thank you for teaching me many things about being a scientist and a teacher and for sharing your humor. To Jeff Holmes, thank you for your patience in teaching me when I showed up to your class with a middle-school-level understanding of biology/physiology and lots of questions – not only did you tolerate it, but you challenged me to expand my skills and confidence in biomedical research. To Jason Kerrigan, thank you for asking tough questions and keeping me grounded in mechanics. To Darryl Thelen, thank you for sharing your knowledge of muscle and tendon. It has been a pleasure working with you and your lab on the triceps surae project.

Thank you to the faculty at the University of Virginia for sharing your time and passion with me during my seven years of grad school. I'd like to share my gratitude especially to Craig Meyer for serving as my tour guide through MRI, Shayne Peirce-Cottler for your mentorship and constant advocacy for BME students, Matt Panzer for offering mechanics classes to biomedical engineering students, Jake Resch for cuss & discussing anatomy with an engineer, and Joe Hart for being the man to talk to about all things muscles. There are so many people who work at UVA in the Engineering School, the Center for Teaching Excellence, Student Health, PhD+, and more who have helped make my graduate experience possible. I could not have gone far without the superstars of the BME office who helped me with so many things.

I would not have been as successful or had as much fun in grad school without the collegiality of the many members of the Multiscale Muscle Mechanophysiology Lab both past and present. I cannot imagine surviving this pandemic without the many cups of socially distanced coffee enjoyed with Vi, Ridhi, and Allie. While everything has changed with working from home, I'm so glad we have been able to find ways to keep up our workplace routine of getting lunch or Starbucks together. You are amazing scientists and friends, and I am so glad we got to work together. Thank you, Hunter, for navigating the treacherous waters of FEA, viscoelasticity, and Canada with me. Brian, thank you so much for all of your time spent teaching me FEBio. I think almost every epiphany about how to get my model to work this past year happened in your office hours. I want to thank Xiao for helping me troubleshoot AMPS, Megan for your inspiring work ethic, Matt for your humor and insights into muscle modeling, and Adrienne for your work with me on the plantarflexor project. Even though Rem was only in the lab for a short time, your work on the DENSE imaging study was such a huge help. To the many members of the lab who have come and gone during my time in the M3 Lab, while I am right where you left me, I am very grateful for the chance to have worked with you. A big thank you to all of the undergraduates who I got to work with and mentor; I appreciate all of your hard work and contributions. Thank you to Shawn for being there to grab a beer and talk about everything from research to kids to skiing to life in academia. Thanks to Geoff who always came to lab armed with a cardigan and a thought experiment. You were the 1 who recruited me to join the lab in the first place and I will always be grateful that I accepted your offer to come segment MRIs. Thanks to Kelley for demonstrating an insatiable work ethic, for helping me do science experiments, and for walking so many laps around the hospital that we will likely have our photo on the UVA website for evermore. To our other walking partner, Katie P, we had so many adventures including

baseball games, dress shopping, Zumba classes, Wine & Design outings, and conference excursions that it is hard to know what to say. Long story short, I really can't imagine grad school without you! Although I almost do wish I could stay in the M3 lab, it's time to go but I will miss you all!

Thank you to the many friends and colleagues at UVA in biomedical engineering and biomechanics that I have been privileged to get to know through working on projects, taking classes, attending happy hours, serving on committees, and traveling to conferences. Thanks especially to Evan Dooley – it's nice to have a friend who shares so many of my interests like biomechanics, beer, snow sports (even though you snowboard instead of ski), cheese fries, chicken wings, and science facts. Thanks for being a rad trivia co-host and great friend. I am grateful to the many members of the American Society of Biomechanics who have helped me to grow as a researcher in this field and for inspiring me along the way. It was a joy of my graduate career to serve as the Student Representative and I am especially thankful to have worked with the members of the Executive Board and Student Advisory Committee. Although this year could not have been crazier, it was so much better because of the support and friendships built through the International Womxn in Biomechanics. I feel like a very lucky one to be part of the amazing biomechanics community.

This dissertation work would not have been possible without help from many collaborators generous funding. I'm thankful for AnnMarie and everyone else at AceVision for an unforgettable research experience. From of our work together I have my eyes open to the field of ophthalmology that I never thought I'd venture into. I learned so much from my early work on the Coulter-funded project that evolved into Springbok. Working with the Tendonados was a highlight of my graduate experience. It felt like I got to work in two extra labs during my PhD and I am thankful to those 'lab mates' at UW and UNC, especially Darryl and Jason Franz. I also want to express my gratitude to the National Institutes of Health for funding that work.

I want to end by thanking the many family members and friends who have loved me through this process, providing emotional support as I struggled through and offering moments of peace, distraction, and happiness when I needed it most. To my gorgeous Lefevre Ladies, thanks for trips to C'ville and silly Zoom calls. To all of my Wintergreen friends, thank you for providing an outlet when the school stress built up and I needed to shake it off by skiing and hanging out. To the members of the Leagualize It fantasy football team whose money is now mine, thanks for making fall weekends fun. Bridget and Monika, you both knew all too well when I needed a laugh, and our phone calls and texts always made my day. To my many family members- Reads, Tiptons, Knaus', McDevitts, Smiths, Fanos, Burklecas, Breitenbachs, Maugans', and more - I cannot even begin to explain the way I love you or what your encouragement has meant. Thank you to Lucas's parents and siblings who have accepted me into their family. You have helped in so many ways and we have had a lot of fun together at family meals, ski trips, pool parties, football and baseball games, and campouts. Thank you to my brother, James, who will tell me why I am a nerd but love me anyway and Leighton for also being a nerd (two is better than one so nerds win :) Thank you to my mom and dad for everything you have done to help me get to this point. You have been there for the entire journey leading up to the August I started grad school and all the way through to the endgame of finishing this dissertation. I wouldn't be today without your help and advice and I am so grateful for how you have demonstrated dedication, hard work, and a passion for learning.

Finally, I'll speak now to Lucas, Carter, and Max who have motivated me and made getting a PhD possible. Max will never read this, but I think he knows that I love him, and he is a good boy. Lucas, you have been my tree-ski buddy, road trip co-pilot, kayaking companion, nacho and beer pitcher sharer, parenting partner, and my best friend. Thank you for going on this journey with me. I am excited for our continued adventures together as we begin again in a new city. Carter – your hard work and joy inspire me. Thank you for sharing me with muscles.

– Katie

Charlottesville, VA

Table of Contents

"The making of pictures is a stern discipline. One may 'write around' a subject where one is not quite sure of the details, but, with brush in hand before the drawing board, one must be precise and realistic. The white paper before the artist demands the truth."

– Frank H. Netter, M.D., *Atlas of Human Anatomy*

List of Figures

List of Tables

List of Equations

Chapter 1

Introduction

"Muscle is the only known piece of machinery which can be cooked in many ways. This knowledge, by itself, is not good for much.... Muscle is illuminated in wonderful ways by mathematical arguments about how it works."

– Thomas A. McMahon, *Muscles, Reflexes, and Locomotion*

1.1 Overview

Aging is associated with pervasive mechanical dysfunction that occurs at a different scale and rate than any disease or injury, due to the body's tissue behavior changing ubiquitously over the course of several decades. Many clinical problems that present with aging are rooted in muscle dysfunction. Muscle actuates all movement required for daily life and understanding muscle function is critical in addressing these problems.

The production of forces required for motion depends on many factors spanning the multiple scales of muscle's hierarchical structure. Protein interactions within the sarcomere govern a relationship between force and length that scales up to the fiber (cell) and even the full muscle so that the coordination of many muscles ultimately enables multi-joint movement of the body (Zajac 1989, 1993). Forces generated by a muscle also depend on its architecture, the arrangement of fibers within the muscle (Lieber and Fridén 2000; Roberts et al. 2019). Muscle architecture is interdependent with the morphology of connective tissues to which the muscle attaches. In turn, these compliant tissues, like tendon, affect muscle force production. For muscles with complex fiber arrangements, it is difficult to intuit the full relationship between structure and function; therefore, the effects of age-related structural changes on function remain unclear. Further, changes in connective tissues may contribute to dysfunction in aging by altering coupled muscle-tissue dynamics. Age-related changes to muscle and connective tissues occur concurrently and it is difficult to isolate how these changes interact and cause dysfunction using experimental methods alone, especially in structures that have complicated anatomy. Mathematical models have been used describe complexities of muscle function, from protein dynamics to muscular coordination of walking, however, few models represent the interaction of muscle and connective tissues with complex anatomy. Many previous models rely on simplifying assumptions about the uniformity of muscle fascicles and their connections to soft tissues (Delp et al. 1990; Millard et al. 2013; Zajac 1989). Finite element modeling presents an opportunity to better represent the complexities of three-dimensional (3D) muscle architecture (Blemker and Delp 2005; Blemker, Pinsky, and Delp 2005; Fiorentino et al.

2014; Fiorentino and Blemker 2014; Rehorn and Blemker 2010). The goal of my dissertation is to create finite element models informed by imaging of complex muscle systems to reveal relationships of tissue morphology and material properties with biomechanical function and use these models to investigate changes with age.

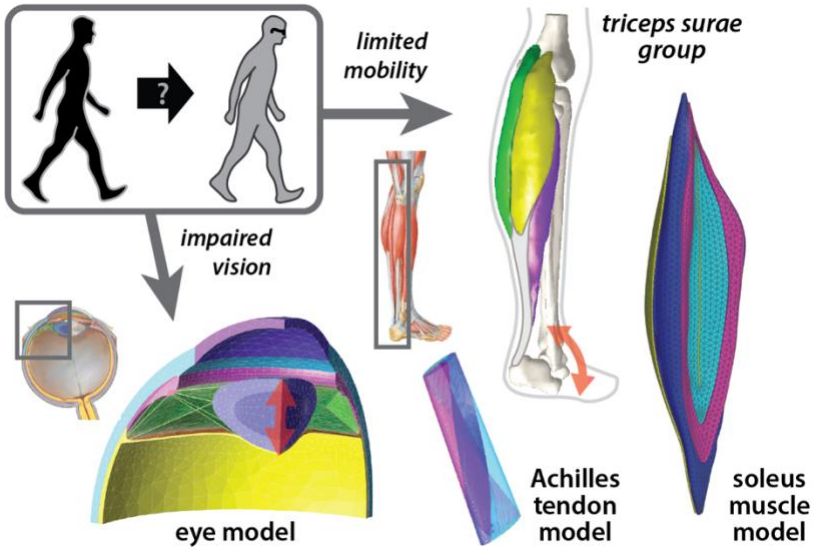

Figure 1.1: Overview of dissertation. 3D computational modeling of complex biomechanical systems is used to study muscle-connective tissue interactions and how they are affected by changes with age.

In my dissertation, I have developed models to investigate unique examples of architecturally complex muscle-driven systems that experience significant age-associated mechanical dysfunction. In the first application of this work, I have developed a model to simulate accommodation of the eye. The process of accommodation involves changing the eye's focal length from far to near, for tasks such as reading. This complicated process is actuated by the ciliary muscle which comprises three architecturally different sections, though it is poorly understood how these sections act collectively to displace the lens to alter its optic power (Croft, Glasser, and Kaufman 2001; Helmholtz 1855; Kaufman, Alm, and Adler 2003). Adults progressively lose their ability to accommodate as they age so that by the fifth decade of life this function is completely gone in a condition called presbyopia (Croft et al. 2001; Kaufman et al. 2003). Presbyopia is often attributed to changes in the lens that occur with age (Burd, Judge, and Cross 2002; Krag, Olsen, and Andreassen 1997; Wilde, Burd, and Judge 2012), but mechanical changes have

been observed in other connective tissues of the eye, like the sclera (Friberg and Lace 1988; Grytz et al. 2014), as well as in the ciliary muscle (Tamm, Tamm, and Rohen 1992), and it is unclear how each change impacts the muscle's function and thus contributes to presbyopia. Experimental methods are limited in their ability to isolate how the action of each ciliary muscle section affects displacements of the lens that occur during accommodation. This capability is needed to investigate how muscle-tissue interactions affect the accommodative mechanism. Furthermore, the effect of specific tissue changes on dysfunction in aging is unclear; knowledge of these effects could inform targeted treatments for presbyopia. In Chapter 3, I developed a 3D FEM of a healthy young adult muscle-driven accommodative mechanism The FEM was constructed based on measurements available in the literature. After validation of model-predicted lens accommodation by comparison with *in vivo* measurements, I performed sensitivity analysis by varying muscle activation to investigate the role of each section in accommodation. In Chapter 4, I used this model to vary material properties of the lens, sclera, and ciliary muscle across the range observed in aging populations to assess the extent of impairment imposed by age-related changes.

In the second application of my work, I aimed to investigate the triceps surae group in ankle plantarflexion by examining age-related differences and using models to probe the effects of morphology and material properties on function of the Achilles tendon and soleus muscle. The triceps surae muscles generate plantarflexion power during walking, and reduction of this power is the most universal hallmark of elderly gait impairment (Boyer et al. 2017; DeVita and Hortobagyi 2000; Franz 2016; Kerrigan et al. 1998; McGibbon 2003; Winter et al. 1990). Muscle size relates to force output, and translation of that force at the ankle depends on tendon geometry. While differences between young and older adults have been observed in both the tendon and the muscles (Onambele, Narici, and Maganaris 2006; Stenroth et al. 2012), little is known about how these age-related differences correspond with each other. Furthermore, it is not well known how age-related differences in tendon and muscle structure compare to measurements of plantarflexion output. In Chapter 5, we used magnetic resonance imaging to measure muscle volumes and tendon cross sectional area (CSA) to determine if age-related differences correlated with each other,

body size, and joint torque during walking. To further investigate the role of the Achilles tendon, I aimed to better understand its unique morphology. The Achilles tendon comprises three subtendons from each triceps surae muscle that twist around each other (Edama et al. 2015; Pękala et al. 2017; Szaro et al. 2009). Anatomical torsion varies within each tendon and between individuals, and it is unclear how this variation in structure influences the function of the Achilles. In Chapter 6, I created finite element models of tendons with different internal twisting structure in order to simulate loading that represented walking, in order to understand how strain experienced by the tendon during a given elongation would vary with different amounts of twist, and to elucidate how differences in twist change the amount of energy stored during that same stretch. Models were used further to investigate how subtendon twist affects how Achilles tendon behavior is quantified with *in vivo* measurements. The soleus muscle is the largest of the triceps surae muscles and has a very complex architecture comprising multiple compartments and interdigitating aponeuroses (Agur et al. 2003; Bolsterlee et al. 2018; Hodgson et al. 2006). Although aponeuroses morphology is well described, its effects on fascicle behavior within the muscle compartments are not well understood. Further differences in aponeurosis mechanical properties have been linked to changes in muscle function of aging rats (Holt et al. 2016). In Chapter 7, I created an image-based finite element model representing the 3D structure of the soleus muscle and aponeuroses, including compartments fascicle architecture, and used it to simulate passive and active soleus lengthening during ankle motion. Predicted tissue displacements and fascicle architecture changes were verified by comparing to results from a dynamic imaging experiment as well as previous *in vivo* measurements. Additional model simulations were used to investigate the effects of aponeuroses material properties on muscle deformation.

Ultimately, this dissertation provides new insights into complex actions of muscles in the eye and ankle, helping to reveal how dysfunction arises as age-related changes alter muscle-connective tissue interactions. These computational models advance our knowledge so we might one day reverse or stall mobility and vision impairments that occur with aging.

1.2 Dissertation Outline

The next chapters of this dissertation are as follows. Chapter 2 provides background information on the different topics that are discussed in this dissertation. Chapters 3-7 represent five bodies of work that are either published or prepared journal articles. As such, each provides some portion of the information presented in Chapter 2. These chapters were made possible by multiple collaborations. This is often reflected in the use of the word "we" to describe the work done in these studies – this dissertation is the result of a team effort! Co-authors of these publications are listed here. Chapter 3 describes the development of a 3D model of the accommodative mechanism of the eye and investigation with this model of ciliary muscle action in deforming the lens. This work is published in *Biomechanics and Modeling in Mechanobiology* with coauthors AnnMarie Hipsley and Silvia Blemker. Chapter 4 describes application of the 3D FEM of the accommodative mechanism to investigate the effects of changes in material properties associated with aging. This work is in preparation for submission to *Investigative Ophthalmology and Vision Science* with coauthors AnnMarie Hipsley and Silvia Blemker. Chapter 5 describes the comparisons of triceps surae muscle volumes and Achilles tendon cross sectional areas, measured with magnetic resonance imaging, to body sizes and peak joint torque during walking in young and older adults. This work is published in *Frontiers in Sports and Active Living* with coauthors Ana Ebrahimi, Jack Martin, Isaac Loegering, Darryl Thelen, and Silvia S. Blemker. Chapter 6 describes simulation results of finite element models of the Achilles tendon with different internal twisted geometry to examine effects of anatomic variability on function. This work is published in *Frontiers in Bioengineering and Biotechnology* with coauthor Silvia S. Blemker. Chapter 7 describes a model of the soleus used to investigate effects of aponeuroses morphology and material properties on muscle fascicle behavior. This work is in preparation for submission to *Journal of Biomechanics* with coauthors Geoff Handsfield and Silvia Blemker. I conclude with a chapter that first summarizes the work presented in this dissertation and how it contributes to the biomechanics field, and then discusses exciting additional applications and future directions for this science.

Chapter 2

Background

"The strategic deployment of muscles to control the mechanisms of animal locomotion is itself a subject of great beauty and importance.... How marvelously our muscles are arranged so that we can do all the things we want to do!"

– Y.C. Fung, *Biomechanics: Mechanical Properties of Living Tissues*

2.1 Eye Anatomy

There are six extraocular skeletal muscles that attach to the eye to control its movement, and three intraocular muscles. Two of the intraocular muscles are located in the iris and control the size of the pupil. The last is the ciliary muscle which controls the accommodative mechanism and is the focus of the early chapters of this dissertation. The ciliary muscle is a multi-unit smooth muscle, but it is atypical in many ways. This complex smooth muscle exhibits fast contraction, large motor neurons that are distanced from the muscle fibers, and structural arrangement that is similar to a skeletal muscle (Croft et al. 2001; Ishikawa 1962; Kaufman et al. 2003). The ciliary muscle is located deep to the anterior sclera and posterior to the iris, forming a ring shape in at the anterior of the posterior compartment. The ciliary muscle is within the ciliary body, which is a region of tissue connecting the iris and choroid. The anterior portion of the ciliary body (the *pars plicata*), where the muscles is thickest, is covered in a layer of folded epithelium called the ciliary processes. The posterior portion of the ciliary body (the *pars plana*), where the muscle is thinnest, extends to a region called the *ora serrata*. When the muscle contracts, its mass moves anteriorly towards the cornea and centrally towards the eye's axis. As this movement happens, the inner circumference of the ring decreases, similar to the action of a sphincter muscle (Croft et al. 2001; Kaufman et al. 2003). Ciliary muscle fibers are organized into bundles by surrounding connective tissues (Ishikawa 1962). These muscle cell bundles are then arranged into three sections with different orientations: longitudinal, radial, and circular (sometimes referred to as meridional, reticular, and circumferential) (Croft et al. 2001; Hogan, Alvarado, and Weddell 1971; Kaufman et al. 2003). Fibers in the longitudinal section originate at the scleral spur and insert into the choroid at the *ora serrata*, running parallel to the inner surface of the sclera. Fibers in the radial section also originate at the scleral spur then fan towards the anterior chamber to insert on the inner boundary of the ciliary processes. Fibers in the circular section are oriented circumferentially around the ring and are therefore perpendicular to the longitudinal and radial fiber directions.

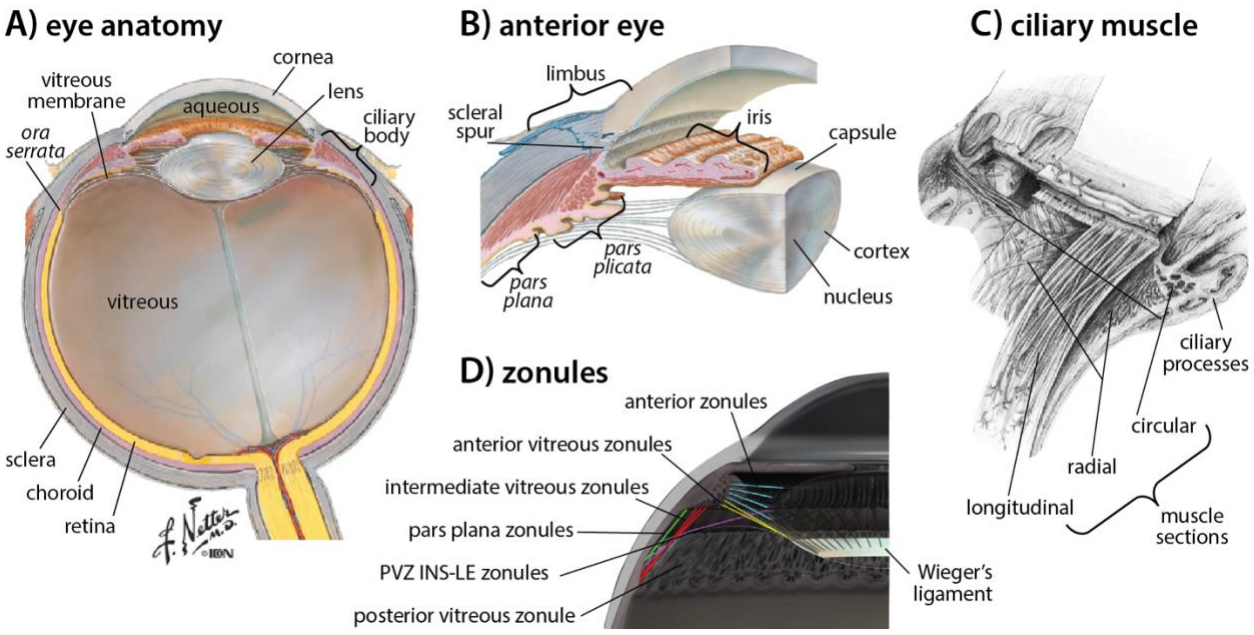

Figure 2.1: Anatomy of the eye. A) The lens and ciliary are incased within the globe of the eye by three layers of tissue along with two different fluids. **B)** The anterior eye houses the components of the accommodative mechanism (A & B adapted from Netter 2014). **C)** Within the ciliary body, muscle fibers are arranged in three sections with different orientations (adapted from Hogan et al. 1971). **D)** Divisions of the zonules are arranged in the anterior eye, connecting structures in this region (adapted from Goldberg 2015).

The lens is located in the center of the ciliary muscle ring. It is biconvex and has an elliptical shape. Often called the crystalline lens, it is transparent due to the shape, structure, and arrangement of its cells (Hogan et al. 1971; Kaufman et al. 2003). Lens substance comprises two compartments: nucleus and cortex. The lens nucleus is present at birth and forms the center of the lens, while the cortex surrounds it and grows throughout life as new layers of epithelial cells are added. The capsule surrounds the lens substance and is responsible for regulating lens shape. This elastic tissue layer has nonuniform thickness that is thickest on the anterior surface and thinnest near the lens equator (Barraquer et al. 2006; Kaufman et al. 2003). The lens is responsible for approximately one third of the refractive power of the eye. The other two thirds are determined by the cornea, which is a transparent layer of tissue at the anterior eye that has a convex and concave surface (Hall 2010). The surfaces of the cornea and lens form refractive interfaces with the adject fluids to determine how images are projected onto the retina along the visual

axis. Of the components of the eye's refractive mechanism only the lens can change shape and modify optic power.

The cornea along with sclera forms the tough protective cover of the ocular tissues. Tissue transitions gradually from cornea to sclera in a region called the limbus (Hogan et al. 1971). The sclera is opaque connective tissue, referred to as the white of the eye. Scleral shape defines the diameter of the eye's globe, differing in curvature from the cornea (Hogan et al. 1971; Stitzel et al. 2002), and varies in thickness regionally (Boote et al. 2020; Norman et al. 2010). The scleral spur is a small extension of scleral tissue on the inner boundary of the posterior limbus that forms a ring that is significantly stiffer than the surrounding tissue (Boote et al. 2020; Hamanaka 1989; Hogan et al. 1971; Moses and Grodzki 1977). The scleral spur is suspected to help maintain the curvature of the cornea as the tissues is stressed by fluid pressure and ciliary muscle contraction. The sclera is the outermost of three primary layers of the posterior eye. The middle layer is the choroid, which is layer of pigmented vascular tissue with a primarily collagen base membrane, called Bruch's membrane. The choroid extends posteriorly at the *ora serrata* and forms a continuous vascular tract with the ciliary body and iris (Hogan et al. 1971). The choroid and ciliary body are believed to be loosely attached to the inner surface of the sclera in a region called the supra-choroidal or sub-scleral space (Kaufman et al. 2003; Moses 1965). The retina is the inner most layer and is more tightly bound to the inner surface of the choroid. The retina covers the inner eye surface, posterior to the *ora serrata*, and contains photoreceptor cells that process light as an extension of the nervous system (Hall 2010; Hogan et al. 1971). The eye is filled with two fluids that create and intraocular pressure (IOP) of approximately 15 mm Hg. The vitreous humor fills that posterior eye is a gel-like substance which is contained at a constant volume by the vitreous membrane. The anterior portion of this membrane (sometimes called the anterior hyaloid or vitreous face) attaches to the ciliary body in the *par plana* region near the *ora serrata* and to the lens capsule on its posterior surface, creating a region called Wieger's ligament (Croft, Nork, et al. 2013; Lütjen-Drecoll et al. 2010). The anterior of the eye is filled with the aqueous humor, that is similar to water, and constantly produced by the ciliary

processes. An aqueous outflow apparatus in the limbus allows fluid to leave the eye, regulating IOP (Hogan et al. 1971). Ciliary muscle fibers originate in this region may play a role in pressure regulation (Croft, Lütjen-Drecoll, and Kaufman 2017).

The lens and ciliary muscle are connected to the via a complex network of fibers called zonules (Hogan et al. 1971; Kaufman et al. 2003). Referred to as suspensory ligaments, the zonules act to stabilize the lens, maintaining tension between it and the ciliary muscle. Zonule fibers range in diameter from 4 to 50 um and are arranged radially around the anterior eye. Fibers are organized into groups (called divisions or pathways) that are identified in the meridional cross section and defined by the attachment locations of their end points. The anterior zonules (sometimes called zonules of Zinn) originate between the ciliary processes on the *pars plicata* near the widest point of the ciliary muscle (ciliary apex). This group spits to form a fork with anterior, equatorial, and posterior divisions that insert onto the lens capsule above, on, and below the equator, respectively (Farnsworth and Shyne 1979; Goldberg 2015; Rohen 1979). The *pars plana* zonules extend along the interior of the ciliary muscle form the *ora serrata* to the *pars plicata* (Kaufman et al. 2003; Rohen 1979). The vitreous zonules are groups of zonules located near the vitreous membrane. Anterior vitreous zonules originate near the ciliary muscle apex and insert near the vitreous membrane's attachment to the posterior lens capsule at Wieger's ligament (Goldberg 2015; Lütjen-Drecoll et al. 2010). Intermediate vitreous zonules also originate near the ciliary muscle apex and insert posteriorly at the *ora serrata* bridging the cleft between the *pars plana* zonules and the vitreous membrane (Goldberg 2015; Lütjen-Drecoll et al. 2010). Fine fibrils extending from the intermediate vitreous zonules form a multilayered spongelike ring at the base of this cleft and are called the posterior vitreous zonule (Goldberg 2015; Lütjen-Drecoll et al. 2010). The final division of zonules (called the PVZ INS-LE) originate at the Posterior Vitreous Zonule INSertion area, which is near the *ora serrata*, then insert into the Lens Equator (Croft et al. 2016; Croft, Nork, et al. 2013; Goldberg 2015).

2.2 Accommodation

Accommodation is the dynamic process in which the optical power of the eye changes to focus from distant to near objects. Optical power change occurs as the lens changes shape so that the radius of curvature of its posterior and anterior surfaces increase (Hall 2010; Kaufman et al. 2003). Modern understanding of accommodation is primarily founded on classic theories developed by Helmholtz based on early experiments in humans (Croft et al. 2001; Helmholtz 1855; Kaufman et al. 2003). Classic theory proposes that contraction of the ciliary muscle actuates the accommodative process. When the muscle is activated, its mass moves anteriorly and centrally, displacing the zonules that are attached to the ciliary body. At their other end, these zonules are attached to the lens. When the ciliary muscle is at rest, the lens is held in tension by the zonules. Excursion of the ciliary muscle displaces the zonules towards the lens. Tension on the lens is relieved allowing it to change shape and become rounder. Increasing lens surface curvature alters refractive power along the eye's visual axis.

All structures in the anterior eye that interact during accommodation are considered to be part of the accommodative mechanism. The optical part of the process is centered on the lens, but mechanically depends on many parts of the eye. These other components are referred to as the extralenticular structures (Croft, McDonald, et al. 2013). The geometry and resting tension of the lens play a role in how it is able to change shape. Fibers in the different sections contract to produce excursion of the ciliary muscle, defining how it moves and deforms when contracted (Sheppard and Davies 2010), though how these sections contribute to and coordinate this excursion is not well understood. Ciliary muscle excursion is translated to the lens via the zonules, and their arrangement may play a role in this process. The vitreous membrane, choroid, and sclera all move during accommodation (Croft, Nork, et al. 2013), indicating that they play a role as elastic components in this mechanism and likely influence muscle and lens deformations at their interfaces. Knowledge of how these components interact is dependent on current methods for investigating the accommodative mechanism.

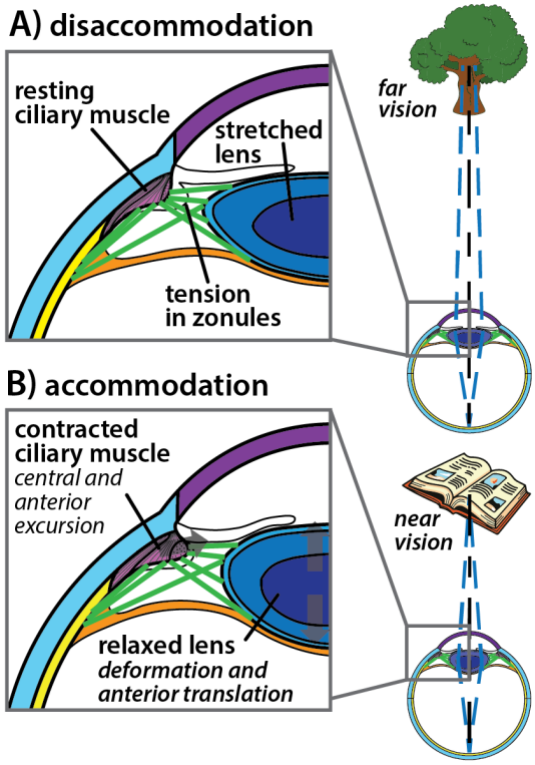

Figure 2.2: Diagram of accommodation. A) In disaccommodation, the lens is stretched due to resting tension in the zonules, which connect the lens to the ciliary muscle. In this configuration, the lens surfaces are less curved, extending the focal length of the eye so that it is suited for focusing on far objects. **B)** During accommodation, the ciliary muscle contracts so that it moves towards the center pole and anterior surface of the eye. This muscle excursion relieves tension on the lens, allowing the lens to deform so that its surfaces increase in curvature while the lens equator translates anteriorly towards the cornea. This lens displacement reduces the focal length of the eye so that it adapts for viewing near objects.

Much of what is known about accommodation relies on the ability to observe deformations and movements of the eye in human patients. Refractometers are used to measure patients' accommodative amplitude (change in optical power during accommodation) by shining light on the lens through the pupil, but the rest of the accommodative mechanism is not visible from the exterior. Many imaging modalities have been used to study accommodation, but each comes with advantages and tradeoffs. Magnetic resonance imaging (MRI) allows the whole globe to be imaged at once but is limited to gross measurements of the lens and ciliary body due to resolution (Richdale et al. 2013; Strenk et al. 1999). Further MRI can only image the eye statically, and due to time requirements of image collection has only been used to measure pharmaceutically induced disaccommodation and accommodation. Optical

coherence tomography (OCT) provides greater resolution but is limited to a smaller field of view so that either the lens or ciliary muscle are visible (Richdale et al. 2013; Sheppard and Davies 2010), though dual systems have been used to image both simultaneously (Ruggeri et al. 2016; Shao et al. 2013). Ultrasound biomicroscopy (UBM) have a similarly limited field of view, but also like OCT, provide an opportunity to observe *in vivo* accommodative dynamics (Croft, McDonald, et al. 2013; Croft, Nork, et al. 2013; Lütjen-Drecoll et al. 2010). Histology and scanning electron microscopy (SEM) reveal more of the anatomic details of the accommodative mechanism (Hogan et al. 1971; Lütjen-Drecoll et al. 2010; Rohen 1979). Since these methods require dissection the eye, images and measurements do not reflect the *in vivo* tension state of the eye. Further eyes used in these studies are from donors who are typically older adults. Almost all animals have accommodative mechanisms that differ significantly from humans (Kaufman et al. 2003). Nonhuman primates are the best comparison so rhesus monkeys are often used as an animal model as the have similar anatomy and accommodative function and also exhibit comparable changes in that function with age (Croft, McDonald, et al. 2013; Croft, Nork, et al. 2013; Kaufman et al. 2003; Lütjen-Drecoll et al. 2010).

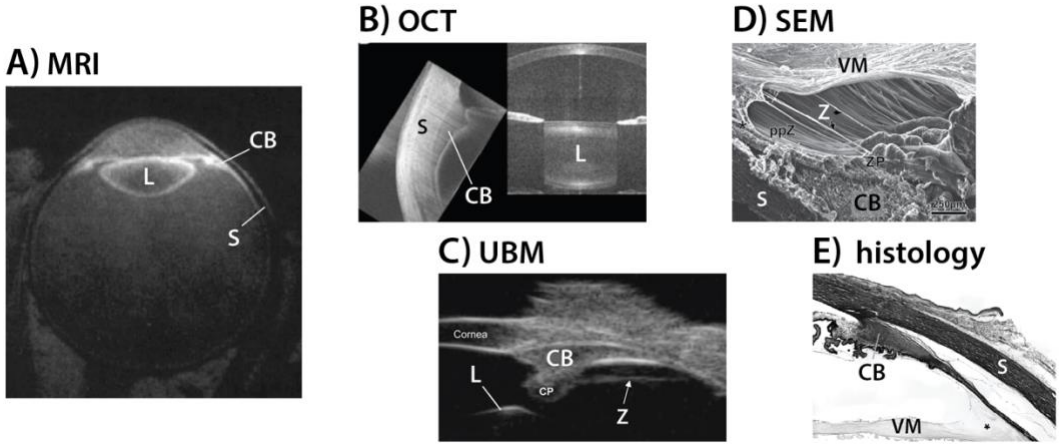

Figure 2.3: Imaging of the human eye. A) Magnetic resonance imaging (MRI) reveals the full eye (adapted from Strenk et al. 1999). **B)** Optical coherence tomography (OCT) can view the lens or ciliary *in vivo*, or both with dual systems (adapted from Ruggeri et al. 2016). **C)** Ultrasound biomicroscopy (UBM) can be used to observe *in vivo* ciliary dimensions while partially viewing the lens (adapted from Croft, McDonald, et al. 2013). **D)** scanning electron microscopy (SEM) and **E)** histology help visualize details of the anterior eye when dissected (adapted from Lütjen-Drecoll et al. 2010). The lens (L), ciliary body (CB), sclera (S), zonules (Z), and vitreous membrane (VM) are labeled in images when visible.

2.3 Presbyopia

In the last 10 years in the United States, the number of people who are 65 and older has increased by 34% (to 50 million), so that one in every seven Americans (15.6%) is considered an older adult (U.S. Department of Health and Human Services. 2018). Last year, ten million of these older adults (19.6%) were in the labor force, with a participation rate that has gradually risen over the last 20 years (U.S. Department of Health and Human Services. 2018). Presbyopia effects the entire population of older adults, an estimated one billion people world-wide (Holden BA et al. 2008), impacting their daily activities, especially those who are still working. Reading glasses and contact lens are the status quo in correcting presbyopia (Glasser 2008; Richdale, Mitchell, and Zadnik 2006; Wolffsohn and Davies 2019), but vision impairment remains globally uncorrected at high rates, even in the developed world.

Clinically, presbyopia is defined as a decline in accommodative ability such that an individual's focusing range is insufficient to provide visual clarity for near and distance vision tasks without corrective measures (Croft et al. 2001; Richdale et al. 2013; Wolffsohn and Davies 2019). This definition considers the dysfunction that occurs in presbyopia from an optical perspective. Refractive measurements show that accommodative response in older adults lags behind presented stimulus demands (Richdale et al. 2013). Refractive alterations in accommodation have been clearly associated with ocular tissue displacement (Croft, McDonald, et al. 2013; Richdale et al. 2013; Strenk et al. 1999), demonstrating the link between optical dysfunction and reduced tissue mobility. There are multiple changes in the dynamics of the accommodative mechanism that change with age. Optical deficiencies result directly from changes in lens displacements. Lens deformation, measured at its thickness and equatorial diameter, is significantly reduced with age in response to accommodative stimulus (Croft, McDonald, et al. 2013; Richdale et al. 2013; Strenk et al. 1999). Anterior movement of the lens measured at its equator also decreases with age (Croft, McDonald, et al. 2013). Reduced lens displacement is not the only dynamic change that occurs in presbyopia. Ciliary muscle excursion associated with accommodation is similarly reduced. Decreased muscle apex thickening has been observed in humans (Croft, McDonald, et al. 2013) as well as smaller

length changes in rhesus monkeys (Croft, McDonald, et al. 2013; Lütjen-Drecoll et al. 2010). Accommodative movements of other extralenticular structures change with age as well, including the zonules, choroid, vitreous membrane, and sclera (Croft, McDonald, et al. 2013; Croft, Nork, et al. 2013). Although presbyopia is the result of optical dysfunction at the lens, dynamic dysfunction occurs throughout the components of the accommodative mechanism.

Age-related changes occur in nearly every part of the eye and each has been proposed as a potential mechanism of presbyopia (Croft et al. 2001). Age-related changes in lens structure have been proposed to cause these functional deficits. The lens capsule becomes thicker and stiffer until the age of thirty-five then plateaus (Krag and Andreassen 2003; Krag et al. 1997). The lens cortex stiffens until the age of forty then declines (Fisher 1971; Krag and Andreassen 2003; Wilde et al. 2012), while stiffness of the nucleus dramatically increases after the age of thirty (Wilde et al. 2012). Computational modeling has demonstrated that age-related changes in lens stiffness can certainly lead to deficits in lens deformation required for accommodation (Burd et al. 2002; Wilkes and Reilly 2016). However, the functional losses predicted by these models did not account for the full decline in accommodative amplitude demonstrated in presbyopia. Evidence that the ciliary muscle decreases in contractility with age may explain changes in its excursion. Quantification of human ciliary morphology at different ages revealed muscle atrophy, increased intramuscular connective tissue, and fiber reorganization(Tamm et al. 1992) which would all effect muscle excursion. If the excursion of the muscle is reduced then it can no longer alter tension transmitted the lens via the zonules, which allows the lens to deform. Ciliary muscle excursion may also become impeded with age by stiffening of its posterior attachments. The sclera has consistently been found to stiffen linearly with age with different mechanical testing of samples from donors of different ages (Boote et al. 2020; Friberg and Lace 1988; Geraghty et al. 2012; Grytz et al. 2014). Other tissues properties change with age too, like the choroid (Friberg and Lace 1988; Tamm 1992; Tamm et al. 1991; Ugarte, Hussain, and Marshall 2006). There are changes in the anatomy of the aging eye that might also contribute to presbyopia by altering how tissues deform as they interact in accommodation. The lens is

believed to grow throughout life and increases in its dimensions have been measured *in vivo* (Richdale et al. 2013; Strenk et al. 1999) and in isolation (Glasser and Campbell 1999; Urs et al. 2009). The resting width and position of the ciliary muscle apex (its widest point) has also been found to change with age (Strenk et al. 1999; Tamm et al. 1992). Attachment locations of the zonules also differ (Farnsworth and Shyne 1979). Dimensional differences also suggest that the *in vivo* stress state of the lens is altered with age, though no experimental evidence exists to confirm this. While many age-related changes have been measured, it remains unclear how all of these changes interact, nor do we completely understand what happens as the eye ages.

Due to the uncertainty of the pathophysiology of presbyopia, many approaches exist to treat or correct this condition. The most rudimentary and most common correction for presbyopia is with an optical device placed in front of the visual system, i.e., reading glasses (Croft et al. 2001; Glasser 2008; Wolffsohn and Davies 2019). Most spectacles used by presbyopia patients have lenses to improve near vision and distance vision is achieved by removing them. More sophisticated designs (e.g., bifocals, progressive lens) allow the wearer to vary optical power by directing their gaze through different areas of the lens. Monovision takes advantage of the two eyed visual system by adjusting one for near vision and the other for distance using contact lenses, intraocular lenses, or laser refractive surgery (Wolffsohn and Davies 2019). These corrective strategies don't actually restore accommodative ability but rather provide incomplete corrections for presbyopia symptoms. Efforts have been made to soften the lens using lasers or pharmaceuticals (Wolffsohn and Davies 2019). Replacing the lens is an appealing alternative as artificial intraocular lenses (IOL) are widely used to correct other visual impairments, like cataracts. The design of "accommodating" IOLs that can adapt and interact with the accommodative mechanism have reached significant barriers (Glasser 2008; Wolffsohn and Davies 2019). Other treatments to restore accommodation have focused on extralenticular structures. Some presbyopia treatments have employed pharmaceuticals or electro-stimulation to increase ciliary muscle contraction (Wolffsohn and Davies 2019). Sclera surgeries also offer potential for restoring accommodative function, rather than correcting

vision (Boote et al. 2020; Hipsley, Hall, and Karolinne M Rocha 2018). There have been mixed results of early attempts at sclera surgeries using implants which has called the biomechanical justification for treating presbyopia at the sclera into question (Glasser 2008; Hipsley, Hall, and Karolinne M Rocha 2018; Wolffsohn and Davies 2019). Extralenticular treatments do not directly alter the visual axis, so these procedures involve a lower risk of vison lost (Hipsley, Hall, and Karolinne M Rocha 2018). Work is needed to understand which treatments for presbyopia might be most effective and what is the appropriate age that patients should receive these treatments.

2.4 Triceps Surae and Achilles Tendon Anatomy and Function

The triceps surae is group of muscles that are the primary occupants of the superficial posterior compartment of the lower leg (Dalmau-Pastor et al. 2014; Netter 2014). Often referred to as the gastrocnemius-soleus complex or simply the calf muscles, the triceps surae comprises the gastrocnemius and soleus muscle which share a common tendon: the Achilles or calcaneal tendon. These muscles differ significantly in their structure. The gastrocnemius comprises two unipennate muscle heads, medial and lateral, that originate via proximal tendons on either side of the posterior aspect of the distal femur. As the gastrocnemius inserts onto the calcaneus via the Achilles tendon, it is a biarticular muscle, spanning both the knee and ankle joints. The soleus has long narrow attachments to the tibia and fibula, therefor the muscle only spans the ankle and is uniarticular. The soleus and gastrocnemius also differ greatly in volume (Bolsterlee, D'Souza, and Herbert 2019; Handsfield et al. 2014; Ward et al. 2009), pennation angles (Bolsterlee et al. 2019; Rana, Hamarneh, and Wakeling 2013; Ward et al. 2009), fascicle lengths (Bolsterlee et al. 2019; Cronin et al. 2013; Ward et al. 2009), fiber types (Johnson et al. 1973), and aponeurosis structure (Dalmau-Pastor et al. 2014; Shan et al. 2019).

The soleus has the largest physiological cross sectional area (PCSA) of human lower limb muscles (Ward et al. 2009) due to its large volume (Handsfield et al. 2014) and relatively short fascicles (~10% of the muscle length) (Bolsterlee et al. 2018). The soleus's fascicles are organized into multiple compartments (Agur et al. 2003; Bolsterlee et al. 2018; Hodgson et al. 2006; Sopher et al. 2017), and the

fascicle architecture of these compartments differ in lengths and pennation angles. Soleus architecture is further complicated by morphologically complex aponeuroses structures (Finni et al. 2003a; Hodgson et al. 2006). The soleus' sheet-like anterior aponeurosis attaches proximally to the tibia and fibula, at the muscle surface without an external proximal tendon. The anterior aponeurosis forms a U-shape in cross section so that it is mostly internal over the length of the muscle (Hodgson et al. 2006). The anterior aponeurosis separates the anterior and posterior compartments and serves as the origin of fascicles from both (Bolsterlee et al. 2018). The posterior aponeurosis is continuous with the Achilles at the muscle-tendon-junction (MTJ), and fascicles in the posterior compartment insert onto its anterior surface. While the posterior aponeurosis primarily covers the posterior surface of the soleus, a protrusion called the medium septum extends from approximately the center of the anterior surface of the posterior aponeurosis, though its medial-lateral location varies between individuals (Bolsterlee et al. 2018; Hodgson et al. 2006). The median septum spans the posterior compartment distally then diverges from the posterior aponeurosis proximally to protrude through a gap in the anterior aponeurosis into the anterior compartment, whose fascicles insert onto it. As the posterior aponeurosis interdigitates with the anterior aponeurosis via the median septum, fascicles in both compartments are in series with the Achilles tendon.

The Achilles free tendon is shared by the soleus and gastrocnemius and is the largest tendon in the body. The internal structure of the Achilles free tendon comprises three subtendons (Handsfield, Slane, and Screen 2016), which are distinguishable groups of fascicles that originate from either the gastrocnemius lateral head, medial head, or soleus. These subtendons have been observed in cadavers to twist around each other before inserting into the calcaneus (Cummins and Anson 1946; Edama et al. 2015; Szaro et al. 2009). The twisted structure occurs in all Achilles tendons and the direction of twist is consistent across individuals but the amount of subtendon twist varies between individuals (Cummins and Anson 1946; Edama et al. 2015; Pękala et al. 2017). The Achilles tendon inserts onto the posterior aspect of the calcaneus (Dalmau-Pastor et al. 2014; Netter 2014), but due to variations in twist the attachment area can vary between subtendons (Pękala et al. 2017; Szaro et al. 2009). The soleus MTJ marks the

proximal boundary of the Achilles free tendon. A wide thin tendon, that is continuous with the gastrocnemius subtendons, extends proximally over the posterior surface of the soleus to the MTJs of the gastrocnemius medial and lateral heads. Definitions of the Achilles tendon vary to only describe the free tendon, between the calcaneus and distal soleus MTJ, or the full tendon that is external to the triceps surae muscles, spanning the calcaneus to distal gastrocnemius MTJ.

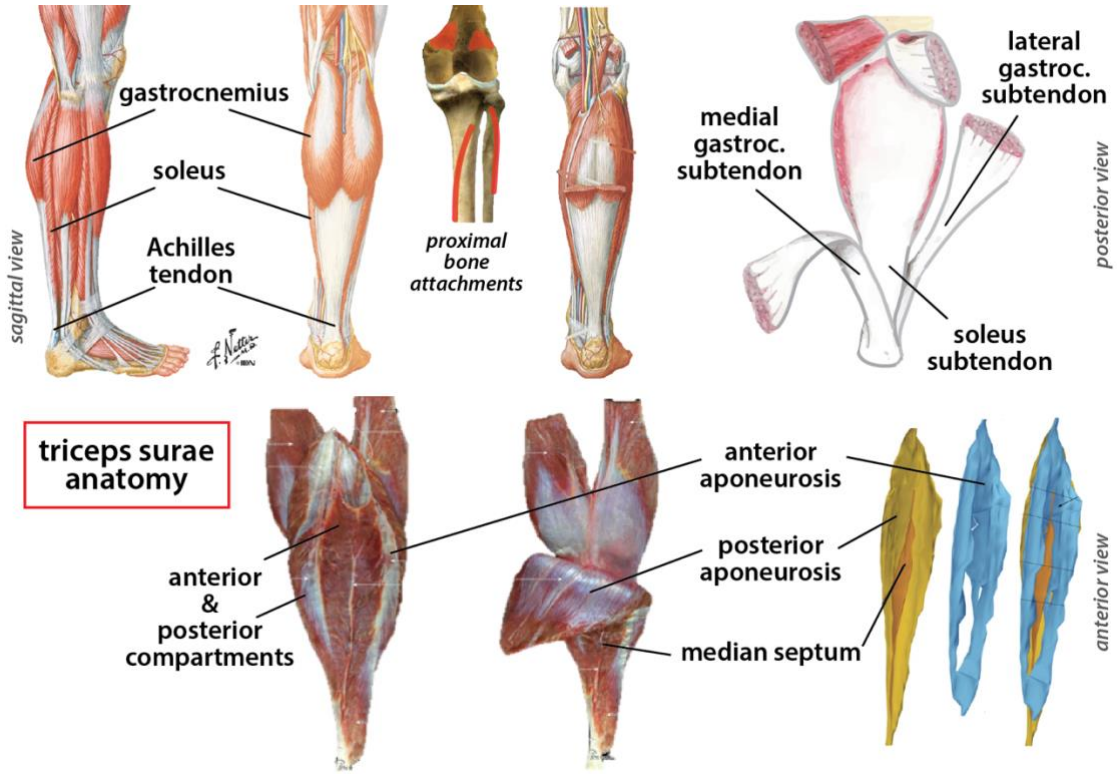

Figure 2.4: Anatomy of the Triceps Surae. The triceps surae group comprises the two-headed biarticular gastrocnemius muscle which originates on the femur and the multicompartment uniarticular soleus muscle which originates on the tibia and fibula. These muscles insert on the calcaneus through their shared connection in the Achilles tendon, which is divisible into subtendons associated with each muscle. The soleus' compartments are bounded by its interdigitating aponeuroses. (adapted from Dalmau-Pastor et al. 2014, Hodgson et al. 2006, Netter 2014, and Szaro et al. 2009)

The biarticular gastrocnemius and the uniarticular soleus both play vital roles in walking, as they activate in the mid- and terminal stance phases of gait (Anderson and Pandy 2003; McGowan, Neptune, and Kram 2008; Neptune, Kautz, and Zajac 2001). Empirical (Francis et al. 2013) and modeling studies (Anderson and Pandy 2003; Clark, Pimentel, and Franz 2020; Neptune et al. 2001) have demonstrated

differences in how these muscles affect whole-body motion, as they respectively contribute more to forward propulsion and to vertical support. The Achilles tendon experiences substantial loading as it transmits forces developed by these muscles. Achilles tendon dynamics play a significant role in muscle function in the production of movement (Lichtwark and Wilson 2007; Orselli, Franz, and Thelen 2017; Uchida et al. 2016). The Achilles tendon stores and returns energy as it stretches and recoils (Lichtwark and Wilson 2005; Zelik and Franz 2017). Measurements of *in vivo* tendon dynamics have been used to determine material properties of the Achilles tendon (Kubo et al. 2002; Lichtwark and Wilson 2005; Onambele et al. 2006; Stenroth et al. 2012), although characterization of *in vivo* tendon behavior from non-invasive measurements are dependent on the assumptions of the analysis (Zelik and Franz 2017).

Kinematics of triceps surae tissue has been used to better understand role of muscle-tendon interaction producing movement. Non-uniform displacements have been observed in the *in vivo* free tendon during walking, providing evidence of complex loading conditions. Visualized using ultrasound imaging, the deep portion of the Achilles tendon displaces more than the superficial portion between toe-off and mid-stance, indicating greater elongation of this region (Franz et al. 2015). A finite element model of Achilles subtendons (Handsfield, Inouye, et al. 2017) demonstrated how sliding and differential loading are possible mechanisms underlying observed nonuniform tendon displacements (Slane and Thelen 2015). The triceps surae muscles apply different forces to the Achilles tendon (Arndt et al. 1998), and recent imaging with dual ultrasound probe found differing muscle fascicle length changes that correspond with the differential tendon displacements associated with the respective subtendons of the gastrocnemius and soleus. Due to the triceps surae muscles' large compliant tendons and complex architecture, the relationship between fascicle kinematics measured in a small region of the muscle and the production of movement remains difficult to intuit.

2.5 Age-related Walking Deficits

A recent study found that 22% of older adults self-reported having difficulties walking that affected their ability to perform daily tasks (U.S. Department of Health and Human Services. 2018).

Survival rates in this population are strongly associated with their walking speed (Studenski et al. 2011), and reduced plantarflexion power output at the ankle is the biomechanical factor most associated with impaired gait characterized by a decline in walking speed (Boyer et al. 2017; DeVita and Hortobagyi 2000; Franz 2016; Kerrigan et al. 1998; McGibbon 2003; Winter et al. 1990). As deficits at the ankle increase, older adults adapt by increasing power production at the hip with a distal-to-proximal shift in muscle coordination (DeVita and Hortobagyi 2000; McGibbon 2003).

Diminished ankle power production in older adults might be attributable to changes in their muscles. Sarcopenia and muscle weakness have been well documented during aging (Brooks and Faulkner 1994; Dufour et al. 2013; Faulkner et al. 2007; Janssen et al. 2000; Morse et al. 2004; Narici and Maganaris 2007). Evidence that older adults can improve muscle strength through exercise but still experience deficits in walking suggests that muscle weakness alone is not the cause of dysfunction. Also, older adults have demonstrated an ability to draw upon a propulsive reserve in response to increased demands such as uphill walking or to biofeedback (Franz and Kram 2014; Franz, Maletis, and Kram 2014). Independent triceps surae muscle function may be diminished with age if subtendon interactions are altered (Chavaunne T. Thorpe et al. 2013), a theory supported by observations of reduced differential displacements in the Achilles tendons of older adults (Franz and Thelen 2015). Furthermore, differences exhibited by older adults in tendon deformation were well correlated with changes in these subjects' change in peak ankle power (Franz and Thelen 2015). Dual ultrasound imaging has revealed that more uniform tendon displacements in older adults correspond with more uniform fascicle behavior between the gastrocnemius and soleus (Clark and Franz 2020).

In contrast to muscle size changes with age, the Achilles tendon cross-sectional area (CSA) is maintained or even increased (Onambele et al. 2006; Stenroth et al. 2012). An additional age-related tendon change that has been documented is increasing compliance (Onambele et al. 2006; Stenroth et al. 2012), which may also impact triceps surae function. Simulations have indicated that altered tendon compliance affects gastrocnemius and soleus efficiency, operating length, and power production (Franz

and Thelen 2016; Lichtwark and Wilson 2007; Orselli et al. 2017; Uchida et al. 2016). If changes with age are the result of tendon constitutive changes that also extend to the aponeuroses it could affect the 3D deformations of these muscles in non-intuitive ways (Arellano et al. 2016; Azizi, Halenda, and Roberts 2009; Azizi and Roberts 2009). While aponeurosis properties have not been compared in humans of different ages, studies in rats have shown correlations between differences in transverse aponeurosis stiffnesses and dynamic muscle function (Holt et al. 2016).

Effective gait interventions could extend life expectancy and improve quality of life in older individuals. A fundamental understanding of the role that complex muscle architecture plays in walking and how that role is altered by age-related changes to connective tissues is necessary to design such interventions.

2.6 Three-Dimensional Modeling of Muscle and Connective Tissues

Biomechanical modeling provides an opportunity to synthesize different experimental measurements and observations to create a more complete understanding of geometry and mechanics of complex muscle systems, however, many challenges exist in representing the multiscale properties of muscle and connective tissue dynamics. Muscle has a nonlinear stress-strain relationship that varies with time due to activation dynamics (Blemker et al. 2005; Zajac 1989). At the tissue level, muscle exhibits large variations in force production and strain patterns due to architectural complexity (Blemker and Delp 2005; Blemker et al. 2005; Fiorentino and Blemker 2014). Muscle's connection to tendons, aponeurosis, and other connective tissues create complex boundary conditions on muscle displacement (Blemker and Delp 2005; Blemker et al. 2005; Fiorentino and Blemker 2014; Inouye et al. 2016), acting both in series and parallel with the fibers (Epstein, Wong, and Herzog 2006; Zajac 1989). Force transmission to joints or soft tissues that determines motion is the result of several muscles working synergistically, adding redundancy to the system (Herzog 2017; Zajac 1993; Zajac and Gordon 1989).

Because of these challenges, current models have been limited in their representation of complex muscle-driven systems like those responsible for accommodation and plantarflexion. In the context of

accommodation, many previous modeling studies investigated the accommodative mechanism by probing the relationship between the material properties and the accommodative potential of the isolated lens. These models developed detailed geometric and constitutive representations of the lens with simplified representation of the zonules, which apply traction to the accommodated lens to simulate disaccommodation (Abolmaali, Schachar, and Le 2007; Burd et al. 2002; Liu et al. 2006; Ljubimova, Eriksson, and Bauer 2008; Schachar, Abolmaali, and Le 2006; Stachs et al. 2006), ignoring the complex dynamics of ciliary muscle excursion. A more recent model included the effects of initial zonule tension on lens accommodation (Wilkes and Reilly 2016), demonstrating the forward dynamics of relieving tension applied to the lens. Similar to previous models, the simulated changing traction was achieved by prescribing a displacement to the simplified zonules and did not represent the 3D excursion that occurs during contraction of the multi-sectioned ciliary muscle.

In the context of plantarflexor function, computer simulations of gait have demonstrated the influential role that muscle-tendon interaction plays in the production of movement (Lichtwark and Wilson 2007; Orselli et al. 2017; Uchida et al. 2016) as well as the vital contributions of the plantarflexor muscles (Anderson and Pandy 2003; Dorn, Schache, and Pandy 2012; Neptune et al. 2001). These simulations often represent muscle-tendon units using a "lumped-parameter" model for multiple muscles represented as isolated one-dimensional (1D) actuators with tendon and aponeurosis in series with the muscle fascicles (Delp et al. 1990; Millard et al. 2013; Zajac 1989). The assumption that muscles behave independently is not true for the triceps surae which share a common distal tendon, and simulations with varied coupling of the gastrocnemius and soleus actuators show differences in the predicted muscle-tendon dynamics (Franz and Thelen 2016). Non-uniform strains have been measured during *in vivo* function of muscles with complex fiber arrangement (Fiorentino, Epstein, and Blemker 2012; Pappas et al. 2002) and 3D models of these muscles that replicate observed behavior and architecture predict very different results than simplified 1D simulations (Blemker and Delp 2005, 2006; Blemker et al. 2005; Fiorentino and Blemker 2014). The triceps surae muscles have very complex fiber architecture and

deformation (Agur et al. 2003; Bolsterlee et al. 2017, 2018, 2019; Kawakami, Ichinose, and Fukunaga 1998; Rana et al. 2013; Rana, Hamarneh, and Wakeling 2014) which must be considered in examining their force production for human movement. The 1D models also lump aponeurosis and tendon as an elastic element that is purely in series with muscle, but the mechanical relationship between these structures is far more complicated. The aponeuroses behavior is both parallel and in series with the muscle fascicles (Epstein et al. 2006; Raiteri 2018). Aponeuroses experience biaxial loading due to the isovolumetric properties of muscle that is different than the uniaxial loading of the free tendon (Arellano et al. 2016; Azizi and Roberts 2009). The triceps surae muscles, especially the soleus, have large aponeuroses with unique morphology (Finni et al. 2003a; Hodgson et al. 2006; Shan et al. 2019) and non-uniform strains have been measured in the aponeuroses (Finni et al. 2003b; Lee et al. 2006) and the free tendon (Farris et al. 2013; Franz et al. 2015; Slane and Thelen 2014).

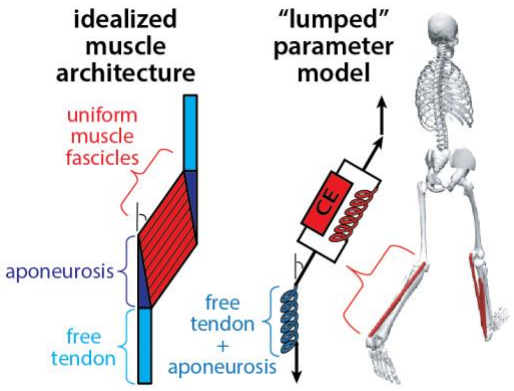

Figure 2.5: One-dimensional modeling of muscle

Also 1D models rely on calculation of a muscle-tendon unit's (MTU) moment, and it is assumed that this parameter quantifies how effectively that muscle contributes to producing a moment at a joint of interest (Sherman, Seth, and Delp 2013). This quantification of muscle effectiveness comes from a simple mechanical relationship and can be calculated in multibody dynamics using the tendon excursion method, assuming that moment arm is only a function of rigid body kinematics (An et al. 1984; Murray, Delp, and Buchanan 1995; Sherman et al. 2013). This assumption becomes invalid as MTUs undergo large tissue deformations. It has been shown that Achilles tendon moment arms estimated with tendon

excursion do not correspond with estimates made using musculoskeletal geometry (Baxter and Piazza 2018). For muscles like the triceps surae with large compliant tendons and complex fiber architecture, the relationship between fiber excursion and the production of movement is less intuitive than a simple mechanical quantity that can transform a single muscle force into a joint torque. In the case of the soleus which has multiple compartments (Agur et al. 2003; Bolsterlee et al. 2018), a single set of architectural parameters derived from a sample of the muscle fascicles does not accurately quantify the contributions of the whole muscle. Many muscles, like the ciliary muscle of the eye, have functions that are characterized by their role in deforming soft tissue structures rather than manipulating boney kinematics. In these cases, the relationship describing the effectiveness of the muscle in producing adynamic outcome becomes less straightforward. Therefore, 3D models that address these challenges and limitations of previous models are needed to understand the multifaceted behavior of muscle-connective tissue interactions in order to determine how 3D muscle excursions produce functional motion.

Finite element modeling enables representation of muscle and connective tissue behavior that spans the scale of their hierarchical organizations. Constitutive formulas used to define these biological materials mathematically describe the behavior of proteins, like actin-myosin dynamics within muscle sarcomeres or collagen straightening within the extracellular matrix (Blemker et al. 2005; Weiss, Maker, and Govindjee 1996). Complex multipart geometry of organ-level anatomy can be explicitly represented with 3D element meshes and material directions assigned to the elements can characterize internal architecture from cellular organization. Boundary conditions then integrate models into organism function, with assignments representing multibody dynamics and coordinated neuroactivations.

Members of the Multiscale Muscle Mechanophysiology Lab have utilized finite element modeling for numerous applications to investigate 3D muscle function. FE modeling has been used to understand the three-dimensional shape changes associated with multiple muscles that have complex fiber architectures (Blemker and Delp 2005; Blemker et al. 2005; Fiorentino et al. 2014; Fiorentino and Blemker 2014). These models have predicted non-uniform strains in the muscle tissue and fascicles

models and have in some cases enabled fascicle behavior and tissue deformation to be related directly to aponeurosis morphology (Fiorentino and Blemker 2014; Rehorn and Blemker 2010). Models of the musculature of the palate have been used to tor investigate the role of these muscles in the production of speech, demonstrating how muscle excursions mechanically affect the displacements of the soft tissues around them (Inouye et al. 2015). A model of the Achilles subtendons demonstrated how boundary conditions defining the interaction of multiple tissue structures affect predicted tissue deformations, by simulating inter-subtendon sliding and prescribed muscle loading (Handsfield, Inouye, et al. 2017). In multiple applications, models were built from high resolution images enabling the representation of anatomic and subject-specific geometry (Blemker and Delp 2005; Handsfield, Inouye, et al. 2017). Further, predictions by many of these models have been successfully validated with dynamic imaging of *in vivo* tissue motion (Blemker and Delp 2005; Blemker et al. 2005; Fiorentino et al. 2014), demonstrating their unique ability to predict *in vivo* function of muscle-connective tissue systems. This prior work has inspired and motivated the FE modeling applications described in this dissertation.

Transversely isotropic constitutive model for muscle and connective tissue

In this work, complex smooth (ciliary) and skeletal (soleus) muscle and connective tissues (zonules, tendon, aponeurosis) were modeled as transversely isotropic, hyperelastic, quasi-incompressible material (Blemker et al. 2005). The stress and strain of hyperelastic materials are related through the 2nd Piola-Kirchoff stress tensor ($\boldsymbol{S}$), the right Cauchy-Green deformation tensor ($\boldsymbol{C}$), and the strain energy density function (Φ):

$$\boldsymbol{S} = 2\frac{\partial \Phi}{\partial \boldsymbol{C}} \qquad \text{Equation 2.1}$$

Strain energy density function determines tissue deformation in response to assigned boundary conditions and this constitutive model uses an uncoupled form to simulate nearly incompressible behavior (Weiss et al. 1996). This model separates the dilatational (volumetric – Φ_{vol}) and deviatoric (distortional – Φ_{iso}) tissue responses and utilizes physically-based strain invariants (Criscione, Douglas, and Hunter 2001;

Weiss et al. 1996) that relate material parameters to physically meaningful measures resulting in the following strain energy density function:

$$\Phi(J, B_1, B_2, \lambda) = \Phi_{vol}(J) + \Phi_{iso}(B_1, B_2, \lambda) \quad \text{Equation 2.2}$$

$$\Phi_{vol}(J) = \frac{K}{2} ln(J)^2 \quad \text{Equation 2.3}$$

$$\Phi_{iso}(B_1, B_2, \lambda) = G_1 {B_1}^2 + G_2 {B_2}^2 + W_3(\lambda) \quad \text{Equation 2.4}$$

Volumetric changes are penalized in dilatational portion (Equation 2.3) where J is the relative volume change and K is the bulk modulus of the tissue. The terms in the deviatoric portion (Equation 2.4) represent strain energy contributions from the along-fiber shear (B_1), cross-fiber shear (B_2), and along-fiber stretch (λ). G_1 and G_2 are the along- and cross-fiber shear moduli.

For connective tissue, the function for the strain energy associated with along-fiber stretch ($W_3(\lambda, p_z)$) characterizes the relationship between Cauchy stress in the tissue (σ) and the fiber stretch (λ) and is defined with an exponential piece-wise stress-strain relationship:

$$\lambda \frac{\partial W_3}{\partial \lambda} = \begin{cases} \sigma(\lambda, p_z) = P_1\left(e^{P_2(\lambda - 1 + p_z)} - 1\right) & 1 - p_z < \lambda < \lambda^* - p_z \\ \sigma(\lambda, p_z) = P_3\lambda + P_4 & \lambda \geq \lambda^* - p_z \end{cases} \quad \text{Equation 2.5}$$

λ^* represents the fiber stretch at which σ becomes linear and P_3 and P_4 were defined so σ is C^0 & C^1 continuous at $\lambda = \lambda^*$. The parameter p_z was added in order to vary the initial tension in connective tissue by shifting the stress-stretch curve during a prescribed model initialization period and has a value of zero when no initial tension is applied. The along-fiber stretch strain energy function ($W_3(\lambda, \alpha)$) for muscle includes summed passive ($f_{passive}$) and active (f_{active}) fiber force contributions that are related to the maximum isometric stress (σ_{max}) which occurs at the optimal fiber stretch (λ_{ofl}):

$$\lambda \frac{\partial W_3}{\partial \lambda} = \sigma_{max}\left[f_{passive}(\lambda) + \alpha f_{active}(\lambda)\right]\lambda/\lambda_{ofl} \quad \text{Equation 2.6}$$

Passive fiber force takes an exponential piece-wise form (Equation 2.5), and active fiber force is defined with a piece-wise quadratic form that is scaled by the activation (α) during simulations:

$$f_{active}(\lambda) = \begin{cases} 9\left(\frac{\lambda}{\lambda_{ofl}} - 0.4\right)^2 & \lambda \geq 1.4\lambda_{ofl} \\ 9\left(\frac{\lambda}{\lambda_{ofl}} - 1.6\right)^2 & \lambda \leq 0.6\lambda_{ofl} \\ 1 - 4\left(1 - \frac{\lambda}{\lambda_{ofl}}\right)^2 & 0.6\lambda_{ofl} < \lambda < 1.4\lambda_{ofl} \end{cases} \quad \text{Equation 2.7}$$

This constitutive formula was implemented in two finite element solvers for the work in this dissertation: AMPS (AMPS Technologies, Pittsburgh, PA) and FEBio (Maas et al. 2012). Descriptions of how simulations using these solvers were performed and the parameters chosen are described for each model in the following chapters.

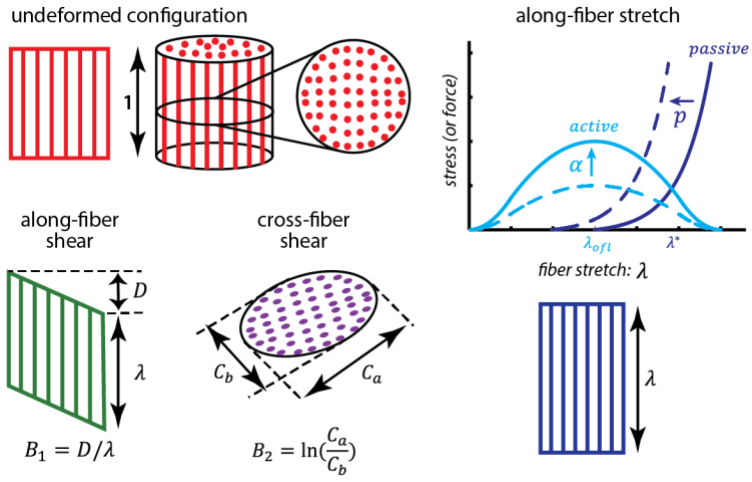

Figure 2.6: Physically-based strain invariants. The deviatoric strain energy density function includes contributions from along-fiber shear, cross-fiber shear, and along fiber stretch. The along-fiber stretch-stress relationship for connective tissues can be shifted during simulations by increasing the tension parameter (p_z). The along-fiber active force component of the stress-stretch relationship for muscle tissues be scaled during simulations by increasing the activation (α). (figure adapted from Blemker et al. 2005)

Representation of 3D fiber and fascicle architecture

For the transversely isotropic material formulation, each element is assigned a local fiber direction. To generate fiber architecture within a geometrically complex volume we use a tractography method that utilizes Laplacian flow simulations (Handsfield, Bolsterlee, et al. 2017). Performed with computational fluid dynamics software (Autodesk CFD – Autodesk Inc. San Rafael, CA), simulations of highly viscous, incompressible, laminar flow within the geometry are bounded by assigning inlet and

outlet regions. Inlet regions are assigned by applying a pressure condition of zero to model surfaces which serve as fiber origins, and outlet regions are assigned by applying a pressure condition of one to model surfaces which serve as fiber insertions. All other surfaces in the model geometry are prescribed with slip boundary conditions. Flow guides can be implemented to constrain simulation results by creating additional impenetrable slip surfaces which subdivide the model volume and contain flow withing a specific region (Handsfield, Bolsterlee, et al. 2017). Flow guides were used in several cases to enforce fascicle orientations to be consistent with *in vivo* physiology.

To generate muscle fascicle architecture, streamlines are mapped through the model's field of local fiber direction vectors, traveling in one or two directions from designated seed points using Matlab (Mathworks Inc., Natick, MA, US). Fascicle tracts created from the points defining the streamlines as the propagate through the model geometry and terminate at the edge of the fiber vector field using a method adapted from Bolsterlee et al., 2017. All nodes outside of the model volume are deleted to truncate the fascicle tracts. To constrain fascicle tracts to begin on the origin surface and end on the insertion surface, tracts are then extrapolated to those surfaces. Fascicle tract length is computed from the distances between the set of points that define it. Pennation angles are defined as the average of the angles between the tract and the terminating surface at each end. Points defining the fascicle tracts are mapped to parent elements within the finite element model mesh in order to compute changes in these architectural parameters from simulation predictions.

Chapter 3

The action of ciliary muscle contraction on accommodation of the lens explored with a 3D model

"Begin each day by asking a question. Let the answer lead you to another question and you will discover that learning and knowledge are an infinite playground."

– Dr. Patricia Bath, *The Doctor with an Eye for Eyes*

3.1 Abstract

The eye's accommodative mechanism changes optical power for near vision. In accommodation, ciliary muscle excursion relieves lens tension, allowing it to return to its more convex shape. Lens deformation alters its refractive properties, but the mechanics of ciliary muscle actions are difficult to intuit due to the complex architecture of the tissues involved. The muscle itself comprises three sections of dissimilarly oriented cells. These cells contract, transmitting forces through the zonule fibers and extralenticular structures. This study aims to create a finite element model (FEM) to predict how the action of the ciliary muscle sections leads to lens displacement. The FEM incorporates initialization of the disaccommodated lens state and ciliary muscle contraction, with three muscle sections capable of independent activation, to drive accommodative movement. Model inputs were calibrated to replicate experimentally measured disaccommodated lens and accommodated ciliary muscle shape changes. Additional imaging studies were used to validate model predictions of accommodative lens deformation. Models were analyzed to quantify mechanical actions of ciliary muscle sections in lens deformation and position modulation. Analyses revealed that ciliary muscle sections act synergistically: the circular section contributes most to increasing lens thickness, while longitudinal and radial sections can oppose this action. Conversely, longitudinal and radial sections act to translate the lens anteriorly with opposition from the circular section. This FEM demonstrates the complex interplay of the three sections of ciliary muscle in deforming and translating the lens during accommodation, providing a useful framework for future investigations of accommodative dysfunction that occurs with age in presbyopia.

3.2 Introduction

The accommodative mechanism of the eye is a complex dynamic system responsible for modifying optical power to see objects clearly when changing focus from far to near. While refractive change is the direct result of changing curvature and anterior position of the lens, lens displacement occurs as a response to excursion of the ciliary muscle (Croft et al. 2001; Helmholtz 1855). Previous imaging studies have demonstrated that the ciliary muscle functions similar to a sphincter; when

activated, the ciliary muscle moves anteriorly and centrally and its inner circumference decreases (Croft, McDonald, et al. 2013). The ciliary muscle is connected to the lens via a complex network of suspensory ligaments called zonules (Hogan et al. 1971; Kaufman et al. 2003), which hold the lens in tension while the muscle is resting (Figure 2.2A). Contraction of the ciliary muscle causes a release in tension in the zonules, leading to relaxation and movement of the lens (Figure 2.2B) (Croft, McDonald, et al. 2013; Croft et al. 2001; Helmholtz 1855; Hogan et al. 1971; Kaufman et al. 2003).

Accommodative function is dependent on the complex action of the ciliary muscle; an action that is complicated by the muscle's architecture and its interaction with surrounding tissue. The ciliary muscle comprises three sections in which bundles of muscle cells are oriented either longitudinally, radially, or circularly (Hogan et al. 1971; Kaufman et al. 2003; Tamm et al. 1992). The influence of muscle architecture on tissue excursion is well established in a variety of skeletal muscles (Blemker and Delp 2005; Lieber and Fridén 2000); however, the role of the ciliary muscle's unique architecture in determining its action is difficult to probe experimentally. Furthermore, the excursion of the ciliary muscle is constrained by its attachments to extralenticular structures, including the choroid and sclera, making them essential mechanical components to consider when investigating accommodative function.

Because the ciliary muscle does not contact the lens directly, influence of its excursion is transmitted via the zonules and is therefore regulated in part by their configuration. The zonules are a network of fibers distributed radially around the lens and organized into divisions identified by their origin and insertion points, which vary in their proximity to the ciliary muscle. Newly developed computer animations have illustrated the complex geometric arrangement of the zonules in accommodation (Goldberg 2011, 2015), raising questions about the relationship between ciliary muscle structure and accommodative function. Importantly, how do the three sections of the ciliary muscle independently and collectively influence lens deformation and anterior translation? The answer to this question is important because it has significant implications on the biomechanics of accommodation and presbyopia, which is the inevitable loss of accommodative function occurring with age (Croft et al. 2001).

The specific actions of the ciliary muscle cannot be discerned from geometry of the system alone due to the complex biomechanical interactions that occur in accommodation. Further, it is difficult to glean answers from experiments because muscle function cannot be isolated *in vivo*.

Physics-based computer models provide a powerful framework for investigating the complex mechanical properties of biological structures. Many previous modeling studies probed connections between the material properties of structures within the eye and the accommodative potential of the lens. These models developed detailed geometric and constitutive representations of the lens with varying complexity in their representation of the zonules, which apply traction to the accommodated lens (Burd et al. 2002; Liu et al. 2006; Ljubimova et al. 2008; Schachar et al. 2006; Stachs et al. 2006). More recent models have included the effects of initial zonule tension on lens accommodation (Wilkes and Reilly 2016), demonstrating the importance of 3D ciliary muscle excursion to relieve zonular tension. Understanding the accommodative mechanism requires more complete knowledge of how the architecture of the ciliary muscle, in particular the relative arrangement of the three sections, enables the muscle to drive displacement of the lens.

Previous work by our group has utilized finite element modeling of muscle to understand the three-dimensional shape changes associated with muscles that have complex fiber architectures (Blemker and Delp 2005; Blemker et al. 2005; Fiorentino et al. 2014; Fiorentino and Blemker 2014) and how these muscle excursions mechanically affect the displacements of the soft tissues around them (Inouye et al. 2015). Further, predictions by these models have been successfully validated with dynamic imaging of *in vivo* tissue motion (Blemker and Delp 2005; Blemker et al. 2005; Fiorentino et al. 2014), demonstrating their unique ability to predict *in vivo* function of muscles.

In the present study, we aim to leverage these developments in finite-element muscle modeling along with newly developed imaging techniques that track synchronous changes in the lens and ciliary muscle (Ruggeri et al. 2016), to create and test a simulation of the accommodative mechanism that is driven by ciliary muscle tissue contraction. Specifically, the goals of this work were to: (I) create a finite

element model of the accommodative mechanism that is driven by active contraction of the three-part ciliary muscle; (II) use previously published experimental measurements to calibrate activations of the ciliary muscle sections required for accommodative muscle excursions and perform independent testing to confirm the accuracy of the resulting lens deformation; and (III) use the model to quantify the mechanical actions of the ciliary muscle sections in deforming and translating the lens during accommodative function.

3.3 Methods

3.3.1 Model Components

We developed a 3D model of the accommodative mechanism that represents the anterior portion the human eye of an average 30-year-old human by incorporating geometric measurements from over 20 published studies *(see Table 3.1 for a detailed list of studies and measurements).* The posterior portion of the eye was assumed to have a negligible effect on accommodative movement, per previous studies (Croft, Nork, et al. 2013). The model was assumed to be radially symmetric because it has been shown that there is little difference in accommodative behavior of the nasal and temporal sides (Croft, McDonald, et al. 2013). The key components of the model included: the sclera, the cornea, the choroid, the vitreous membrane, the lens, the zonules, and the ciliary muscle. The shape of each of these components was generated by creating outlines of the boundary in a two-dimensional symmetry plane (Figureb), ensuring that the shape followed the published measurements. These outlines were then revolved by 90° about the central anterior-posterior axis to generate the 3D shape (Figure 3.1A).

With the exception of the lens capsule and the scleral spur, all the components of the model were meshed automatically into solid 4-node strain-enriched tetrahedral elements (AMPS Technologies, Pittsburgh, PA) (total of 260927 tetrahedral elements). The strain-enrichment improves the accuracy of low order elements by incorporating a dilatational strain formulation that avoids locking, while maintaining their robustness and lower computational cost by not increasing the number of nodes per

element. This formulation enables greater stability during non-linear simulation conditions for the tetrahedral mesh with varied density required for the model's complex geometry (Lin 2013). The lens capsule and the scleral spur were meshed automatically into triangular shell elements with uniform thickness (total of 1787 shell elements).

Boundaries between all adjacent structures were represented as shared surfaces, with the exception of intersecting zonules. Since the zonules comprise fibers that cross and slide with negligible friction *in vivo* (Croft, Nork, et al. 2013; Goldberg 2015), in the model, we assumed that the zonules did not interact in the regions that they intersect. All nodes located at the equator, the posterior face of the model, were fixed, per the assumption that the accommodative movement occurs in the anterior eye (Croft, Nork, et al. 2013). Nodes located on the two symmetry boundary planes at 0° and 90° were constrained to only move within that plane to impose symmetry boundary conditions (Figure 3.2A). Below we describe in detail our approach to defining the shape and material properties of each component in the model.

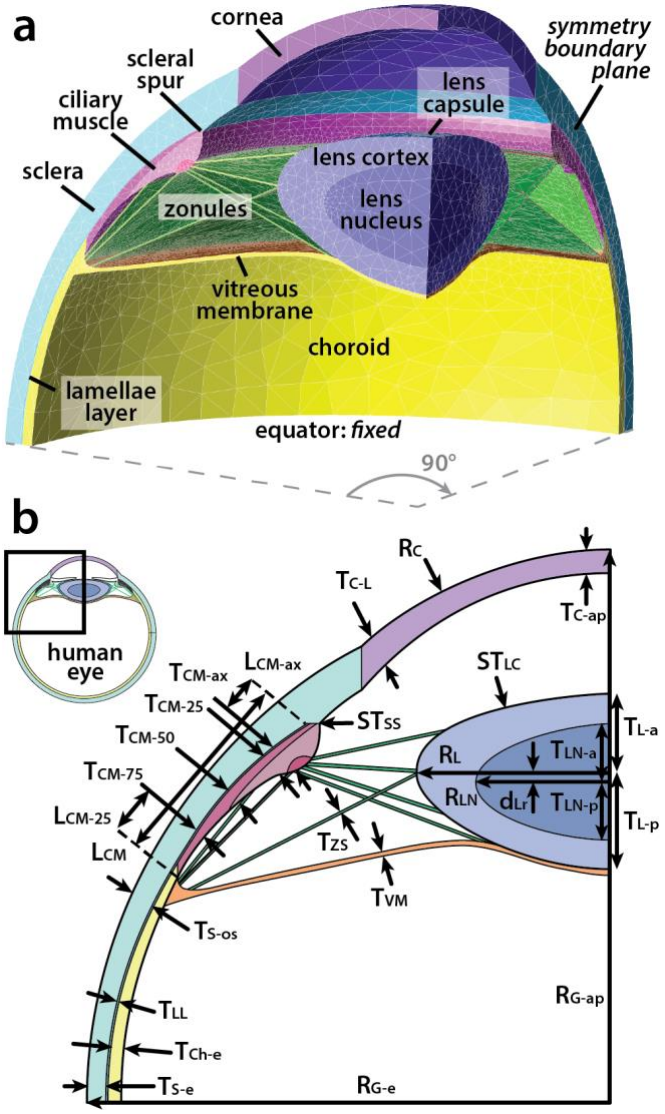

Figure 3.1: Structures and dimensions of the finite element model (a) The 3D finite element model of the anterior eye is axially symmetric and rotated 90° around the center pole and is subdivided into the following discrete regions: cornea, sclera, scleral spur, lamellae layer, choroid, vitreous membrane, lens (divided into capsule, cortex, and nucleus), ciliary muscle (divided into three sections), and zonule fibers (representing seven divisions as sheets). At the boundaries, nodes at the equator are fixed and nodes on the symmetry boundary planes are constrained to in-plane motion. **(b)** Dimensions of ocular geometry in the plane of symmetry are based on measurements from the imaging literature of healthy humans near 30 years old and listed in Table 3.1.

Table 3.1 Dimensions of ocular geometry in the plane of symmetry

Dimension	Label	Value (μm)	Source
Globe radius at equator	$R_{G\text{-}e}$	12,250	(Stitzel et al. 2002)
Globe radius at anterior pole	$R_{G\text{-}ap}$	13,530	(Stitzel et al. 2002)
Sclera thickness at equator	$T_{S\text{-}e}$	490	(Norman et al. 2010; Stitzel et al. 2002)
Choroid thickness at equator	$T_{Ch\text{-}e}$	270	(Manjunath et al. 2010; Croft, Nork, et al. 2013)
Lamellae layer thickness	T_{LL}	50	(Stitzel et al. 2002; Moses 1965)
Sclera thickness at ora serrata	$T_{S\text{-}os}$	590	(Norman et al. 2010; Stitzel et al. 2002)
Cornea thickness at limbus	$T_{C\text{-}L}$	670	(Norman et al. 2010; Stitzel et al. 2002)
Cornea thickness at anterior pole	$T_{C\text{-}ap}$	520	(Stitzel et al. 2002)
Cornea outer radius	R_C	7,280	(Stitzel et al. 2002)
Scleral spur shell thickness	ST_{SS}	100	(Moses and Grodzki 1977; Hamanaka 1989; Hogan, Alvarado, and Weddell 1971)
Zonular sheet thickness	T_{ZS}	40	(Lütjen-Drecoll et al. 2010; Rohen 1979; Croft et al. 2016)
Vitreous membrane thickness	T_{VM}	100	(Croft, Nork, et al. 2013)
Ciliary muscle length	L_{CM}	4,600	(Sheppard and Davies 2010; Wasilewski et al. 2008; Croft, McDonald, et al. 2013)
Ciliary muscle length: spur to apex	$L_{CM\text{-}ax}$	880	(Croft, Nork, et al. 2013)
Ciliary muscle thickness at apex	$T_{CM\text{-}ax}$	720	(Croft, Nork, et al. 2013; Wasilewski et al. 2008)
Ciliary muscle thickness at 25% length	$T_{CM\text{-}25}$	540	(Sheppard and Davies 2010)
Ciliary muscle thickness at 50% length	$T_{CM\text{-}50}$	330	(Sheppard and Davies 2010)
Ciliary muscle thickness at 75% length	$T_{CM\text{-}75}$	160	(Sheppard and Davies 2010)
Ciliary muscle length: spur to 25% length	$L_{CM\text{-}25}$	1,150	(Sheppard and Davies 2010; Wasilewski et al. 2008; Croft, McDonald, et al. 2013)
Lens anterior thickness	$T_{L\text{-}a}$	1,820	(Urs et al. 2009; Brown 1973; Burd, Judge, and Cross 2002)
Lens posterior thickness	$T_{L\text{-}p}$	2,270	(Urs et al. 2009; Brown 1973; Burd, Judge, and Cross 2002)
Lens equatorial radius	R_L	4,400	(Urs et al. 2009; Burd, Judge, and Cross 2002; Strenk et al. 1999)
Lens nucleus anterior thickness	$T_{LN\text{-}a}$	1,360	(Judge and Burd 2002; Brown 1973)
Lens nucleus posterior thickness	$T_{LN\text{-}p}$	1,360	(Judge and Burd 2002; Brown 1973)
Lens nucleus equatorial radius	R_{LN}	3,060	(Judge and Burd 2002; Brown 1973)
Distance from lens to nucleus eq. radius	d_{Lr}	230	(Judge and Burd 2002; Brown 1973)
Lens capsule shell thickness	ST_{LC}	10	(Wilkes and Reilly 2016)

3.3.1.1 Ciliary Muscle

The geometry of the sagittal cross section of the ciliary muscle was based upon measurements of relaxed muscle made with optical coherence tomography (OCT) and ultrasound biomicroscopy (UBM) (Croft, McDonald, et al. 2013; Sheppard and Davies 2010; Wasilewski et al. 2008). The volume of the muscle was divided into longitudinal, radial, and circular sections based on previous imaging and A0histology studies (Hogan et al. 1971; Tamm et al. 1992).

We utilized a previously described tractography method (Handsfield, Bolsterlee, et al. 2017) to define the local fiber direction ($\boldsymbol{a}_0$) in each element of the ciliary muscle. These fiber directions were assigned to all three muscle sections to reproduce the three dimensional muscle cell orientation described in those regions (Hogan et al. 1971). The inputs to this tractography method include: the shape of each region, the area in which the fibers originate and the area in which the fibers insert. Fibers in the longitudinal section originated at the scleral spur and inserted into the choroid interface, running parallel to the inner sclera. Fibers in the radial section originated at the scleral spur and fanned towards the anterior chamber. Fibers in the circular section ran circumferentially and therefore perpendicular to the longitudinal and radial fiber directions and therefore extended out of the plane of symmetry (Figure 3.2A)

The ciliary muscle tissue was modeled as transversely isotropic, hyperelastic, quasi-incompressible material with passive and active non-linear tensile behavior (see Blemker, Pinsky, and Delp 2005 for details). In brief, the deviatoric response (Φ_{iso}) of the uncoupled strain energy density function is:

$$\Phi_{iso}(\boldsymbol{C}, \boldsymbol{a}_0) = W_1(\bar{I}_4, \bar{I}_5) + W_2(\bar{I}_1, \bar{I}_4, \bar{I}_5) + W_3(\bar{I}_4, \alpha) \qquad \text{Equation 3.1}$$

$\boldsymbol{a}_0$ is the local fiber direction defined via tractography, $\boldsymbol{C}$ is the right Cauchy-Green deformation tensor, $\bar{I}_1$ is the first isotropic deviatoric invariant of $\boldsymbol{C}$, $\bar{I}_4$ and $\bar{I}_5$ are additional invariants that arise in transverse isotropy, and J is the square root of the determinant of $\boldsymbol{C}$ and represents the relative volume change. The function W_1 represents the strain energy associated with along-fiber shear, W_2 represents the strain energy

associated with cross-fiber shear, and W_3 represents the strain energy associated with along-fiber stretch. W_3 incorporates the input activation parameter (α) as well as on the length-tension relationship in muscle (Gordon, Huxley, and Julian 1966; Zajac 1989), and takes the following general form:

$$\lambda \frac{\partial W_3}{\partial \lambda} = \sigma_{max} f_{total}(\lambda, \alpha)\lambda/\lambda_{ofl} \quad \text{Equation 3.2}$$

In Eq. 2, λ is the local fiber stretch and is equal to $\sqrt{\bar{I}_4}$ and the peak isometric stress (σ_{max}) is assumed to occur at the optimal fiber stretch (λ_{ofl}). The normalized force in the fiber direction (f_{total}) is a function of the stretch (λ) and the activation level (α) and is the sum of the passive fiber force ($f_{passive}$) and the active fiber force (f_{active}) which scaled by α and is expressed:

$$f_{total}(\lambda, \alpha) = f_{passive}(\lambda) + \alpha f_{active}(\lambda) \quad \text{Equation 3.3}$$

This model was chosen because the ciliary muscle is often described as complex smooth muscle with many functional and structural similarities to skeletal muscle (Croft et al. 2001; Croft and Kaufman 2006; Flügel, Bárány, and Lütjen-Drecoll 1990; Ishikawa 1962; Kaufman et al. 2003), however parameters describing along fiber behavior were modified to represent the force-length curves generated from experimental measurements of smooth muscle (Hai and Murphy 1988; Herlihy and Murphy 1973; Schmitz and Böl 2011) (Table 3.2, Figure 3.2B)

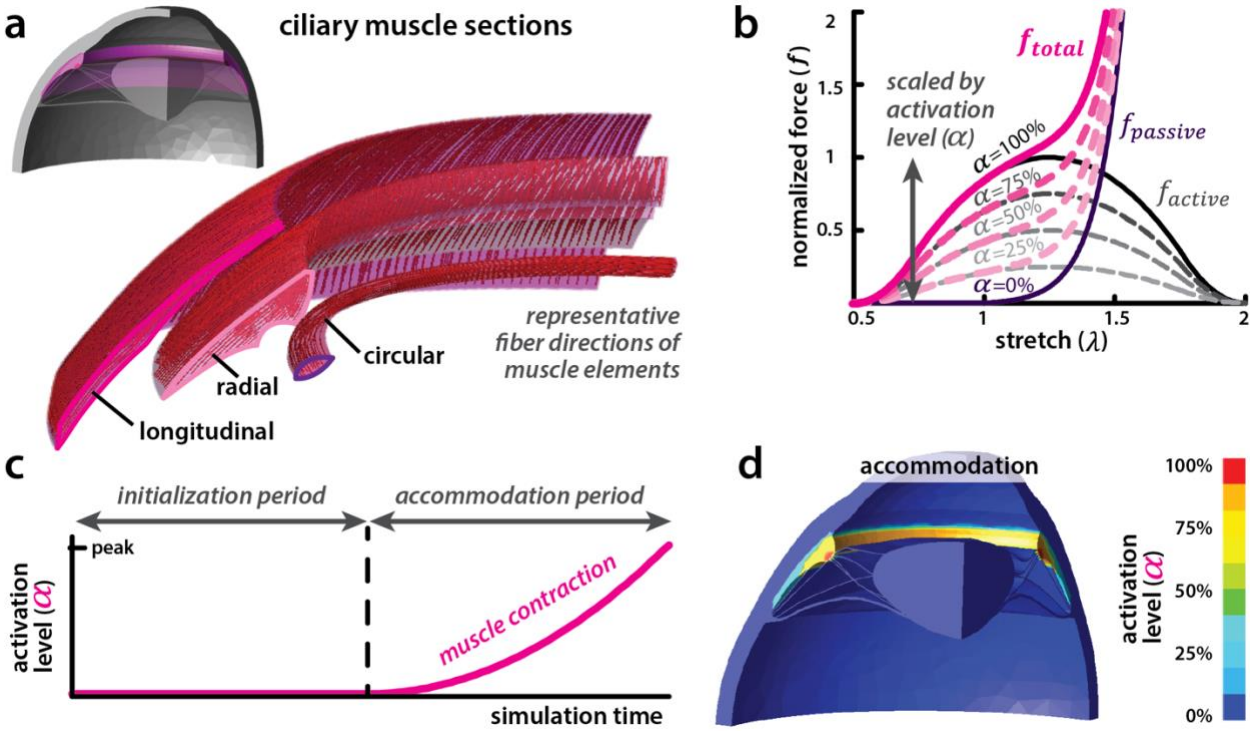

Figure 3.2: Modeling the ciliary muscle subsections (A) The illustration shows the representative fiber directions assigned to the tetrahedral elements in the ciliary muscle sections; these directions were required for the transverse isotropy of the constitutive model for the ciliary muscle elements and represents the orientation of the muscle cells. The fiber directions were assigned to reproduce the orientations of the longitudinal, radial, and circular sections of the ciliary muscle reported in the literature. **(B)** The curve for active force-stretch relationship in the fiber direction of the ciliary muscle scales with increasing activation level (α). The total force-stretch curve is the sum of the active and passive curves. **(C)** The simulation time was divided into two periods: initialization and accommodation. During initialization, the activation level (α) was held at 0, then increased exponentially to its peak value during accommodation. (**D)** The peak value of the activation level (α) for each muscle section when the model was calibrated is shown (jet color bar).

3.3.1.2 Lens

The geometry of the lens was defined to represent unstretched lens shape, and was determined from measurements of isolated relaxed lens made *ex vivo* with shadow-photogrammetric images (Urs et al. 2009; Wilkes and Reilly 2016) and the accommodated lens measured *in vivo* with slit-image photography and magnetic resonance imaging (MRI) (Brown 1973; Strenk et al. 1999). The lens was subdivided into two solid regions that represented the cortex and nucleus, and we assigned the corresponding material properties to each region based on published measurements (Burd et al. 2002; Liu et al. 2006; Wilde et al. 2012). Finally, the capsule was represented using a single layer of triangular shell elements located on the exterior surface of the cortex, similar to previous models (Wilkes and Reilly 2016).

Each lens material was modeled as an isotropic Neo-Hookean material with a bulk modulus (K) of 5000 MPa to enforce near-incompressibility and with the deviatoric strain energy density function:

$$W = C_1(\bar{I}_1 - 3) \qquad \text{Equation 3.4}$$

C_1 is the material constant (Table 3.3) defined based on published values determined from mechanical testing of cortex, capsule, and nucleus of lenses extracted from thirty-year-old young adult specimens (Krag and Andreassen 2003; Krag et al. 1997; Wilde et al. 2012).

3.3.1.3 Zonules

Zonules were represented as continuous sheets of material extending between the origin and insertion points, representing seven identified divisions. While the zonules are comprised of thousands of discrete fibers, this continuous-sheet approach represents the primary action of zonules of transferring tensile loads between the ciliary muscle and the lens, using an anisotropic material oriented in the direction of these fibers.

We defined seven divisions of the zonules based on the current understanding of zonular anatomy. The anterior zonules have been clearly identified by scanning electron microscopy (SEM) for

decades (Farnsworth and Shyne 1979; Rohen 1979); however, the zonular divisions in the region of the ora serrata and vitreous membrane have been discovered more recently (Croft, Nork, et al. 2013; Lütjen-Drecoll et al. 2010).

The anterior (AAZ), equatorial (EAZ), and posterior (PAZ) divisions of the anterior zonules all originate near the ciliary muscle apex, and they insert anterior to, on, and posterior to the lens equator, respectively (Farnsworth and Shyne 1979; Goldberg 2015; Rohen 1979). The pars plana zonules (PPZ) extend along the interior of the ciliary muscle. The anterior vitreous zonules (AVZ) originate near the ciliary muscle apex and insert near the vitreous membrane's attachment to the lens (Goldberg 2015; Lütjen-Drecoll et al. 2010). The intermediate vitreous zonules (IVZ), originate near the ciliary muscle apex and insert towards the posterior end of the muscle where the vitreous membrane attaches (Goldberg 2015; Lütjen-Drecoll et al. 2010). The final division of zonules originate at the posterior vitreous zonule insertion area, and they insert into the lens equator (PVZ INS-LE) (Croft et al. 2016; Croft, Nork, et al. 2013; Goldberg 2015).

The tractography method (Handsfield, Bolsterlee, et al. 2017) was also applied to assign local fiber directions ($\boldsymbol{a}_0$) to the elements of each zonule division, using the origins and insertions described above. Zonule fiber directions were assigned to run in-plane for each sheet from origin to insertion (Figure 3.3A)

Zonule elements were modeled as transversely isotropic, hyperelastic, quasi-incompressible material using the previously described constitutive model modified for passive connective tissue (Blemker et al. 2005; Weiss et al. 1996). Shear properties across and along the fiber direction (W_1 and W_2) were minimized in order to represent the fact that there is minimal interaction *in vivo* between discrete fibers represented by the zonule sheets (Table 3.2). Because few reports exist on zonule constitutive behavior, this model was chosen because it simulates directional connective tissue, and parameters were chosen so that the toe region was minimized to represent the reported nearly linear behavior of zonule fibers (Michael et al. 2012). In the fiber direction, the strain energy density function is:

$$\lambda \frac{\partial W_3}{\partial \lambda} = \sigma(\lambda, p_z)$$ Equation 3.5

where the relationship between the stress (σ) and the stretch (λ) is defined by the following piece-wise equation (Blemker et al. 2005; Zajac 1989):

$$\lambda \frac{\partial W_3}{\partial \lambda} = \begin{cases} \sigma(\lambda, p_z) = P_1\left(e^{P_2(\lambda - 1 + p_z)} - 1\right) & 1 - p_z < \lambda < \lambda^* - p_z \\ \sigma(\lambda, p_z) = P_3\lambda + P_4 & \lambda \geq \lambda^* - p_z \end{cases}$$ Equation 3.6

P_3 & P_4 are defined so σ is C0 & C1 continuous at $\lambda = \lambda^* - p_z$. The parameter p_z was used to vary zonular tension by shifting the stress-stretch curve (Figure b) and therefore radially apply stress to the lens to initialize the model. The tensioning parameter (p_z) was increased to stretch the lens to the unaccommodated position. The process by which we determined the tensioning parameter is described in section 3.3.2.

	P_1	P_2	λ_{ofl}	λ^*	σ_{max}	G_1	G_2	K
ciliary muscle	1e-2	12.5	1.25	1.45	1 MPa	5e-3 MPa	5e-3 MPa	5000 MPa
zonules	1.03e-1 MPa	50	N/A	1.03	N/A	5e-5 MPa	5e-5 MPa	500 MPa

Table 3.2 Ciliary muscle and zonular parameters for transversely isotropic constitutive model. Ciliary muscle and zonules were modeled using previously described transversely isotropic model (Blemker et al. 2005) of skeletal muscle and passive connective tissue, respectively, with the parameters: P_1, along-fiber extension multiplicative modulus; P_2, along-fiber extension exponential modulus; λ_{ofl}, stretch at optimal fiber length; λ^*, stretch at which stress-strain becomes linear; σ_{max}, peak isometric stress; G_1, along-fiber shear modulus; G_2,cross-fiber shear modulus; K, bulk modulus. Model parameters for ciliary muscle along-fiber behavior were adjusted to represent experimentally-based smooth muscle force-length curves (Herlihy and Murphy 1973; Schmitz and Böl 2011). Zonule parameters represented fibers embedded within continuous sheets with along-fiber passive properties based on experimental measurements (van Alphen and Graebel 1991; Michael et al. 2012).

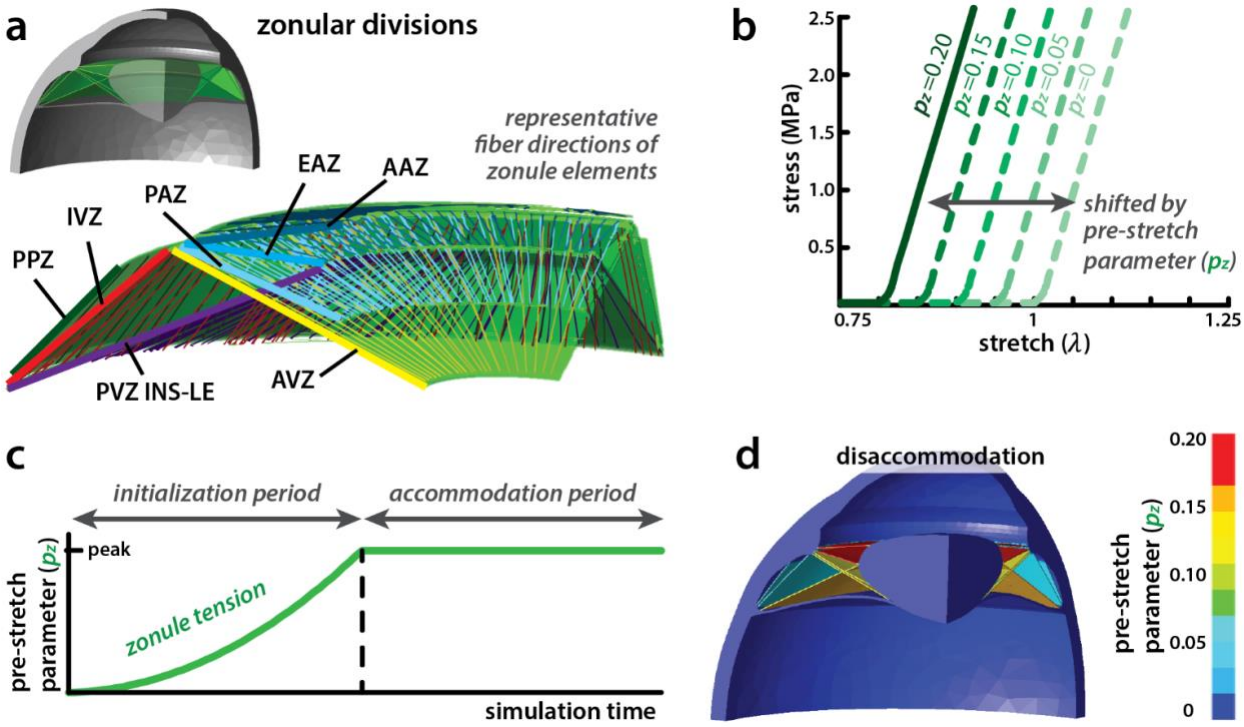

Figure 3.3: Modeling the zonules (A) The illustration shows the orientation of the representative fiber directions assigned to the tetrahedral elements in the zonular division sheets; these directions were required for the transverse isotropy of the constitutive model for the zonule elements and represent the arrangement of discrete fibers that the model represents with these continuous sheets. The fiber directions, colored by division sheet, are in-plane of the axially symmetric sheet for each zonular pathway: anterior (AAZ, dark blue), equatorial (EAZ, blue), and posterior (PAZ, light blue) portions of the anterior zonules, anterior (AVZ, yellow) and intermediate (IVZ, red) vitreous zonules, pars plana zonules (PPZ, dark green), and posterior vitreous zonule insertion to the lens equator zonules (PVZ INS-LE, purple). **(B)** The curve for stress-stretch relationship in the fiber direction of the zonules shifts to the left with increasing tensioning parameter (p_z). **(C)** The simulation time was divided into two periods: initialization and accommodation. During initialization, the zonule tensioning parameter (p_z) was increased exponentially to its peak value, then held constant during accommodation. **(D)** The peak value of the tensioning parameter (p_z) for each zonule pathway when the model was calibrated is shown (jet color bar).

	cornea	sclera	scleral spur	lamellae layer	choroid	vitreous membrane	lens cortex	lens nucleus	lens capsule
C_1 (MPa)	0.889	0.270	2.299	1e-10	9.1e-4	1e-5	5.4e-4	1e-4	0.201
References	*Wang et al. 1996**	*Eilaghi et al., 2010*; Friberg & Lace, 1988**	*Moses & Grodzki, 1977**	*Moses, 1965**	*Friberg & Lace, 1988*; Worthington et al., 2014***	*Sharif-Kashani, Hubschman, Sassoon, & Kavehpour, 2011***	*Wilde, Burd,& Judge 2012; Burd, Judge,& Cross 2002*	*Wilde, Burd,& Judge 2012; Burd, Judge,& Cross 2002*	*Krag & Andreassen, 2003*

Table 3.3: Lens and extralenticular structure parameters for Neo-Hookean constitutive model. The passive ocular tissues were modeled as isotropic Neo-Hookean materials (Eq. 4) with material stiffness parameters (C_1) based on measurements from approximately 30 year old specimens (Burd et al. 2002; Krag and Andreassen 2003; Wilde et al. 2012), when available, or estimated from measurements of older human specimens* (H. Wang et al. 1996; Eilaghi et al. 2010; Friberg and Lace 1988; Moses and Grodzki 1977; Moses 1965) or from measurements of porcine** specimens (Sharif-Kashani et al. 2011; Worthington et al. 2014).

3.3.1.4 Extralenticular Structures

The extralenticular structures represented in our model included: the sclera (Croft, Nork, et al. 2013; Norman et al. 2010; Stitzel et al. 2002), the cornea (Stitzel et al. 2002), the choroid (Croft, Nork, et al. 2013; Manjunath et al. 2010), and the vitreous membrane (Croft, Nork, et al. 2013). An interconnected lattice of fibers forming a sponge-like structure, termed the posterior vitreous zonule, has been described in the posterior region of the ciliary muscle where zonules attach to the vitreous membrane (Goldberg 2015; Lütjen-Drecoll et al. 2010). While we did not represent this structure explicitly, we incorporated a wide posterior attachment zone of the vitreous membrane that would provide the suspected mechanical damping that occurs in this region (Lütjen-Drecoll et al. 2010). A 3D lamellae layer was added to separate the sclera from the ciliary muscle and choroid structures. This compliant layer simulates the observation that these structures are loosely attached in the supra-choroidal/sub-scleral space (Moses 1965). The scleral spur was added on the interface between the sclera and anterior surface of the ciliary muscle as triangular shell elements that were much stiffer than the surrounding sclera material (Moses and Grodzki 1977; Hamanaka 1989). The extralenticular tissues were also modeled as isotropic Neo-Hookean with the deviatoric strain energy density function defined in Equation 3.4. All extralenticular tissues had a bulk

modulus (K) of 5000 MPa and the material constants (C_1) listed in Table **.** Material parameters were chosen to represent an average thirty-year-old young adult human based on mechanical testing measurements (H. Wang et al. 1996; Worthington et al. 2014; Sharif-Kashani et al. 2011; Eilaghi et al. 2010; Friberg and Lace 1988; Moses and Grodzki 1977; Moses 1965). In cases where data from specimens of this age were not available, material property values where extrapolated from measurements made in older adults or estimated from studies in animals (Table 3.3).

3.3.2 Simulations to Calibrate Model Parameters

Calibration simulations were run in the AMPS finite-element package (AMPS Technologies, Pittsburgh, PA), and were divided into two distinct periods: initialization and accommodation.

3.3.2.1 Calibration of Model Initialization

The first simulation period initialized the disaccommodated state. Zonules served as tension actuators to stretch the lens. Also during initialization, a global pressure of 2 kPa was applied to interior ocular surfaces to represent normal, healthy inter-ocular pressure of 15 mmHg (Kaufman et al. 2003). Zonule tensioning parameters (p_z) were increased to peak input values. Tensioning parameters (p_z) were assumed to be the same for all zonule elements within the same zonular division, but the p_z values were different across divisions (Figure 3.3D).

Tension parameters of the seven zonular divisions were calibrated such that model predictions of lens deformation during initialization were consistent with *in vivo* measurements of the lens in disaccommodation. For this comparison, we used data from published measurements of lens thickness and equatorial radius (Figure 4A) from magnetic resonance imaging (MRI) of four young healthy subjects (30±1 years) during accommodation and disaccommodation (Strenk et al. 1999). Subjects focused on a far target (a weak accommodative stimulus) to represent the disaccommodated state. Subjects then focused on a near target (strong accommodative stimulus) to represent a accommodated state. The differences between these states were used to determine the change in *in vivo* lens shape. In order to

determine the tension parameters that best matched the disaccomodated state, the peak tension parameter values (p_z) for each division were initially varied independently then they were varied combination. Final combined tensions were chosen so that the model predictions of lens thickness and equatorial radius changes during initialization, calculated as the difference in those dimensions between initial and final time steps, were within one standard deviation of the measured experimental changes (Figure 3.4B) (Strenk et al. 1999).

3.3.2.2 Calibration of Simulated Accommodation

The second period of the simulation represented the action of the ciliary muscle to cause deformation of the lens from a disaccomodated shape to an accommodated shape. The simulation produced accommodation by increasing ciliary muscle activation (α) to peak input levels, which in turn caused excursion of the muscle and deformation of the lens. All elements in the same section were assigned the same activations, but α was different for each section (Figure 3.2D).

Activation parameters (α) of the three ciliary muscle sections were calibrated such that predictions of ciliary muscle excursion (as measured by shape change) during accommodation were consistent with published *in vivo* measurements of ciliary muscle excursions (Sheppard and Davies 2010). Specifically, we made use of data from published optical coherence tomography (OCT) measurements of ciliary muscle length and thickness at regions corresponding to 25%, 50%, and 75% of the muscle's length (Figure 3.5A) in fifteen young healthy subjects (26±4 years) focusing on visual stimuli with demands for disaccommodation and accommodation (Sheppard and Davies 2010). Peak activation levels (α) for each muscle section were varied independently then in combination. Final combined activations were chosen so that model predictions of muscle excursion during accommodation, calculated as the difference in those dimensions between initial and final time steps, were within one standard deviation of average experimental values (Figure 3.5B) (Sheppard and Davies 2010).

3.3.3 Testing Model Predictions of Lens Deformation in Response to Ciliary Muscle Excursion

To independently test that the tuned parameters for zonular tension and muscle activation predicted appropriate lens deformation in response to ciliary muscle excursion during simulated accommodation, we compared model results to additional measurements of both the lens and ciliary muscle motion made during *in vivo* accommodation in young healthy eyes. For this comparison, we used three published experimental studies. The first study measured changes in ciliary muscle apex thickness and lens thickness observed synchronously in a single 22-year-old subject as they accommodated to focus on targets at two steps of increasing stimulus demand (Ruggeri et al. 2016). These experimental measurements were averaged from multiple frames during accommodation using OCT, verifying the coupled effect of ciliary muscle excursion and lens deformation. The second study collected asynchronous OCT images to measure muscle and lens shape to determine how each changes with accommodative response averaged in twenty-six subjects (39±8 years) responding to three step increases in accommodative stimuli (Richdale et al. 2013). The third study utilized ultrasound biomicroscopy (UBM) to measure changes in muscle and lens shape in four subjects (29±2 years) as disaccomodation and accommodation were induced with homatropine and pilocarpine, respectively (Croft, McDonald, et al. 2013). We reasoned that combining these studies allowed a test that our model generally predicts the average corresponding changes in muscle and lens shape observed across subjects as they exhibit a range of accommodative responses.

3.3.4 Quantifying the Individual Mechanical Action of the Ciliary Muscle Sections

Once model parameters were validated, we used the model to investigate the mechanical action of each muscle section to produce two optically relevant outputs of accommodative lens displacement. In order to quantify and illustrate these actions, we propose a new metric of "mechanical effectiveness," that can be calculated based on simulations of each muscle's action in isolation. An analogous quantification of a muscle's mechanical effectiveness that is often reported is a moment arm, which is determined as the derivative of the muscle length vs. joint angle relationship, according to the principle of virtual work (Sherman et al. 2013). Inspired by this definition, we determined muscle effectiveness by calculating the

derivative of each muscle section's fiber length vs. lens thickness or lens equator anterior position relationship. These defined our motions of interest in accommodation which is either deformation or anterior translation of the lens.

Simulations were run in which each ciliary muscle section was activated individually from α = 0% to α = 100% while others were held at α = 0%. Based on each simulation, the length change in the activated muscle section in its fiber direction was characterized as a function of the resulting lens thickness change as well as the anterior translation of the lens equator. We quantified the "mechanical effectiveness" of each section in lens deformation [d(fiber length)/d(lens thickness)] and in lens anterior translation [d(fiber length)/d(anterior position of lens equator)]. For each of these measures, a high positive value indicates high potential to contribute to lens thickness increases and anterior translations, respectively. A high negative value would indicate the muscle section acts as an antagonist to each function.

3.4 Results

3.4.1 Calibration of Zonular Tension Values for Model Initialization

To initialize the model, varied tension was required in the different zonule divisions to replicate experimental measurements of disaccommodated lens shape (Strenk et al. 1999). The anterior (AAZ) and equatorial (EAZ) portions of the anterior zonules required the greatest tension value (p_z =0.17), followed by the posterior insertion zone to lens equator zonules (PVZ INS-LE, p_z =0.15). The posterior portion (PAZ) of the anterior zonules and the anterior vitreous zonules (AVZ) , both required p_z =0.12, and finally, the intermediate vitreous (IVZ) and pars plana zonules (PPZ) required the least tension (p_z =0.05) (Figure 3.3D). Resulting changes in lens thickness of -323 μm and lens equatorial radius of 197 μm were within experimentally measured values as lens stretched to its disaccommodated shape (Figure 3.4B).

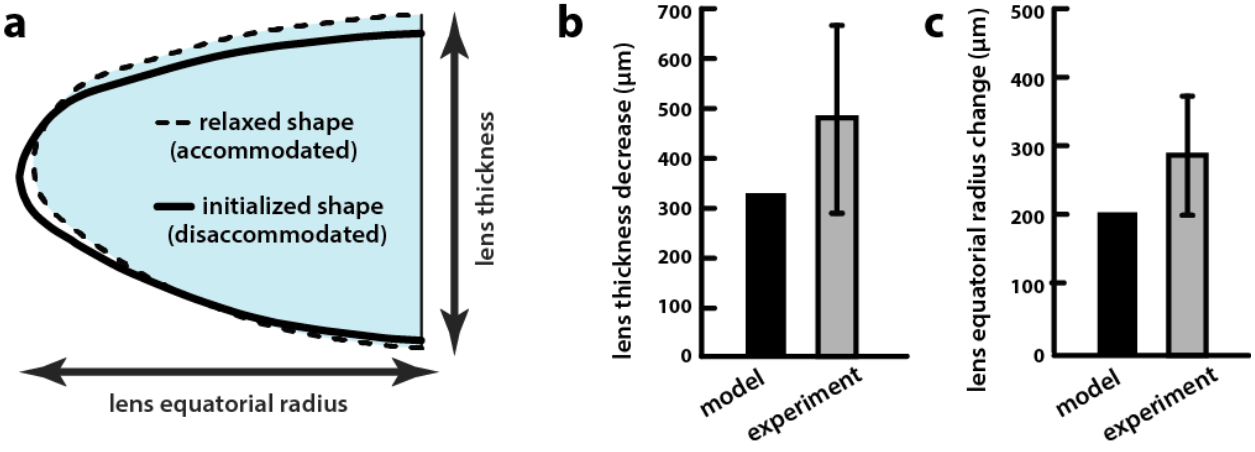

Figure 3.4: Calibration of zonular tension for model initialization. The tensioning parameters in each zonule were calibrated so that at the conclusion of simulation initialization **(A)** the predicted lens shape was consistent with experimental measurements of the disaccommodated state. Model predictions of changes in lens **(B)** thickness and **(C)** equatorial radius were within a standard deviation of magnetic resonance imaging (MRI) measurements from Strenk et al. 1999.

3.4.2 Calibration of Ciliary Muscle Activation Values for Simulated Accommodation

Each ciliary muscle section required a unique activation level (α) to replicate published measurements of ciliary muscle excursion during accommodation (Sheppard and Davies 2010): 25% in the longitudinal section, 90% in the radial section, and 100% in the circular section (**Error! Reference source not found.**d). These calibrated activations resulted in the ciliary muscle shortening by 268 μm and thickening by 30, 14, and 8 μm at 25%, 50%, and 75% of its length, respectively (Figure 3.5).

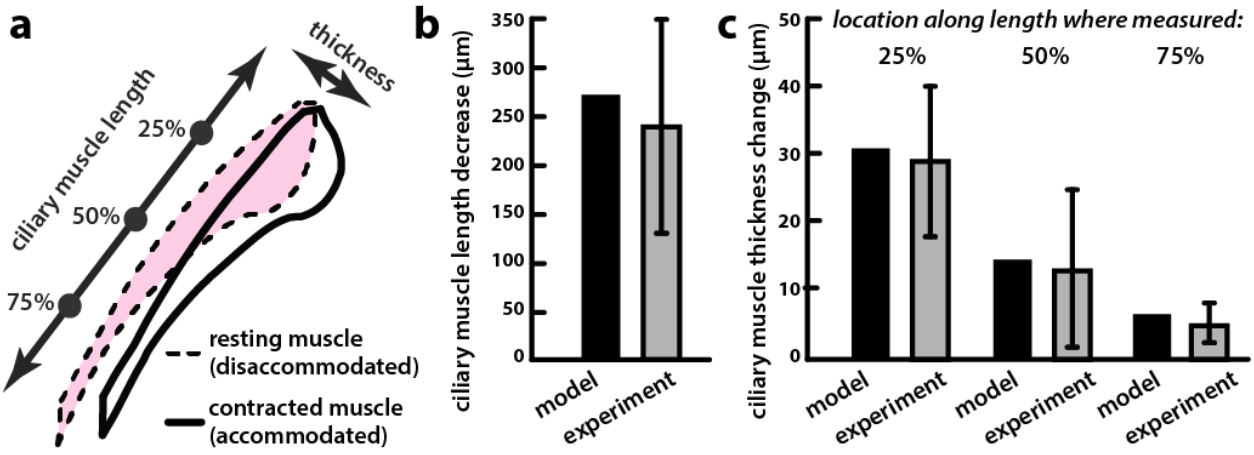

Figure 3.5: Calibration of ciliary muscle activation for accommodation. The ciliary muscle activation levels in each section of the muscle were calibrated so that at the conclusion of simulated accommodation **(A)** predicted changes in ciliary muscle shape were consistent with experimental measurements made before and after accommodation. Model predictions of changes in ciliary muscle **(B)** length and **(C)** thickness at 25%, 50%, and 75% of the length were within a standard deviation of optical coherence tomography (OCT) measurements from Sheppard and Davies 2010.

3.4.3 Test of Predicted Lens Deformation in Response to Ciliary Muscle Excursion

Model predictions of ciliary muscle excursions and the corresponding lens deformation during accommodation were within the range of experimental measurements described in the literature (Croft, McDonald, et al. 2013; Richdale et al. 2013; Ruggeri et al. 2016), demonstrating a positive relationship between ciliary muscle apex thickening and lens thickening with maximum changes in ciliary muscle apex and lens thickness of 96 and 320 µm, respectively, (Figure 3.6).

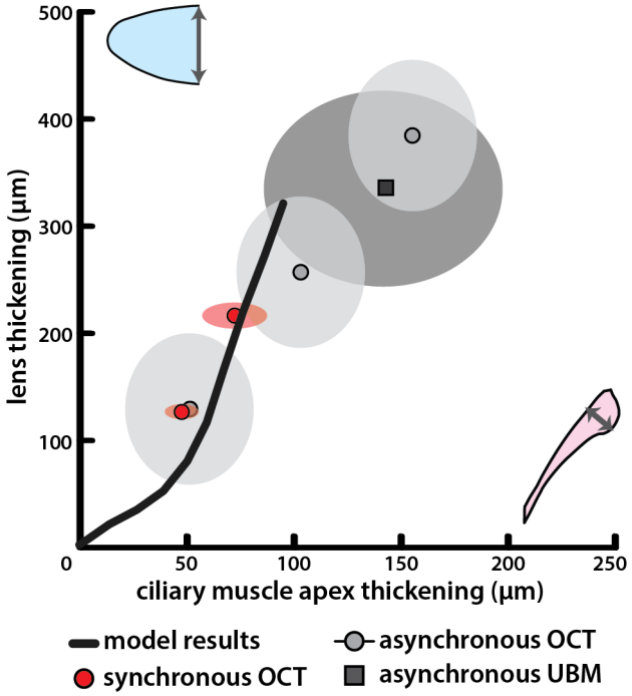

Figure 3.6: Test of predicted lens deformation in response to ciliary muscle excursion. The model predicted change in ciliary muscle apex thickness and corresponding lens thickness that occurred during simulations of accommodation were compared to muscle and lens changes measured *in vivo* in different studies. In the first, optical coherence tomography (OCT) measurements were made synchronously in a single subject (22 years old) accommodating to two stimulus demands. Average changes in multiple frames were determined between each step and the disaccommodated state (red circles – Ruggeri et al., 2016)). In the second, ciliary muscle and lens regions were imaged separately and asynchronously with OCT at three increasing accommodative stimuli in 26 subjects (39±8 years old). A linear relationship with accommodative response for lens thickening and ciliary muscle apex thickening was determined from the average of this subject group (gray circles – Richdale et al., 2013). In the final study, four subjects (29±2 years old) were imaged with ultrasound biomicroscopy (UBM) in disaccomodation and accommodation, induced with homatropine and pilocarpine, respectively, and the difference in lens thickness and ciliary apex thickness was calculated (gray squares –(Croft, McDonald, et al. 2013). Ellipses show standard deviations of experimental measurements.

3.4.4 Mechanical Effectiveness of the Ciliary Muscle Sections

The simulations with the three muscle sections activated in isolation to 100% revealed that ciliary muscle sections act distinctively and synergistically to perform accommodation. The circular section contributes most to increasing lens thickness, while longitudinal and radial sections have the capacity to oppose this action. By contrast, the longitudinal and radial sections act to translate the lens anteriorly while the circular section has the capacity to oppose this action. The circular section experienced the greatest muscle shortening with a maximum change of 3389 μm, while the longitudinal and radial sections experienced length changes with maximums of 416 μm and 250 μm, respectively (Figure 3.7A-B). The average along fiber stretch (λ) across each muscle section at 100% activation in the longitudinal, radial, and circular muscle sections was 0.895, 0.861, and 0.904, respectively. These values indicate that the fibers shortened by an average of 10.5% in the longitudinal section, 13.9% in the radial section, and 9.6% in the circular section. For muscle effectiveness in deformation [d(fiber length)/d(lens thickness)], the longitudinal section had the greatest magnitude which was in the negative direction (-17.37 at maximum contraction). The radial and circular were similar in magnitude (-9.02 and 9.78, respectively, at maximum contraction) with only the circular in the positive direction (Figure 3.7C). For muscle effectiveness in displacement [d(fiber length)/d(lens anterior position)], the circular section had the greatest magnitude (-3.98 at maximum contraction) which was in the negative direction. The longitudinal and radial sections were similar in magnitude (0.91 and 0.65, respectively, at maximum contraction) and were in the positive direction (Figure 3.7D).

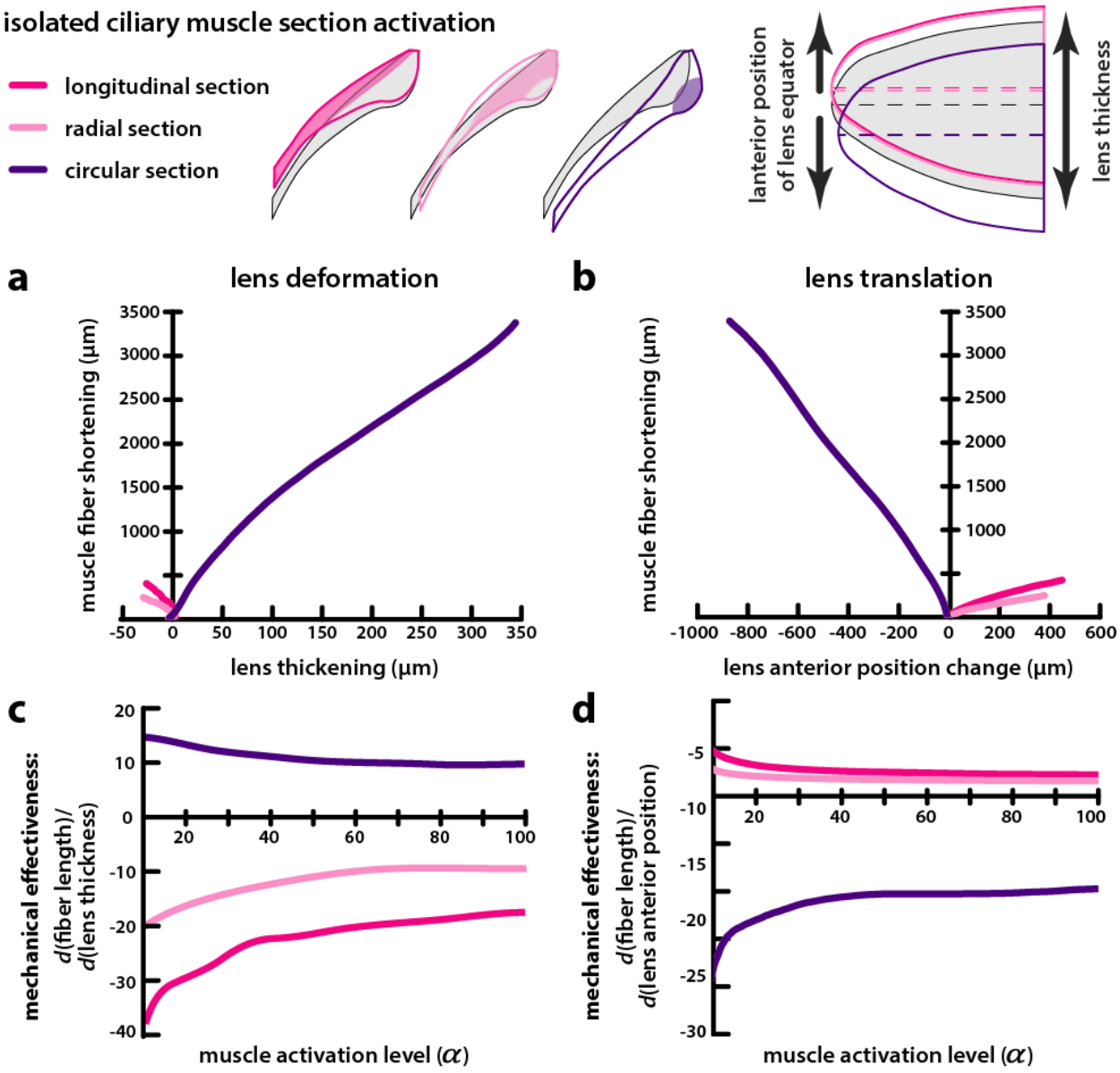

Figure 3.7: Mechanical effectiveness of ciliary muscle sections during isolated activation. The model predicted ciliary muscle excursions in three simulations where each muscle section in turn was activated to 100% in isolation. To show the geometric correspondence between muscle action during isolated contraction and accommodative function, muscle fiber length change in each section, calculated along the fiber direction, is plotted with **(A)** the change in lens thickness and **(B)** the change in the anterior position of the lens equator. Across its range of activations, each muscle section's mechanical effectiveness during accommodation can be calculated **(C)** in lens deformation by dividing fiber length change by lens thickness change, and **(D)** in lens translation by dividing fiber length change by lens anterior position change.

3.5 Discussion

The goal of this study was to develop a model of the accommodative mechanism that is driven by the action of the ciliary muscle in order to quantify how the action of each of the three ciliary muscle sections leads to lens deformation and displacement. The model predicts excursion of the ciliary muscle and deformation of the lens that resulted from activated contraction by a three-part muscle structure. Predictions of ciliary muscle excursion and lens deformation were compared with experimental measures made in healthy subjects as they responded to a range of accommodative stimuli (Croft, McDonald, et al. 2013; Richdale et al. 2013; Ruggeri et al. 2016). These results demonstrate the model's ability to predict lens changes corresponding with muscle action that are consistent with documented *in vivo* behavior of this system. Balanced activation of the three sections of the ciliary muscle is necessary to reproduce excursion seen *in vivo*. There also appears to be a clear relationship between the action of full ciliary muscle and the change in the lens required to alter optical power. The model allowed us to probe the unique mechanical roles of each section of the ciliary muscle. Due to the variation in the architecture of the ciliary muscle fibers, each section behaved distinctively. The circular section had the greatest capacity to induce lens thickening while the longitudinal and radial sections were most able to translate the lens anteriorly. These deformations are the primary functional outputs of accommodation.

We witnessed clear distinctions in the mechanical roles of the three ciliary muscle sections while they were activated in isolation (Figure 3.7). Interestingly, neither the longitudinal nor radial section caused the lens to deform or translate as much as the circular section did alone. The longitudinal and radial sections acted in the opposite direction of the circular section by causing the lens' thickness to decrease rather than increase. The longitudinal and radial sections further caused the lens' equatorial position to move anteriorly rather than posteriorly as the lens was moved by the circular section (Figure 3.7A-B). The longitudinal and radial sections do not act synchronously with the circular section in deforming the lens for accommodation, and act to oppose the circular section's effect on the lens anterior position. In our model, the circular section deforms the lens and translates it posteriorly away from the

cornea, which would counteract the optical gains of changing lens shape. The longitudinal and radial sections offset lens translation via the circular section, thus modulating lens position, despite their effect of decreasing lens thickness. The different muscle sections behave synergistically through their distinctive actions to perform the complex task of accommodation, with the longitudinal and radial sections acting as stabilizers to the circular section to achieve ideal lens displacement. The differences in the mechanical effectiveness of the individual muscle sections explains the differences in activation requirements of each section during calibration (Figure 3.2D). In order to recapitulate accommodation, the nearly full activation was required by the circular section to optimize lens deformation. Lower activations of the radial and longitudinal sections were required to modulate lens position, opposing the circular section's action to translate the lens posteriorly (Figure 3.7D). The longitudinal section's activation was less than half of the activation of the radial section; the longitudinal section had a larger opposing effect on lens thickening than the radial section (Figure 3.7C). These new insights into the specific functions of each muscle section should be considered when interpreting how the mechanical properties of the tissues of the eye lead to presbyopia (van Alphen and Graebel 1991; Friberg and Lace 1988; Wilde et al. 2012). The longitudinal section shares the most contact with the extralenticular structures. As the mechanical properties of the extralenticular structures change with age, they could impact the longitudinal section's capacity to translate the lens anteriorly.

There are several assumptions and limitations in our model that should be discussed. First, the material and geometric parameters of the model were chosen to represent an average healthy 30-year-old emmetropic eye; however, complete anatomical measurements and material property data for adults of this age were not available, and natural variability would occur among adults even of the same age. Geometry was measured using different imaging modalities with varied resolution and often from different subject sets within this age group to capture the full scale of information needed for the model. Therefore, model dimensions were chosen to be compatible while falling within the range of anatomical measurements present in the literature. The current work lays the foundation for future versions of the

model that incorporate subject-specific material properties and geometric measurements and can explore how variations in anatomy and material properties influence accommodative function. Second, there is considerable variability to the experimental measurements of accommodative function that may be explained by many factors. Examples include averaging subject results from an age range where some may be developing presbyopia (Croft, McDonald, et al. 2013; Richdale et al. 2013), comparing between different image modalities of OCT (Richdale et al. 2013; Ruggeri et al. 2016) and MRI (Croft, McDonald, et al. 2013; Richdale et al. 2013), and differing the amount of accommodative stimulus presented as well as inconsistently reporting stimulus versus response (Croft, McDonald, et al. 2013; Lossing et al. 2012; Sheppard and Davies 2010; Strenk et al. 1999). Models built from and compared to data collected from the same subject, rather than average data from multiple subjects, could allow for more precise calibration of the model, by matching predicted movement to the corresponding anatomy.

Calibrating the model required determining tension values for seven zonular divisions and activation levels for three ciliary muscle sections in order to fit *in vivo* data with significant variability, so multiple zonular tension inputs and ciliary muscle activation inputs that would satisfy the criteria in each test case. Therefore, we chose the inputs that provided the most compatible predictions of corresponding lens displacement and ciliary muscle excursion within the ranges of the comparison tests that we performed. The complexity of the model lead to large simulation times so we were unable to determine all possible solution sets. While the results we present may not represent a unique set of zonular tensions and muscle activations required by the eye in accommodation, it does demonstrate how specific combinations of these inputs are critical to this mechanical function. Biologically, it is quite plausible for there to be multiple ways in which the zonules and ciliary muscle sections coordinate to perform accommodative function, just as groups of muscles in other parts of the body interact in different combinations to result in the same observed movement. In addition, due to the complexity of the model, it was impossible to perform a mesh convergence study with our reported simulations. We did perform an element sensitivity analysis by modeling the isolated zonules, ciliary muscle, and lens in turn and repeating simulations with

different mesh densities where an activation, pretension, and prescribed load, were applied respectively. Using the prescribed mesh size of the presented model, the predicted deformation in each isolated model differed by less than 2% when the number of elements was increased by a factor of ten.

Simulation predictions from our model compared favorably with experimental measurements of ciliary length and thickness and lens radius, thickness, and position. However, some detailed aspects of shape changes were not all captured by the model geometry. For example, the simulations do not predict 'notching' of the ciliary muscle, which has been noted by several authors (Ke et al. 2017; Schachar 2015) though not quantitatively measured as a function of accommodative change. Though this behavior was not specifically captured, gross excursion of the ciliary muscle was validated with quantitative shape changes reported in multiple studies (Croft, McDonald, et al. 2013; Richdale et al. 2013; Ruggeri et al. 2016; Sheppard and Davies 2010). Pressure boundary conditions were used to represent intraocular pressure, which were able to recapitulate the mechanical effects of the vitreous and aqueous fluids on the components of the accommodative mechanism (Kaufman et al. 2003). The intersecting zonule divisions (PVZ INS-LE, AVZ, and PAZ) were assumed to not mechanically interact in the model because *in vivo* studies demonstrate that these zonules interact with negligible frictional effects (Croft, Nork, et al. 2013; Goldberg 2015). If future evidence suggests some level of interaction between these divisions, this would present an opportunity for future studies to incorporate this added complexity in the model. The geometry and material properties that were incorporated to represent the lens varied slightly compared to those used in some previous models (Burd et al. 2002; Schachar et al. 2006; Stachs et al. 2006), but they were still able to replicate the overall bulk properties of the lens in these studies. For instance, we chose to represent the cortex and nucleus as discrete structures, similar to some authors (Abolmaali et al. 2007; Burd et al. 2002; Judge and Burd 2002; Wang et al. 2017). This representation allows us to define different material properties for each of these structures, which is particularly applicable in studying aging, as they experience different property changes with age. (Heys, Cram, and Truscott 2004; Wilde et al. 2012). We represented the capsule with shell elements of uniform thickness. Although this approach

was similar to other previous FEMs (Wilkes and Reilly 2016), non-uniform capsular thickness has been shown to affect predictions of optical power changes (Wang et al. 2017) as the capsule is thicker anteriorly than posteriorly. Our chosen thickness of 10 μm was within the range of capsular thicknesses for adults in their thirties (Barraquer et al. 2006), and another modeling study predicted only small effects on optical power by changing capsular thickness in a range of 5 to 24 μm (Abolmaali et al. 2007). The predicted changes in general parameters of lens thickness and anterior position that we assessed in our model were similar to those reported by other groups, therefore, we do not believe these assumptions would significantly impact our ability to draw conclusions about lens response to ciliary muscle action, though they may limit direct calculation of optical gain. The model solved quasi-statically and was not a complete representation of activation dynamics of the ciliary muscle, thus the displacements between the initial and final timepoints were primarily considered in determining the extent of predicted accommodation. We did find that corresponding lens and muscle changes were in agreement with *in vivo* measurements over the range of accommodative response which were both simulated and documented in the literature (Figure 3.6). However, it should be noted that there were no measurements at very low levels of stimuli of which to compare the lower range of model behavior to. Furthermore, simulated accommodative response did not predict the full range of the literature data (Croft, McDonald, et al. 2013; Richdale et al. 2013; Ruggeri et al. 2016), given the differences in stimuli used in the experiments from which data was used for testing and calibration of the model (Sheppard and Davies 2010; Strenk et al. 1999). Characterizing a greater range of corresponding lens and muscle changes during *in vivo* accommodation would be an exciting area of future study to better understand this important ocular function.

A novel feature of this model was the capability to simulate ciliary muscle-driven accommodation, achieved by defining detailed zonular geometry and a period of lens initialization, during which tensile and material property conditions were varied. Many previous FEMs were only capable of simulating disaccommodation (Abolmaali et al. 2007; Burd et al. 2002; Liu et al. 2006; Ljubimova et al.

2008; Schachar et al. 2006; Stachs et al. 2006), or lens stretching, using prescribed displacements of the zonules. While these studies provided insight into lens mechanics and the zonule displacements were determined from *in vivo* measurements of ciliary muscle position (Stachs et al. 2006; Strenk et al. 1999), the modeling approach had no ability to apply forward dynamics of ciliary muscle action in accommodation. One previous model used thermal strain to simulate tension in the zonules (Wilkes and Reilly 2016) , thereby stretching the lens into its unaccommodated shape. It then used a prescribed uniform zonule displacement to represent ciliary muscle excursion during accommodation, thereby relieving tension on the lens to simulate accommodation. Our model relied on a slightly different approach, using a tension parameter to the shift zonular stress-strain relationship to apply tension, and expanded upon it by using an anatomically based representation of the ciliary muscle, with three-dimensional fiber directions. Furthermore, our model included representation of the extralenticular structures, which enabled simulation of physiologically relevant boundary conditions on ciliary muscle excursion. Ciliary muscle excursion and lens displacement were primarily analyzed in the plane of symmetry for consistent comparisons with two-dimensional imaging studies (Croft, McDonald, et al. 2013; Richdale et al. 2013; Ruggeri et al. 2016; Sheppard and Davies 2010; Strenk et al. 1999); however, displacement of the model occurred in response to the three dimensional ciliary muscle force development that resulted from its fiber architecture being in part directed out of the plane of symmetry. Our modeling framework enabled representation of three-dimensional stresses produced by ciliary muscle contractions that are required for accommodation. Whereas, axisymmetric models, such as those used in previous investigations of lens accommodation (Abolmaali et al. 2007; Burd et al. 2002; Liu et al. 2006; Ljubimova et al. 2008; Schachar et al. 2006; Stachs et al. 2006), are unable to predict these stresses.

3.6 Conclusions

The current study presents a novel finite element model which allows for investigation into the mechanical action of the ciliary muscle and the functional role it plays in the accommodative mechanism. Moreover, it lays the foundation for further modeling work to investigate how changes to ciliary muscle

and other components of the mechanism that occur with age may contribute to presbyopia progression. Further investigations can provide new insights and may lead to the development of improved or novel treatments for presbyopia such as enhanced design of intraocular lenses or other surgical and therapeutic procedures.

Chapter 4

A new look at an old problem: 3D modeling of accommodation reveals how age-related biomechanical changes contribute to dysfunction in presbyopia

"But it is our duty, my young friends, to resist old age; to compensate for its defects by a watchful care; to fight against it as we would fight against disease"

– Cicero, *Cato Maior de Senectute*

"When asked 'What do you want people to say about you 100 years from now?' I hope it's 'Dang, don't she still look good for her age?'"

– Dolly Parton

4.1 Abstract

Purpose

Presbyopia is an age-related ocular disorder where accommodative ability declines so an individual's focusing range is insufficient to provide visual clarity for near and distance vision tasks without corrective measures. With age, the eye exhibits changes in mechanical properties of many components involved in accommodation, including the lens, sclera, and ciliary muscle. Changes occur at different rates, and it is unknown how each affect accommodative biomechanics, thus contributing to presbyopia. We used a finite element model (FEM) of the accommodative mechanism to simulate age-related changes in lens stiffness, scleral stiffness, and ciliary contraction to predict differences in accommodative function.

Methods

The FEM predicts how ciliary muscle action leads to lens displacement by initializing the unaccommodated lens state then simulating ciliary muscle contraction. Model inputs were calibrated to replicate experimentally measured unaccommodated lens and accommodated ciliary muscle shape changes of the thirty-year-old eye. Predictions of accommodative lens deformation were verified with additional imaging studies. Model variations were created with altered lens component stiffnesses, scleral stiffness, or ciliary muscle section activations, representing fifteen-year incremental age-related changes.

Results

Model variations predict significant changes in accommodative function with age-related mechanical property changes. Lens changes only significantly altered lens thickening at seventy-five years old while sclera changes produced progressive dysfunction with increasing age. Ciliary muscle changes effected lens position modulation.

Conclusions

Model predictions identified potential mechanisms of presbyopia that likely work in combination to reduce accommodative function and indicate that effective treatment strategies may depend on patient age or relative ocular mechanical properties.

4.2 Introduction

Human vision includes the ability to accommodate, where the eye adapts to focus on near or far objects. The loss of this ability is an inevitable and ubiquitous condition of aging, known as presbyopia. Presbyopia affects the entire population of older adults, an estimated one billion people world-wide (Holden BA et al. 2008), impacting their daily activities, especially those who are still working. Reading glasses and contact lens are the status quo in correcting presbyopia (Glasser 2008; Richdale et al. 2006; Wolffsohn and Davies 2019), but vision impairment remains globally uncorrected at high rates, even in the developed world. Available corrective options do not restore the visual ability of a healthy young eye; thus, a demand exists for treatment options that require less compromise.

Clinically, presbyopia is a decline in accommodative ability such that an individual's focusing range is insufficient to provide visual clarity for near and distance vision tasks without corrective measures (Croft et al. 2001; Richdale et al. 2013; Wolffsohn and Davies 2019). Refractive measurements show that accommodative response in older adults lags behind presented stimulus demands (Richdale et al. 2013). Refractive alterations in accommodation are clearly associated with ocular tissue displacement (Croft, McDonald, et al. 2013; Richdale et al. 2013; Strenk et al. 1999), demonstrating that optical dysfunction coincides with reduced tissue mobility. Specifically, lens deformation, measured at its thickness and equatorial diameter, is significantly reduced with age in response to accommodative stimulus (Croft, McDonald, et al. 2013; Richdale et al. 2013; Strenk et al. 1999). Anterior movement of the lens measured at its equator also decreases with age (Croft, McDonald, et al. 2013). Age-related changes in lens structure have been proposed to cause these functional deficits. The lens capsule becomes thicker and stiffer until the age of thirty-five then plateaus (Krag and Andreassen 2003; Krag et al. 1997). The lens cortex stiffens until the age of forty then declines (Fisher 1971; Krag and Andreassen 2003;

Wilde et al. 2012), while stiffness of the nucleus dramatically increases after the age of thirty (Wilde et al. 2012). Computational modeling has demonstrated that age-related changes in lens stiffness can certainly lead to deficits in lens deformation required for accommodation (Burd et al. 2002; Wilkes and Reilly 2016). However, the functional losses predicted by these models did not account for the full decline in accommodative amplitude demonstrated in presbyopia.

Reduced lens displacement is not the only functional loss that occurs in presbyopia. Ciliary muscle excursion associated with accommodation is similarly reduced. Decreased muscle apex thickening has been observed in humans (Croft, McDonald, et al. 2013) as well as smaller length changes in monkeys (Croft, McDonald, et al. 2013; Lütjen-Drecoll et al. 2010). Evidence that the ciliary muscle decreases in contractility with age may explain changes in its excursion. Quantification of human ciliary morphology at different ages revealed muscle atrophy, increased intramuscular connective tissue, and fiber reorganization (Tamm et al. 1992) which would all effect muscle excursion. Ciliary muscle excursion may also become impeded with age by stiffening of its posterior attachments. The sclera has consistently been found to stiffen linearly with age with different mechanical testing of samples from donors of different ages (Boote et al. 2020; Friberg and Lace 1988; Geraghty et al. 2012; Grytz et al. 2014). The sclera's role in accommodation and presbyopia is further evidenced by observed accommodative movements that differ with age (Croft, Nork, et al. 2013). Sclera surgeries offer potential for treating presbyopia, providing the advantage of restoring accommodative function, rather than correcting vision (Boote et al. 2020; Hipsley, Hall, and Karolinne M Rocha 2018). Additionally, by not directly altering the visual axis, these procedures involve a lower risk of vison lost (Hipsley, Hall, and Karolinne M Rocha 2018). However, due to mixed results of early attempts at sclera surgeries, (i.e., scleral implants), the biomechanical justification for treating presbyopia at the sclera remains in question (Glasser 2008; Hipsley, Hall, and Karolinne M Rocha 2018; Wolffsohn and Davies 2019).

Concurrent changes with age in the lens, sclera, and ciliary muscle raises the question of how each change may impact the biomechanics of accommodative function. Understanding how age-related

changes in each of these structures impact accommodative function will provide insight into appropriate targets for treatments. Physics-based computational modeling enables such investigation when used to simulate isolated changes in properties to compare effects on predicted outcomes. While previous studies have used computational models to explore age-related changes in the lens, they were unable to investigate changes in the sclera and ciliary as these components were not represented in their models (Burd et al. 2002; Wilkes and Reilly 2016). We have developed a finite element model of the accommodative mechanism in which simulated ciliary muscle contraction results in lens deformation (Knaus, Hipsley, and Blemker 2021). This model predicts healthy accommodative function by representing the interactions of the lens, ciliary muscle, and extralenticular structures in the pre-presbyopic eye. Our goal is to use this model to quantify how these interactions are altered in response to isolated changes in (i) lens stiffness, (ii) scleral stiffness, and (iii) ciliary muscle contraction, to determine how each might contribute to presbyopia.

4.3 Methods

4.3.1 Finite Element Modeling of Accommodation in the 30-year-old Eye

A three-dimensional (3D) finite element model (FEM) representing the accommodative mechanism in the thirty-year-old human eye was previously developed and validated for simulating accommodation (Knaus et al. 2021). In summary, the 3D FEM was developed by incorporating geometric measurements from over 20 published studies. Since no single study has completely documented the included ocular anatomy, compatible model dimensions were chosen from the range of measurements made using different scales and imaging modalities (Brown 1973; Burd et al. 2002; Croft et al. 2016; Croft, McDonald, et al. 2013; Croft, Nork, et al. 2013; Hamanaka 1989; Hogan et al. 1971; Judge and Burd 2002; Lütjen-Drecoll et al. 2010; Manjunath et al. 2010; Moses 1965; Moses and Grodzki 1977; Norman et al. 2010; Rohen 1979; Sheppard and Davies 2010; Stitzel et al. 2002; Urs et al. 2009; Wasilewski et al. 2008; Wilkes and Reilly 2016). The FEM included representations of the lens, divided into cortex, nucleus and capsule, the ciliary muscle, with distinct longitudinal, radial, and circular

sections, and zonules, with seven divisions represented as continuous material sheets, and the extralenticular structures: the cornea, choroid, vitreous membrane, and sclera (Figure 4.1). 3D geometry of these components was generated by creating outlines of the boundary in 2D then revolving by 90° about the central anterior-posterior axis. Components of the model were meshed automatically (AMPS Technologies, Pittsburgh, PA) into tetrahedral elements (260927 tetrahedral elements), except the lens capsule and the scleral spur which were triangular shell elements with uniform thickness (1787 shell elements). Adjacent structures had shared surfaces at their boundaries. All nodes located at the equator were fixed, per the assumption that the accommodative movement occurs in the anterior eye (Croft, Nork, et al. 2013), while nodes located on symmetry boundary planes were constrained to only move in that plane.

The ciliary muscle and zonules had assigned fiber directions that were defined using a Laplacian flow simulation-based method (Handsfield, Bolsterlee, et al. 2017). Ciliary muscle and zonules were modeled as transversely isotropic, hyperelastic, quasi-incompressible material based on a previously described constitutive model for skeletal muscle and connective tissue (Blemker et al. 2005). The ciliary muscle is often described as complex smooth muscle with many functional and structural similarities to skeletal muscle (Croft et al. 2001; Croft and Kaufman 2006; Flügel et al. 1990; Ishikawa 1962; Kaufman et al. 2003). To represent experimental measurements of smooth muscle force-length behavior (Hai and Murphy 1988; Herlihy and Murphy 1973; Schmitz and Böl 2011), parameters of the passive and active force curves in this model were modified in the equations defining the relationship between along-fiber stress (σ) and the local fiber stretch (λ):

$$\sigma(\lambda, \alpha) = \sigma_{max} f_{total}(\lambda, \alpha)\lambda/\lambda_{ofl} \quad \text{Equation 4.1}$$

The peak isometric stress (σ_{max}) occurs at the optimal fiber stretch (λ_{ofl}) and the normalized force in the fiber direction (f_{total}) is the sum of the passive fiber force ($f_{passive}$) and the active fiber force (f_{active}):

$$f_{total} = f_{passive}(\lambda) + \alpha f_{active}(\lambda). \quad \text{Equation 4.2}$$

The activation parameter (α) was increased during simulated accommodation to induce ciliary muscle contraction (Figure 4.1). To simulate accommodation, an initial tension needs to be applied to the lens, so the constitutive model (Blemker and Delp 2005; Zajac 1989) used for the zonules was modified in order to actuate the required lens deformation. A tensioning parameter (p_z) was added to the piecewise equation defining the model along-fiber stress (σ) and the local fiber stretch (λ):

$$\begin{cases} \sigma(\lambda, p_z) = P_1\left(e^{P_2(\lambda - 1 + p_z)} - 1\right) & 1 - p_z < \lambda < \lambda^* - p_z \\ \sigma(\lambda, p_z) = P_3\lambda + P_4 & \lambda \geq \lambda^* - p_z \end{cases} \quad \text{Equation 4.3}$$

The tensioning parameter (p_z) was increased during simulation initialization, applying radial stress to the lens (Figure 4.1). Since little data describing zonule material properties exist, the zonule along-fiber multiplicative (P_1) and exponential (P_2) moduli were defined to be similar to other biological connective tissues (Blemker and Delp 2005; Weiss et al. 1996) to exhibit small toe region and mostly elastic behavior (Michael et al. 2012). P_3 and P_4 are defined so σ is C0 & C1 continuous at $\lambda = \lambda^* - p_z$, where λ^* is the stretch at which the stress-stretch relationship becomes linear. Because the zonules are individual discrete fibers *in vivo* that are represented within zonule sheets in the model, zonule shear properties were seven orders of magnitude lower than along-fiber properties. Components of the lens and all extralenticular structures were modeled as isotropic Neo-Hookean material with deviatoric strain energy density (W) function:

$$W = C_1(\bar{I}_1 - 3) \quad \text{Equation 4.4}$$

Where $\bar{I}_1$ is the first isotropic deviatoric invariant of the right Cauchy-Green deformation tensor and C_1 is the material constant which was assigned to represent approximately 30-year-old humans, based on mechanical testing measurements (Burd et al. 2002; Eilaghi et al. 2010; Friberg and Lace 1988; Krag and Andreassen 2003; Krag et al. 1997; Moses and Grodzki 1977; Sharif-Kashani et al. 2011; Wang et al. 1996; Wilde et al. 2012; Worthington et al. 2014).

Simulations were performed using the AMPS finite-element package (AMPS Technologies, Pittsburgh, PA), and with two distinct time periods: initialization and accommodation. During

initialization, the zonule tensioning parameter (p_z) increased so that the lens was stretched into the unaccommodated position. Tension of each zonule division was tuned so that predicted lens shape was consistent with measurements made with MRI (Strenk et al. 1999). During accommodation, ciliary muscle activation (α) was increased, inducing muscle excursion. Activation of individual muscle sections were tuned so that predicted ciliary muscle excursion matched muscle shape changes measured with OCT (Sheppard and Davies 2010). The model with tuned zonule tension and ciliary activation parameters was independently tested to ensure predicted lens deformation in response to ciliary muscle excursion were appropriate. Model results were compared to synchronous *in vivo* measurements of both the lens and ciliary muscle motion made during accommodation (Ruggeri et al. 2016), as well as asynchronous measurements made with OCT (Richdale et al. 2013) and MRI (Croft, McDonald, et al. 2013). To investigate the function of the different ciliary sections in altering the eye's optic power, simulations were performed where each muscle section was activated in isolation. Model predictions were examined to determine how each section deformed the lens by changing its thickness and translated the lens anteriorly by shifting the position of the lens equator towards the cornea.

Simulation results using this model with the previously defined parameters (Knaus et al. 2021) are called the original model. Model variations were created by altering material parameters of either the lens components, the sclera, or the ciliary muscle. Parameters chosen for model variations represented changes in these tissues with age in fifteen-year increments and simulation results were compared to the original model. Model predictions of lens deformation and translation in response to ciliary excursion were determined in each variation. These movements of the lens determine the accommodative amplitude, or change in optical power, during accommodation (Knaus et al. 2021). Reduced lens thickening or increased posterior lens translation compared to the original model indicate a deficit in accommodative function due to the simulated age-associated material change.

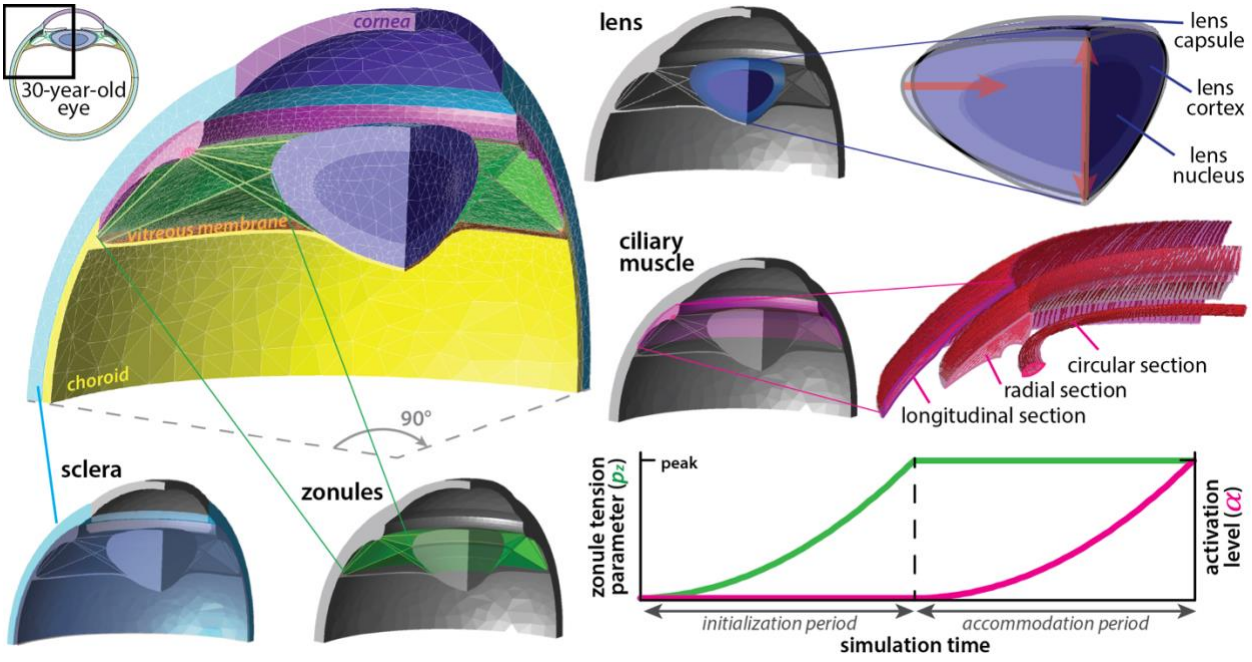

Figure 4.1: 3D finite element model of the anterior eye based on measurements of 30-year-old humans is axially symmetric and rotated 90° around the center axis. The model was subdivided into discrete anatomical regions with shared boundary nodes. Most regions were assigned passive non-linear isotropic material properties including the sclera, cornea, choroid, vitreous membrane, and the regions of the lens: capsule, cortex, and nucleus. The zonule and ciliary muscle structures were assigned transversely isotropic material properties. The constitutive law assigned to the zonules included a tensioning parameter (p_z) that was increased from zero in order to stretch the lens into the unaccommodated position during the initialization period of the model simulation, then held constant at the assigned peak value for the rest of the simulation time. Unique peak values were assigned to each zonule division sheet. The constitutive law assigned to the ciliary muscle included an activation level (α) that was increased from zero at the start of the accommodation period to an assigned peak value at the end of the simulation time in order to simulate muscle contraction. Unique peak activation levels were assigned to the longitudinal, radial, and circular sections of the muscle. The elements in each ciliary section were assigned fiber directions to represent the physiologic orientation of the muscle cells.

4.3.2 Model Variations with Age-related Changes in Lens Properties

In order to simulate age-related stiffening of the lens, the Neo-Hookean material constants (C_1 -

$$W = C_1(\bar{I}_1 - 3) \quad \text{Equation .4)}$$

of the lens components (capsule, cortex, and nucleus) were concurrently changed. Measurements of the mechanical properties of the lens capsule indicate that it becomes stiffer until the age of thirty-five, after which it no longer changes (Krag and Andreassen 2003; Krag et al. 1997). The regression analysis from that study has been used previously (Burd et al. 2002; Wilkes and Reilly 2016) to determine the elastic modulus of the capsule as it increases to age thirty-five then becomes constant (Figure 4.2A). For this study, we used the elastic modulus divided by six to determine the capsule's material constant (C_1), assuming near incompressibility as the capsule has been measured to have a Poisson's ratio of 0.47 (Fisher 1969). Mechanical testing of the lens was previously used to determine age-related regression models for the shear modulus of the lens substance (Wilde et al. 2012). Using Model D from that study, which also represented the cortex and nucleus as separate homogenous materials, we determined material constant (C_1) for each by dividing the shear modulus by two (Figure 4.2B-C). Using these relationships, we created three model variations using lens material constants that corresponded with fifteen-year incremental increases from our original model: variation 1 = 45-year-old lens, variation 2 = 60-year-old lens, variation 3 = 75-year-old lens. All other parameters were the same as the original model.

4.3.3 Model Variations with Age-related Changes in Scleral Properties

To simulate age-related scleral stiffening in this study, we used a linear regression for the sclera elastic modulus measured with uniaxial mechanical testing of anterior sclera samples (donor ages: 16-81 years)(Friberg and Lace 1988), divided by six assuming near incompressibility (Boote et al. 2020), to determine its material constant (C_1) at different ages (Figure 4.2D). We created three model variations using sclera material constants that corresponded with fifteen-year incremental increases from our original model: variation 4 = 45-year-old sclera, variation 5 = 60-year-old sclera, variation 6 = 75-year-old sclera. All other parameters were the same as the original model.

4.3.4 Model Variations with Age-related Changes in Ciliary Muscle Properties

A quantitative histological study of the ciliary muscle in human eyes (donor ages: 33-87 years) found that the area of the ciliary muscle in meridional cross sections decreases with age (Tamm et al. 1992). Changes in area were relatively different between the muscle sections, with greater area decreases in the longitudinal and radial sections compared to the circular section. Further, reduced area fractions of the longitudinal and radial sections were accompanied by increases in the connective tissue within the muscle boundary. Model geometry was the same in all variations, so in order to represent age-related ciliary muscle changes in our FE simulations, we altered the activations assigned to the muscle sections. Area and volume of skeletal muscles have previously been shown to correspond with functional capacity (Fukunaga et al. 2001; Holzbaur et al. 2007; Narici et al. 1996), and we assumed the ciliary muscle's force production capacity might be similarly linked to its size. Therefore, reduction in contractile tissue of the ciliary muscle, due to the combine effects of selective atrophy and intramuscular connective tissue fraction changes, suggests that force production by the muscle is reduced and redistributed between the sections with age. The activation level (α) scales the active force component of the stress-strain relationship in the fiber direction of the ciliary muscle material (Equation 4.2). Using the linear regression models of area in the whole muscle and each section, and data for connective tissue fraction with age (Tamm et al. 1992), we determined a relative change in contractile tissue of each muscle section. We used these relative changes to scale the activation levels used in the original model to create three model variations representing fifteen-year incremental age increases: variation 7 = 45-year-old ciliary muscle, variation 8 = 60-year-old ciliary muscle, variation 9 = 75-year-old ciliary muscle (Figure 4.2E). All other parameters were the same as the original model.

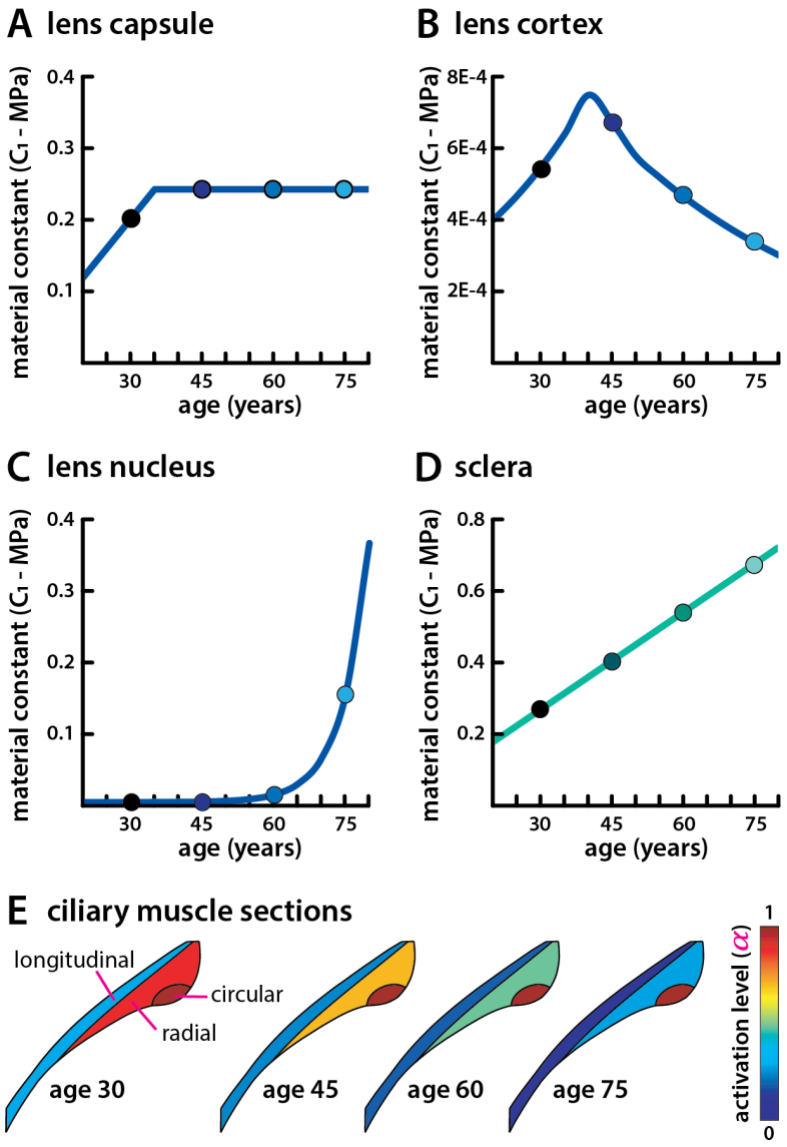

Figure 4.2: Model parameters variations to represent age-related changes in the lens, sclera, and ciliary muscle. **A)** Lens capsule material constants (C_1) were determined from previous measurements and linear regression of changes in the elastic modulus with age to thirty-five years old, after which the stiffness is constant (Krag and Andreassen 2003). **B)** Lens cortex and **C)** lens nucleus material constants (C_1) were determined from previous measurements and modeling of changes in the shear moduli with age(Wilde et al. 2012). **D)** Sclera material constants (C_1) were determined from previous measurements and linear regression of changes in the elastic modulus with age (Friberg and Lace 1988). **E)** Ciliary muscle section activations were changed to represent redistribution of force production in the different sections due to selective atrophy and increased intramuscular connective tissue observed with age (Tamm et al. 1992).

model variation	original	var 1	var 2	var 3	var 4	var 5	var 6	var 7	var 8	var 9
"age"	30	45	60	75	45	60	75	45	60	75
Neo-Hookean material constant: C_1 (MPa)										
capsule	0.20	***0.24***	***0.24***	***0.24***	0.20	0.20	0.20	0.20	0.20	0.20
cortex	5.40E-4	***6.70E-4***	***4.70E-4***	***3.40E-4***	5.40E-4	5.40E-4	5.40E-4	5.40E-4	5.40E-4	5.40E-4
nucleus	1.00E-4	***1.70E-4***	***1.08E-2***	***1.52E-1***	1.00E-4	1.00E-4	1.00E-4	1.00E-4	1.00E-4	1.00E-4
sclera	0.27	0.27	0.27	0.27	***0.405***	***0.540***	***0.675***	0.27	0.27	0.27
Ciliary activation level: α (dimensionless)										
longitudinal	0.25	0.25	0.25	0.25	0.25	0.25	0.25	***0.208***	***0.142***	***0.075***
radial	0.9	0.9	0.9	0.9	0.9	0.9	0.9	***0.671***	***0.443***	***0.214***
circular	0.999	0.999	0.999	0.999	0.999	0.999	0.999	0.999	0.999	0.999

Table 4.1: Parameters used in model variations. Material parameters were altered (bold and italicized) from values in the original model to represent the properties of either the lens components (variations 1-3), sclera (variations 4-6), or ciliary muscle sections (variations 7-9) at that variation's assigned "age", while all other parameters were held constant. The Neo-Hookean material constant (C_1) was changed in simulations to represent age-related changes in the lens components and the sclera. The activation level (α) was changed in simulations to represent age-related changes in the ciliary muscle sections.

4.4 Results

4.4.1 Model Predictions with Changes in Lens Properties

Altering lens properties did not result in changes to predicted ciliary muscle apex thickening, and only the model with lens properties representing a 75-year-old (variation 3) predicted a reduction in lens thickening during simulated accommodation (Figure 4.3). The change in lens thickening was a result of greater unaccommodated lens thickness, while accommodated lens thickness was similar between model variations (1-3) with altered lens properties (Figure 4.4). Lens deformation was only affected by parameter changes corresponding with ages greater than 60-years-old (Figure 4.5A), but lens translation was unchanged by altering lens properties for any age (Figure 4.5B).

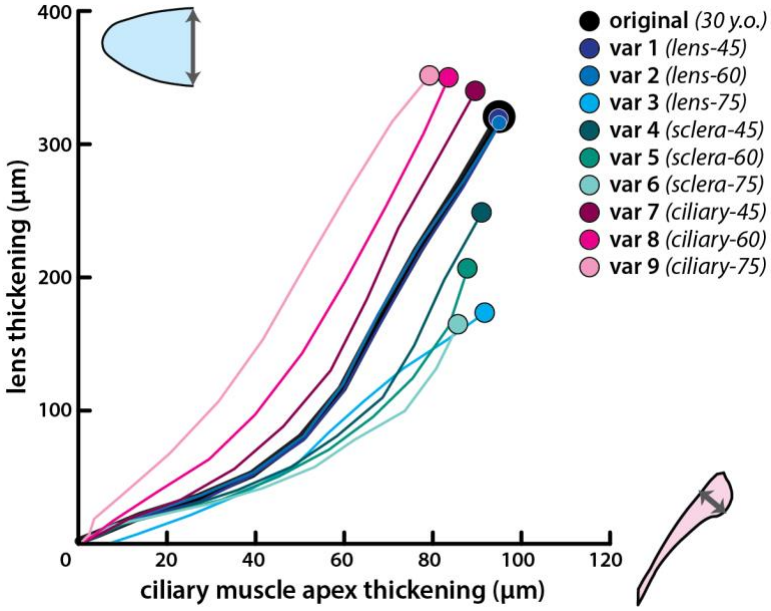

Figure 4.3: Variations in predicted lens deformation in response to ciliary muscle excursion. The model predicted the change in ciliary muscle apex thickness and corresponding lens thickness that occurred during simulations of accommodation. Predicted lens deformation in response to ciliary muscle excursion is shown for the original model, which represents a thirty-year-old eye, and for nine variations of this model. For variations 1-3, the material constants of the lens components were assigned to values for a forty-five-, sixty-, and seventy-five-year-old eye (var 1 and var 2 overlap with the original model). For variations 4-6, the material constant of the sclera was assigned to values for eyes of these same ages. For variations 7-9, the activations of the ciliary muscle sections were assigned to values for aged eyes. Lens and apex thickening at the end of each simulation is indicated with a circle.

4.4.2 Model Predictions with Changes in Scleral Properties

Increasing the age represented by sclera properties (variations 4-6) resulted in decreasing thickness changes of the ciliary muscle apex and the lens during simulated accommodation (Figure 4.3). The change in lens thickening was a result of decreasing accommodated lens thickness, while unaccommodated lens thickness was similar between model variations (4-6) with altered scleral properties (Figure 4.4). Lens deformation progressively decreased with parameter changes corresponding with increasing sclera ages (Figure 4.5A), but lens translation was unchanged by altering scleral properties for any age (Figure 4.5B).

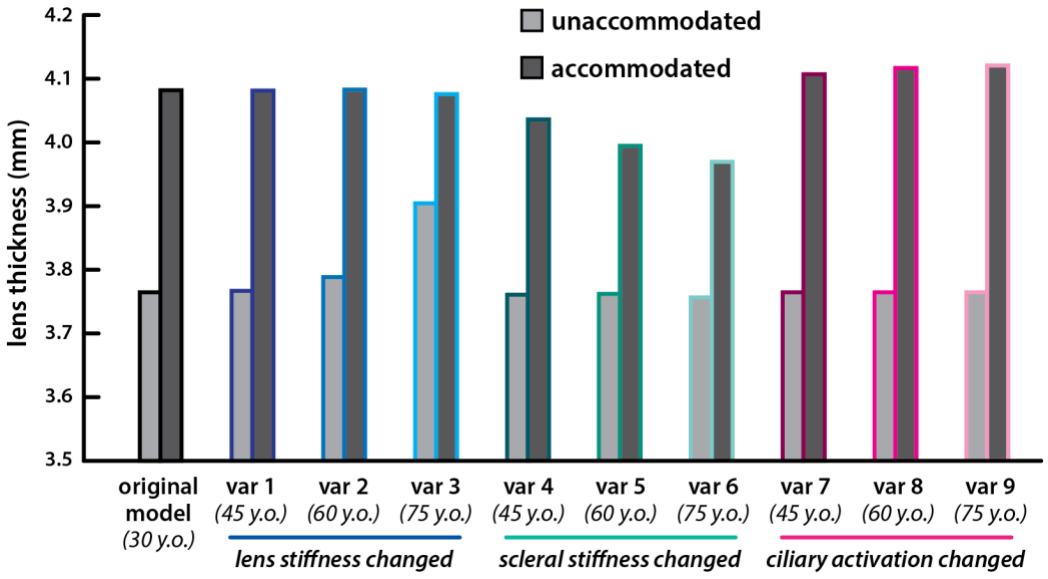

Figure 4.4: Predicted lens thickness in the unaccommodated position and the accommodated position is shown for the original model and nine model variations. Unaccommodated lens thickness was measured at the end of the simulation initialization period and accommodated lens thickness at the end of the accommodation period.

4.4.3 Model Predictions with Changes in Ciliary Muscle Properties

Increasing the age represented by ciliary muscle properties (variations 7-9) resulted in decreased thickening of the ciliary apex but slightly increased thickening of the lens during simulated accommodation (Figure). The change in lens thickening was a result of increasing accommodated lens thickness, while unaccommodated lens thickness was similar between model variations (7-9) with altered ciliary properties (Figure). Lens deformation slightly increased with parameter changes corresponding with increasing ages (FigureA), however, lens translation dramatically increased in the posterior (negative) direction with increasing age associated with ciliary properties (FigureB).

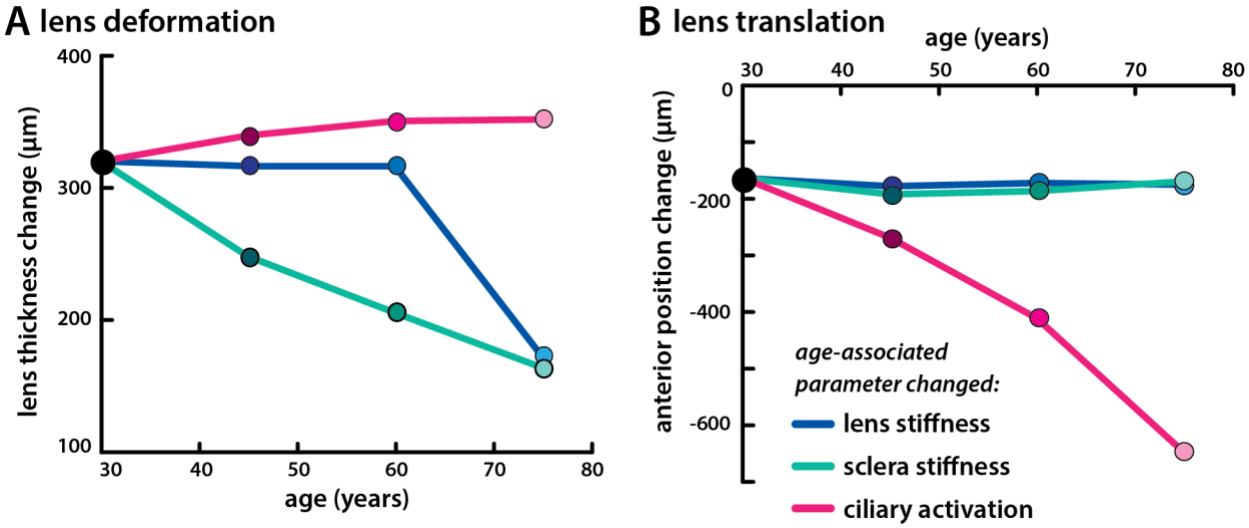

Figure 4.5: Predicted changes in lens deformation and translation with age. Results of simulation variations are plotted to show how changes with age affect lens deformation and translation. **A)** The change in lens thickness during simulated accommodation is used as a metric of lens deformation. Lens thickness change predicted by each variation is plotted with the age associated with the changed parameters. The parameters changed were either the material constants of the lens components, modulating lens stiffness, the material constant of the sclera, modulating sclera stiffness, or the activation of the muscle sections, modulating ciliary excursion. **B)** The change in the anterior position of the lens equator during simulated accommodation is used as a metric of lens translation. Lens anterior position change predicted by each variation is plotted with the age associated with the changed parameters.

4.5 Discussion

Using our finite element model of the accommodative mechanism driven by the action of the ciliary muscle we were able to examine how age-related changes contribute to functional deficits in presbyopia. Model variations were created with altered lens stiffness, scleral stiffness, or ciliary activation in order to compare differences in predicted accommodative lens displacements. Changes is each component altered accommodative lens displacements, though the effect varied in mechanism and time scale for each.

With model changes in lens stiffness, differences in predicted accommodative behavior depended on the age associated with the new parameters. Model variations with lens properties representing a 45 and 60-year-old show very little difference from the original model, representing a thirty-year-old (Figure 4.3). However, the 75-year-old lens variation predicted significant decreases in accommodative function. The material constant of the capsule did not differ in the aging lens variations as it reaches a constant stiffness at the age of 35 (Figure 4.2A), and the cortex stiffness only increased in the 45-year-old variation, before decreasing (Figure 4.2B). Therefore, differences with age seem to be attributed to changes in the lens nucleus stiffness, which increased by orders of magnitude to nearly the same stiffness of the capsule by 75 years old (Figure 4.2C). The model variation with this lens age predicted a large reduction in lens thickening during accommodation that resulted from increased unaccommodated lens thickness (Figure 4.4). Zonule tensioning was used to stretch the lens to the unaccommodated position. Tension parameters were not altered in simulations with varied stiffness. With a stiffer lens, the tuned zonule parameters created insufficient tension on the lens to stretch it into the unaccommodated shape of the original model. Unaccommodated lens shape has been measured to be larger in older adults *in vivo* (Richdale et al. 2013; Strenk et al. 1999). Lens stiffness may contribute in part to accommodative dysfunction by disrupting the resting tension between the lens, zonules, and ciliary muscle. If the lens is not sufficiently stretched when the muscle is relaxed, then contraction of the ciliary muscle is unable to induce enough lens deformation to produce a healthy accommodative amplitude.

A previous modeling study by Wilkes and Reilly similarly found that age-related changes in lens material properties led to accommodative deficits, though not enough to fully explain presbyopia (Wilkes and Reilly 2016). Results from this study indicate that lens changes may have a greater effect at younger ages than predicted by our model. However, they used a homogenous model of the lens substance which exhibits different changes with age than the model we used with separated cortex and nucleus (Wilde et al. 2012). Wilkes and Reilly also started simulations by stretching the lens with zonule tension before producing accommodation by prescribing a displacement to the zonule boundary to represent ciliary muscle excursion. Unlike our approach when varying age-related material properties, zonular force increased with material age to produce the same unaccommodated lens thickness and accommodative deficits were instead the result of reduced accommodated lens thickness (Wilkes and Reilly 2016). These different approaches highlight an important gap in our knowledge of the aging lens. While lens dimensions at different ages have been measured *in vivo* (Richdale et al. 2013; Strenk et al. 1999) and in isolation (Glasser and Campbell 1999; Urs et al. 2009), it remains unknown how the *in vivo* stress state of the lens differs with age. Simulations show that unaccommodated lens tension plays a large role in accommodation so future work to quantify changes with age will be critical in better understanding presbyopia.

Changes in sclera stiffness resulted in progressive age-related decreases in predicted accommodative function. Model variations demonstrated a negative linear relationship between predicted lens thickening and the age associated with new parameters (Figure 4.5A). These results correspond with the linear increase in sclera material constant with age (Figure 4.2D). Decreasing lens thickening with age resulted from lower accommodated lens thickness (Figure 4.4), indicating that tension on the lens was not reduced enough during accommodation for it to return to its unstretched thickness. Stiffening of the sclera inhibited ciliary muscle excursion so that it thickened less at its apex and induced less lens shape change per muscle shape change (Figure 4.3). These results indicate that changing properties of the sclera can contribute to accommodative dysfunction and supports the hypothesis that therapeutically altering its

properties could restore function (Boote et al. 2020; Hipsley, Hall, and Karolinne M Rocha 2018). Therapies that reduce scleral stiffness might especially aid younger patients who have or are developing presbyopia, as scleral changes might impact function at an earlier age than lens changes (Figure 4.5A).

Ciliary muscle section activations changes representing relative contractile tissue changes with age did not decrease predicted lens thickening. In fact, the lens thickened slightly during accommodation (Figure 4.4) and lens thickening increased relative to muscle apex thickening (Figure 4.3). While these differences in lens thickening suggest that the aging ciliary muscle may facilitate optic gain, there is another difference to consider. We also looked at translation of the lens equator in the anterior-posterior direction and found that with activations representing increasing age, the lens' posterior translation increased (Figure 4.5B). This would move the lens further away from the cornea, negating any optic gains that are achieved by thickening. Age-related ciliary muscle changes primarily reduce the force production of the longitudinal and radial sections. We previously used our model to quantify mechanical effects of each ciliary muscle section on accommodative lens behavior and found that these two sections don't contribute to lens thickening, however, they do act synergistically with the circular section to modulate the anterior position of the lens (Knaus et al. 2021). With simulated aging, decreased of longitudinal and radial section contraction reduces position modulation, resulting in more dominate effects of circular section contraction during accommodation. These results are consistent with measured changes of anterior movement of the lens equator in older humans that is correlated with decreasing accommodative amplitude (Croft, McDonald, et al. 2013). Further measurements in rhesus monkeys evidence predicted changes in ciliary muscle excursion, finding decreased anterior movement of the posterior insertion zone of the vitreous zonule (Croft, McDonald, et al. 2013; Lütjen-Drecoll et al. 2010). Our simulations indicate that this movement relies on ciliary length change with is most influenced by contraction of the longitudinal section (Knaus et al. 2021) and therefore most affected with age. Some presbyopia treatments have employed pharmaceuticals or electro-stimulation to increase ciliary muscle contraction (Wolffsohn

and Davies 2019), but more work is needed to understand how these techniques might by applied to improve the synergistic behavior of the ciliary muscle sections.

There are multiple limitations of this model, which relies on several assumptions to simplify ocular mechanics and fill in gaps of current knowledge. Selected material properties are based on *ex vivo* mechanical measurements and models of age-related changes. While we assume these properties adequately describe the *in vivo* behavior of these tissues, they may not entirely capture mechanical changes with age. However, the model does help us to contextualize assumed material property changes with accommodative function changes. Additional studies confirm the age-related changes assumed in this study, but these studies are also subject to their own limitations. For example, uniaxial tensile tests of cadaveric sclera samples also show increased tangent stiffness with age in anterior, posterior, and equatorial samples but were limited to an age range of 50-90 years old (Geraghty et al. 2012), while inflation tests show increased shear modulus across a larger age range (20-90 years old) but only used posterior sclera samples (Grytz et al. 2014). Further, we only simulated aging by changing material properties, while model geometry was unchanged. Geometric changes, like lens growth (Glasser and Campbell 1999; Urs et al. 2009) and resting ciliary muscle apex changes (Strenk et al. 1999; Tamm et al. 1992), might also contribute to presbyopia by altering how these tissues deform as they interact in accommodation. We assumed that zonular tension did not changes with age, but different *in vivo* dimensions of the aging lens and ciliary muscle (Croft, McDonald, et al. 2013; Lütjen-Drecoll et al. 2010; Richdale et al. 2013; Strenk et al. 1999; Tamm et al. 1992) could indicate that tension between these structures has also changed. There are other tissues whose properties change with age, like the choroid (Friberg and Lace 1988; Tamm 1992; Tamm et al. 1991; Ugarte et al. 2006), that we did not investigate in this study but may play a role in presbyopia. We also assumed interactions between tissues remained the same and made no changes to the boundary conditions of our model. Our model included a compliant lamellae layer that separated the sclera from the ciliary muscle and choroid to allow more relative movement between these structures (Knaus et al. 2021). Experiments in rhesus monkeys showed greater

age-related differences in accommodative ciliary muscle excursion when attachments to the sclera are intact compared to disrupted (Tamm 1992). While unknown if phenomenon is true of aging humans, simulations that combine stiffening of the lamellae layer in combination with scleral stiffening predicted greater accommodative deficits (Knaus, et al. IOVS 2017;58: ARVO E-Abstract 2062). We assumed a single material property value was associated each range, when in fact these properties do vary between individuals with similar ages (Friberg and Lace 1988; Krag and Andreassen 2003; Tamm et al. 1992; Wilde et al. 2012). To address this limitation in future work, simulations could be performed with a range for each value to quantify uncertainty in each variation. Although our knowledge of the pathophysiology of presbyopia is still incomplete, the model allows us to simulate changes we believe occur in the eye with age. While changes occur concurrently *in vivo*, by examining changes in isolation we can quantify how each might reduce accommodative function. A direction for future work is to create model variations with combinations of age-related changes to different components to understand how specific changes may collectively contribute to presbyopia.

Model predictions have identified multiple potential mechanisms of presbyopia that likely work in combination to reduce accommodative function with age. Model results indicate that the most effective treatment strategies for symptoms of presbyopia may depend on the patient's age or at least the relative mechanical properties of these ocular structures.

Chapter 5

Achilles tendon morphology is related to triceps surae muscle size and peak plantarflexion torques during walking in young but not older adults

"All that is gold does not glitter,

Not all those who wander are lost;

The old that is strong does not wither,

Deep roots are not reached by the frost."

– J.R.R. Tolkien, *The Lord of the Rings*

5.1 Abstract

The interaction of the triceps surae muscles and the Achilles tendon is critical in producing the ankle plantarflexion torque required for human walking. Deficits in plantarflexor output are a hallmark of reduced mobility in older adults and are likely associated with changes in the triceps surae muscles that occur with age. Structural differences between young and older adults have been observed in the Achilles tendon and in the triceps surae muscles. However, less is known about how age-related differences in muscle and tendon morphology correspond with each other, and furthermore, how those morphology differences correlate with age-related deficits in function. The goal of this work was to investigate whether there is a correlation between age-related differences in triceps surae muscle size and Achilles tendon CSA and whether either is predictive of ankle plantarflexion torque during walking. We used magnetic resonance imaging (MRI) to measure triceps surae muscle volumes and tendon cross-sectional areas in young (n = 14, age: 26± 4 years) and older (n = 7, age: 66 ± 5 years) adults, and we determined peak plantarflexion torques during treadmill walking. We found that individual muscle volumes as a percent of the total triceps surae volume did not differ between young and older adults, though muscle volumes per body size (normalized by the product of height and mass) were smaller in older adults. Achilles tendon CSA was correlated with body size and muscle volumes in young adults but not in older adults. The ratio of tendon CSA to total triceps surae muscle volume was significantly greater in older adults. Peak ankle plantarflexion torque during walking correlated with body size and triceps surae volume in young and older adults but was correlated with tendon CSA only in the young adults. Structure-function relationships that seem to exist between the Achilles tendon and the triceps surae muscles in young adults are no longer evident in all older adults. Understanding mechanisms that determine altered Achilles tendon CSA in older adults may provide insight into age-related changes in function.

5.2 Introduction

The interaction of the triceps surae muscles with the Achilles tendon is critically important to human walking. This complex muscle-tendon interplay is the primary source of plantarflexion torque at the ankle and is implicated in the development of walking deficits that occur with age. Gait differences between young and older adults are clearly associated with differences in plantarflexor output (Boyer et al. 2017; DeVita and Hortobagyi 2000; Kerrigan et al. 1998; Winter et al. 1990). Numerus studies have investigated age-related differences in the morphology and the mechanical properties of the Achilles tendon and triceps surae muscles (Karamanidis and Arampatzis 2006; Onambele et al. 2006; Stenroth et al. 2012), but it remains unclear how muscle and tendon structure relate to each other in both young and older adults. Further, the association between age-related changes in muscle and tendon structure and changes in plantarflexor output has not been fully explored.

The triceps surae muscles share a common series elastic element in the Achilles tendon but are an anatomically complicated group of muscles that may experience complex changes with age. The biarticular gastrocnemius and uniarticular soleus muscles within this group differ greatly in volume (Handsfield et al. 2014; Ward et al. 2009), architecture (Bolsterlee et al. 2019; Dalmau-Pastor et al. 2014; Rana et al. 2013; Ward et al. 2009), and fiber type (Johnson et al. 1973). It is not surprising that empirical and modeling studies suggest functional differences between these muscles, predicting unequal contributions to propulsion and support during walking (Anderson and Pandy 2003; Francis et al. 2013; McGowan et al. 2008; Neptune et al. 2001). Each muscle's function is rooted in its intricate architecture. The gastrocnemius comprises distinct medial and lateral heads with different origins (Dalmau-Pastor et al. 2014). The soleus is divided by its aponeuroses into bipennate anterior compartments and unipennate posterior compartments (Agur et al. 2003; Bolsterlee et al. 2018; Hodgson et al. 2006). Age-related sarcopenia leads to reduced muscle volumes in the triceps surae (Janssen et al. 2000; Morse et al. 2005); however, it is unclear whether sarcopenia similarly affects each individual triceps surae muscle. It is

possible that the individual muscles' susceptibility to atrophy may vary due to differences in mechanical stimuli and fiber type composition (Nilwik et al. 2013).

Triceps surae muscle volume is indicative of ankle plantarflexion torque capacity (Fukunaga et al. 2001), such that smaller triceps surae volume may explain why older adults employ lower ankle plantarflexion torques than young adults when walking at the same speed (DeVita and Hortobagyi 2000; Franz and Thelen 2015). However, direct comparisons between plantarflexion torques during walking and triceps surae muscle volumes have not been performed across age groups to assess age-related differences. Further, given the functional differences between triceps surae muscles, age-related changes in individual components of this muscle group may better explain torque deficits.

In contrast to changes in muscle size, Achilles tendon cross-sectional area (CSA) is maintained or even increased with age (Onambele et al. 2006; Stenroth et al. 2012). Healthy tendons adapt to changes in mechanical loading (Bohm, Mersmann, and Arampatzis 2015), suggesting that the ratio of muscle size to tendon size should remain constant. However, the correlation between muscle size and tendon size has not been well studied, nor have age-related differences in this correlation been observed. Understanding the morphological relationship between the Achilles tendon and individual components of the triceps surae, in addition to the full muscle group, may provide further insight into age-related changes in walking.

The goal of this work was to investigate how triceps surae muscle volumes collectively and individually differed with age. We aimed to determine (1) if age-related differences in muscle size correlated with age-related differences in Achilles tendon cross-sectional area and (2) if age-related differences in muscle size and tendon CSA were predictive of age-related differences in joint torque during walking. We used magnetic resonance imaging (MRI) to measure muscle volumes and tendon cross-sectional areas in young and older adults and determined peak plantarflexion torques during treadmill walking. We tested the hypotheses that (i) triceps surae muscle volumes would negatively correlate with age and positively correlate with body size while Achilles tendon CSA would positively

correlate with both age and body size, (ii) age-related changes in volume would differ between individual muscles of the triceps surae, and (iii) differences in tendon and muscle size would positively correlate with differences in ankle plantarflexion torque during walking in both young and older adults.

5.3 Methods

5.3.1 Subjects

Fourteen healthy young (6 females/8 males, age: 26 ± 4 years, height: 1.78 ± 0.10 m, mass: 74.87 ± 12.11 kg) and seven healthy older adults (4 females/3 males, age: 66 ± 5 years, height: 1.76 ± 0.07 m, mass: 74.57 ± 15.26 kg) participated in this study (Table). No subjects had a history of orthopedic or neurological impairment or injury to the lower limb, and all could walk comfortably on a treadmill. All older adult subjects reported participating in daily physical activity. All subjects provided written consent, and the study protocol was approved by the University of Wisconsin-Madison Health Sciences Institutional Review Board.

	age (years)	**height (m)**	**mass (kg)**	**tendon CSA (mm^2)**	**moment arm (mm)**
young	25.5 ± 4.3	1.78 ± 0.1	74.87 ± 12.11	61.35 ± 12.24	46.64 ± 3.87
older	66 ± 4.8	1.76 ± 0.07	74.57 ± 15.26	65.54 ± 6.96	43.54 ± 8.13
***p*-value**	**0.0003**	0.601	0.911	0.248	0.086
	peak ankle torque (Nm)	**stride length (m)**	**step length (m)**	**stride time (s)**	**cadence (steps/min)**
young	114.23 ± 24.01	1.38 ± 0.09	0.69 ± 0.04	1.11 ± 0.07	108.74 ± 6.83
older	106.04 ± 27.72	1.27 ± 0.1	0.64 ± 0.05	1.02 ± 0.08	118.48 ± 9.84
***p*-value**	0.478	**0.036**	**0.035**	**0.036**	**0.040**

Table 5.1: Subject characteristics (mean ± standard deviation). All gait characteristics are reported for subjects walking at a speed of 1.25 m/s. Young and older adults did not differ significantly in body size, Achilles tendon geometry, or peak torque produced during walking. However young and older adults did differ in their gait spatio-temporal parameters, with older adults using shorter strides at a higher cadence than young adults walking at 1.25 m/s. P-values < 0.05 were considered significant and written in bold.

5.3.2 Triceps Surae Muscle Volume Measurements

The triceps surae muscles and Achilles tendon were imaged with a 3T Signa PET/MR scanner (GE Healthcare) using a spoiled gradient recall-echo sequence that used iterative decomposition of water and fat with echo asymmetry and least squares estimation (IDEAL-SPGR)(Reeder et al. 2007). Subjects lay supine with their right ankle relaxed and wrapped in a GEM Medium Flex Coil. Two sets of three-dimensional images were collected with the following scanning parameters: in-plane resolution: 0.72 x 0.72 mm; slice thickness: 2 mm; imaging matrix: 512 x 512 x 76; flip angle: 14°. Continuous axial images were obtained from the calcaneus to the femur proximal to the condyles.

The triceps surae muscles in the right limb were segmented using a Matlab (Mathworks Inc., Natick, MA, US) software package that was developed in the Multiscale Muscle Mechanophysiology lab at the University of Virginia for measuring lower limb muscle volumes (Handsfield et al. 2014). In each axial image, a single researcher manually outlined the boundaries of four unique muscles: the medial gastrocnemius (MG), the lateral gastrocnemius (LG), the posterior soleus (PS), and the anterior soleus (AS) (Figure 5.1). The heads of the gastrocnemius and the soleus muscles were identified based on a detailed slice-by-slice segmentation atlas of lower limb muscles (Handsfield et al. 2014), and the posterior and anterior compartments of the soleus were identified based on descriptions of the aponeurosis that visibly separates these regions of the muscle (Bolsterlee et al. 2018; Hodgson et al. 2006). Individual muscle volumes were calculated by summing the volume of voxels from the segmentation in each image. Previously, we determined the average intra-user variability in measuring muscle volumes using this segmentation method to be 4.4% (Handsfield, Meyer, et al. 2016). Total triceps surae muscle volume was defined as the sum of the volumes of the four individual muscles. Relative muscle volumes were determined by dividing individual muscle volumes by the total triceps surae muscle volume.

To determine differences in muscle size independent of body size differences, we normalized individual and total muscle volumes by dividing by the product of subject height and mass. Triceps surae

muscle volumes have been shown to vary with height*mass as a metric of body size in healthy adults (Handsfield et al. 2014).

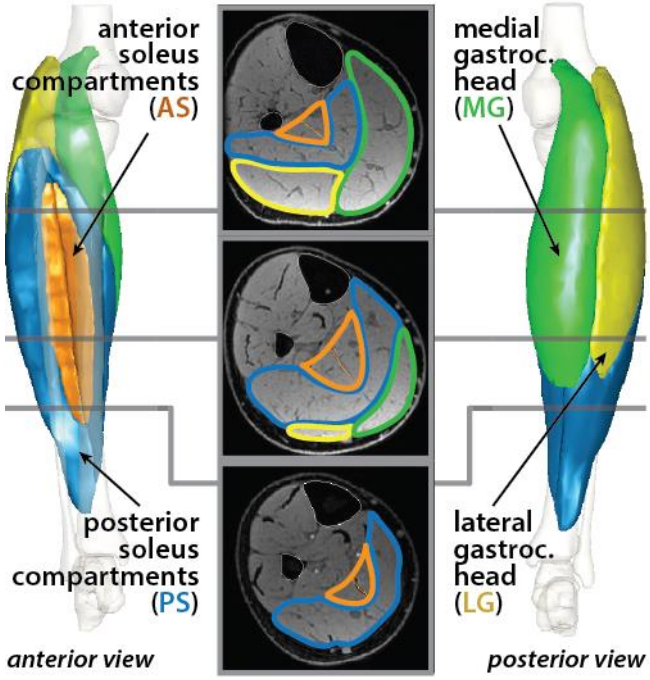

Figure 5.1: Triceps surae muscles segmented in axial MR images. The muscle cross sections were defined for the medial (green) and lateral (yellow) heads of the gastrocnemius and the posterior (blue) and anterior (orange) compartments of the soleus. Each muscle was reconstructed in 3D.

5.3.4 Achilles Tendon Cross-Sectional Area Measurements

The Achilles free tendon was also segmented in the axial MR images from the most proximal image where the calcaneus was visible to the soleus muscle-tendon junction (MTJ), which was defined as the most distal image where the soleus was visible. The tendon volume was determined from the summed CSA multiplied by the slice thickness, while the tendon length was computed as the summed distance between the centroids of adjacent cross sections (Handsfield et al. 2014).

To test our hypotheses, a representative Achilles cross-sectional area (CSA) was determined from the middle slice of the free tendon. A ratio of tendon size per muscle size was calculated by dividing

Achilles tendon CSA by individual and total triceps surae muscle volumes, just as tendon size per body size was found by dividing tendon CSA by the product of height and mass.

5.3.5 Achilles Tendon Moment Arm Measurements

Achilles tendon moment arms were measured using a previously described method combining ultrasonography and motion capture (Ebrahimi et al. 2020; Keuler et al. 2019; Rasske, Thelen, and Franz 2017). Briefly, subjects lay prone with their right knee flexed 20° while their ankle was rotated from maximum dorsiflexion to maximum plantarflexion. Subjects were asked to provide resistance during ankle rotation to engage their triceps surae muscles. An ultrasound transducer positioned over the Achilles tendon was used to collect B-mode images. The superficial and deep edges of the tendon were manually identified, and a tendon line of action was determined from the best fit between them. Marker clusters on the shank, foot, and transducer were used to record kinematics in order to transform ultrasound images into the reference frame of the shank. A best-fit screw axis that described the foot motion with respect to the shank was computed to define a functional axis (Siston et al. 2005). Achilles tendon moment arm was computed in each image frame as the perpendicular distance between the tendon line of action and the functional axis (Wade, Lewis, and Piazza 2019). The moment arm was estimated for a 0° posture using a quadratic fit of moment arm relative to ankle angle.

5.3.6 Peak Ankle Torque Measurements During Walking

Subjects walked on an instrumented treadmill (sample rate: 1900Hz, Bertec Corp.) at 1.25 m/s. Ground reaction forces were recorded during at least two 10-second trials (minimum 10 strides). Motion capture (sample rate: 190Hz, Motion Analysis Corp.) was used to record 3D trajectories of markers positioned on the pelvis, thigh, and shank during walking. Lower extremity kinematics and kinetics were computed using standard inverse dynamics techniques (Visual3D, C-Motion, Inc.). Peak ankle plantarflexion moments were averaged across gait cycles for each subject. Plantarflexion torque was

assumed to be generated entirely by the triceps surae muscles. Peak ankle torque was divided by Achilles tendon moment arm to provide an estimate of Achilles tendon force at these peaks.

5.3.7 Statistical Analyses

We used a Mann-Whitney rank sum test, a non-parametric test, to determine differences in our measurements between young and older subject groups. For tests that were repeated over the 4 individual muscles, we corrected for family-wise error rate using the Holm-Bonferroni method. Linear regression analysis was used to determine correlations between different measurements in either young or older subjects. Significance was set at $p = 0.05$.

5.4 Results

5.4.1 Relative volumes of triceps surae muscles did not differ between young and older adults

Relative volumes of individual triceps surae muscles, compared to total volume, were similar in young (percent of total volume: PS = 41.9%, AS = 8.8%, MG = 30.9%, LG = 18.3%) and older (PS = 42.4%, AS = 8.5%, MG = 29.7%, LG = 19.4%) adults (Figure 5.2), with no significant difference for any muscle (Table 5.2).

5.4.2 Triceps surae muscle volumes were correlated with body size and were smaller per body size in older adults

Total triceps surae volume was positively correlated with the product of height and mass in both young and older adults (Figure 5.3A). The scaling relationship between total triceps surae muscle volume and body size as well as the relationships for all individual muscles in young adults and older adults are provided in Table 5.3. Triceps surae volumes normalized by height*mass were smaller in older adults (Figure 5.3B), and all individual muscles were smaller per body size in older adults (percent difference: PS = 15.4%, AS = 17.9%, MG = 20.3%, LG = 10.7%) (Figure 5.3C). Triceps surae muscle volumes were not significantly different between young and older adults but trended towards being smaller in older adults (percent difference: PS = 17.2%, AS = 22.7%, MG = 23.1%, LG = 14.2%) (Table 5.2).

		posterior soleus	anterior soleus	medial gastroc.	lateral gastroc.	total triceps surae
muscle volume (cm^3)	**young**	391.4 ± 84.3	83.8 ± 32	291.6 ± 81.9	175.1 ± 54.3	941.9 ± 229.9
	older	329.4 ± 81.7	66.7 ± 20.5	231.1 ± 56.1	151.9 ± 47.2	779.1 ± 189.6
	***p*-value**	0.668	0.668	0.576	0.436	0.167
normalized volume (cm^3/ kg*m)	**young**	2.93 ± 0.26	0.62 ± 0.19	2.17 ± 0.3	1.28 ± 0.21	7.00 ± 0.6
	older	2.51 ± 0.35	0.52 ± 0.18	1.77 ± 0.3	1.15 ± 0.24	5.95 ± 0.93
	***p*-value**	0.060	0.218	0.060	0.248	**0.015**
relative volume (%)	***young***	41.94 ± 2.76	8.83 ± 2.55	30.91 ± 3.13	18.32 ± 2.23	N/A
	older	42.38 ± 2.89	8.53 ± 2.02	29.7 ± 2.25	19.39 ± 2.44	N/A
	***p*-value**	1.588	1.588	1.256	1.256	N/A
tendon CSA / volume (/cm)	**young**	1.58 ± 0.18 e-3	8.38 ± 3.77 e-3	2.15 ± 0.27 e-4	3.71 ± 0.88 e-4	6.62 ± 0.77 e-5
	older	2.09 ± 0.55 e-3	1.14 ± 0.66 e-2	3.03 ± 0.10 e-4	4.68 ± 1.56 e-3	8.91 ± 2.68 e-4
	***p*-value**	0.069	0.069	**0.048**	0.218	**0.019**

Table 5.2: Triceps surae muscle volumes (mean ± standard deviation) compared between young and older adults. Muscle volumes were normalized to account for body size differences by dividing by the product of each subject's height and mass. Relative volumes are the individual muscle volumes compared to the total triceps surae volume. Older adults had smaller absolute muscle volumes than young adults, but differences were not significant. The Mann-Whitney rank sum test was used to determine significance. The Holm-Bonferroni method was used to correct for family-wise error in tests repeated for individual muscle volumes. P-values < 0.05 were considered significant and appear in bold.

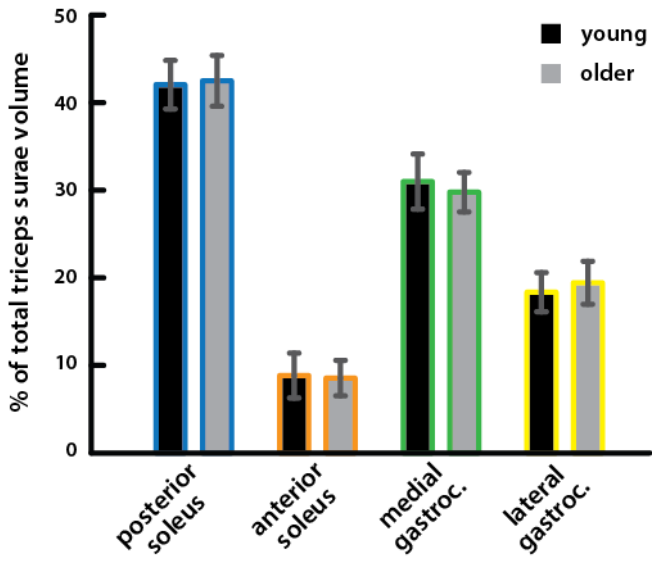

Figure 5.2: Relative volumes of triceps surae muscles did not differ between young and older adults. Relative volumes of individual triceps surae muscles as a percent of the total triceps surae volume are shown for young (black) and older (gray) adults. A Mann-Whitney rank sum test detected no significant differences between young and older adults for any muscle (Table 5.2).

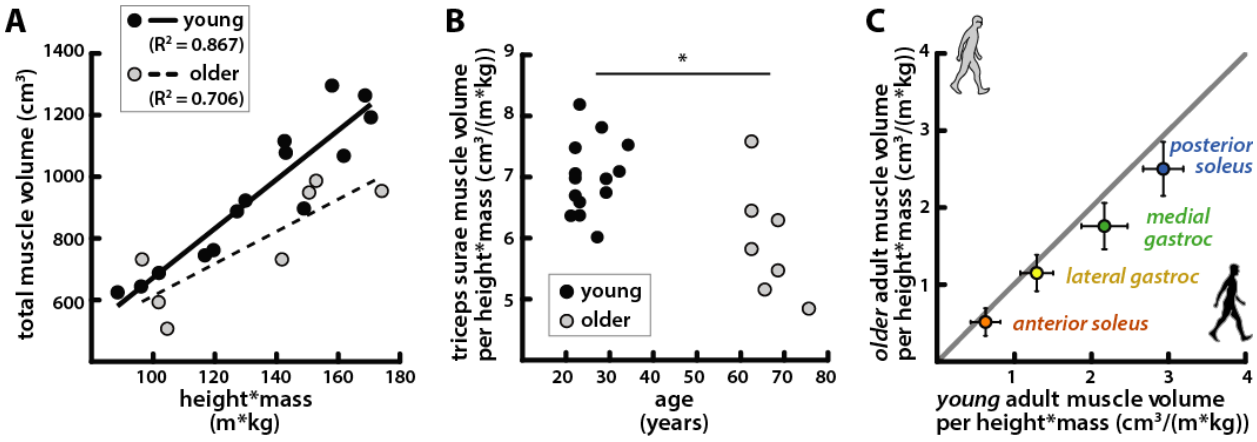

Figure 5.3: Triceps surae muscle volumes per body size were correlated with body size and were smaller per body size in older adults. (A) Total triceps surae volumes versus the product of height and mass for young (black circles, solid line: R^2 = 0.867, *p*-value = 1.33e-6) and older (gray circles, dashed line: R^2 = 0.706, *p*-value = 0.018) adults. (B) Total triceps surae muscle volumes normalized by height*mass versus age; a Mann-Whitney rank sum test determined muscle volume normalized by body size was significantly different between young and older adults (*p*-value = 0.015). (C) Average individual triceps surae muscle volumes normalized by height*mass for older adults versus young adults; error bars indicate standard deviation. Points falling below the unity line (gray) indicate muscles that are smaller in older adults than in young adults (Table 5.2).

5.4.3 Tendon CSA was correlated with body & muscle size in young adults but not older adults

Achilles tendon cross sectional area varied along its length from the top of the calcaneus to the soleus MTJ (Figure 5.4). There were no significant differences in average CSA between young (53.71±14.88 mm^2) and older (51.22±13.18 mm^2) adults or in CSA measured at the top of the calcaneus (young = 64.87±16.34 mm^2; older = 51.59±18.02 mm^2) and CSA measured at the soleus MTJ (young = 49.76±14.05 mm^2; older = 51.83±10.89 mm^2). Free tendon lengths also varied greatly between individuals but were not significantly different between young (50.95±17.94 mm) and older (45.26±20.39 mm) adults (Figure 5.4A&D). There were no significant differences in free tendon volume between young (2.65±1.05 cm^3) and older (2.25±1.07 cm^3) adults. Cross-sectional area at half of the free tendon's length was used for further analysis and is subsequently referred to as Achilles tendon CSA.

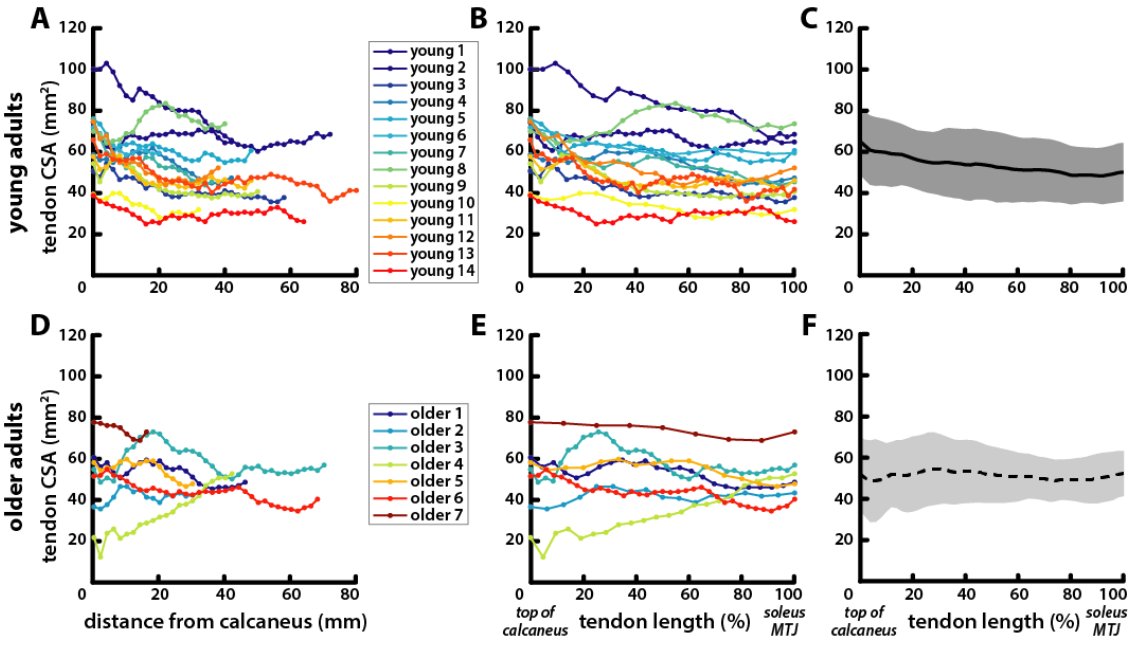

Figure 5.4: Achilles tendon cross sectional area variation. Tendons exhibited greater variation in length and CSA within age groups than between young and older adults. Achilles tendon cross sectional area (CSA) was measured in axial MR images of (A) young and (D) older adults from the most proximal image where the calcaneus was visible to the most distal image where the soleus was visible. CSA locations are reported as their distance from the calcaneus in the proximal-distal direction. To account for variations in free tendon length, CSA locations were normalized to length for (B) young and (E) older adults with the top of the calcaneus being the most distal point at 0% and the soleus muscle-tendon junction (MTJ) the most proximal point at 100%. Average tendon CSA is plotted with normalized tendon length in (C) young (solid line, gray shading for standard deviation) and (F) older (dotted line, light gray shading) adults.

Achilles tendon CSA trended towards being larger in older adults but the difference was not significant (Table 5.1). Tendon CSA was positively correlated with height *mass in young adults but not in older adults (Figure 5.5A). Similarly, tendon CSA was positively correlated with total triceps surae volume in young adults (Figure 5.5B), while CSA was not related to total muscle volume in older adults.

Tendon CSA normalized to height*mass increased with age but was not significantly different between young and older adults (Figure 5.5C). However, tendon CSA normalized to total triceps surae muscle volume was significantly greater in older adults (Figure 5.5D). Additionally, the ratio of tendon size to muscle size was greater in older adults for all individual muscles, though the difference was only significant for the medial gastrocnemius (Table 5.2).

5.4.4 Peak ankle plantarflexion torque during walking was correlated with body and muscle size in young and older adults but was correlated with tendon size only in young adults

Peak torque during walking at 1.25 m/s was positively correlated with height*mass (Figure 5.6B) and was not significantly different between age groups (Table 5.1). Peak torque was positively correlated with total triceps surae muscle volume in young and older adults (Figure 5.6C). Peak torque was positively correlated with Achilles tendon CSA in young adults but not in older adults (Figure 5.6D).

5.4.5 Estimated peak Achilles tendon force was correlated with triceps surae muscle volume in young adults but not in older adults

Achilles tendon moment arms were slightly smaller in older adults compared to young adults, but the difference was not significant (Table 5.1). Estimated peak Achilles tendon forces were also positively correlated with the total triceps surae volume in young adults (Figure 5.6E). However, in older adults, estimated peak force was not significantly correlated with total triceps surae muscle volume.

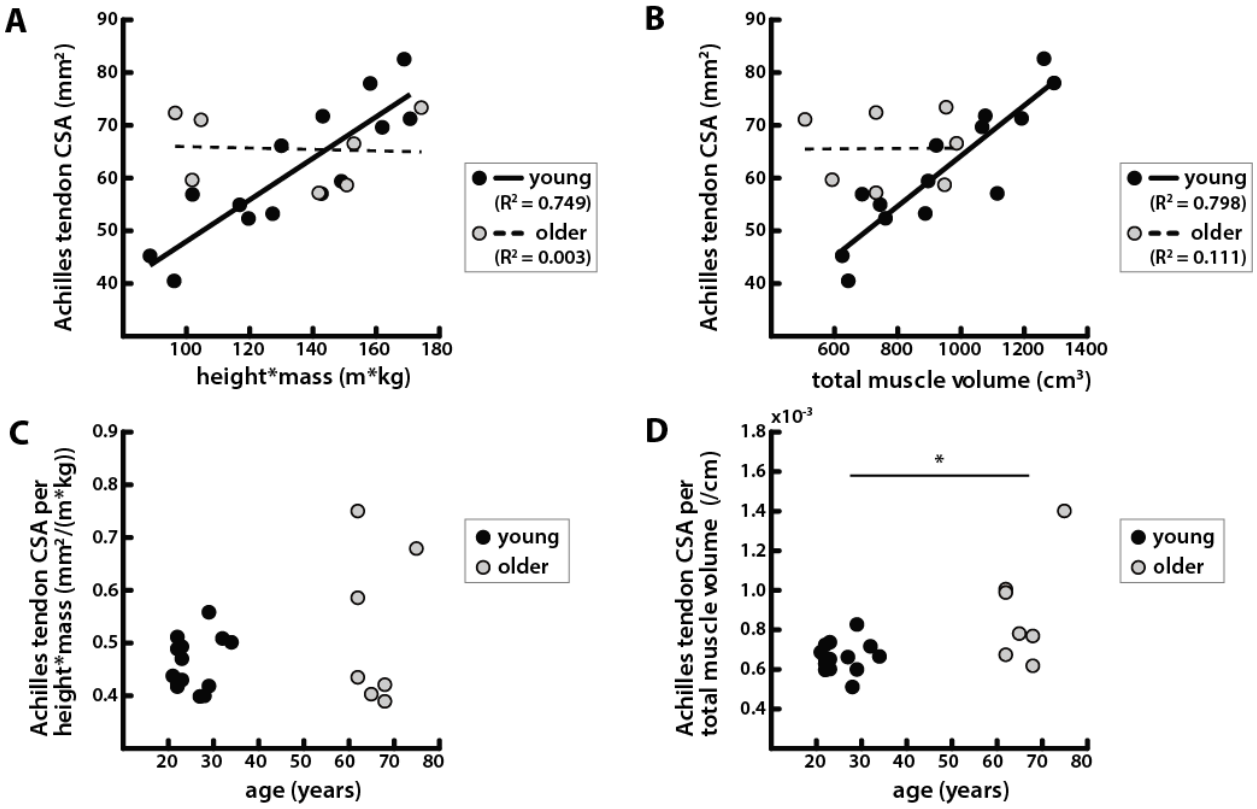

Figure 5.5: Achilles tendon CSA was correlated with body and muscle size in young adults but not in older adults. (A) Achilles tendon cross-sectional areas (CSA) versus the product of height and mass in young (black circles, solid line: $R^2 = 0.749$, *p*-value = 6.42e-5) and older (gray circles, dashed line: $R^2 = 0.003$, *p*-value = 0.901) adults. **(B)** Achilles tendon CSA versus total triceps surae muscle volume in young (black circles, solid line: $R^2 = 0.798$, *p*-value = 1.69e-5) and older (gray circles, dashed line: $R^2 = 0.111$, *p*-value = 0.139) adults. **(C)** Achilles tendon CSA normalized by height*mass versus age; a Mann-Whitney rank sum test determined that there were no significant differences between age groups in tendon CSA normalized by body size (*p*-value = 0.737). **(D)** Achilles tendon CSA normalized by total triceps surae muscle volume versus age; a Mann-Whitney rank sum test determined that tendon CSA normalized by muscle size was significantly different between young and older adults (*p*-value = 0.019).

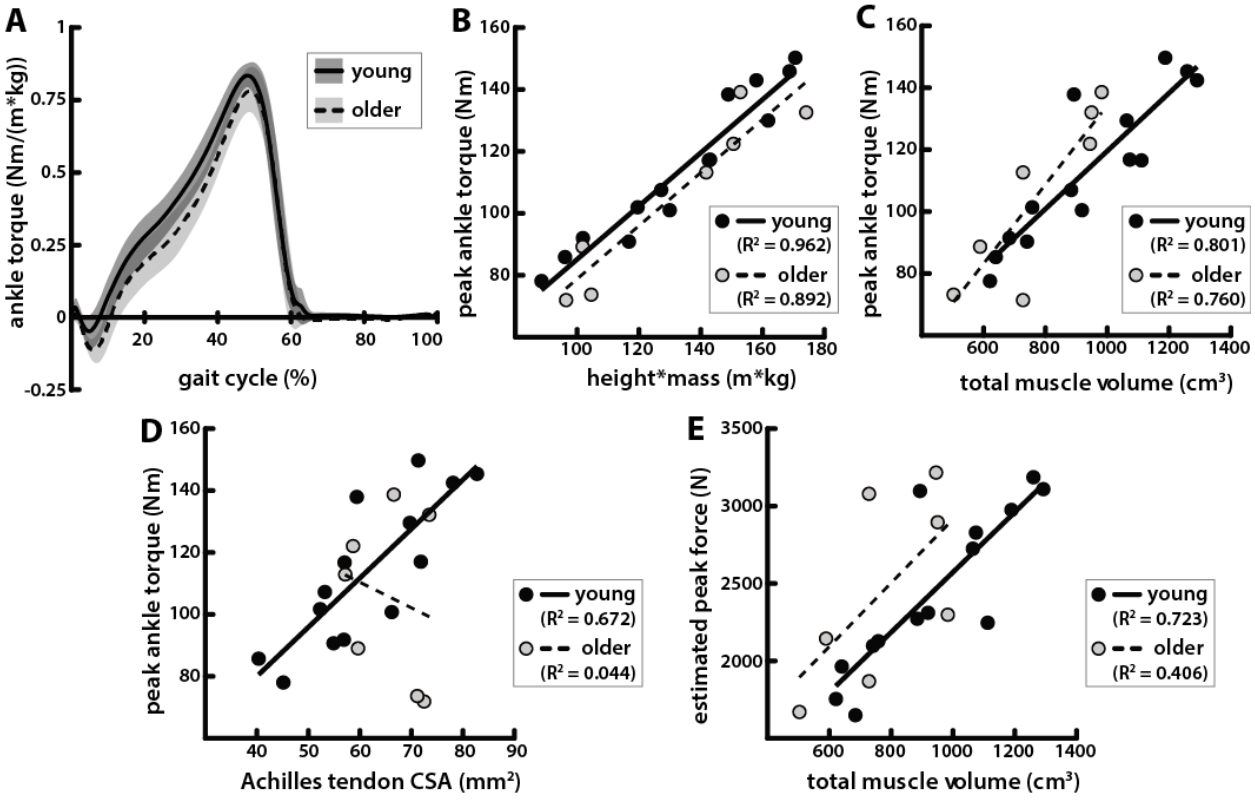

Figure 5.6: Peak ankle plantarflexion torque during walking was correlated with body and muscle size in young and older adults but correlated with tendon size only in young adults. (A) Average ankle torque normalized by body size, calculated as the product of height and mass, in young (solid line, gray shading for standard deviation) and older (dotted line, light gray shading) adults walking at 1.25m/s plotted over one gait cycle. **(B)** Peak plantarflexion torque during walking at 1.25m/s versus the product of height and mass in young (black circles, solid line: R^2 = 0.926, *p*-value = 3.77e-8) and older (gray circles, dashed line: R^2 = 0.892, *p*-value =1.35e-3) adults. **(C)** Peak torque versus total triceps surae muscle volume in young (black circles, solid line: R^2 = 0.801, *p*-value = 1.56e-5) and older (gray circles, dashed line: R^2 = 0.760, *p*-value = 0.010) adults. **(D)** Peak torque versus Achilles tendon CSA in young (black circles, solid line: R^2 = 0.672, *p*-value = 3.31e-4) and older (gray circles, dashed line: R^2 = 0.044, *p*-value = 0.651) adults. **(E)** Estimated peak forces, calculated by dividing peak torques by Achilles tendon moment arms, versus total triceps surae muscle volume in young (black circles, solid line: R^2 = 0.723, *p*-value = 1.16e-4) and older (gray circles, dashed line: R^2 = 0.406, *p*-value = 0.124) adults.

			posterior soleus muscle volume (cm^3)	anterior soleus muscle volume (cm^3)	medial gastroc muscle volume (cm^3)	lateral gastroc muscle volume (cm^3)	total triceps surae muscle volume (cm^3)
height * mass (kg*m)	**young**	R^2	0.801	0.412	0.713	0.812	0.867
		equation	0.29x + 22.09	0.54x + 88.64	0.28x + 53.05	0.45x + 55.7	0.11x + 31.26
		***p*-value**	**< 0.001**	**0.013**	**< 0.001**	**< 0.001**	**< 0.001**
	older	R^2	0.762	0.253	0.658	0.465	0.706
		equation	0.33x + 24.39	0.75x + 81.81	0.44x + 29.79	0.44x + 64.81	0.14x + 26.36
		***p*-value**	**0.010**	0.250	**0.027**	0.092	**0.018**
Achilles tendon CSA (mm^2)	**young**	R^2	0.749	0.229	0.838	0.602	0.798
		equation	0.13x + 12.17	0.18x + 46.01	0.14x + 21.47	0.17x + 30.73	0.05x + 16.56
		***p*-value**	**< 0.001**	0.084	**< 0.001**	**0.001**	**< 0.001**
	older	R^2	0.041	0.027	0.033	0.028	<0.001
		equation	0.02x + 59.84	0.06x + 61.84	-0.02x + 70.75	-0.02x + 69.28	0.00x + 65.26
		***p*-value**	0.662	0.726	0.697	0.721	0.983
peak plantar-flexion torque (Nm)	**young**	R^2	0.808	0.294	0.644	0.745	0.801
		equation	0.26x + 14.03	0.41x + 80.12	0.24x + 45.65	0.38x + 47.39	0.09x + 26.22
		***p*-value**	**< 0.001**	**0.045**	**< 0.001**	**< 0.001**	**< 0.001**
	older	R^2	0.725	0.279	0.650	0.707	0.760
		equation	0.29x + 10.9	0.71x + 58.41	0.40x + 14.05	0.49x + 31.1	0.13x + 6.75
		***p*-value**	**0.015**	0.223	**0.029**	**0.018**	**0.010**
estimated peak tendon force (N)	**young**	R^2	0.765	0.163	0.621	0.668	0.723
		equation	5.44x + 329.21	6.62x + 1904.1	5.04x + 988.16	7.89x + 1077.13	1.94x + 631.56
		***p*-value**	**< 0.001**	0.153	**< 0.001**	**< 0.001**	**< 0.001**
	older	R^2	0.313	0.167	0.653	0.204	0.406
		equation	4.19x + 1078.59	12.19x + 1645.4	8.81x + 423.04	5.85x + 1569.86	2.05x + 857.57
		***p*-value**	0.191	0.363	**0.028**	0.309	0.124

Table 5.3: Linear regression was used to determine the relationship between individual and total muscle volumes and body size, calculated as height*mass; Achilles tendon cross-sectional area (CSA); peak plantarflexion torque during walking at 1.25 m/s; and peak Achilles tendon force, estimated by dividing peak torque by moment arm, in young and older adults. The equation and R^2 value for each linear regression are reported. *P*-values < 0.05 were considered significant and appear in bold.

5.5 Discussion

We investigated how triceps surae muscle volumes and Achilles tendon cross-sectional area correlate with each other, body size, and peak ankle plantarflexion torque during walking and determined how those relationships differ between age groups. Although peak plantarflexion torques did not differ between young and older adults walking at the same speed, we found evidence of sarcopenia as triceps surae muscle volume per body size was lower in older adults. However, the relative volumes of the triceps surae muscles were the same in young and older adults. Both young and older adults' triceps surae muscle volumes were positively correlated with both body size and peak walking torques, but triceps surae muscle volumes were positively correlated with Achilles tendon size only in young adults.

We found that volume distribution between the gastrocnemius and soleus was similar between age groups, and furthermore that the volume distributions between the unique heads and compartments within the respective muscles was also similar between age groups (Figure 5.2). The distribution of triceps surae muscle volume between the soleus and the heads of the gastrocnemius is similar to what has been reported previously in young adults (Albracht, Arampatzis, and Baltzopoulos 2008). A previous study found that although physiological cross-sectional area (PCSA) distribution of the gastrocnemius heads and soleus within the triceps surae was similar in young and older adults, volume distribution between these muscles differed with age (Morse et al. 2005). The authors considered the soleus as a whole and did not image the full muscle, estimating volume of the distal portion using local multiple regression in each subject. Our findings were not consistent with our hypothesis that we would see age-related differences in volume distribution between the individual muscles of the triceps surae, which we expected due to the different functional roles of each muscle. Specifically, we expected the gastrocnemius would experience greater atrophy because it is composed of a higher percentage of fast twitch fibers than the soleus (Johnson et al. 1973; Nilwik et al. 2013). Additionally, we posited that differences in gait between young and older adults might be explained by an altered balance of force production between muscles with different contributions to propulsion and support in walking (Anderson and Pandy 2003;

Francis et al. 2013; McGowan et al. 2008; Neptune et al. 2001). Older adults can respond to biofeedback to match the propulsive forces that young adults produce during walking but also increase support forces (Franz et al. 2014). If the soleus contributes more to support while the gastrocnemius contributes more to propulsion (Francis et al. 2013), a greater soleus to gastrocnemius size ratio could correspond with greater support to propulsive force generation. However, we did not see a redistribution of muscle volumes that would correspond with an imbalance between propulsive and support forces.

Older adults exhibited a proportional relationship between triceps surae muscle volumes and body size (Figure 5.3A) but with a lower ratio of muscle volume to body size than the young adults (Figure 5.3B-C). This is consistent with prior work in healthy young adults which showed that lower limb muscle volumes scale with body size, computed as the product of height and mass (Handsfield et al. 2014). In our current work, we found that the posterior and anterior compartments of the soleus each exhibit a scaling relationship between their volume and height*mass, which has been previously unexplored. Our results demonstrate that this relationship is generally preserved with sarcopenia but with a smaller scaling factor. In previous studies, individual triceps surae muscle volumes were found to also be predicted by the product of the maximum anatomical cross sectional area and the muscle length when combined with a shape factor (Albracht et al. 2008; Karamanidis et al. 2019). Interestingly, a unique shape factor was required to accurately predict muscle volumes in older adults, as the use of the shape factor for muscle volumes measured in young adults (Albracht et al. 2008) overestimated volumes of older adult muscles (Karamanidis et al. 2019). Our work provides further evidence that while the muscle scaling relationships that are present in young adults are not eliminated by aging, they are certainly altered.

Achilles tendon CSA scaled with body size as well as with triceps surae muscle volumes in young adults (Figure 5.5A-B), which is consistent with the hypothesis that there is a mechanical relationship between muscle loading and tendon adaptation that determines CSA (Bohm et al. 2015). The correspondence of tendon CSA with muscle volumes that we have shown provides morphological evidence of the structure-function relationship between muscle and tendon in young adults. This work

complements previous mechanical evidence showing correlations between normalized Achilles tendon stiffness and tendon forces estimated during maximum isometric maximal voluntary plantarflexion contractions (Arampatzis et al. 2007). The lack of relationship between muscle and tendon size in older adults suggests that an alternative mechanism may be driving tendon adaptation. Altered tendon adaptation does not appear to result in a positive correlation between CSA and age; we did not find that Achilles tendon CSA was significantly larger in older adults (Figure 5.4C) as has been found in previous studies (Onambele et al. 2006; Stenroth et al. 2012). Those studies also found that tendon material properties change with age, showing that older adults have more compliant tendons. Increases in tendon CSA may be an adaptation to conserve the level of strain experienced in physiologic loading conditions in order to avoid failure, which occurs at similar strain levels even as material properties vary (LaCroix et al. 2013). This theory is supported by our finding that older adults had a significantly larger ratio of tendon CSA to muscle volume than the young adults (Figure 5.5D). The relationship between tendon and muscle size can be used to assess how much older adults deviate morphologically from young adults (Figure 5.5B) and may be indicative of the quality of the structure-function relationship between the Achilles tendon and triceps surae muscles in older adults. Such a metric might provide a more biomechanically relevant way to estimate the functional potential of adults, instead of the number of years they have been alive.

Peak plantarflexion torques during walking were positively correlated with body size, and the ratio of peak torque to height*mass was very similar in young and older adults (Figure 5.6B). This result is not surprising since the mechanical demands of walking are tied to body size. Body mass determines the load applied at the center of mass, while height is proportional to the lever arm of that load. Peak plantarflexion torques have been shown to differ between young and old adults when walking at the same speed (Boyer et al. 2017; DeVita and Hortobagyi 2000; Franz and Thelen 2015). Older adults in our studies did not walk with significantly lower peak torques, but it should be noted that the heights and masses of the young and older adults were similar in our study and also that they walked at a speed of

1.25m/s, which was slower than in some previous studies (Boyer et al. 2017; DeVita and Hortobagyi 2000). We did observe age-related differences in spatiotemporal parameters (Table 5.1). Peak torques during walking observed here were positively correlated with triceps surae muscle volumes (Figure 5.6C). Previous studies have shown positive correlations in young adults between plantarflexor muscle volumes and maximal plantarflexion torques measured both isokinetically and isometrically with a dynamometer (Baxter and Piazza 2014; Morse et al. 2004), but the correlations were not as strong as those found in this study. In one of these studies, torque measured during isometric MVC in older adults was not found to be significantly correlated with muscle volumes (Morse et al. 2004).

Achilles tendon CSA was positively correlated with body and muscle size, as well as with peak plantarflexion torque in young adults, but was correlated with none of these in older adults (Figure 5.6D). These results indicate that the mechanical relationships governing tendon size may differ between young and older adults. Additionally, estimated Achilles tendon forces were not correlated with triceps surae muscle volumes in older adults. We expected that accounting for moment arms would improve correlations between plantarflexor output and muscle size by removing variation due to differences in musculoskeletal geometry such that muscle size would be compared directly to force production. In a previous study, Achilles tendon moment arms were shown to positively correlate with plantarflexion torque measured by dynamometry, as well as with plantarflexor muscle volumes (Baxter and Piazza 2014). In our study, moment arms were not directly correlated with muscle volumes, body size, or peak plantarflexion torques during walking in either young or older adults. Older adults in our study had slightly smaller moment arms than the young adults, as has been shown previously (Rasske and Franz 2018), though the difference was not significant here.

There are several limitations of this study that should be mentioned. First, we were limited by a relatively small sample size, especially in the older adult group. Furthermore, the average age of the older adults in this study (66 ± 5) may have been too low to be associated with substantial age-related changes in function, considering adults can be considered in “mid-life” under the age of 65 years old (Boyer et al.

2017). Previous authors have posited that age-related changes in tendon and muscle exhibit different time courses, as they observed lower muscle strength but similar tendon properties in older adults in their sixties (Karamanidis and Arampatzis 2006). The observed age-related differences in muscle-tendon relationships may vary in older adults in their late seventies and eighties. Also, we did not control for physical activity level between the two age groups. All older adults reported engaging in regular physical activity, and while seven of the young adults also engaged in regular physical activity, we did not have reports from the other seven subjects so we cannot confirm a similar activity level between groups. We may have been more likely to see differences in peak plantarflexion torque between young and older adults in a group over 75 years old. However, we did see differences between triceps surae muscles and Achilles tendons between our age groups, suggesting that structural changes may precede mobility deficits that arise with aging. Here, we used volume as a metric of muscle size, and therefore strength, since we did not measure fascicle or sarcomere lengths necessary for computing PCSA. Because the ratio of muscle belly length to muscle fiber length in the triceps surae was shown not to differ with age (Morse et al. 2005), we assumed volume remains reasonably proportional with strength in a comparison between young and older adults. Furthermore, moment arms used to estimate peak force were measured at an ankle position of 0° rather than the joint position at which peak torque occurred. However, peak torque occurred at very similar plantarflexion angles, so we do not believe this contributed to differences in estimated peak force between young and older adults.

This study reveals that the relationship between plantarflexor muscle and tendon structure may differ between young and older adults. The distribution of individual muscle volumes within the triceps surae was similar between young and older adults, as was the positive correlation between muscle volume and both body size and ankle plantarflexion torque. However, the same was not true for Achilles tendon CSA; CSA was only clearly related to body size and plantarflexion torque in young adults. Structure-function relationships that seem to exist between the Achilles tendon and the triceps surae muscles in young adults are no longer evident in all older adults. It appears that mechanisms affecting Achilles

tendon morphology may be somehow altered with aging. Future work aimed at identifying factors affecting muscle-tendon relationships may provide a target for efforts to improve mobility in aging adults.

Chapter 6

3D models reveal the influence of Achilles subtendon twist on strain and energy storage

"I twirl on my haters"

– Beyonce

6.1 Abstract

The Achilles tendon (AT) has complex function in walking, exchanging energy due to loading by the triceps surae muscles. AT structure comprises three subtendons which exhibit variable twist among themselves and between individuals. Our goal was to create 3D finite element (FE) models to explore AT structure-function relationships. By simulating subtendon loading in FE models with different twisted geometries, we investigated how anatomical variation in twisted tendon geometry impacts fascicle lengths, strains, and energy storage. Three tendon FE models, built with elliptical cross sections based on average cadaver measurements, were divided into subtendons with varied geometric twist (low, medium, high) and equal proportions. Tendon was modeled as transversely isotropic with fascicle directions defined using Laplacian flow simulations, producing fascicle twist. Prescribed forces, representing AT loading during walking, were applied to proximal subtendon ends, with distal ends fixed, and tuned to produce equal tendon elongation in each case, consistent with ultrasound measurements. Subtendon fascicle lengths were greater than free tendon lengths in all models by 1-3.2 mm and were longer with greater subtendon twist with differences of 1.2-1.9 mm from low to high twist. Subtendon along-fiber strains were lower with greater twist with differences of 1.4-2.6%, and all were less than free tendon longitudinal strain by 2-5.5%. Energy stored in the AT was also lower with greater twist with differences of 1.8-2.4 J. With greater subtendon twist, similar elongation of the AT results in lower tissue strains and forces, so that longitudinal stiffness of the AT is effectively decreased, demonstrating how tendon structure influences mechanical behavior.

6.2 Introduction

The Achilles tendon plays an important but complex role in human movement. This unique tendon transmits forces from the three muscles of the triceps surae to the calcaneus during production of ankle plantarflexion torque. Due to muscle loading, the Achilles tendon stores and returns energy as it stretches and recoils (Lichtwark and Wilson 2005; Zelik and Franz 2017). Each of the triceps surae muscles perform different functions in the generation of propulsion and vertical support during walking

(Anderson and Pandy 2003; Francis et al. 2013; McGowan et al. 2008; Neptune et al. 2001), and each muscle has a unique architecture (Bolsterlee et al. 2019; Handsfield et al. 2014; Ward et al. 2009). Therefore, the three triceps surae muscles apply different forces to the Achilles tendon (Arndt et al. 1998), which means that the Achilles tendon functions as three combined tendons, leading to a more complex relationship between structure and function than in a tendon attached to a single muscle.

The evidence of complex loading conditions can be visualized using ultrasound imaging during walking. For example, non-uniform displacements have been observed in the *in vivo* free tendon; the deep portion of the tendon displaces more than the superficial portion between toe-off and mid-stance, indicating greater elongation of this region (Franz et al. 2015). These kinematic results likely occur due to the combination of complex loading and the complicated structure of the Achilles tendon. The internal structure of the Achilles free tendon comprises three subtendons (Handsfield, Slane, et al. 2016), which are distinguishable groups of fascicles that originate from individual muscles: the gastrocnemius lateral head, medial head, and the soleus. These subtendons have been observed in cadavers to twist around each other before inserting into the calcaneus (Cummins and Anson 1946; Edama et al. 2015; Szaro et al. 2009). The twisted structure occurs in all Achilles tendons and the direction of twist is consistent across individuals. However, the amount of subtendon twist varies between individuals, such that previous authors have used that variation to classify tendons into three groups (Cummins and Anson 1946; Edama et al. 2015; Pękala et al. 2017). These detailed anatomical studies present many questions about the functional consequences of Achilles tendon internal structure and how mechanical behavior may vary with differences in anatomy. For example, would strain experienced by the tendon during a given elongation vary with differences in the twisted structure of its subtendons? Would differences in subtendon twist change the amount of energy stored during that same stretch?

Computational models enable exploration into the relationships between tendon structure and function. A finite element model of Achilles subtendons (Handsfield, Inouye, et al. 2017) demonstrated how sliding and differential loading are possible mechanisms underlying observed nonuniform

displacements (Slane and Thelen 2015). Shim et al. (2018) developed subject-specific models of the Achilles free tendon in which they incorporated variations in fascicle twist. Their study confirmed that varying tendon twist does impact mechanical behavior. However, tendon geometry and material properties also varied in this study and have been shown to be highly variable between individuals and contribute to differences in mechanical behavior (Shim et al. 2014). It remains unclear to what extent observed fascicle twist within the subtendons may influence tendon mechanics, independent of these other variations in the Achilles tendon.

Variation in subtendon twisted morphology could also affect *in vivo* measurements of tendon mechanical behavior. For example, strains in the Achilles tendon are generally estimated by tracking the distance between the distal and proximal endpoints (Kubo et al. 2002; Lichtwark and Wilson 2005; Onambele et al. 2006), assuming that strain is a linear measure between these two endpoints. Similar methods are employed in combination with force estimation to determine tendon work (Lichtwark and Wilson 2005; Zelik and Franz 2017). It is possible that tendon fibers twisted along the length of the tendon may affect the relationship between the tendon tissue strain and energy storage and the longitudinal estimates of strain and energy storage.

The goal of this work was to investigate how differences in subtendon internal twisted structure influences Achilles tendon fascicle morphology, strains, and energy storage. Our secondary goal was to explore how subtendon twisting may affect quantification of Achilles tendon strain and energy storage made with *in vivo* measurements. In order to quantify the effects of twist geometry, independent of differences in free tendon shape and material properties, we built a finite element model of the Achilles tendon with three different internal structures. The different versions of the model represented the average of the three classifications of Achilles subtendon fascicle twisting observed in unloaded cadaver tendons (Pękala et al. 2017) and simulations were performed in which the tendon models were loaded to represent tendon displacement in walking. We analyzed the simulations to (1) determine how functional tendon

behavior varied with differences in subtendon twisted morphology, and (2) assess how varied morphology contributed to errors in quantification of strain and energy storage *in vivo*.

6.3 Methods

6.3.1 Model geometries

A three dimensional (3D) Achilles free tendon geometry was created in Autodesk Inventor (Autodesk Inc. San Rafael, CA) based on measurements from Pękala et al. (2017). Two elliptical axial cross sections were defined a distance of 60 mm apart and a surface was lofted between them to create a 3D geometry with a volume of 5804.85 mm^3 (Figure 6.1). The proximal cross section (major axis = 17.83 mm, minor axis = 5.76 mm, area = 80.66 mm^2) represented the point on the tendon that is just distal to the soleus musculotendinous junction (MTJ). This location was chosen as the most proximal location that the free tendon can be assumed to be in series with all three triceps surae muscles (Epstein et al. 2006). The distal cross section (major axis = 22.04 mm, minor axis = 6.42 mm, area = 111.13 mm^2) represented the point on the tendon that is just proximal to the superior portion of the insertion into the calcaneus.

Using this 3D tendon geometry, three models were created with different internal structures characterized by the amount of subtendon twist. Surfaces divided each 3D model into three subtendons that corresponded with each of the triceps surae muscles: lateral gastrocnemius (LG), medial gastrocnemius (MG), and soleus (SOL). Subtendon divisions were defined such that the proximal cross sections were the same in each model while the distal cross sections varied, resulting in three unique undeformed models with differing sub-structure geometries: low twist, medium twist and high twist (Figure 6.1). The distribution of volume between the three subtendons was the same in all models (LG = 44%, MG = 27.5%, SOL = 28.5%). The three model geometries corresponded with the average of the classifications of Achilles tendon torsion (Type I, Type II, and Type III) described by Pękala et al. (2017). These twisted model geometries were the undeformed or resting configuration of models where there was zero stress.

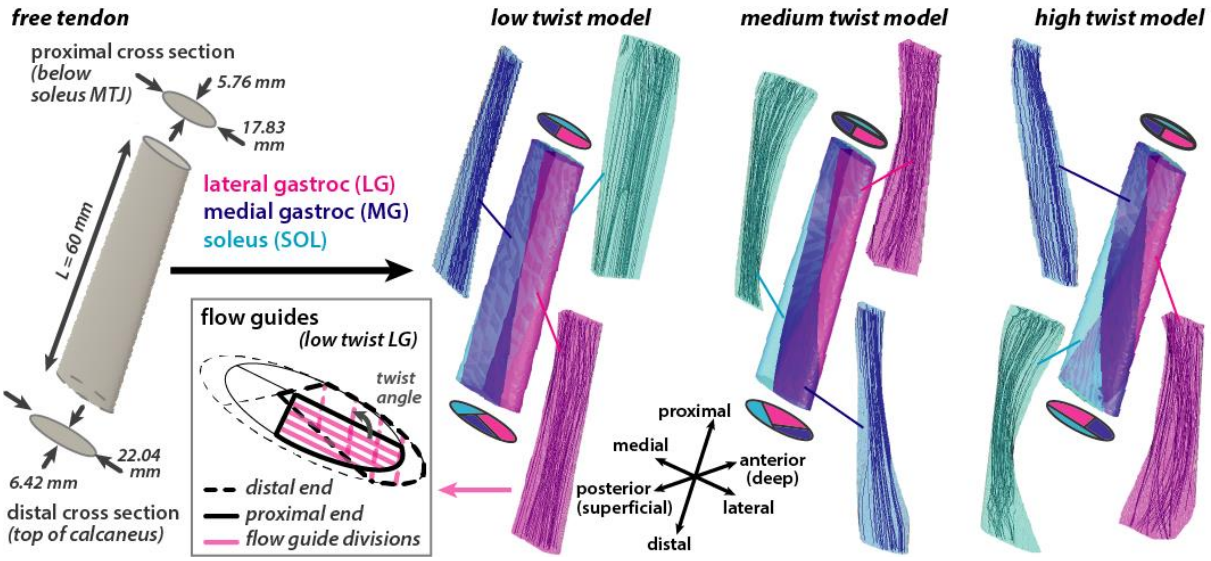

Figure 6.1: Achilles free tendon geometry was developed with elliptical cross sections at the ends. Three unique models with differing amounts of subtendon twist in the undeformed configuration were created by subdividing the free tendon geometry using internal surfaces. These surfaces had the same proximal subtendon cross section divisions and differing distal cross section divisions. Flow guides were used to direct the amount of fascicle twist in each subtendon by creating surfaces that were parallel in the axial cross sections that divided the subtendon volume. Flow guide surfaces are shown in the axial plane for the proximal and distal ends of the lateral gastrocnemius (LG) subtendon in the low twist model. The angle between the flow guides at the ends defined the *twist angle* of the fascicles within the subtendon. Fascicle tracts in the undeformed models, reconstructed from the resulting fiber directions, are shown.

6.3.2 Model fascicles

Each model was meshed automatically into 3D tetrahedral elements (AMPS Technologies, Pittsburgh, PA). The low twist model contained 4336 nodes and 16595 elements, the medium twist model contained 4147 nodes and 16168 elements, and the high twist model contained 4291 nodes and 16355 elements. Each subtendon was meshed independently so that nodes on adjacent surfaces were not shared. An element convergence analysis was performed by repeating simulations of the low twist model with different mesh densities. The selected mesh was chosen such that the differences in the primary metrics of average *along-fiber strain* was less than 0.1% and in total *strain energy* was less than 3% when the number of elements increased by a factor of ten. Additionally, the maximum and minimum strain differed by 5% and 3%, respectively, and the first principal stress differed by less than 3%.

A local fiber direction ($\boldsymbol{a}_0$) was defined for each element to represent the tendon fascicle structure, with a previously described method utilizing Laplacian simulations (Handsfield, Bolsterlee, et al. 2017). For each 3D subtendon, fibers were directed from the proximal cross section (inlet surface) to the distal cross section (outlet surface). When characterizing of three tendon twist types, Pękala et al. (2017) dissected the individual subtendons and quantified the average degree of twist of the fascicles in each unloaded subtendon. Based on these measurements, fascicle twist in each undeformed subtendon was enforced by implementing flow guides (Handsfield, Bolsterlee, et al. 2017) that were internal surfaces that divided the subtendons into four twisting portions. These surfaces were parallel in axial cross sections. The *twist angle* was defined as the angle in the axial plane between the proximal and distal edges of the flow guides (Figure 6.1). Unique flow guides resulted in different fascicle *twist angles* in each model (low twist model: LG = 107°, MG = 17°, SOL = 105°; medium twist model: LG = 157°, MG = 35°, SOL = 145°; high twist model: LG = 211°, MG = 68°, SOL = 200°).

To compute the lengths of the subtendon fascicles in the undeformed models, streamlines, generated at seed points on the proximal surface, were mapped through the field of local fiber direction vectors ($\boldsymbol{a}_0$) in Matlab (Mathworks Inc. Natick, MA). These streamlines defined fascicle tracts, which were then truncated to not extend beyond the volume of the subtendon geometry or extrapolated to terminate on the distal surface using a method adapted from Bolsterlee et al. (2017). We defined *fascicle lengths* as the lengths of the adjusted fascicle tracts as they twisted from the proximal origin to distal insertion were calculated as previously described (Bolsterlee et al. 2017). At least 250 fascicle tracts were created for each model subtendon, representing the internal fascicle geometry in the undeformed condition with zero strain.

6.3.3 Constitutive model

Subtendons were modeled as transversely isotropic, hyperelastic, quasi-incompressible material (Weiss, Maker, and Govindjee 1996; Criscione, Douglas, and Hunter 2001; Blemker, Pinsky, and Delp

2005). The constitutive model has been described in detail by Blemker et al. (2005) and has the strain energy density function:

$$\Phi(\boldsymbol{C}, \boldsymbol{a}_0) = W_1 + W_2 + W_3 + \Phi^{vol} \quad \text{Equation 6.1}$$

where $\boldsymbol{a}_0$ is the local fiber direction, $\boldsymbol{C}$ is the right Cauchy-Green deformation tensor. The dilatational portion of the strain energy ($\Phi^{vol} = \frac{K}{2}\ln(J^2)$) relates to the volume change where $J = \sqrt{\det(\boldsymbol{C})}$ and depends on a bulk modulus with a value set to K = 5e3 MPa. The strain energy associated with along-fiber shear ($W_1 = G_1(B_1(\bar{I}_4, \bar{I}_5))^2$) depends on a shear modulus set to G_1 = 3 MPa and the strain energy associated with cross-fiber shear ($W_2 = G_2(B_2(\bar{I}_1, \bar{I}_4, \bar{I}_5))^2$) depends on a shear modulus set to G_2 = 15 MPa (Fiorentino and Blemker 2014). $\bar{I}_1, \bar{I}_4, \bar{I}_5$ are deviatoric invariants of $\boldsymbol{C}$. The function for the strain energy associated with along-fiber stretch (W_3) characterizes the relationship between Cauchy stress in the tendon (σ) and the fiber stretch ($\lambda = \sqrt{\bar{I}_4}$) and is defined to be consistent with a piece-wise tendon stress-strain relationship:

$$\lambda \frac{\partial W_3}{\partial \lambda} = \begin{cases} \sigma(\lambda) = P_1\left(e^{P_2(\lambda-1)} - 1\right) & 1 < \lambda < \lambda^* \\ \sigma(\lambda) = P_3\lambda + P_4 & \lambda \geq \lambda^* \end{cases} \quad \text{Equation 6.2}$$

where λ^* represents the fiber stretch at which σ becomes linear and was set to λ^*=1.03. In the piece-wise equation, P_3 and P_4 were defined so σ is C^0 & C^1 continuous at $\lambda = \lambda^*$ P_1 and P_2 were set to values of 1.75 MPa and 48.3, respectively, so that the slope in the linear region was 360 MPa (Onambele et al. 2006).

The constitutive model was implemented in the multi-physics finite element analysis program, AMPSol (AMPS Technologies, Pittsburgh, PA), by creating a user-defined hyperelastic material with explicit strain energy function specification.

6.3.4 Model boundary conditions

Frictionless sliding contact was assigned between the surfaces of adjacent subtendons in each model. The mechanics of the inter-subtendon matrix in the human Achilles tendon are unknown and the

interfascicular matrix has been shown to allow relative sliding of tendon fascicles in comparative studies (Thorpe et al. 2015), so this approach has been used previously to model Achilles subtendon interaction (Handsfield, Inouye, et al. 2017). The distal end of each sub tendon was fixed, and the proximal end was constrained to move only in the proximal-distal direction.

To simulate uniaxial loading applied to the Achilles tendon during walking, pressure boundaries were applied to the proximal surface of each subtendon. The applied pressure on each subtendon was tuned so that in each model the displacement of the proximal surfaces of the MG and LG subtendon were 7.6 mm and the displacement of the proximal SOL subtendon surface was 5.9 mm. These displacements were determined based on measurements of the maximum elongations measured in the superficial and deep portions of the Achilles tendon during walking (Franz et al. 2015). These *in vivo* subtendon elongations were estimated from the change in distance between average nodal positions of tendon tissue measured with ultrasound speckle tracking and calcaneus marker positions from motion capture of healthy young adults walking at a speed of 1.25 m/s.

6.3.5 Calculating strain and energy storage

We determined subtendon strain in the longitudinal direction, which we called *longitudinal strain*, by dividing the change in length by the original length of the subtendon measured in the proximal-distal direction, consistent with *in vivo* methods of measuring Achilles tendon strain (Kubo et al. 2002; Lichtwark and Wilson 2005; Onambele et al. 2006). *Longitudinal strain* was equivalent to the proximal surface displacement divided by the initial distance between the distal and proximal cross sections (60mm). We determined strain the fiber direction at the tissue-level, which we called *along-fiber strain*, by calculating the average along-fiber stretch (λ) in each subtendon and subtracting 1.

We calculated the energy stored in the tendon during loading by integrating the average tendon work relationship for the full Achilles tendon (force in all subtendons versus the average subtendon length change), which we called *full tendon stored energy*. This approach was chosen to be consistent with *in vivo* methods of calculating Achilles tendon negative work (Lichtwark and Wilson 2005; Zelik and Franz

2017). We alternatively calculated the energy stored in the tendon during loading by integrating the average tendon work relationship for the individual subtendons (force in individual subtendon versus that subtendon's length change) then summing the work done by each subtendon; we called this value *summed-subtendon stored energy*. We also determined the total *strain energy* in the Achilles tendon by integrating the strain energy density (Φ) across all the elements in the subtendon; the strain energy density is directly calculated using the tendon constitutive model.

Kruskall-Wallis tests were used to determine whether differences in *fascicle lengths* and *along-fiber strain* occurred between subtendons of the three models. Post-hoc Wilcoxon rank sum tests were used to test for differences in subtendon *fascicle lengths* and *along-fiber strains* between each pair of models. The Holm-Bonferroni method was used to correct for family-wise error rate for tests repeated over the three subtendons. Significance was set at $p = 0.05$.

6.4 Results

6.4.1 Undeformed subtendon fascicle lengths are increasingly longer than free tendon length at greater twist angles.

All subtendon *fascicle lengths* were longer than the free tendon length of 60mm in the undeformed configuration (Figure 6.2). For the low twist model, subtendon *fascicle lengths* were: LG = 61.09 ± 0.19 mm, MG = 61.03 ± 0.12 mm, SOL = 61.33 ± 0.30 mm. For the medium twist model, subtendon *fascicle lengths* were: LG = 61.53 ± 0.28 mm, MG = 62.02 ± 0.27 mm, SOL = 61.85 ±0.52 mm. For the high twist model, subtendon *fascicle lengths* were: LG = 62.39 ± 1.13 mm, MG = 62.24 ± 0.39 mm, SOL = 63.18 ± 0.78 mm. The MG subtendon had the shortest fascicles and the SOL subtendon had the longest fascicles in low and high twist models. *Fascicle lengths* were more variable in subtendons with higher *twist angles*. For all subtendons, resting *fascicle lengths* were significantly shorter ($p < 0.00001$) in the low compared to the medium twist model, in the low compared to the high twist model, and in the medium compared to the high twist model. The percent differences in average *fascicle lengths*

compared to the free tendon length were relatively small (low twist: LG = 1.80%, MG = 1.71%, SOL = 2.19%; medium twist: LG = 2.52%, MG = 3.32%, SOL = 3.04%; high twist: LG = 3.90%, MG = 3.66%, SOL = 5.16%).

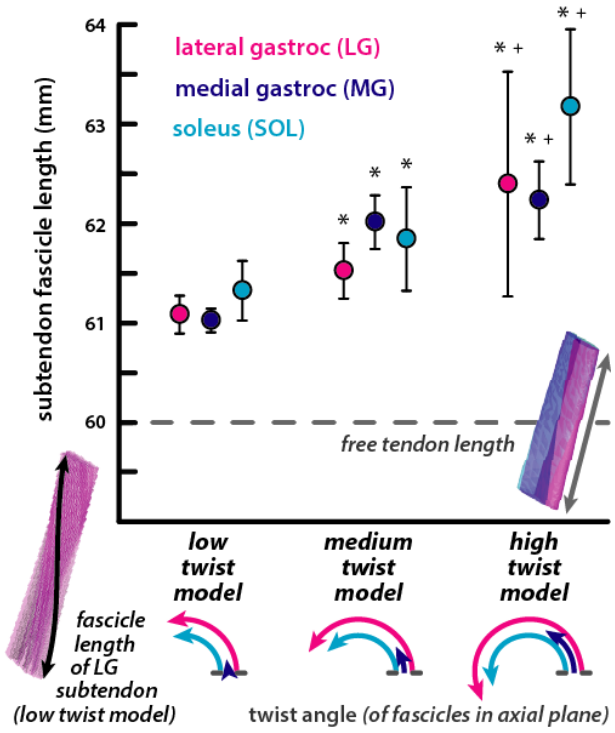

Figure 6.2: Subtendon *fascicle lengths* in the undeformed models are longer than resting free tendon length. *Fascicle lengths* are longer in subtendons of models with more twisted geometry. The average length of fascicle tracts in each subtendon are plotted with error bars indicating standard deviations. Significant differences ($p < 0.00001$) in lengths were found in subtendons compared to the low twist (*) and medium twist (+) models. The dotted line indicates the length of the free tendon, which would be consistent with *fascicle lengths* if no twisting among or within the subtendons occurred. The *twist angle* of the fascicles within each subtendon are illustrated in the axial plane for each model.

6.4.2 Subtendon along-fiber strains are lower than longitudinal strain during elongation and are lower with greater subtendon twist.

The *longitudinal strain* was the same in all models with higher strain in the LG and MG subtendon (12.7%) than the SOL subtendon (9.8%) (Figure 6.3A&B), corresponding with differential displacement between the deep and superficial portions of the Achilles tendon (Franz et al. 2015). Average *along-fiber strains* were lower than *longitudinal strains* in all models with values for each subtendon decreasing from the low twist model (LG = 9.9±0.8%, MG = 10.5±0.6%, SOL = 7.9±0.7%) to the medium twist model (LG = 9.2±1.0%, MG = 9.0±1.4%, SOL = 7.1±0.9%) to the high twist model (LG = 7.2±1.2%, MG = 8.8±0.9%, SOL = 6.4±1.2%), with significant differences ($p < 0.002$) in the LG of the low and medium twist models compared to high twist The MG subtendon had the highest average *along-fiber strain* in the low and high twist models and the SOL subtendon had the lowest average *along-fiber strain* in all three models (Figure 6.3A). *Along-fiber strains* were non-uniform throughout all subtendons in all of the models (Figure 6.3C). The percent differences in average *along-fiber strains* compared to the *longitudinal strains* ranged from 20-55% (low twist: LG = -25.7%, MG = -19.5%, SOL = -22.5%; medium twist: LG = -33.0%, MG = -37.0%, SOL = -32.3%; high twist: LG = -55.0%, MG = -38.6%, SOL = -41.8%).

6.4.3 Energy stored in the tendon for similar elongations is lower with greater subtendon twist.

The average subtendon length change was the same in all models, but the tendon force required to achieve the same displacement was lower in models with greater twist (low twist = 2.49 kN, medium twist = 2.18 kN, high twist = 1.90 kN). Therefore, the *full tendon stored energy* was also lower in models with greater twist (low twist = 7.91 J, medium twist = 6.92 J, high twist= 6.04 J) (Figure 6.4). Similarly, the *summed-subtendon stored energy* was lower in models with greater twist (low twist = 8.10 J, medium twist = 7.09 J, high twist= 6.22 J), though values were slightly higher than the *full tendon stored energy*. Total *strain energy* showed a similar trend as tendon stored energy and was lower in models with greater

twist (low twist = 6.73 J, medium twist = 5.63 J, high twist = 4.34 J), though *strain energy* in all models was less than the energy determined with both longitudinal methods. The strain energy density was non-uniform throughout all subtendons in all of the models, with areas of high energy corresponding with areas of high strain. (Figure 6.3C). The percent differences in total *strain energy* from the *full tendon stored energy* increased with greater twist (low twist = -16.2%, medium twist = -20.5%, high twist = -32.7%), while percent differences in total *strain energy* from the *summed-subtendon stored energy* displayed a similar trend and were slightly larger (low twist = -18.5%, medium twist = -23.0%, high twist = -35.7%).

Discussion

The primary goal of this study was to use models of the Achilles free tendon to explore how mechanical behavior varies with morphology differences in subtendon and fascicle twist. Models predicted that, with more twisted resting geometry, the Achilles tendon had longer *fascicle lengths* when undeformed and exhibited reduced *along-fiber strain* and lower energies stored during elongation, thus altering the free tendon's response to loading.

Models predicted that increasing the amount of twist of the Achilles subtendon resting morphology effectively lowered stiffness in the free tendon even though the tissue level material properties were held constant. In the models, the tissue-level strain varied with twist while the elongation was the same. The average *along-fiber strain* was lower in models with greater twist (Figure 6.3A), leading to larger differences in the strain at the tissue-level compared to the tendon-level strain. The distribution of strains within the tissue differed as well (Figure 6.3C). Similar to our results, Achilles tendon FE models with twisted geometry developed by Shim et al. (2018) predicted that greater geometric twist redistributed internal stresses during loading allowing larger loads to be applied in simulations before stress in the tissue reached a given rupture limit. Tendon twisted geometry could be a mechanism to reduce the tendon tissue strains experienced during a given muscle-tendon-unit (MTU) excursion. A

more twisted morphology may therefore aid in avoiding rupture as failure strain of tendon has been shown to be highly conserved between different tendons in different species (LaCroix et al. 2013).

In our simulations where tendon elongation was the same, greater twist corresponded with lower stored energy at both the tendon level (longitudinal stored energy) and at the tissue level (strain energy) (Figure 6.4A). Longitudinal energy differences can be attributed to the varied forces applied in each model for the same elongation (Figure 6.4B), while the *strain energy* differences were also influenced by variation in tissue-level strain (Figure 6.4A). Twisting may actually improve the efficiency of energy return by the tendon, as tendon-level strain and energy storage requires less tissue deformation that could lead to conformational changes at the collagen level that would result in energy loss. In fact, equine energy storing tendons with helical substructures have been shown to experience less hysteresis loss than postural tendons with less fascicle rotation (Chavaunne T Thorpe et al. 2013). Furthermore, the lower forces required in higher twist tendon models to elongate as much as the low twist model (Figure 6.4B), suggest that the amount of twist would impact series-elasticity of the musculotendon unit. A more compliant Achilles tendon may enable greater force control by the triceps surae muscles (Alexander 2002) and has the potential to alter the efficiency of these muscles (Lichtwark and Wilson 2007; Uchida et al. 2016).

It is unknown if the variation in morphologic twist between individuals is an adaptation to mechanical stimuli or simply a product of anatomical variability. However, the amount of twist seems to provide tradeoffs in injury prevention and energetic efficiency. The twist of the subtendons and the *twist angle* of their fascicles may be an important consideration in the repair of Achilles tendon ruptures. As the amount of twist does not vary much between the right and left sides (Pękala et al. 2017), twist in the contralateral tendon could serve as a reference in reconstructing the ruptured tendon. Alternatively, twist could be applied before suturing in an effort to preserve compliance as elasticity decreases (Karatekin et al. 2018) or to protect the repaired tendon from further injury. This approach to improving Achilles tendon reconstruction is an exciting opportunity for further studies.

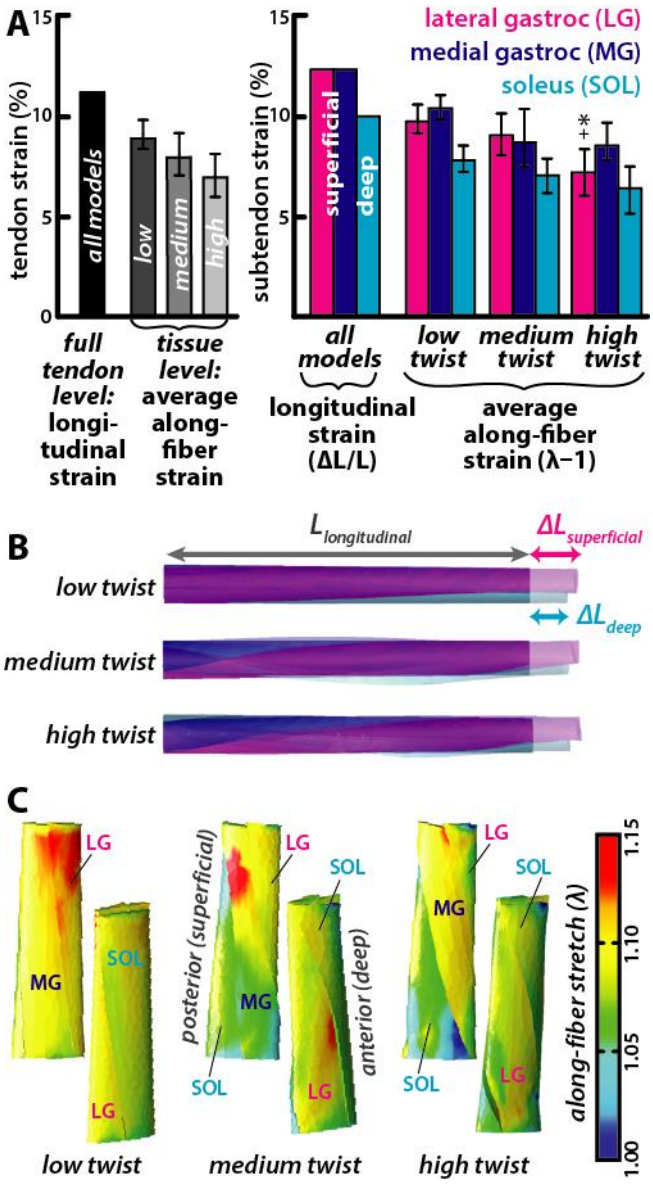

Figure 6.3: Subtendon along-fiber strains are lower than longitudinal strain and was lower in subtendons of models with greater twist. **(A)** The longitudinal strain was the same in all models and measured as the change in length in the proximal-distal direction divided by the initial length. The average along-fiber strain was determined in each full tendon model as well as in the individual subtendons, with error bars indicating standard deviations. Significant differences ($p < 0.002$) in along-fiber strain were found in high twist LG subtendon compared to the low twist (*) and medium twist (+) models. **(B)** All twist models experienced the same elongation in the proximal-distal direction, with greater displacement in the superficial (at the proximal end) subtendons (LG and MG) than the deep subtendon (SOL). **(C)** Posterior and anterior view of each model show the along-fiber stretch (λ) from each simulation, where a stretch value of one is the zero-strain or undeformed condition.

Each of the three subtendons had different twist angle in all undeformed models, resulting in different average *fascicle lengths* (Figure 6.2). The medial gastrocnemius (MG) subtendon had lower *twist angles* and generally shorter fascicles compared to the lateral gastrocnemius (LG) subtendon, and therefore experienced higher *along-fiber strains* even though *longitudinal strains* were the same in both subtendons (Figure 6.3). These results suggest that the MG subtendon is more vulnerable to injury due to its lower twist angle, which may help explain how failure of a single subtendon occurs, resulting in a partial tear in the Achilles (Smigielski 2008). Further studies could work to determine if tears occur more often in the less twisted MG subtendon. The soleus (SOL) subtendon had the greatest *twist angle* in all models and generally had longer fascicles. Subtendon twist within the free tendon influenced *fascicle lengths* in addition to the fascicle *twist angle*, so in the case of the medium twist model, the MG subtendon had longer fascicles despite its lower *twist angle*. The difference in *twist angles* between these subtendons could be associated with the diversity in morphology of the muscles they attach to. Dean et al. (2007) demonstrated that a twisted tendon in the jaw of a spotted ratfish facilitated more uniform strains in the fibers of a muscle with a broad attachment, so that these fibers could operate at similar lengths on the force-length curve. The triceps surae muscles also have broad attachments though the attachment morphology of each muscle is different (Dalmau-Pastor et al. 2014), possibly necessitating different subtendon twist angles to achieve the same equalizing effect on fiber operating lengths.

Our secondary goal was to assess how morphological complexity of the Achilles tendon impacts how *in vivo* measurements of tendon behavior should be interpreted. We hypothesized that varying lengths and geometry resulting from twisted morphology may lead to errors during *in vivo* calculations of strain and energy. We found that resting *fascicle lengths* were only slightly underestimated by 1.5-5.5% by using measurements of tendon length. However, strains and energy storage measured at the fascicle level were both overestimated by 20-55% and 15-35% respectively when using longitudinal methods that are consistent with *in vivo* measurements. The amount of error increases with twist. Unfortunately, definitively calculating measurement errors due to subtendon twist is not possible as methods of

determining the amount of twist *in vivo* have not been developed, to our knowledge. Hopefully the future development of imaging techniques will allow for correction of such measurement errors in the future. Additionally, the high twist group accounts for less than 6% of the population studied in Pękala et al. (2017) so most tendons will likely have a low (48% of population) or medium (46% of population) amount of twist. Therefore, the extent of error associated with the low (strain = 19-26%, energy = 16-19%) and medium (strain = 32-37%, energy = 20-23%) twist models will represent most of the population included in *in vivo* studies.

There are several limitations to this study that should be noted. Our goal was to characterize the mechanical consequences of varying subtendon twist, independent of variation in tendon geometry or material properties. To this end we developed a model with a generic geometry so that we could create variations in internal structure and examine the effects on tendon behavior when loaded uniaxially. Future work to develop more detailed models is needed to fully investigate how subtendon twist influences *in vivo* Achilles tendon behavior. Methods enabling *in vivo* quantification of subtendon twist would improve subject-specific models. Twist could be incorporated with other model inputs, like geometry and material properties, that tendon behavior is sensitive to (Shim et al. 2014). Furthermore, validation with *in vivo* data is required to better understand the predictions made in this study. We chose to use the measurements of subtendon structure reported by Pękala et al. (2017) because of the extent of quantitative anatomical data provided. We are aware that the subtendon proportions and cross section in that study (Pękala et al. 2017), deviate somewhat from those reported by previous authors (Edama et al. 2015; Szaro et al. 2009). Since measurements in these studies were performed *ex vivo* in dissected tendons, a major assumption of our model was that subtendon twist was a morphological characteristic that could exist independent of loading. Therefore, we implemented twist in the geometry of the undeformed models, as opposed to applying a torsional loading condition to achieve twist. Achilles tendon rotation has been observed in response to *in vivo* loading (Obst et al. 2014), and model twist likely changes during simulated loading. All model *twist angles* are reported for the undeformed configuration.

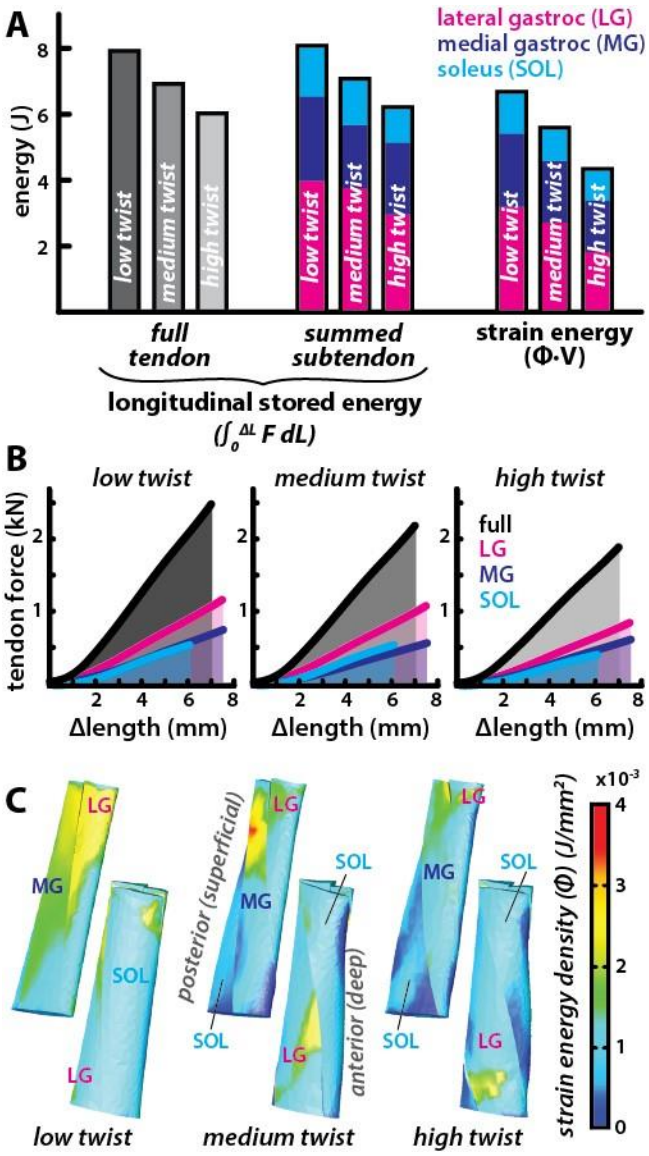

Figure 6.4: Energy stored in the tendon for similar elongations is lower in models with greater subtendon twist. (A) The total energy stored in each twist type was calculated longitudinally using two methods. *Full tendon stored energy* was calculated by integrating the force (F) from all subtendons over the average length change (ΔL) of the all subtendons. *Summed-subtendon stored energy* was calculated by integrating the force (F) from each subtendon over the average length change (ΔL) of that subtendon then summing the results . Total *strain energy* was also computed using the strain energy density (Φ) and volume (V) of each element. Colored bars show the proportion of energy stored in each subtendon. **(B)** The average tendon length change is plotted with the total force in black and the area under the curve was calculated to find *full tendon stored energy*. Subtendon length changes and forces are plotted with colored lines and area under each curve was summed to compute the *summed subtendon stored energy*. **(C)** Posterior and anterior view of each model show the strain energy density (Φ) from each simulation, which was multiplied with element volumes and summed to calculate total strain energy.

All tendon measurements used to create model geometries were made in fresh frozen cadavers (Pękala et al. 2017), though simulation conditions were chosen to represent *in vivo* tendon loading (Franz et al. 2015). Displacements of subtendon proximal ends were controlled to match elongations estimated with speckle tracking in the free tendon. In the *in vivo* experiments, elongation was calculated from the proximal end to the calcaneal marker. The distal end of the models was located at the superior edge of the calcaneus, which resulted in shorter model tendons and therefore higher strains than in the *in vivo* study. Although Achilles tendon strains of this magnitude have been reported during one-legged hopping (Lichtwark and Wilson 2005), model predicted strains are likely larger than what occurs during walking. However, all models experienced the same *longitudinal strains*, allowing for comparison of tissue level strains due to differences in subtendon twist. Further, conclusions about strain in each subtendon are difficult to interpret from these results as the free tendon modeled here does not capture full external portion of proximal tendon associated with lateral or medial gastrocnemius head. Simulations were performed quasi-statically and only included tendon loading. Further work is needed to incorporate more detailed viscoelastic behavior of Achilles tendon in order to accurately simulate full tendon work loops. We assumed the tendon was unloaded prior to simulated elongation and, thus, we applied no initial stretch to the models. Estimates of *in vivo* Achilles tendon loading show that the tendon is not stress-free at the beginning of the gait cycle (Keuler et al. 2019). As the start of our simulations correspond to this time point, it may be appropriate to apply a pre-stretch to the subtendons, which would affect when the tendon would transition from the toe region to the linear portion of the stress-strain curve, leading to higher stresses at the strains enforced in this study. While estimates of stress in the full tendon exist, it is unclear how loading may be distributed between the subtendons. Evidence of differences in slack angles of the triceps surae muscles (Hirata et al. 2015) suggests that the initial stretch at a given joint angle would vary between the subtendons, though current methods are unable to estimate what these loads should be. An exciting direction for future work would be to investigate how inhomogeneous subtendon loading in addition to variation in subtendon morphology influence the behavior of the Achilles tendon.

In conclusion, the models developed in this paper of the Achilles tendon with varied subtendon twisted geometry help us understand how this morphological characteristic can result in different amounts of tissue strain and energy storage within the tendon in response to similar loading. High *twist angles* in tendon fascicles can contribute to errors in quantifying these mechanical behaviors when methods that rely on 2D measurements at the endpoints are employed. The knowledge of this effect will aid in the interpretation of future studies of Achilles tendon behavior and inspire future work to design methods that enable measurements of *in vivo* subtendon structure.

Chapter 7

A 3D model of the soleus reveals effects of aponeuroses morphology and material properties on complex muscle fascicle behavior

"Muscles – that's all it takes to build anything in the world."

– Ayn Rand, *Atlas Shrugged*

"Muscles constitute an 'organ of sense' through which we come to understand ourselves as individuals."

– Kelly McGonigal, *The Joy of Movement*

7.1 Abstract

The soleus is an important plantarflexor muscle that has a complex aponeurosis morphology accompanied by complicated fascicle architecture. In this study we created an image-based finite element model representing the 3D structure of the soleus muscle and aponeuroses, including fascicle architecture of the posterior and anterior compartments. The model was used to simulate passive and active soleus lengthening during ankle motion to predict tissue displacements and fascicle architecture changes. Model initial architecture and changes with passive lengthening were consistent with *in vivo* soleus architecture measured previously with diffusing tensor imaging. We verified model predictions of tissue displacements during active lengthening with dynamic imaging. Distal muscle displacements were measured in an axial plane of the lower leg in eight subjects using cine DENSE (Displacement Encoding with Stimulated Echoes) magnetic resonance imaging while eccentrically dorsiflexing. The model predicts regional variations in muscle displacements that are consistent with dynamic imaging measurements. Regional strains throughout the model elements were nonuniform, but average fascicle strains in the posterior and anterior compartment were similar to each other and greater than the muscle belly strain. We used additional model simulations to investigate the effects of aponeuroses material properties on muscle deformation, by independently varying the longitudinal or transverse stiffness of the posterior or anterior aponeurosis. Results of model variations elucidate how properties of the soleus aponeuroses modulate spatial distribution of muscle tissue deformation, facilitate fascicle architecture changes, and mediate differences in passive and active soleus lengthening, helping us to better understand the function of this complex muscle.

7.2 Introduction

The soleus muscle is an important generator of the plantarflexion torque required for locomotion (Anderson and Pandy 2003; Dorn et al. 2012; Neptune et al. 2001). Knowledge of soleus function is currently limited by understanding of the role of this muscle's complex structure. The complexity of soleus morphology has been examined in detail using cadavers and *in vivo* imaging. The soleus has the

largest physiological cross sectional area (PCSA) of all human lower limb muscles (Ward et al. 2009) with a large volume (Handsfield et al. 2014) and relatively short fascicles (~10% of the muscle length) (Bolsterlee et al. 2018). The soleus's large PCSA maybe contributed to the compartmentalized organization of its fascicles (Agur et al. 2003; Bolsterlee et al. 2018; Hodgson et al. 2006). Fascicle architecture within the soleus compartments have been comprehensively quantified in cadavers (Agur et al. 2003) and more recently *in vivo* with diffusion tensor imaging (DTI) (Bolsterlee et al. 2018). Soleus architecture can be further described by fascicle connections to the morphologically complex aponeuroses (Finni et al. 2003a; Hodgson et al. 2006). The soleus' sheet-like anterior aponeurosis attaches proximally to the tibia and fibula but curves so that it is mostly internal over the length of the muscle (Hodgson et al. 2006). The anterior aponeurosis separates the anterior and posterior compartments and serves as the origin of fascicles from both (Bolsterlee et al. 2018). Fascicles in the posterior compartment insert onto the posterior aponeurosis which is continuous with the Achilles at the muscle-tendon-junction (MTJ). Fascicles in the anterior compartment insert onto the medium septum that protrudes from the posterior aponeurosis and interdigitates with the anterior aponeurosis (Bolsterlee et al. 2018; Hodgson et al. 2006) (Figure 7.1).

While aponeurosis morphology is well described, the effects of this morphology on the *in vivo* behavior of fascicles within the compartments is not well understood due to limited quantification during ankle motion. Many studies have examined soleus fascicles using ultrasound (Clark and Franz 2019; Lai et al. 2015; Nuckols et al. 2020; Rubenson et al. 2012), but they have been limited to a small region of the posterior compartment. Architecture changes throughout the anterior and posterior compartments have only been measured *in vivo* with passive changes in ankle angle (Bolsterlee et al. 2018). Dynamic MRI has been used to map intramuscular tissue velocities during isometric contraction (Finni et al. 2003a; Hodgson et al. 2006) but do not provide measures of soleus fascicle behavior. Simulations can predict architecture changes during muscle function (Anderson and Pandy 2003; Dorn et al. 2012; Neptune et al. 2001) but are limited in representing the soleus using "lumped parameter" models. These models assume

a simplified representation of fascicle architecture while combining the mechanical behavior of the external tendon and aponeuroses into a single series elastic element (Delp et al. 1990; Millard et al. 2013; Zajac 1989), which maybe especially problematic for the soleus given its complex morphology.

Our group has previously used three-dimensional (3D) finite element modeling to examine functional characteristics of muscles with complex architecture, such as non-uniform strains in the muscle tissue and fascicles (Blemker and Delp 2005, 2006; Blemker et al. 2005; Fiorentino et al. 2014; Fiorentino and Blemker 2014; Rehorn and Blemker 2010). Similar models could enable better understanding soleus function by representing the muscle's complexities, like its compartment structure. Such models have further allowed fascicle behavior and tissue deformation to be related to aponeurosis morphology (Fiorentino and Blemker 2014; Rehorn and Blemker 2010), which could aid in examining the role of the soleus' large interdigitating aponeuroses. Additionally, dynamic imaging of *in vivo* tissue motion has been used to successfully verify model predictions (Blemker and Delp 2005; Blemker et al. 2005; Fiorentino and Blemker 2014).

3D modelling of the soleus would also enable investigation of isolated changes in the material properties of the aponeuroses. There is increasing evidence demonstrating the interdependence of biaxial aponeurosis deformation with muscle contraction and force production (Arellano et al. 2016; Azizi and Roberts 2009). For example, changes in transverse aponeurosis properties alter muscle fascicle behavior (Eng and Roberts 2018; Holt et al. 2016). This raises questions about how aponeurosis material properties might affect the human soleus muscle whose large internal anterior aponeurosis constrains both compartments so that short highly pennate fibers' behavior varies dramatically from the full muscle.

Our goal was to develop a finite element (FE) model of the soleus that represents its complex 3D structure in order to simulate passive and active lengthening of this muscle during ankle motion. Using this model, we aim to (i) examine how muscle fascicle deformations within the soleus relate to aponeurosis morphology, (ii) verify model-predicted tissue displacement by comparing to *in vivo* soleus

displacements, and (iii) investigate how variations in aponeurosis material properties alter predicted tissue displacements and fascicle architecture changes.

7.3 Methods

7.3.1 Generating model geometry and architecture

Three-dimensional (3D) soleus geometry was created based on the segmentations from high resolution (in-plane resolution: 0.72 x 0.72 mm; slice thickness: 2 mm) magnetic resonance images (MRI) of a single subject (male, 22 years old, height: 191 cm, mass: 88.4 kg). The subject's lower limb was imaged with a spoiled gradient recall-echo sequence using iterative decomposition of water and fat with echo asymmetry and least squares estimation (IDEAL-SPGR) (Reeder et al. 2007) while he lay supine with his right ankle relaxed at 35 degrees plantarflexion (Knaus et al. 2020). The soleus aponeuroses and muscle compartment were identified and outlined in axial slices from the soleus's most proximal visible portion to its distal muscle tendon junction (MTJ) with the Achilles tendon using an in-house Matlab (Mathworks Inc., Natick, MA, US) software (Handsfield et al. 2014) (Figure 7.1A). These segmentations were used to guide the model geometry created in Autodesk Inventor (Autodesk Inc. San Rafael, CA). The geometry included distinct structures (Figure 7.1B) for the posterior aponeurosis that included a protrusion for the median septum and an anterior aponeurosis the was partially internal to the muscle (Hodgson et al. 2006), dividing the volume into the posterior compartment and anterior compartment (Agur et al. 2003; Bolsterlee et al. 2018). 3D muscle compartment structures were lofted from 2D axial contours and aponeuroses were created as surfaces on the boundaries of these shapes that were extruded to a uniform thickness (Shan et al. 2019) (Table 7.1A).

The geometry was meshed into tetrahedral elements (71592 elements, 13998 nodes) using Trelis software (Coreform, Orem, UT, US). Muscle compartments and aponeuroses structures were attached rigidly by coincident nodes. Mesh sensitivity was tested by repeating simulations of passive muscle stretch using models with different mesh densities. The simulations with the selected mesh predicted

along-fiber strains that did not vary more than 1% than predictions using meshes with density increased by a factor of ten.

Each element was assigned a local fiber direction. Aponeuroses fiber directions were assigned by setting axes to the curvature of the surface using PreView (Maas et al. 2012) then aligning fiber vectors with the muscle line of action (distal direction), in the surface plane (Figure 7.1B). Muscle compartment fiber directions were assigned with a tractography method using Laplacian flow simulations (Handsfield, Bolsterlee, et al. 2017), where highly viscous, incompressible, laminar flow within the geometry is determined by assigning inlet and outlet regions. Inlet regions, which serve as fiber origins, were the anterior and posterior surface of the anterior aponeurosis for the anterior and posterior compartments, respectively. The outlet region, fiber insertion, for the posterior compartment was on the anterior surface of the posterior aponeurosis and for the anterior compartment on the lateral and medial surfaces of the median septum. Flow guides were implemented to constrain simulations in each compartment (Handsfield, Bolsterlee, et al. 2017) to enforce fascicle orientations to be consistent with *in vivo* physiology (Bolsterlee et al. 2018) (Figure 7.1B).

To generate muscle fascicle architecture, streamlines were mapped through the local fiber direction vectors in both compartments from seed points on the anterior aponeurosis surfaces using Matlab (Mathworks Inc., Natick, MA, US). Fascicle tracts were created from the streamlines by truncating or extrapolating to terminate on the aponeurosis surface using a method adapted from Bolsterlee et al., 2017. Muscle architecture measurements of length and pennation angle were computed from these fascicle tracts (Bolsterlee et al. 2017, 2018) in the initial model configuration (Figure 7.1C). Points defining the tracts were mapped to parent elements within the finite element mesh in order to compute changes in muscle architecture from simulation predictions.

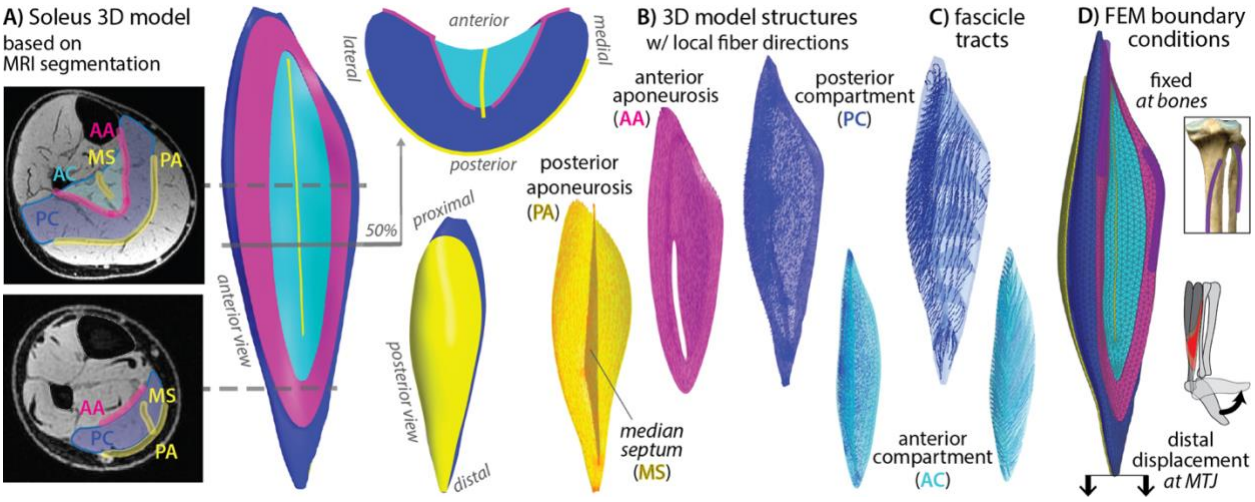

Figure 7.1: Soleus finite element model. A) 3D geometry was constructed based on segmentations from MR images of the lower limb of a single subject. FEM geometry is shown in the anterior, posterior and axial view, with the axial plane cut at 50% of the muscle's length in the proximal-distal direction. **B)** The model comprises four structures for the posterior aponeurosis (PA – yellow), anterior aponeurosis (AA – magenta), the muscle's posterior compartment (PC – blue), and anterior compartment (AC – cyan). The posterior aponeurosis included a protrusion for the median septum (MS). Local fiber directions were assigned to each element in the aponeuroses by using the surface curvature to find the distally oriented in-plane vector. Fiber directions in the muscle compartments were generated using Laplacian flow simulations. **C)** Fascicle tracts were constructed in both muscle compartments using the local fiber direction vectors. Points defining tracts were mapped to the finite element mesh. **D)** Simulations of muscle passive stretch and active lengthening were performed by displacing the distal end of the posterior aponeurosis at the location of the muscle-tendon junction (MTJ) with the Achilles tendon. The proximal end of the model was fixed on the surface of the anterior aponeurosis in regions where it attaches to the tibia and fibula bones.

A) Model measurements

Soleus				Anterior Compartment				Posterior Compartment			
length	LM width	AP thickness	volume	length	LM width	AP thickness	volume	length	LM width	AP thickness	volume
344.8 mm	86.5 mm	42.4 mm	510.5 cm^3	236.1 mm	40.2 mm	23.3 mm	108.2 cm^3	344.8 mm	86.5 mm	19.1 mm	402.3 cm^3

Anterior Aponeurosis				Posterior Aponeurosis				Median Septum			
length	LM width	thickness	prox. loc.	length	LM width	thickness	prox. loc.	length	lateral loc	thickness	prox. loc.
290.4 mm	74.2 mm	1.5 mm	2 %	315.2 mm	88.1 mm	1.5 mm	8 %	278.3 mm	62 %	1.5 mm	10 %

B) Material Parameters

Muscle								Aponeurosis							
K	G_1	G_2	P_1	P_2	λ_{ofl}	λ^*	σ_{max}	K	C_1 (PA)	C_1 (AA)	C_2	α	β	ksi (PA)	ksi (AA)
25 MPa	3.87E-3 MPa	2.24E-2 MPa	0.04	6.6	1 dimensionless	1.06	0.3 MPa	1E+4 MPa	45 MPa	55 MPa	0 MPa	0	2.5	500 MPa	15 MPa

Table 7.1: Soleus model measurements and material properties. A) Measurements of soleus finite element model geometry were based on MRI segmentations of a single subject. Length measurements were made in the proximal-distal direction. Lateral-medial (LM) and anterior-posterior (AP) measurements were made in the axial plane at 50% of the soleus length. Aponeurosis proximal-distal locations (prox. loc.) are specified as the percent of the length that they are offset from the proximal soleus end. The median septum lateral-medial location (lateral loc.) is specified as the percent of the width that it is offset from the lateral side of the soleus in the 50% length axial plane. **B)** The material parameters were defined to implement the transversely isotropic, hyperelastic, quasi-incompressible material models. The muscle material has been detailed by Blemker et al., 2005 and includes the following parameters: bulk modulus (K), along-fiber shear modulus (G_1), cross-fiber shear modulus (G_2), exponential stress coefficient (P_1), fiber uncrimping factor (P_2), optimal fiber length ($\boldsymbol{\lambda}_{ofl}$), stretch at which the stress-strain relationship becomes linear ($\boldsymbol{\lambda}^*$), peak isometric stress ($\boldsymbol{\sigma}_{max}$). Muscle parameters were chosen based on previous modeling studies (Blemker et al. 2005; Fiorentino et al. 2014; Fiorentino and Blemker 2014) and experimental measures of muscle tissue properties (Morrow et al. 2010). The aponeurosis material was an uncoupled solid mixture with a Mooney-Rivlin ground matrix [parameters: coefficient of first invariant term ($\mathbf{C_1}$), coefficient of second invariant term ($\mathbf{C_2}$)] combined with fibers with an exponential power law [parameters: coefficient of exponential argument ($\boldsymbol{\alpha}$), power exponential of argument (**β**), fiber modulus (**ksi**)]. Multiple values are specified for parameters that varied between the posterior aponeurosis (PA) and the anterior aponeurosis (AA). Aponeurosis material parameters were chosen to produce model predictions of physiologic muscle architecture changes (Bolsterlee et al. 2018).

7.3.2 Finite element simulations of muscle lengthening

Both muscle and aponeuroses were modeled as transversely isotropic, hyperelastic, quasi-incompressible materials (Blemker et al. 2005; Criscione et al. 2001; Weiss et al. 1996). The constitutive formula for muscle included passive and active non-linear tensile behavior and has been described in detail (Blemker et al. 2005). The constitutive formula for aponeurosis was an uncoupled solid mixture with a Mooney-Rivlin ground matrix combined with fibers with an exponential power law. Aponeurosis material parameters (Table 7.1B) were chosen to produce model predictions of physiologic muscle architecture changes (Bolsterlee et al. 2018).

Boundary conditions were assigned in PreView (Maas et al. 2012) to produce muscle lengthening during ankle dorsiflexion. The anterior aponeurosis was fixed in regions corresponding to its attachments the tibia and fibula, determined from MRI. A 20 mm displacement in the distal direction was prescribed on the posterior aponeurosis at the MTJ (Figure 7.1D). Muscle activation was held at 0 during passive stretch simulations and was linearly ramped during active lengthening simulations. All simulations were performed quasi-statically in the nonlinear implicit solver FEBio (Maas et al. 2012).

7.3.3 Predicting muscle changes during lengthening

Fiber strain was found for each element in the muscle compartments by subtracting 1 from the along-fiber stretch, from the constitutive formula (Blemker et al. 2005). Average fiber strain was calculated for the anterior and posterior compartments, as well as proximal, middle, and distal thirds of the posterior compartment volume, to examine regional strains. Fascicle strain was calculated for each fascicle tract by dividing the change in length by the initial length. Pennation changes were calculated by finding the angle between the vector connecting the tract's end points in initial and deformed positions. Model predictions of muscle architecture changes during passive stretch were compared to physiologic muscle behavior of subjects with similar muscle length change measured with MRI (Bolsterlee et al. 2018). Differences in average fascicle lengths and pennation angles, determined with diffusion tensor

imaging (DTI) of the soleus compartments at relaxed and stretched positions, were found to compare to model-predicted changes.

7.3.4 Comparing model predictions with dynamic imaging

Dynamic MRI of the soleus was used to verify that the predicted regional variations in muscle displacement agreed with *in vivo* physiologic behavior. The imaging experiment was conducted in accordance with the University of Virginia's Institutional Review Board guidelines and included eight healthy subjects (4 females, 24±3 years old, height: 175±13 cm, mass: 66±12 kg) who provided informed consent. Subjects lay prone in the MR scanner positioned in a non-ferrous exercise device (Silder, Westphal, and Thelen 2009) that had been adapted from use on the knee to the ankle. Subjects performed ankle dorsiflexion-plantarflexion motions guided by a metronome as rotation of the device's inertial disks resulted in active lengthening of triceps surae muscles (Fiorentino et al. 2012). Static images were collected with a turbo spin echo sequence (Fiorentino et al. 2012) in an axial plane (in-plane resolution 0.49 x 0.49 mm^2, slice thickness: 5 mm) located at approximately one third of the soleus muscle's length from the proximal end. Cine DENSE (Displacement Encoding with Stimulated Echoes) images (Aletras et al. 1999) were acquired in the same plane (in-plane resolution 3.125 x 3.125 mm^2, slice thickness: 8 mm, 35 time frames), where pixel-wise muscle displacement during ankle motion was encoded into the MR signal's phase (Fiorentino et al. 2012; Zhong et al. 2008). Time-varying tissue displacement directed out of the plane was reconstructed from the DENSE images (Spottiswoode et al. 2007) within an outline of the soleus muscle, where the distal direction was positive.

Regions of interest (ROI) were defined in the static images to identify muscle tissue near the anterior aponeurosis, posterior aponeurosis, and median septum (Figure 7.2A). ROIs were overlayed and registered with the DENSE images to calculate average time-varying tissue displacement in each aponeurosis region (Figure 7.2B). The peak frame was defined as the frame with the greatest displacement. ROI displacements were then normalized across subjects by scaling to the range of

displacement values in the peak frame. Peak normalized displacement values for each ROI were calculated in each subjects' peak frame and averaged (Figure 7.2C).

To compare to the results of the dynamic imaging experiment, model predictions of muscle displacements in the distal direction were calculated for evenly spaced grid points in a plane located at 33% of the model's length from the proximal end (33% axial plane). ROIs within the model were determined by each grid points' proximity to an aponeurosis structure so that average displacement in each region could be calculated and compared to DENSE results.

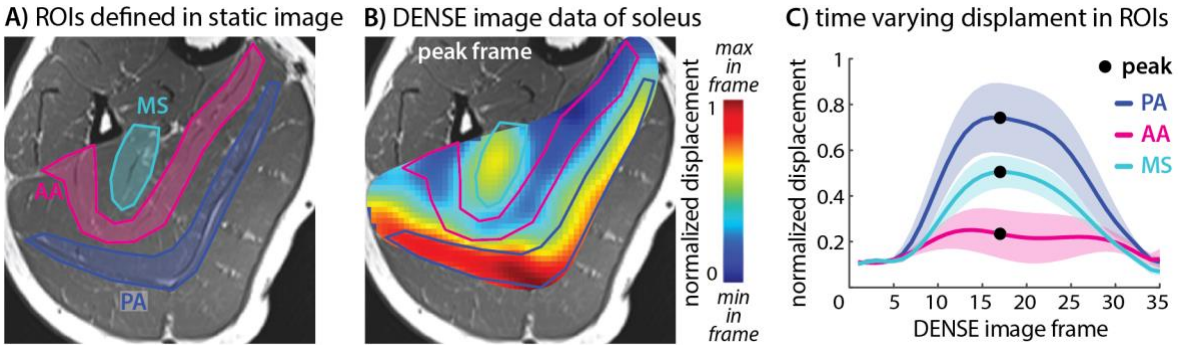

Figure 7.2: Dynamic imaging to compare to model predictions. Static and dynamic imaging was performed in an axial plane at approximately one third of the soleus length from the proximal end in eight subjects. **A)** Regions of interest (ROI) were defined in the static image to identify muscle tissue that was near the aponeurosis structures: posterior aponeurosis (PA – blue), anterior aponeurosis (AA – magenta), and the median septum (MS – cyan). Images are shown for a representative subject. **B)** ROIs were overlayed and registered with the DENSE (Displacement Encoding with Stimulated Echoes) images to calculate average time-varying tissue displacement in each aponeurosis region. DENSE results within the soleus are shown for the peak frame, defined as the DENSE image frame in which the greatest displacement occurred. Results are colored by displacement in the distal direction which is directed out of the image plane. Displacements were normalized, to compare across subjects, by scaling to the range of displacements within the peak frame, so that the maximum displacement in that frame had a value of one while the minimum displacement had a value of zero. **C)** The average normalized displacement was calculated in each ROI in the 35 DENSE image frames as subjects performed a range of ankle motion using an exercise device to produce active soleus lengthening. Peak displacements of all ROIs were identified as the average displacement in the peak frame for that subject.

7.3.5 Varying model aponeuroses properties

Additional soleus model simulations were used to investigate varied muscle fascicle behavior with different ratios of stiffness in the longitudinal and transverse directions as well as between the posterior and anterior aponeurosis. Simulations of soleus passive stretch and active lengthening were repeated with varied material parameters to change either the longitudinal stiffness in the posterior aponeurosis, transverse stiffness in the posterior aponeurosis, longitudinal stiffness in the anterior aponeurosis, or transverse stiffness in the anterior aponeurosis. For each simulated variation in stiffness properties, the other properties were held constant.

To determine a metric of stiffness describing each aponeurosis material variation, we created a simple model with a single hexagonal element. The model was assigned the same transversely isotropic material used for aponeuroses in the soleus FEM. Boundary conditions were prescribed to induce a 10% strain in the element in one direction. A line was fit to the 7-10% strain region of the stress-strain curve predicted to define an effective Young's modulus. To define longitudinal stiffness, the element fiber orientation was parallel to the direction of displacement, and to define transverse stiffness, fiber orientation was perpendicular to the displacement direction. Simulations were repeated for each aponeurosis variation.

To compare effects of aponeurosis stiffness variations on muscle behavior we examined regional strain. Along-fiber strain was averaged for elements in ten regions along the length of the model in the posterior and anterior compartments. Compartment fiber strain along the muscle length during passive lengthening was compared for each model variation. Fascicle architecture changes were also compared by examining average fascicle strain and rotation, measured from changes in fascicle lengths and pennation angles, respectively, for the anterior and posterior compartments in passive and active lengthening. Finally, normalized distal displacement in the ROI in the 33% axial plane defined in Section 2.5 were compared during active lengthening for each variation.

	original	var1	var2	var3	var4	var5	var6	var7	var8	var9	var10	var11	var12
Posterior Aponeurosis		***PL/5***	***PL/2***	***PL*5***				***PT/50***	***PT/5***	***PT*5***			
C_1 (MPa)	45	45	45	45	45	45	45	**1**	**9**	**230**	45	45	45
ksi (MPa)	500	**32**	**205**	**3400**	500	500	500	**575**	**562**	**185**	500	500	500
$E_{longitudinal}$	1806	**352**	**902**	**8968**	1806	1806	1806	1807	1809	1809	1806	1806	1806
$E_{transverse}$	249	249	249	249	249	249	249	**6**	**50**	**1248**	249	249	249
Anterior Aponeurosis					***AL*2***	***AL*5***	***AL*10***				***AT/50***	***AT/5***	***AT/2***
C_1 (MPa)	55	55	55	55	55	55	55	55	55	55	**1**	**11**	**28**
ksi (MPa)	15	15	15	15	**126**	**480**	**1080**	15	15	15	**107**	**90**	**60**
$E_{longitudinal}$	353	353	353	353	**709**	**1797**	**1797**	353	353	353	353	353	349
$E_{transverse}$	304	304	304	304	304	304	304	304	304	304	**6**	**62**	**155**

Table 7.2: Variations in aponeurosis properties. Model simulations were repeated with twelve variations: three each for changes in the longitudinal stiffness of the posterior aponeurosis (PL), the longitudinal stiffness of the anterior aponeurosis (AL), the transverse stiffness of the posterior aponeurosis (PT), and the transverse stiffness of the anterior aponeurosis (AT). The parameters of the constitutive model that were changed were the coefficient of first invariant term in the Mooney-Rivlin ground matrix (**C_1**) and the fiber modulus of the fibers with an exponential power law (**ksi**). Young's modulus was defined by a line fit to the 7-10% strain region of the stress-strain curve predicted by a model with a single hexagonal element prescribed a 10% strain and assigned the same transversely isotropic material used for aponeuroses in the soleus FEM. Element fiber orientation was parallel to the direction of displacement to define longitudinal stiffness (**$E_{longitudinal}$**), and fiber orientation was perpendicular to the displacement direction to define transverse stiffness (**$E_{transverse}$**).

7.4 Results

7.4.1 Model fascicle architecture

In the soleus model, 1026 fascicle tracts were constructed in the posterior compartment and 230 fascicle tracts were constructed in the anterior compartment, in order to measure muscle architecture (Figure 7.3A). There was a large range in fascicle lengths throughout the soleus geometry, but the average was similar the two compartments (posterior: 28.8±11.0 mm, anterior: 31.4±11.1 mm) (Figure 7.3B). There was also a large range in fascicle pennation angles, and the average pennation in the posterior compartment was greater than in the anterior (posterior: 32.3±10.3°, anterior: 25.8±12.1°) (Figure 7.3B). Model fascicle architecture was validated by comparing to the average lengths and pennation angles of the posterior and anterior compartments determined with DTI in the relaxed soleus of 6 subjects (Bolsterlee et al. 2018). Average model fascicle lengths and pennation angles were within a standard

deviation of the image-based lengths (posterior: 35.8±7.6 mm, anterior: 37.7±9.4 mm) and angles (posterior: 36.6±5.5°, anterior: 24.6±2.8°) (Figure 7.3C).

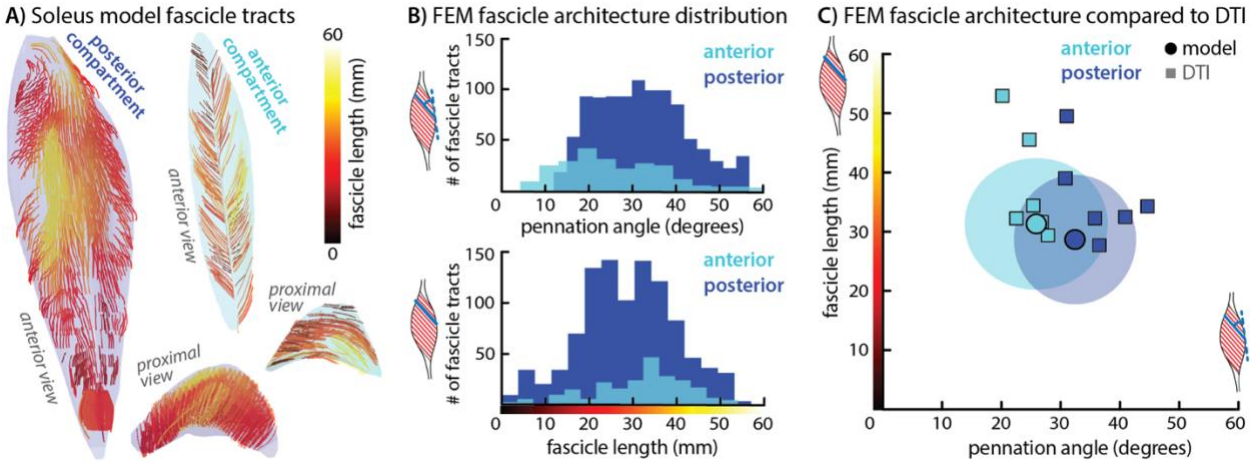

Figure 7.3: **Soleus muscle fascicle tracts** were constructed in the soleus model to determine measures of muscle architecture. **A)** Fascicle tracts are shown in the posterior and anterior compartments from a view of the anterior side and proximal side and are colored according to their length. **B)** There was a broad range of fascicle pennation angles and lengths in both compartments. Average pennation angle was greater in the posterior (blue) compartment compared to the anterior (cyan), and average fascicle length was similar in the two compartments. **C)** Model fascicle architecture was validated by comparing to soleus architecture that was reconstructed using diffusion tensor imaging (DTI) of *in vivo* relaxed muscles (Bolsterlee et al. 2018). Average fascicle lengths and pennation angles in the model (circles) were within one standard deviation of similar architecture measurements determined with DTI (squares) in both the anterior (cyan) and posterior (blue) compartments.

7.4.2 Predictions of muscle strain during passive and active lengthening

Along fiber strain was nonuniform in both compartments of the soleus following passive and active lengthening (Figure 7.4A-B). In passive lengthening, average fiber strain in the anterior compartment (0.24±0.24) was less than in the distal portion of the posterior compartment (0.28±0.24) but greater than the proximal (0.21±0.09) and middle (0.16±0.09) portion of posterior compartment or the combined posterior average (0.19±0.13). In active lengthening, all average regional strains were lower than in passive lengthening but with a similar distribution of regional strains (anterior: 0.15±0.16, distal

posterior: 0.21±0.19, mid posterior: 0.10±0.08, proximal posterior: 0.12±0.09, combined posterior: 0.12±0.11) (Figure 7.4A-C).

Fascicle strains were more uniform than tissue level strains following both passive and active lengthening (Figure 7.4D-E). In passive lengthening, average fascicle strain was similar in the anterior (0.18±0.06) and posterior (0.19±0.05) compartments. In active lengthening, average fascicle strains were also similar between compartments (anterior: 0.12±0.05, posterior: 0.13±0.06), but were less than during passive stretch (Figure 7.4F).

7.4.3 Predictions of muscle architecture changes during passive lengthening

Average fascicle strains in both compartments were greater than the strain in the soleus muscle belly (0.06) during passive and active lengthening (Figure 7.5A-B). Model predicted architecture changes were physiologically consistent with soleus changes quantified using DTI in in four subjects after similar average passive lengthening (muscle belly strain: 0.06±0.03) (Bolsterlee et al. 2018). Fascicle strains computed from average short and long DTI measurements of fascicle lengths in the anterior (0.24±0.08) and posterior (0.25±0.03) compartments were slightly greater on average but within the range of model predicted strains (Figure 7.5A&C). We compared fascicle rotation as an additional metric of architecture changes in passive lengthening and found that although model-predicted pennation angle changes had a large variation in the anterior (8.30±4.95°) and posterior (10.75±4.97°) compartments, the average decrease in pennation angles (anterior: 6.04±1.71°, posterior: 12.26±3.99°) determined with DTI were within one standard deviation of model predictions (Figure 7.5C).

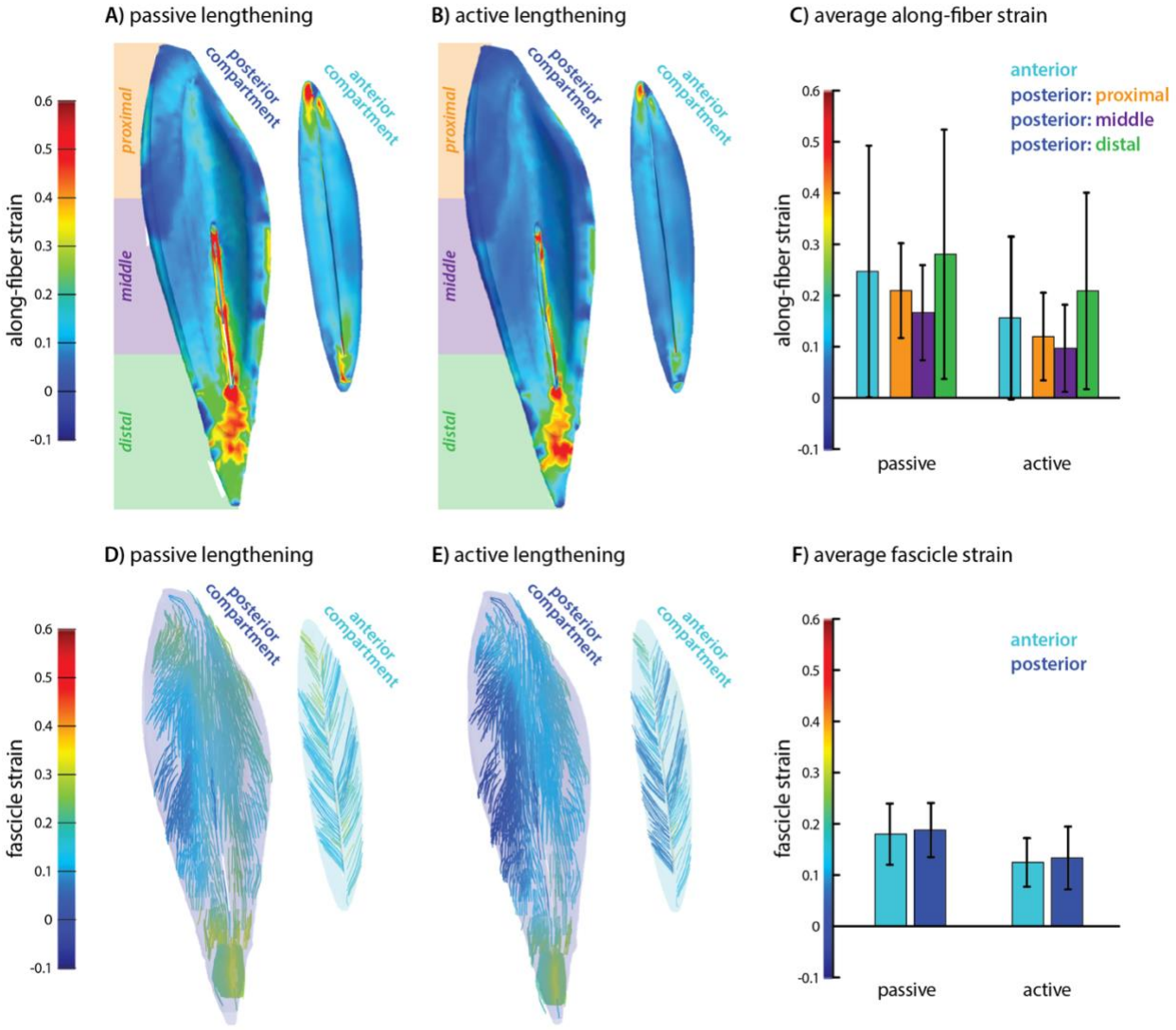

Figure 7.4: Along-fiber strains in elements and fascicle strains. Along-fiber strains, in the muscle tissue elements, were nonuniform throughout the soleus muscle following simulations of **A)** passive lengthening and **B)** active lengthening. Fiber strain distribution is shown in the anterior view of the posterior and anterior compartment. **C)** In passive and active simulations, fiber strains were averaged in the elements of the anterior compartment (cyan) and in three evenly spaced regions along the length of the posterior compartment: proximal (orange), middle (purple), and distal (green). Error bars show standard deviations. Fascicle strains, calculated for each fascicle tract, were more uniform than fiber strains throughout the soleus muscle following simulations of **D)** passive lengthening and **E)** active lengthening. **F)** In passive and active simulations, fascicle strains were averaged in the fascicle tracts from anterior compartment (cyan) and the posterior compartment (blue). Error bars show standard deviations.

7.4.5 Model predicted muscle displacement compared to dynamic imaging of muscle displacement during active lengthening

The FEM predicted nonuniform distal tissue displacement during active lengthening in the 33% axial plane (Figure 7.6A). The greatest normalized out-of-plane displacement was in the muscle tissue in the regions near the posterior aponeurosis (0.777±0.118) and the median septum (0.487±0.059) while the least displacement was in the muscle tissue region near the anterior aponeurosis (0.240±0.121) (Figure 7.6B). From analysis of the DENSE images, all eight subjects exhibited patterns of non-uniform displacement in the peak frame that were similar to the model predictions. Muscle tissue in the posterior aponeurosis ROI had the greatest normalized displacement (0.735±0.138), followed by tissue in the median septum ROI (0.425±0.074) and in the anterior aponeurosis ROI (0.230±0.080) (Figure 7.6B).

7.4.6 The effects of varied aponeuroses properties on predicted muscle behavior

Model simulations were repeated with three variations in each aponeurosis stiffness (Table 7.2). The longitudinal stiffness in the posterior aponeurosis (PL stiffness) was varied to so that its effective Young's modulus was one fifth and one half of its original value and five times larger (Table 7.2, Figure 7.7A). Increasing PL stiffness made passive along-fiber strains in the posterior compartment more uniform but strains in the anterior compartment less uniform along the length of the muscle (Figure 7.7E&I). Increasing PL stiffness, increased fascicle strains and fiber rotations in both compartments in passive and active lengthening (Figure 7.7M). Differences in rotation of anterior and posterior compartment fascicles and differences in fascicle strain between passive and active lengthening both decreased with increasing PL stiffness. Increasing PL stiffness increased the distal displacement of muscle tissue in the median septum ROI and decreased displacement in the anterior aponeurosis ROI in the 33% axial plane during active lengthening (Figure 7.7Q).

The longitudinal stiffness in the anterior aponeurosis (AL stiffness) was varied to so that its effective Young's modulus was two, five, and ten times larger (Table 7.2, Figure 7.7B). Increasing AL

stiffness made passive along-fiber strains in the posterior and anterior compartment less uniform along the muscle length by increasing strains in the distal end (Figure 7.7F&J). Increasing AL stiffness, slightly increased fascicle strains and fiber rotations in the posterior compartment in passive and active lengthening (Figure 7.7N). Increasing AL stiffness did not alter distal displacement of muscle tissue in the 33% axial plane during active lengthening (Figure 7.7R).

The transverse stiffness in the posterior aponeurosis (PT stiffness) was varied to so that its effective Young's modulus was one fiftieth and one fifth of its original value and five times larger (Table 7.2, Figure 7.7C). Increasing PT stiffness made passive along-fiber strains in the posterior compartment slightly more uniform but strains in the anterior compartment less uniform along the length of the muscle (Figure 7.7G&K). Increasing PT stiffness, increased fascicle strains and fiber rotations in both compartments, but with a greater effect in the anterior, in passive and active lengthening (Figure 7.7O). Differences in fascicle strain between passive and active lengthening both decreased with increasing PT stiffness. Increasing PT stiffness increased the distal displacement of muscle tissue in the median septum and posterior aponeurosis ROI in the 33% axial plane during active lengthening (Figure 7.7S).

The transverse stiffness in the anterior aponeurosis (AT stiffness) was varied to so that its effective Young's modulus was one fiftieth, one fifth, and half of its original value (Table 7.2, Figure 7.7D). Increasing AT stiffness made passive along-fiber strains in the posterior compartment less uniform but strains in the anterior compartment more uniform by increasing strains in the distal end (Figure 7.7E&I). Increasing AT stiffness, increased fascicle strains in the posterior compartment in passive lengthening and in both compartments in active lengthening, and also decreased fascicle rotation (Figure 7.7P). Differences in fascicle strain between passive and active lengthening both decreased with increasing AT stiffness. Increasing AT stiffness decreased the distal displacement of muscle tissue in the median septum and anterior aponeurosis ROI in the 33% axial plane during active lengthening (Figure 7.7T).

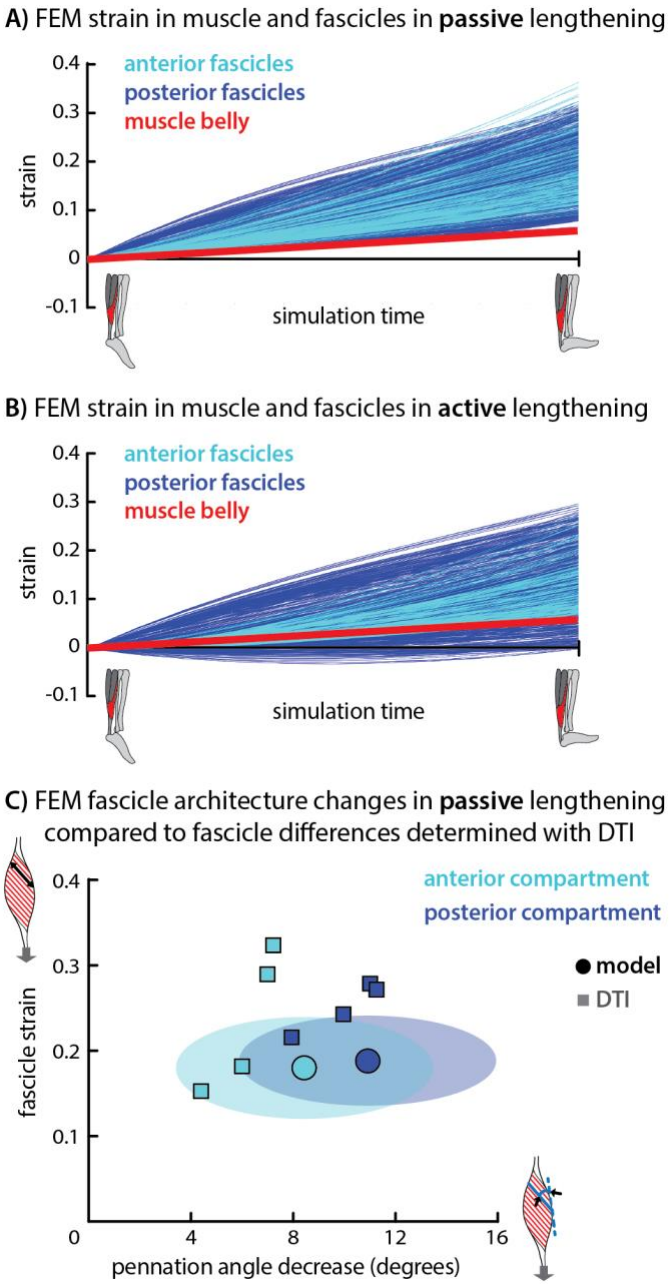

Figure 7.5: Muscle architecture changes compared to DTI. Muscle strain increased throughout simulated soleus lengthening representing ankle dorsiflexion. **A)** In passive lengthening, strain in all individual fascicles of the anterior (cyan) and posterior (blue) compartment were greater than strain of the muscle belly (red). **B)** In active lengthening, the muscle belly strain was the same. Strain in the soleus fascicles was greater on average than the muscle belly, however some fascicles had strains that were lower and even negative (indicating fascicle shortening) during the simulation. **C)** Average model-predicted fascicle strains and rotations (circles with ellipse for standard deviations) were compared to architecture changes in average fascicle lengths and pennation angles (squares) determined with diffusion tensor imaging (DTI) of *in vivo* soleus with similar muscle belly strain between a short (relaxed – plantarflexed) and long (stretched – dorsiflexed) positions (Bolsterlee et al. 2018).

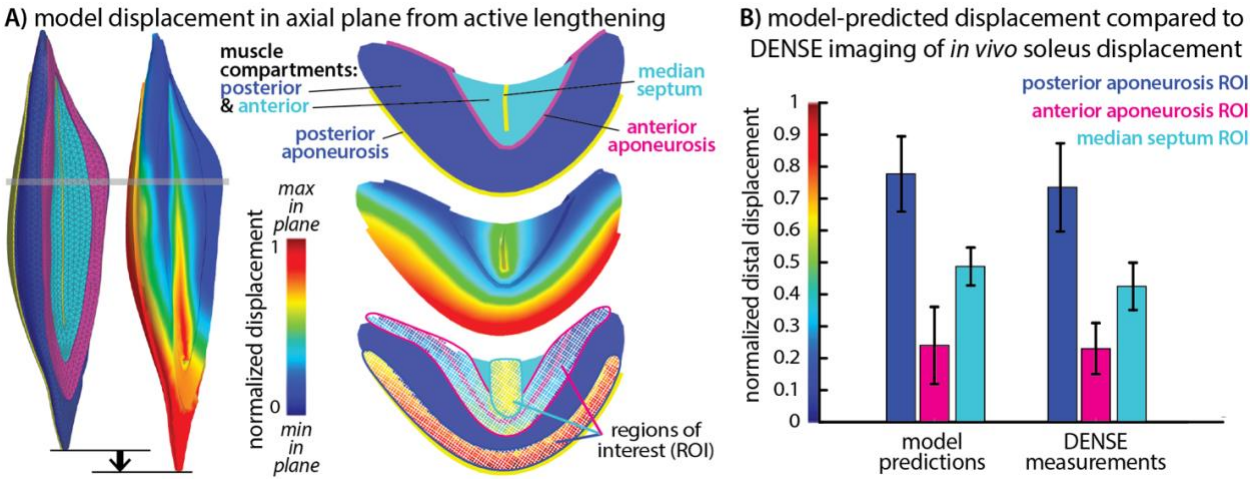

Figure 7.6: Predicted displacements compared to DENSE measurements. A) Model-predicted distal displacements were analyzed in simulated active lengthening. Analyses were performed in the 33% axial plane, located one third of the of the soleus model's length from its proximal end. In this plane the anterior aponeurosis (magenta) bisects the soleus volume into two compartments: anterior (cyan) and posterior (blue). The posterior aponeurosis (yellow) lines much of the superficial surface of the posterior compartment (blue) while the median septum (yellow), that is a protrusion from the posterior aponeurosis, partially bisects the anterior compartment (cyan). Distal displacements, directed out of the axial plane, were nonuniform in the soleus compartments. Model displacements were normalized, to compare to dynamic imaging results, by scaling to the range of displacements within the 33% axial plane, so that the maximum displacement in that plane had a value of one while the minimum displacement had a value of zero. To compare to the results of the dynamic imaging experiment, model-predicted displacements were calculated for evenly spaced grid points. Grid points of muscle tissue displacement within proximity to an aponeurosis structure were assigned to a region of interest (ROI) for that structure. **B)** Model predicted normalized displacements were the average muscle tissue displacements of grid points within the posterior aponeurosis ROI (blue), anterior aponeurosis ROI (magenta), and the median septum ROI (cyan). Displacements measured from the DENSE (Displacement Encoding with Stimulated Echoes) images were the peak displacements for each ROI averaged across subjects. Description of subjects' ROI identification and peak displacement calculation from dynamic imaging experiment are illustrated in Figure 7.2.

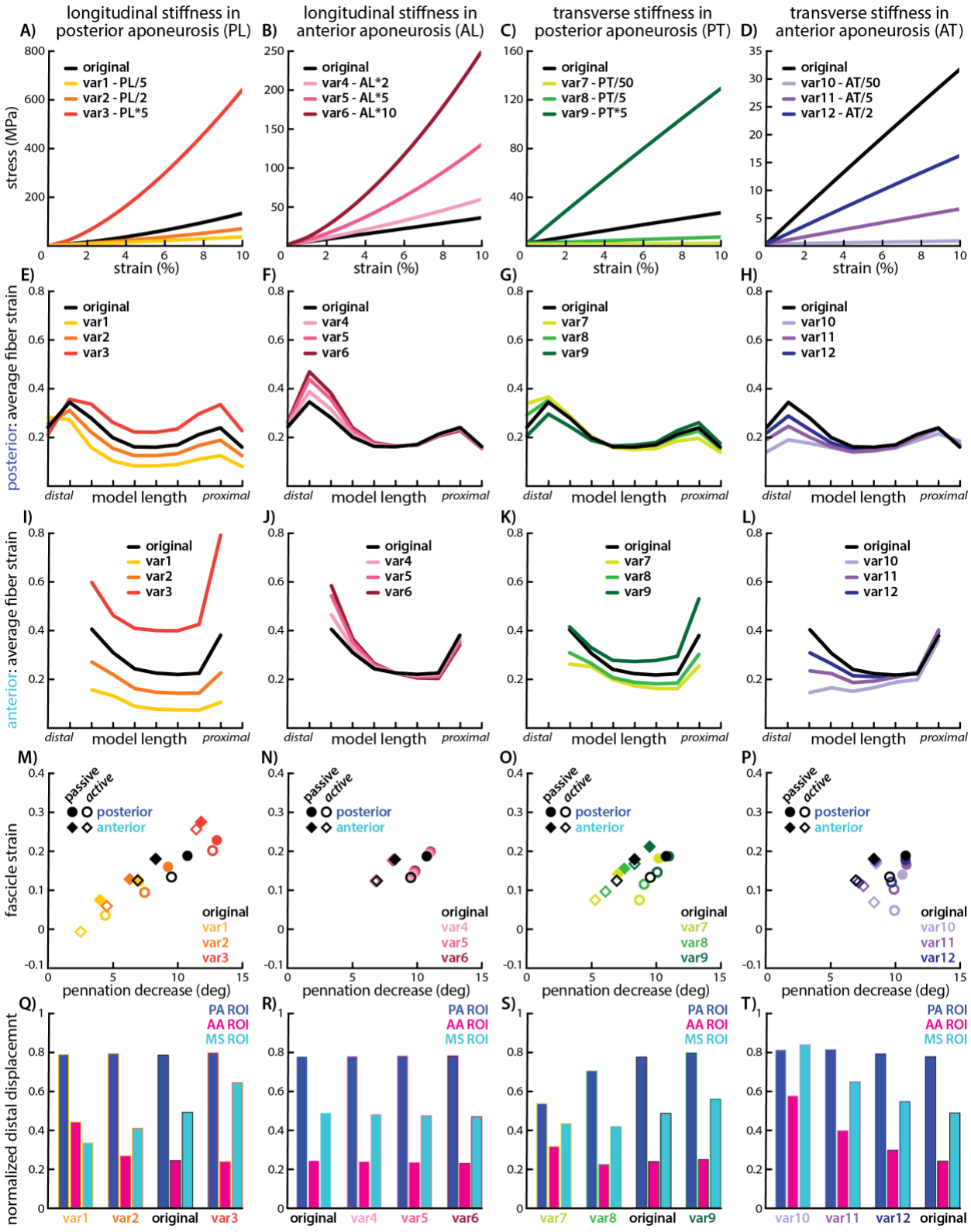

Figure 7.7: Model simulations repeated with varied aponeurosis properties. Single-element stretch simulations were performed for each material variation to generate a stress-strain curve from which Young's

modulus was defined by fitting a line to the portion of the curve between 7-10% strain. **A)** In variations 1-3, properties were adjusted to vary the longitudinal stiffness in the posterior aponeurosis (PL stiffness). Simulation results of single-element stretch parallel to the fiber direction are shown for the posterior aponeurosis material. **B)** In variations 4-6, properties were adjusted to vary the longitudinal stiffness in the anterior aponeurosis (AL stiffness). Simulation results of single-element stretch parallel to the fiber direction are shown for the anterior aponeurosis material. **C)** In variations 7-9, properties were adjusted to vary the transverse stiffness in the posterior aponeurosis (PT stiffness). Simulation results of single-element stretch perpendicular to the fiber direction are shown for the posterior aponeurosis material. **D)** In variations 10-12, properties were adjusted to vary the transverse stiffness in the posterior aponeurosis (AT stiffness). Simulation results of single-element stretch perpendicular to the fiber direction are shown for the posterior aponeurosis material. Following simulations of passive lengthening, muscle along-fiber strain was averaged for elements in ten regions along the length of the model from distal to proximal in the posterior compartment. Shown are spatially varying posterior compartment average fiber strains of the original model and **E)** variations (1-3) with different PL stiffnesses, **F)** variations (4-6) with different AL stiffnesses, **G)** variations (7-9) with different PT stiffnesses, **H)** variations (10-12) with different AT stiffnesses. Average along-fiber strain was found for elements of the anterior compartment in the same regions, following passive stretch simulations. Shown are spatially varying anterior compartment average fiber strains of the original model and **I)** variations (1-3) with different PL stiffnesses, **J)** variations (4-6) with different AL stiffnesses, **K)** variations (7-9) with different PT stiffnesses, **L)** variations (10-12) with different AT stiffnesses. To compare changes in fascicle architecture, average fascicle strain in the posterior compartment (circles) and in the anterior compartment (diamonds) is plotted with average decrease in pennation angle (degrees) in passive (filled markers) and active (open markers) lengthening for the original model and **M)** variations (1-3) with different PL stiffnesses, **N)** variations (4-6) with different AL stiffnesses, **O)** variations (7-9) with different PT stiffnesses, **P)** variations (10-12) with different AT stiffnesses. Average normalized distal displacement in regions of interest (ROI) near the posterior aponeurosis (PA – blue), anterior aponeurosis (AA – magenta), and median septum (MMS – cyan) in the 33% axial plane following active lengthening (Figure) are shown for the original model and **Q)** variations (1-3) with different PL stiffnesses, **R)** variations (4-6) with different AL stiffnesses, **S)** variations (7-9) with different PT stiffnesses, **T)** variations (10-12) with different AT stiffnesses.

7.5 Discussion

We have created a 3D finite element model of the soleus representing its muscle compartment and aponeurosis morphology. Model geometry and fascicle architecture were constructed based on *in vivo* measures of soleus anatomy and material properties were chosen to predict physiological muscle behavior during passive and active lengthening. Using this model, we have investigated the effects of aponeuroses morphology and material properties on predicted fascicle behavior in this complex muscle.

The soleus model helps explore the relationship of aponeurosis morphology with muscle fascicle architecture and behavior. Previous dynamic imaging studies have shown connections between soleus aponeurosis morphology and muscle tissue motion (Finni et al. 2003a, 2003b; Hodgson et al. 2006). Fascicle architecture has been characterized separately at different muscle lengths (Bolsterlee et al. 2018; Sinha et al. 2011). Using our model, we are able to examine direct interactions between the aponeurosis and the muscle fascicle architecture and behavior, which are currently unmeasured *in vivo*. Soleus fascicle lengths were similar between its compartments (Figure 7.3). Aponeurosis structure permits more fascicles that are shorter and more uniform to be packed within the soleus volume. Interdigitating aponeuroses allow for large areas of origin on both sides of the anterior aponeurosis while fascicle insertions from both compartments remain in series with the Achilles tendon. Fascicle strains were also similar between compartments (Figure 7.4D-F) despite differences in initial architecture. Nonuniform tissue strains were contrasted by greater fascicle strain uniformity (Figure 7.4). Variability in fascicle architecture seemed to accommodate variable tissue strain. For example, fascicles were longer in the distal posterior soleus region that experienced the greatest along-fiber strain, resulting in less variable fascicle strains (Figure 7.4A&D).

Model predictions of nonuniform distal displacement were verified by our dynamic imaging experiment, in which all subjects exhibited similar patterns of nonuniform out-of-plane displacement in axial frames that corresponded with the analyzed region of the model. The locations of aponeuroses identified in the static images corresponded with regions of similar displacement (Figure 7.2B). Differential displacements between ROI indicate that posterior aponeurosis and connected median septum move distally relative to the anterior aponeurosis during muscle lengthening (Figure 7.2C). Nonuniform muscle tissue velocities have been shown to correspond with aponeurosis locations in soleus isometric contraction (Finni et al. 2003a; Hodgson et al. 2006), where higher velocities occurred near posterior aponeurosis and median septum compared to anterior aponeurosis. As aponeuroses properties were altered, model variations that predicted similar fascicle kinematics to the original model also predicted

nonuniform tissue displacements that correspond with the dynamic imaging (Figure 7.7). Results of model variations demonstrated a relationship between differential ROI tissue displacement in the axial plane and the average fascicle architecture changes in the compartments (Figure 7.8), suggesting that relative displacement of the aponeuroses facilitates strain and rotation of fascicles in both compartments. These model predictions are consistent with the simple model of soleus fascicle behavior based on MRI-measured tissue velocities in soleus isometric contraction that was previously proposed by Finni et al. (2003a).

Varying the aponeuroses properties in the model elucidated how these tissues influence muscle function. In general, increasing the magnitude of stiffness in either direction of either aponeurosis generally increased strain in the muscle tissue (Figure 7.7). This conclusion could be drawn from a "lumped-parameter" model of muscle (Delp et al. 1990; Zajac 1989) by assuming muscle and aponeurosis tissue are in parallel with each other, so that their relative stiffness would impact the strain distributed between them. Differences in how FEM predictions of muscle behavior are altered by changes in the different aponeuroses support conclusions of a more complex relationship between these tissues (Epstein et al. 2006), which the FEM is able to explore without being bound by explicit designation of being in series or parallel. Decreasing PL stiffness or increasing AL stiffness reduced the uniformity of strain along the length of the posterior compartment by concentrating strain in the distal end of the muscle (Figure 7.7E-F). A larger relative difference in longitudinal stiffness between the aponeuroses seemed to regulate the spatial distribution of strain, although changing AL stiffness did very little to alter average fascicle strain compared to changing PL stiffness (Figure 7.7M-N). Only changes in PL stiffness affected displacements in the 33% axial plane (Figure 7.7Q-R). As PL stiffness decreased, the median septum displaced less (Figure 7.7Q), indicating that it experienced greater longitudinal strain as a prescribed displacement was applied to the distal end of the wider posterior aponeurosis it attaches to. The lowest PL stiffness (var1) allowed for negative fascicle strains (i.e., shortening) during active muscle lengthening in

the anterior compartment (Figure 7.7M) as the anterior aponeurosis ROI displaced relative to the median septum ROI.

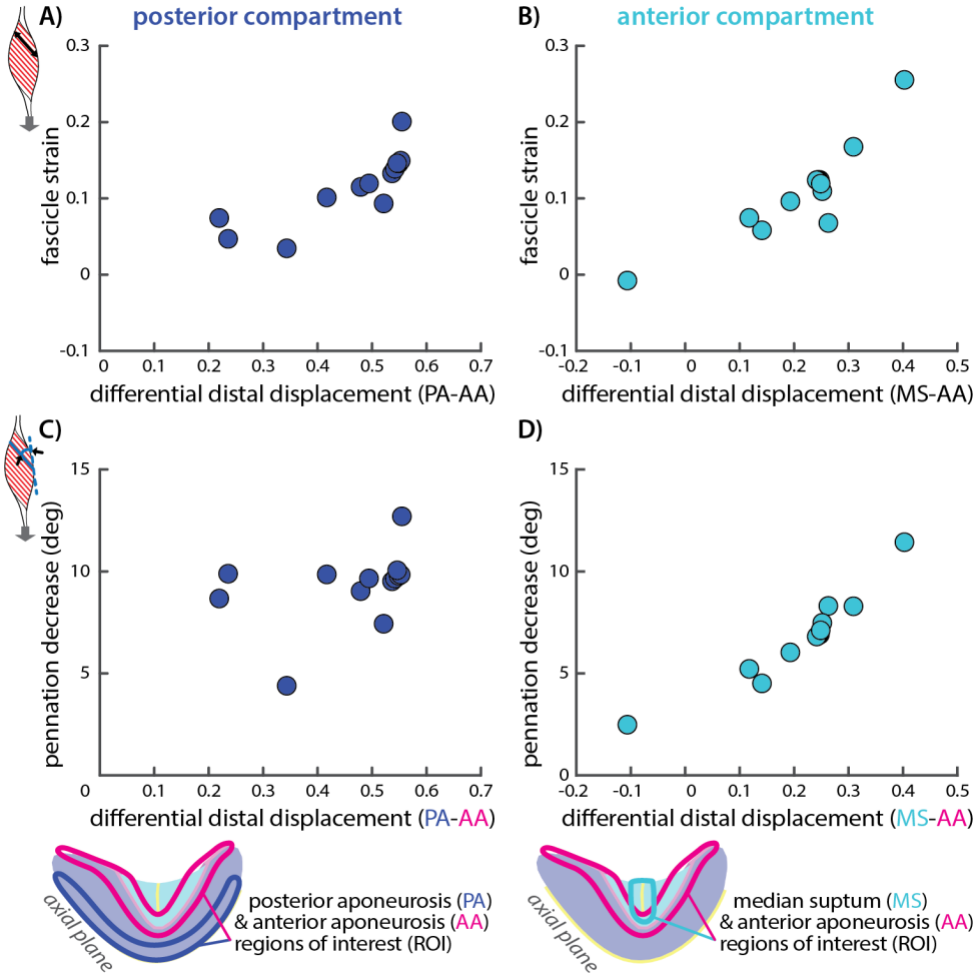

Figure 7.8: Tissue displacements and architecture changes. Model-predicted tissue displacements (Figure Q-T) were compared to fascicle architecture changes (Figure M-P) for all variations. **A)** Average fascicle strain following active lengthening in posterior compartment is plotted with the difference in average distal displacement between the posterior aponeurosis (PA) region of interest (ROI) and the anterior aponeurosis (AA) ROI in the 33% axial plane (Figure). Fascicles in the posterior compartment originated on the AA and inserted onto the PA. **B)** Average fascicle strain following active lengthening in anterior compartment is plotted with the difference in average distal displacement between the median septum (MS) ROI and the AA ROI. Fascicles in the anterior compartment originated on the AA and inserted onto the MS. **C)** Average fascicle pennation angle decrease (degrees) following active lengthening in posterior compartment is plotted with the differential displacement between the PA and AA ROI. **D)** Average fascicle pennation angle decrease (degrees) following active lengthening in anterior compartment is plotted with the differential displacement between the MS and AA ROI.

Changes in transverse stiffness had a greater effect on distal displacements in the 33% axial plane (Figure 7.7S-T), even though the muscle was loaded in the longitudinal direction. Decreases in the PT stiffness appeared to allow along-fiber shearing in the wide aponeurosis as the narrow distal end was displaced, such that the average displacement of tissue in the posterior aponeurosis and median septum ROI was decreased (Figure 7.7S). Decreasing AT stiffness also allowed along-fiber shearing so that the internal portion of the aponeurosis was pulled distally. Although the exterior sections were fixed to the bones, there were larger average distal displacements in the anterior aponeurosis ROI (Figure 7.7T), resulting in lower relative displacements between the aponeuroses and smaller fascicle strains in both compartments (Figure 7.7P). Changes in aponeuroses transverse stiffness had a greater effect on fascicle behavior in active lengthening compared to passive (Figure 7.7O-P). Aponeuroses have been shown to be loaded uniaxially (longitudinally) when muscle is passive but biaxially as muscle produces force actively (Azizi and Roberts 2009), explaining how transverse aponeuroses properties would have a greater effect on active muscle architecture changes. Further animal studies found a relationship between differences in muscle fascicle behavior and transverse aponeurosis properties by applying longitudinal incisions to the lateral gastrocnemius aponeurosis of turkeys (Eng and Roberts 2018). A similar relationship was demonstrated to occur naturally in the rat medial gastrocnemius due to differences associated with aging (Holt et al. 2016). This implies that age-related changes in aponeurosis properties of the human soleus may alter muscle fascicle behavior, helping to explain changes in triceps surae function of older adults (Franz 2016; Krupenevich et al. 2020).

There are several assumptions and limitations in our model that we wish to address. The material properties of the aponeuroses and muscle were determined based on limited available data. Aponeurosis properties were chosen to produce model predictions of physiologic soleus muscle behavior and fit within bounds of physiologic material properties, but measurements of what these properties should be are limited. *In vivo* triceps surae aponeurosis properties have been measured, but only in the longitudinal direction and rely on many assumptions to determine stress and strain from measurements made with

dynamometry and ultrasound (Magnusson et al. 2001). The longitudinal posterior aponeurosis Young's modulus of the model (Table 7.2) was the same as the upper bound from this study (1806 MPa). Longitudinal and transverse properties have been measured with uniaxial testing in regions of the posterior and anterior soleus aponeuroses in cadavers (Shan et al. 2019). The Young's modulus in the longitudinal direction of both aponeuroses were lower than in vivo estimates (Magnusson et al. 2001). The longitudinal anterior aponeurosis Young's modulus of the model (Table 7.2) was within the bounds of the cadaveric measurements (67.69-435.54 MPa). Stiffness of the posterior aponeurosis was greater than of the anterior aponeurosis in both the model (Table 7.2) and cadaver tissue (Shan et al. 2019), however, the ratio between aponeuroses stiffnesses in the model (posterior:anterior = 5 longitudinally) was higher than same ratio in cadavers (posterior:anterior = 1.5 longitudinally). The anterior aponeurosis was also thicker than the posterior aponeurosis in cadavers, but they were the same in the model which would affect this stiffness ratio. Longitudinal aponeurosis stiffness was several orders of magnitude stiffer than transverse stiffness in cadavers, and while longitudinal stiffness was also greater in the model, the ratio was less dramatic. The cadavers were elderly and embalmed which may affect material properties and effects might be nonuniform in longitudinal and transverse directions. The ratio of longitudinal to transverse stiffness in the model's posterior aponeurosis (L:T = 7.25) was similar to the same ratio measured in the medial gastrocnemius aponeuroses of turkeys (L:T = 6.5) (Azizi et al. 2009). The model's anterior aponeurosis was nearly isotropic (Table 7.2), which is less consistent of previous reports of aponeurosis properties. However, cadaver measurements were only made on external portions of anterior aponeurosis while a majority of the structure is internal to the muscle. Further work is needed to investigate the mechanical properties and collagen organization of internal aponeuroses. The mechanical properties of muscle have also been measured but with high variability (Morrow et al. 2010) and the parameters used for this model were used in previously validated models of skeletal muscles (Fiorentino et al. 2014; Fiorentino and Blemker 2014). Variation in the model's muscle properties would affect the fit of the aponeurosis properties as these tissues interact. Even if stiffness magnitudes ultimately vary, model

results clearly demonstrate the how relative stiffnesses between the muscle and the material directions in the two aponeuroses impact fascicle behavior in soleus lengthening.

Our model represents soleus anatomy based on a single subject. The chosen subject's total soleus volume and relative volume distribution between the posterior and anterior compartments was representative of MRI measurements of young adults (Knaus et al. 2020). The chosen subject's aponeuroses were clearly identifiable in the MRI and their morphology was consistent with previous detailed descriptions (Finni et al. 2003a; Hodgson et al. 2006). Although the model is representative of soleus morphology, there is clear evidence of anatomical variability in the soleus across individuals. Variability has been demonstrated by characterizing soleus muscle compartment and aponeurosis morphology in vivo using imaging (Bolsterlee et al. 2018; Hodgson et al. 2006), and by examination and dissection of cadavers (Agur et al. 2003; Olewnik et al. 2020). Our DENSE imaging study showed consistent relative displacement between the aponeuroses despite subject anatomical variability. These results give us confidence that predicted nonuniform displacements and correspond model architecture changes are relevant to general soleus muscle behavior. An interesting direction for further study would be developing subject-specific models to investigate how anatomical variability may impact soleus fascicle behavior and ultimately muscle function.

Chapter 8

Conclusion

"The important thing is not to stop questioning. Curiosity has its own reason for existing. One cannot help but be in awe when he contemplates the mysteries of eternity, of life, of the marvelous structure of reality. It is enough if one tries merely to comprehend a little of this mystery every day."

– Albert Einstein

8.1 Summary

This dissertation introduces multiple finite element models (FEM) designed to study the interaction of complex muscles and connective tissue structures in the production of healthy movement. These models were used to answer critical questions about the relationships between muscle architecture and connective tissue morphology and the production of movement required for daily life. The answers to these questions are fundamentally important in understanding how changes that occur in the body with age interact to limit functional movement.

I first developed a 3D FEM of the accommodative mechanism to reveal how action of the multi-section ciliary muscle changes the ocular lens to alter optical power of the eye for near vision. I then used this model to predict how changes associated with age in the mechanical properties of different tissue structures reduce accommodative capacity, potentially contributing to the pathophysiology of presbyopia.

Second, I investigated the triceps surae group better understand its role in ankle plantarflexion dysfunction associated with age-related mobility loss. I examined differences in triceps surae muscle volumes, Achilles tendon cross sections, body sizes, and peak plantarflexion torques during walking in young and old adults. Next, I built FEMs of Achilles tendons with different twisted morphologies to probe the effects of anatomical variation on strain and energy storage during walking. Finally, I created a 3D FEM of the multi-compartment soleus muscle to elucidate how aponeurosis morphology and material properties influence muscle fascicle behavior in passive and active lengthening.

Insights from this work advance our knowledge of muscle-driven production of movement by illuminating how the form and function of these complex tissues are related. Such knowledge can be used to promote the development of new therapies that will improve or preserve vision and mobility in aging adults.

8.2 Contributions

The work presented in this dissertation presents three novel finite element models of morphological complex muscle and connective tissue structures. These models demonstrate significant innovation in the *in silico* representation of these specific tissues. These models provide insight into the healthy function of their respective systems and help elucidate consequences of aging. Further I have published valuable data comparing measurements of young and old adults. The scientific contributions made in this dissertation will be of interest in multiple broad areas of biomechanics.

3D finite element model of the accommodative mechanism driven by contraction of the ciliary muscle

Accommodative movements of the tissues comprising the accommodative mechanism have been described in detail, however, the mechanical relationships between these different structures were poorly understood prior to this dissertation. The physics-based 3D computer model provides a powerful tool for investigating the complex mechanical properties of muscle function in the accommodative mechanism of the eye. The model was used to simulate contraction of the ciliary muscle sections and included a more anatomical representation of zonules, as well constraints imposed by extralenticular structures. A novel feature of this model was the capability to simulate ciliary muscle-driven accommodation, which was achieved in two parts. The first was by defining detailed zonular geometry and a period of lens initialization, enabled by a modified constitutive formal to generate zonular tension. The second was by creating multipart architecture with uniquely defined element fiber directions, to which was applied a constitutive formula that enabled active and passive behavior that was tailored to this atypical muscle. This model helped to synthesize the copious literature investigating varied aspects of accommodative function and elucidated healthy function of the entire accommodative mechanism. The model was used to investigate the specific actions of the sections of the ciliary muscle in producing the lens displacement required for accommodation. This work provides insight into the multifaceted pathophysiology of presbyopia that could not have been explored with previous modeling methods. The FEM also provides

the potential to explore new presbyopia therapies targeted at restoring healthy accommodative biomechanics as opposed to vision correction.

Comparative measurements of triceps surae muscle volumes, Achilles tendon cross sections, body sizes, and peak plantarflexion torques during walking in young and old adults

Although functional changes in walking that occur with age are likely attributed to changes in the triceps surae muscle-tendon unit, prior to this dissertation, little was known about how age-related differences in tendon and muscle structure correspond with each other or compare to measurements of plantarflexor output. We have published *in vivo* volume measurements of the individual triceps surae muscle portions (the medial and lateral head of the gastrocnemius and the anterior and posterior compartment of the soleus) in young and older adults. We have presented for the first time how these muscles compare between age groups when normalized by body size (height*mass) and by total triceps surae volume, helping understand how muscle size and distribution changes with age. Further, we have compared muscle volumes to Achilles tendon cross sectional area (CSA) and peak plantarflexion torque during walking. These comparisons have illuminated clear structure-function relationships in young adults and have highlighted how these relationships are altered or maintained in older adults. We have identified body size (height*mass) as a clear predictor of ankle walking torque in humans of all ages. We have also identified Achilles tendon CSA normalized by body size as a potential metric of functional deficits in older adults.

3D finite element models of the twisted morphology of the Achilles tendon

The Achilles tendon comprises three subtendons from each triceps surae muscle. These subtendons twist around each other with different amounts of torsion among themselves and between individuals. The variation in the twisted structure of the Achilles tendon has been documented by detailed anatomical studies; however, prior to this dissertation, it was unclear how variation in structure influences the function of this important tendon. I created finite element models of tendons with different internal twisting structure in order to simulate loading that represented walking. This modeling study was the first

to examine variations in subtendon twist, independent of differences in tendon geometry or material properties. The use of flow guides in computational fluid simulations allowed for precise control of the angle of twist of the fascicles within each subtendon. The models were used to understand how strain experienced by the tendon during a given elongation would vary with different amounts of twist, and to elucidate how differences in twist change the amount of energy stored during that same stretch. I also investigated how subtendon twist may affect how Achilles tendon behavior is quantified with *in vivo* measurements. The models predict that, with increasing twist, the Achilles tendon exhibits reduced along-fiber strain and lower energies stored during elongation. Our study reveals that increasing the degree of twist of the subtendons effectively lowers stiffness in the free tendon without altering the tissue level material properties. These findings have implications in the study of Achilles tendon rupture, repair, and aging.

3D finite element model of soleus muscle's complex fascicle architecture and aponeurosis morphology

Knowledge of soleus function was previously limited by understanding of the role of this muscle's complex structure. The 3D FEM of the soleus is the first to represent both the multicompartment architecture of the muscle fascicles and the interdigitating morphology. Due to the soleus' complexity, a lumped parameter model cannot fully represent the interaction of the muscle fascicles and aponeuroses and may not accurately predict this muscles' *in vivo* force generating capacity. The FEM is able to represent passive and active anisotropic behavior of the muscle tissue by incorporating muscle constitutive equations and unique element fiber directions defined through fluid simulations. Construction of fascicle architecture from these fiber directions also for tissue displacements to be directly related to fascicle kinematics as the muscle lengthens. These aspects of muscle deformation have previously only been reported independently and in different conditions of muscle activation and length change. The model predicted fascicle architecture changes that were measured previously with diffusion tensor imaging (DTI) and also predicted regional variations in muscle displacements that were consistent with measurements from cine DENSE (Displacement Encoding with Stimulated Echoes) magnetic resonance

imaging (MRI). Longitudinal and transverse stiffness could be varied independently in the anterior aponeurosis and posterior aponeurosis, enabling the first investigation into how variation of these stiffnesses relative to each other influenced the soleus. Development of this model helps us better understand the relationships between complex fascicle architecture and aponeurosis morphology and material properties in the muscle function. This model improves our ability to predict the *in vivo* force generating capacity of the soleus in order to probe its contributions to human locomotion. Such predictions may be especially important for investigating age-related gait changes, characterized by reduced plantarflexor output, enabling further study of muscle and tendon structure-function relationships.

8.3 Additional Applications

The models developed in this dissertation enable further exploration of the biomechanics of these complex systems. While we have applied these models to investigate many unanswered questions, other gaps in our knowledge of muscular function in the eye and ankle could be illuminated through further simulations. Here we describe proposed methods and some preliminary results for additional *in silico* experiments employing the models in this dissertation.

8.3.1 Eye model

I have demonstrated how I have used the FEM of the accommodative mechanism to better understand the form and function of the ciliary muscle in Chapter 2, and to investigate age-related changes to the material properties in Chapter 3. I have also envisioned using this model to explore other aspects of ocular form and function and as a tool in the application and optimization of the therapies to correct presbyopia.

The anatomy and tension of the zonule fibers

Zonular arrangement regulates how excursions of the ciliary muscle are transmitted to the lens during accommodation. Zonules are organized into divisions of radially distributed fibers, that are

described in the literature based on their origin and insertion points. The anterior and pars plana zonules have been clearly identified by scanning electron microscopy (SEM) (Farnsworth and Shyne 1979; Rohen 1979), and the roles of these divisions widely posited for some time. Zonules in the region of the *ora serrata* and vitreous membrane have been more recently identified (Croft, Nork, et al. 2013; Lütjen-Drecoll et al. 2010) and are likely key structures that influence accommodation. Newly developed computer animations have illustrated the geometric arrangement of the complex zonular divisions in accommodation (Goldberg 2011, 2015), raising several new questions regarding the contributions of zonule structure to accommodative function. Importantly, how does each zonular division influence ciliary muscle excursion and lens deformation?

The eye FEM, presented in Chapter 2, is the first to represent the anatomy of all zonule divisions that are currently described in the literature (Croft, McDonald, et al. 2013; Croft, Nork, et al. 2013; Farnsworth and Shyne 1979; Goldberg 2015; Lütjen-Drecoll et al. 2010; Rohen 1979). This model also used a novel constitutive formula that enabled initialization of tension in the lens via the zonules (Equation 2.6). The tension parameter (p_z) assigned to each zonule division for model initialization was calibrated to produce deformation of the lens to match *in vivo* measurements of unaccommodated lens shape (Section 2.2.2). To determine the effects of individual zonular division tension on lens deformation during initialization, additional simulations were performed in which each zonular division was tensioned individually to $p_z = 0.4$ while others were held at $p_z = 0$.

Tensioning of individual zonular divisions demonstrated that each division with an attachment to the lens plays a unique role in influencing accommodative lens deformation. Zonule divisions that did not contact the lens (IVZ and PPZ) did not alter lens shape during initialization when individually tensioned. Models with only PAZ or PVZ INS-LE zonules tensioned predicted the greatest changes in lens thickness (Figure 7.1A), and models with only EAZ or PVZ INS-LE zonules tensioned predicted the greatest changes in lens equatorial radius (Figure 7.1B). Models with EAZ, PAZ, or AVZ zonules tensioned

predicted movement of the lens equator in the anterior direction, while models with AAZ or PVZ INS-LE zonules tensioned predicted movement of the lens equator in the posterior direction (Figure 7.1C).

Analyses of isolated zonular division tension demonstrated that divisions attached to the lens exhibited similar contributions to lens thickness changes, but disparate contributions to changes in the radius and position of the equator. These results support that a balance of zonular forces is necessary to recapitulate correct shape and positioning of the lens. These effects are consistent with published experiments in monkeys, in which the lens was stretched after anterior zonules were selectively cut and resulting changes in lens shape were compared (Nankivil et al. 2015). The PVZ INS-LE zonules have only recently been documented (Croft, Nork, et al. 2013) and not incorporated into previous models of accommodation (Burd et al. 2002; Liu et al. 2006); however, in our model this division had the greatest individual effect on lens deformation, particularly the anterior displacement of the lens equator. The PVZ INS-LE zonules pull the lens equator posteriorly when tensioned; therefore, forward movement of their insertion zone during accommodation relieves this tension facilitating anterior lens deformation, as posited by Croft et al. (2016).

The simulations described above explored the effects of zonular tension during model initialization. An additional application would be to use varied zonular tension parameters to explore differences in simulated accommodation. Zonular arrangement likely complements ciliary muscle architecture and excursion to delicately modulate tension on the lens during healthy accommodation. Age-related dimensional differences also suggest that the *in vivo* stress state of the lens may be altered in older adults. Lens thickness measured *in vivo* (Richdale et al. 2013; Strenk et al. 1999) and in isolation (Glasser and Campbell 1999; Urs et al. 2009) increases, as does the resting width and position of the ciliary muscle apex (Strenk et al. 1999; Tamm et al. 1992). Additionally the attachment locations of the zonules differs with age (Farnsworth and Shyne 1979). Additional model simulations could be performed to understand how altered unaccommodated lens tension might affect accommodative lens deformations. In these simulations, zonular tension could be calibrated during initialization (similar to methods

described in Section 2.2.2) to reproduce unaccommodated lens dimensions measured in older adults of incrementally increasing ages (similar to methods described in Section 3.2.2).

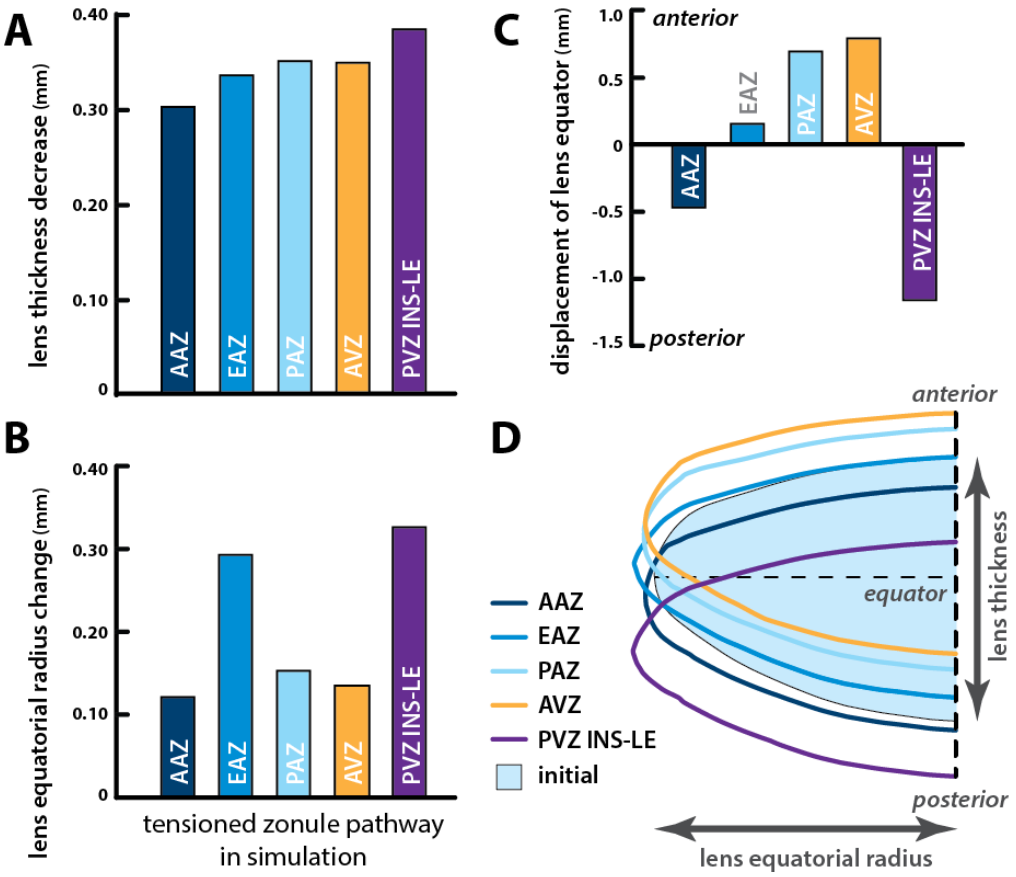

Figure 8.1: Investigation into the contributions of individual zonular divisions. Model simulations were performed in which each zonular division that attached to the lens was tensioned individually to $p_z = 0.4$ while other zonule pathways were passive; the zonule pathways included were the anterior (AAZ), equatorial (EAZ), and posterior (PAZ) portions of the anterior zonules, anterior (AVZ) vitreous zonules, and the posterior vitreous zonule insertion to the lens equator zonules (PVZ INS-LE). Resulting changes in (A) lens thickness, (B) lens equatorial radius, and (C) displacement of the lens equator in the anterior/posterior direction are shown for each case, labeled for the zonular division that was tensioned. (D) The predicted lens shape and position following initialization for each is shown compared to the relaxed lens' initial geometry.

In silico therapies for accommodative dysfunction

Sclera surgeries have the potential to restore accommodative function in older adults by modifying the properties of the aging sclera to improve ciliary muscle mobility (Boote et al. 2020; Hipsley, Hall, and Karolinne M Rocha 2018). Laser Anterior Ciliary Excision (LaserACE) is a procedure using laser ablation of the sclera to alter its biomechanical properties (Ace Vision Group, Silverlake, OH). Measured visual outcomes show that LaserACE is promising for restoring accommodative function to presbyopes (Hipsley et al. 2017; Hipsley, Hall, and Karolinne Maia Rocha 2018), though results are inconsistent. Understanding how this procedure modifies the biomechanics of the accommodative mechanism may help to improve patient outcomes. My model could be used to perform "virtual surgeries" on the eye to understand the biomechanical effects and optimize the procedure for future clinical trials.

LaserACE is performed by using a laser to make excisions in the surface sclera, in a designated treatment area (Hipsley et al. 2017; Hipsley, Hall, and Karolinne Maia Rocha 2018). Treatment areas are chosen to overlap specific zones that are based on ocular anatomic landmarks that are deep to the sclera. The procedure produces regionally inhomogeneous changes in scleral properties, and the shape of the treatment area determines how much of each zone is altered. The changes to the mechanical properties of the treated region depend on the density of excisions (number of micropores per unit of surface area) and the dimension of these pores; the laser can be used to create micropores of different depths and radius (called spot size). Using the model, we could examine how different combinations of affected zones, treatment area shapes, and micropore parameters alter accommodative function.

To represent the varied surgeries, I would change the material parameters in specific regions of the sclera, rather than the whole structure. Various regions could be tested by selecting the sclera elements withing a specific zone or shape. After identifying elements that make up the treatment area, a new Neo-Hookean material would be assigned to this region of the "treated" sclera, with properties that differ from the rest of the sclera structure (i.e., the "untreated" sclera). Due to the dimensions of the micropores

compared to the model it is impractical to incorporate incisions into the model geometry. To determine updated material parameters of the "treated" sclera, micro models of rectangular portions of scleral tissue would be created. These models would have included grids of micropores that vary in density, depth, and spot size. Simulations of prescribed displacement in these micro-models would be used to determine the stress-strain relationship of each combination. Stiffness determined from these simulations would be used to modify the "treated" sclera Neo-Hookean parameters in the FEM of accommodation.

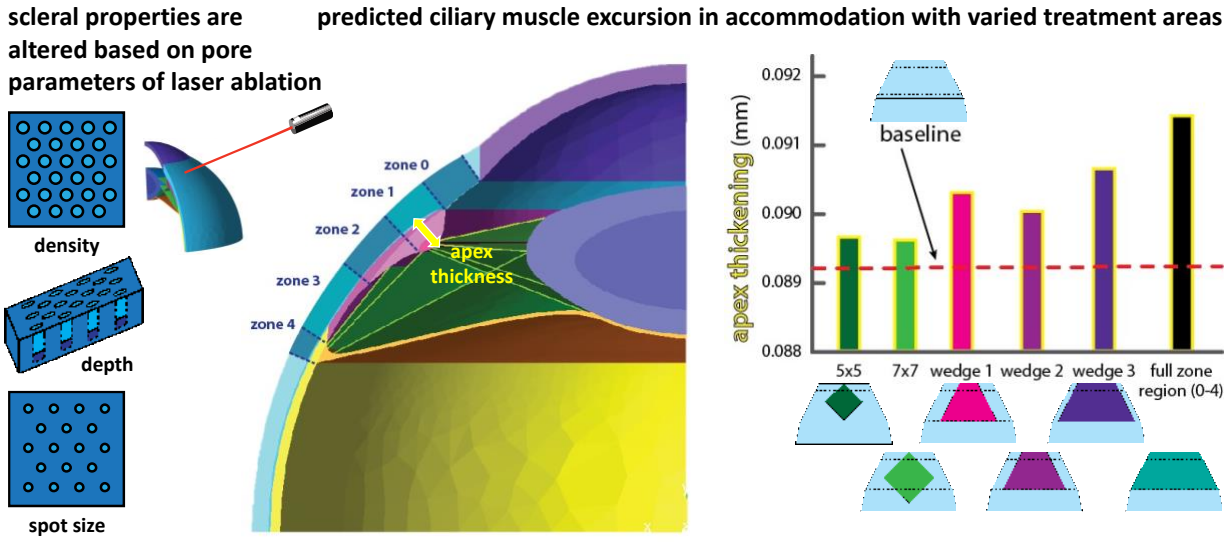

Figure 8.2: *In silico* application of LaserACE scleral surgery. Mechanical properties of the sclera are modified based on the parameters of the laser ablation procedure which can vary in pore density, depth, and spot size. Altered mechanical properties in the treated sclera depends on the treatment area, defined by the shape of the effected surface region and its location with respect to anatomically defined zones. Preliminary results demonstrate that application of "treated" sclera properties to differently shaped treatment areas on the model result in changes to predicted ciliary muscle excursion during accommodation compared to baseline where the entire sclera has "untreated" properties.

Preliminary results demonstrate that altering scleral properties in treatment areas with different sizes and shapes alters ciliary muscle excursion, measured as thickening at the apex. The properties were chosen so that at baseline, the "untreated" sclera had a stiffness comparable to a fifty-year-old and in simulated therapies, the "treated" sclera had a stiffness comparable to a thirty-year-old. Future work is needed to determine how variations affect lens deformation during accommodation. Also, micro model simulations are required to determine how sclera mechanical properties change within the physiologic range of therapy parameters.

The FEM could also be used in future applications to investigate integration of "accommodating" intraocular lenses (IOL) (Wolffsohn and Davies 2019) into the accommodative mechanism. If mechanical properties of novel IOL designs are measured, these could be used to update the model lens to perform simulations to predict deformation in response to ciliary muscle excursion.

8.3.2 Achilles tendon models

I have created FEMs of the Achilles tendon in Chapter 5. These models were specifically designed to investigate the how and aspect of anatomic variation (i.e., twist) influences tendon strain and energy storage, independent of additional variability in geometry or material properties. I describe here some further investigations that could be performed with these same models or with new models representing subject-specific characteristics including unique twist.

Nonuniform initial tension of the Achilles subtendons

As the Achilles tendon is loaded by differing forces from the triceps surae muscles (Arndt et al. 1998) that are applied to the individual subtendons. This loading results in nonuniform tissue displacements within the tendon that have been observed with ultrasound (Franz et al. 2015; Slane and Thelen 2014). Relative sliding of the subtendons is believed to explain these observations and would enable independent modulation of these muscles. Muscle fascicle changes that correspond with displacement of tissue believed to be that muscle's associated subtendon help corroborate this theory

(Clark and Franz 2018). In trying to understand the interactions of the individual muscles and subtendons, assumptions are made about the current stress state of the muscle-tendon unit. The position of the zero-stress state is often assumed to be at the "neutral" ankle angle – In this work we will call this angle 0° as measured between the foot and the horizontal axis, where plantarflexion of the foot results in positive changes in this angle and dorsiflexion results in negative changes, however, this angle has been described by others as 90° measured between the shank and the foot.

Studies with shear wave elastography have been used to measure muscle and tendon stress at different ankle angles. By finding the joint position when stress first develops in the tissue, slack lengths can be identified for muscles and tendons. Interestingly, these measurements did not show that the slack lengths of the triceps surae occur at the "neutral" ankle angle. In fact, the slack lengths of each triceps surae muscle (Hirata et al. 2015) and the Achilles tendon (Hug et al. 2013) all occurred at angles that differed from each other. Only the slack angle of the soleus was close to neutral at -2°, while the medial and lateral gastrocnemius were greater at 20° and 15°, and the Achilles tendon was at 40° ankle plantarflexion (with the knee extended). With inter-muscle and intra-MTU differences in tension within the triceps surae at a given ankle angle, it raises the question of how tension varies between subtendons.

Computational models representing the subtendons of the Achilles tendon are equipped to answer this question. Further, our models could explore the interaction of assumed differences in subtendon tension with differences in anatomy. A modification to the constitutive model for transversely isotropic connective tissues was described in Chapters 1 and 2. Using this formula, a pretension can be applied during an activation period in the model initialization. The second period would simulate prescribed loading of the subtendons to match in vivo measurements of displacement, and differences in subtendon strain could be determined. As *in vivo* tension of individual subtendons is currently unmeasured, modeling allows to estimate what these effects might be.

In a preliminary study, estimated potential subtendon slack angles by scaling the measured Achilles tendon slack angle (Hug et al. 2013) according to the differences in triceps surae slack angles

(Hirata et al. 2015). We used these estimates to prescribe pre-tension to initialize a subject-specific model of Achilles subtendons (Handsfield, Inouye, et al. 2017) before applying boundary conditions to reproduce measured displacement patterns. Simulations with pre-tension predicted more uniform displacements and decreased strain in all subtendons compared to simulations without pre-tension when boundary conditions were unchanged. If boundary conditions in pretension simulations were adjusted to produce similar displacements, then strain in the medial and lateral gastrocnemius increased dramatically.

Future work could be done to see how these results co-vary with twist. Twist led to large differences in strain particularly in the medial gastrocnemius tendon, and differences in pretension would exacerbate those differences. This insight could be especially important in the context of Achilles tendon repair. We suggested earlier that the amount of twist preserved or incorporated during surgery might play a role in recovery and mechanics. Tension as it relates to joint position may also be a factor in determining patient outcomes.

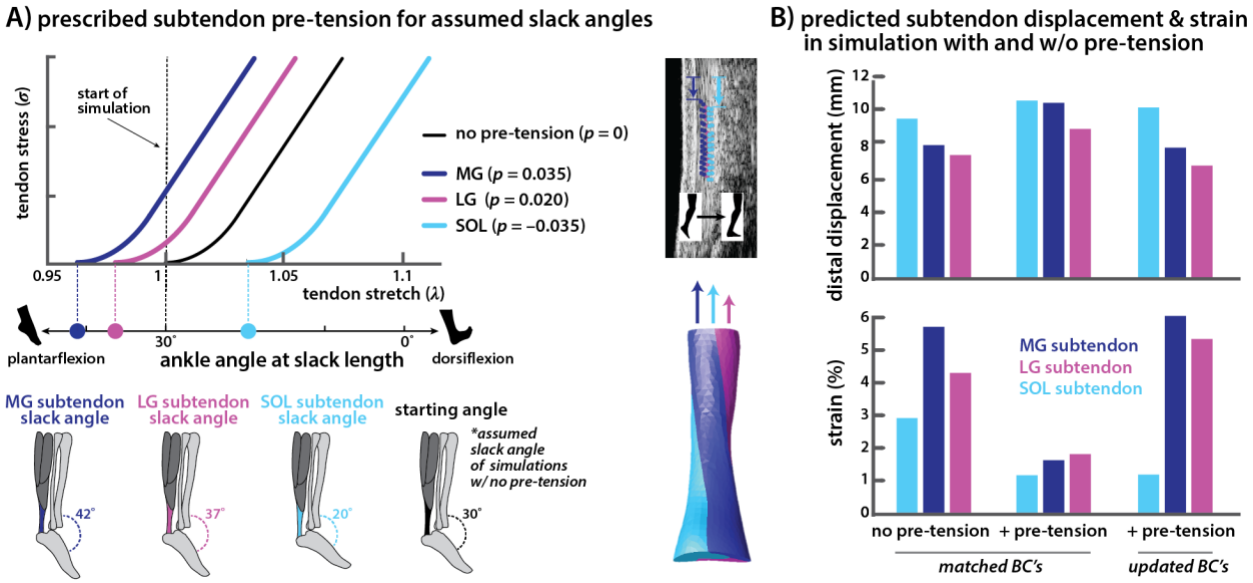

Figure 8.3: Simulated pre-tensioning of Achilles subtendons. A) Pre-tension was prescribed during model initialization based on estimated slack angle of each subtendon. The starting angle, determined from images used to create the FEM was set to a stretch value of one. Subtendon tension was prescribed based on how much the assumed slack angle varied from the starting angle. **B)** Boundary conditions (BC) were prescribed to match model-predicted tissue displacements to *in vivo* measurements. Strains and displacements simulations with no pre-tension were compared to simulations with pre-tension and the same boundary conditions (BC's) or boundary conditions that were updated to better match displacements.

Variations in subtendon sliding

Nonuniform differential tissue displacements observed with ultrasound (Arndt et al. 2012; Clark and Franz 2018; Franz et al. 2015; Slane and Thelen 2014) are believed to be the result of inter-subtendon sliding within the Achilles tendon. Tendon fascicle sliding has been demonstrated in the energy storing tendons of horses (Thorpe et al. 2015). Equine studies also show that this capacity for sliding is reduced with age (Chavaunne T. Thorpe et al. 2013). Assuming the same is true for the human Achilles tendon helps to explain altered tissue displacements in older adults (Clark and Franz 2020; Franz and Thelen 2015; Slane and Thelen 2015). Changes in tendon tissue displacements corresponded with age-related reductions in plantarflexor performance (Franz and Thelen 2015).

Computational modeling can help to elucidate how changes in subtendon sliding might contribute to age-related functional deficits. Simulations of Achilles subtendon loading predicted significant differences in differential displacement if the subtendons are allowed to slide with frictionless contact at their boundaries, compared to when their surfaces are tied (Handsfield, Inouye, et al. 2017). These boundary conditions present the most extreme cases of possible interaction between subtendon. It is more likely that *in vivo* these tissues slide with some resistance in young adults and that this resistance increases to progressively reduce sliding. Model simulations that utilize more complex boundary conditions could be used to study how this continuum of sliding behavior alters tissue displacements. Further, these conditions could be applied to the models with different geometries to see how subtendon sliding and twist interact.

8.3.3 Soleus model

Modeling the soleus muscle became a major focus of this dissertation as investigations into the triceps surae group revealed how complex this important muscle really is and how little we understand about it. In Chapter 6, I have described the soleus FEM and how model predictions were compared to *in vivo* measurements of passive and active soleus lengthening. I further described our investigations into the material properties and morphology of this muscle's unique aponeuroses. We still have much to learn

about this incredible muscle and this model can facilitate further inquiries. In the following sections I discuss a few ideas for ways this model can be used to advance our understanding of soleus function and investigate the three-dimensional nature of skeletal muscle contraction.

Influence of anterior fascicle contraction on posterior fascicle behavior in the soleus

The soleus muscle has a complex 3D morphology with fascicles arranged into multiple compartments with different architecture and innervation (Agur et al. 2003; Bolsterlee et al. 2018). The unipennate posterior compartment wraps around the deeper bipennate anterior compartment. Fascicles from both compartments originate on opposite sides of the broad anterior aponeurosis, separating them within the soleus volume.

Soleus muscle behavior is often measured *in vivo* using ultrasound and electromyography (EMG) to better understand its important function (Krupenevich et al. 2020; Lai et al. 2015; Nuckols et al. 2020; Rubenson et al. 2012). Ultrasound is used to track fascicles in a region of interest in the superficial portion of the muscle while EMG is used to estimate activation from measurements on the calf surface. These measurements are insightful but limited. Only the posterior compartment is accessible from the surface, so these non-invasive measurements are unable to capture fascicle kinematics and activation of the deep anterior compartment. The ultrasound region of interest only includes a small superficial portion of the muscle volume often limiting measurements to that of a single fascicle. Further, these images provided a 2D view of a 3D structure that is subjective to the position and orientation of the ultrasound probe (Bolsterlee, Gandevia, and Herbert 2016) and are unable to fully capture the posterior compartment.

These issues raise the question as to if contraction of the anterior compartment of the soleus influences behavior of fascicles in the posterior compartment. In order to answer this question, we used soleus FEM to simulate varied activation in the anterior and posterior compartments during soleus muscle lengthening to explore how these portions of the muscle interact.

In these simulations, the posterior soleus compartment was either passive (α = 0%) or activated (α = 75%). In each of these conditions, the activation of the anterior soleus compartment was varied (α = 100%, 75%, 50%, 25%, 0%). Activation of the muscle sections was ramped to its assigned level during a model initialization period. Then soleus lengthening in ankle dorsiflexion was simulated as described in in Chapter 6, where the posterior distal end was displaced by 20 mm, at the Achilles muscle-tendon junction (MTJ), while attachments of the anterior aponeurosis to the tibia and fibula were fixed. Muscle force was measured at the MTJ. Fascicle strains were determined from the change in length that occurred during the muscle lengthening period using the length after activation as the initial length.

Posterior soleus fascicle strains determined during muscle lengthening (Figure 7.4B) are similar with the posterior soleus passive (α = 0%) and active (α = 75%). With a passive posterior soleus, varying anterior soleus activation changes posterior soleus fascicle lengths at the start of muscle lengthening, but has a lesser effect on posterior soleus fascicle length change. With an active posterior soleus, varying anterior soleus activation has a low effect on starting posterior soleus fascicle lengths, but creates larger differences in posterior soleus fascicle length changes. There are greater differences in anterior soleus fascicle strains with varied anterior soleus activation. Differences in anterior soleus strains arise due to shorter fascicles lengths associated with activation prior to muscle stretch. With the posterior soleus active (α = 75%) there are greater differences between average strain in the posterior soleus and anterior soleus than when the posterior soleus is passive (α = 0%), regardless of the anterior soleus activation. Differences in activations also led to differences in muscle force during lengthening (Figure 7.4C).

These results suggest activation of the soleus' anterior compartment does not influence the posterior compartment's fascicle behavior. However, only measuring the superficial soleus (i.e., with EMG and ultrasound) would not provide insight into the activation state or fascicle kinematics of the anterior compartment. Metrics of soleus mechanical behavior, i.e., muscle stiffness calculated using force and posterior compartment fascicle length changes (Clark and Franz 2019; Krupenevich et al. 2020), during muscle lengthening are dependent on the activation state of the anterior compartment. These

model predictions help illuminate the relationship between the anterior and posterior compartments of the soleus which is currently unmeasurable.

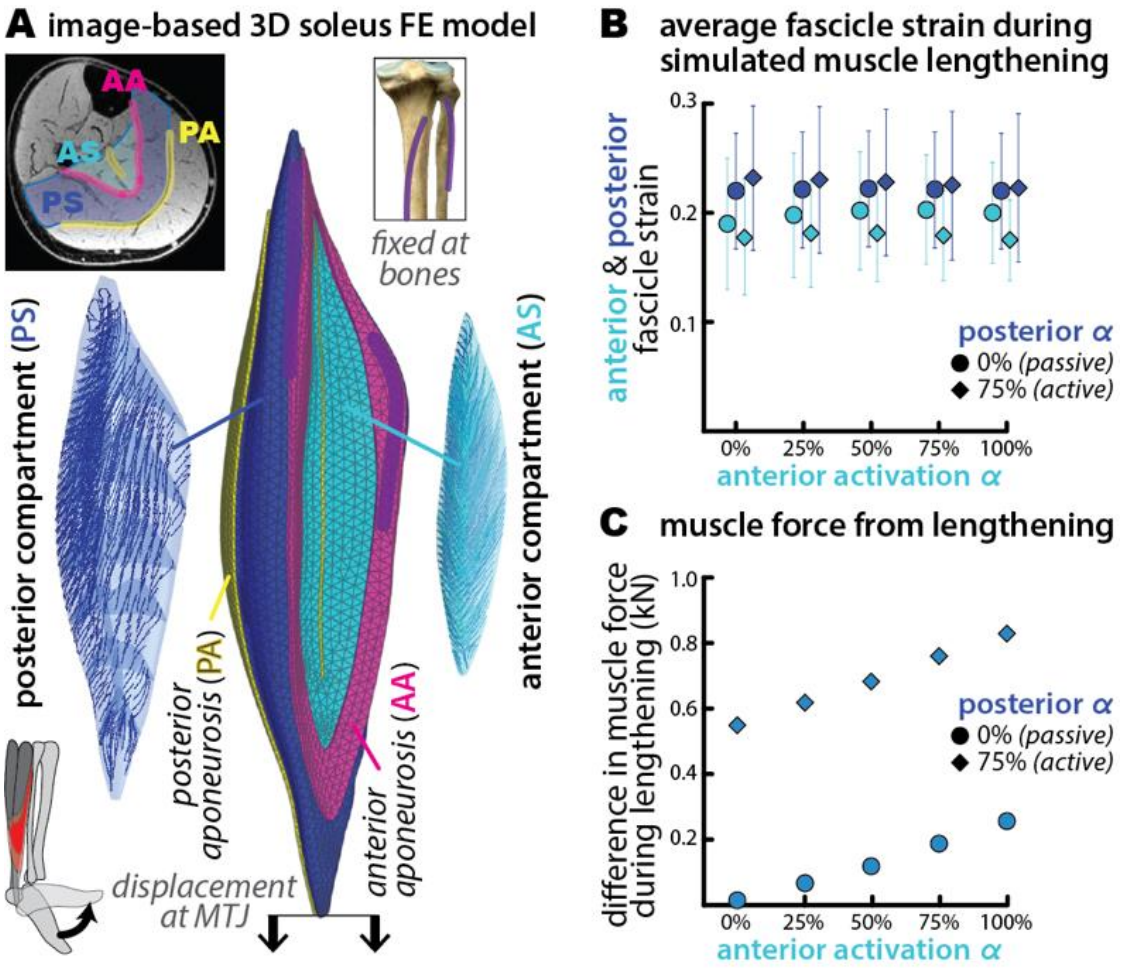

Figure 8.4: Variations in the activations of the soleus anterior and posterior compartments. A) The image-based 3D soleus finite element (FE) model was used to simulate muscle lengthening following model initialization with different activations (α) in the anterior (AS) and posterior (PS) compartments of the soleus. **B)** Average fascicle strains were calculated during muscle lengthening. **C)** The change in muscle force from start to end of lengthening is shown as the difference compared to force when the soleus is entirely passive.

Simulating soleus muscle function in different conditions

So far, we have used this model to investigate deformation of the soleus muscle in relatively simple loading conditions. We have simulated muscle lengthening by displacing the distal soleus MTJ purely in the distal direction in our 3D reference frame. This displacement was applied as a linear ramped increase during the simulations, and fascicle architecture was primarily compared between the start and end lengths. The activation conditions were also simplified to be linearly ramped to prescribed values. Experiments have attempted to characterize *in vivo* muscle function in more complex conditions especially those with physiologic relevance like walking and running (Clark et al. 2020; Lai et al. 2015; Rubenson et al. 2012). Musculoskeletal modeling (i.e., "lumped" parameter modeling) has been applied to understand soleus muscle interactions in these conditions. MSK simulations can be used to define boundary conditions in FE muscle modeling in order to simulate more complex kinematics and activation patterns (Fiorentino et al. 2014; Fiorentino and Blemker 2014). Simulations of MSK modeling-based boundary conditions could be used in combination with the soleus FEM to better understand soleus dynamic function in these applications.

Comparison of 3D soleus model predictions to ultrasound measurements

We have compared our model predictions to measurements of soleus tissue displacements and architecture changes made with different magnetic resonance imaging (MRI) techniques. While these imaging methods provide a comprehensive view into 3D soleus deformation they are limited in several ways. Diffusion tensor imaging generates data to reconstruct muscle fascicle architecture at different joint positions (Bolsterlee et al. 2017, 2018, 2019). While this provides information to estimate quasi-static changes in fascicle architecture with joint and muscle movement, it is unable to track tissue through these motions. Cine DENSE (Displacement Encoding with Stimulated Echoes) MRI enables dynamic tracking of *in vivo* tissue motion, however observable muscle conditions are constrained. We used a method that was adapted from a previous study of hamstring strain injury (Fiorentino et al. 2014, 2012). Subjects used a nonferrous exercise device to elicit active soleus lengthening while the moving their ankle in the bounds

of the MRI machine. Because the machine's imaging space is restricted in size and requires subjects to be reclined, MRI is unable to provide muscle tissue measurements during physiologic movements like walking and running.

Ultrasound imaging is much more accessible and allows for imaging of more dynamic muscle conditions, including walking and running (Clark et al. 2020; Lai et al. 2015; Rubenson et al. 2012). It can also be used in combination with motion capture and force plate or dynamometry measurements in order to relate muscle behavior to joint kinematics and kinetics (Clark et al. 2020; Krupenevich et al. 2020; Lai et al. 2015; Rubenson et al. 2012). I discussed the shortcomings of muscle measurements made with ultrasound in the previous section. Despite these drawbacks it is currently our best option for visualizing *in vivo* muscle function. This is especially true in the case of the soleus. Comparative biology facilitates more invasive observation of dynamic muscle behavior (e.g., sonomicrometry) in different animals that can then be related back to human function. However, there are not current measurements in any animal model with equivalent soleus function or morphology that provides an alternative for comparison.

The soleus FEM presented in this dissertation can be used to better understand existing non-invasive measurements of human soleus function, specifically those made with ultrasound. Model simulations can be altered to represent the conditions of ultrasound experiments (see previous section). Using the model, we can compare the measurements made with ultrasound to predicted fascicle kinematics. With the model, we have the capability to select a region of interest in the model that corresponds with the region of the ultrasound probe window (Williams et al., 2020 *American Society of Biomechanics Meeting*). We can compare fascicle lengths in this region in both 3D and projected in 2D provide more context to ultrasound measurements. By matching simulation predictions to fascicle kinematics measured in a specific region, we can analyze the rest of the model to see how fascicle changes vary spatially. These comparisons will enable us to extrapolate from *in vivo* ultrasound measurements, to predict behavior in the regions of the soleus that are not visible, such as near the

muscle-tendon junctions and in the anterior compartment. Using the model in combination with ultrasound improves our ability to assess soleus changes in the context of ankle function which is critical for investigating gait alterations that result from aging or using wearable devices.

Investigating variable muscle gearing and aponeurosis stiffness

The soleus FEM could also be used to explore mechanisms of phenomena described in 3D muscle shape change. Architectural gear ratio is the relationship between muscle belly length change and muscle fiber or fascicle length change during contraction. AGR decreases in both concentric (Azizi, Brainerd, and Roberts 2008) and eccentric (Azizi and Roberts 2014) contraction with increasing muscle force, demonstrating that muscle gearing is variable depending on the loading conditions. This variability allows muscle to make tradeoffs in order to favor force or velocity in different conditions. Variable gearing is believed to be modulated by muscle 3D shape change but the mechanics of this process are not well understood (Roberts et al. 2019). By simulating isotonic contractions, we could use the FEM to help answer questions about the mechanics of variable gearing as well as quantify AGR in the soleus compartments to see if they different in different loading conditions.

These simulations could also be used to further explore the aponeuroses and understand their role in muscle gearing. Aponeurosis deformation has been found to vary in the same conditions that alter AGR (Arellano et al. 2016). Also in experiments where transverse properties were altered, aponeuroses were shown to directly influence the gearing and force production of the muscle (Eng and Roberts 2018). Aponeuroses have been described to exhibit variable stiffness in different muscle force and length conditions, based on *in situ* and *in vivo* measurements (Azizi and Roberts 2009; Raiteri, Cresswell, and Lichtwark 2018). FE simulations could elucidate how relationships between nonlinear aponeurosis properties, variable muscle loading conditions, and dynamic shape change all interact within the soleus. This may provide further insight into age-related muscle dysfunction, as both variable muscle gearing and transverse aponeurosis properties have been shown to differ between young and older animals (Holt et al. 2016).

8.4 Future Work

By creating models of complex muscle-connective tissue systems. We are able to "connect the dots" of the vast literature describing morphology, tissue material properties, and movement. In connecting these dots by recreating the different components of the systems' biomechanics, we often encountered significant gaps that were not previously apparent. This section discusses some ideas for future work to fill some of the gaps in our knowledge of the form and function of muscle and connective tissue that were revealed by the work in this dissertation.

Simple models of soleus architecture to further explore form and function relationships

The soleus morphology is very complex compared other muscles in the lower limb. In trying to model it, we kept asking why it might be structured the way it is. These questions inspired many of the investigations that were previous described, as we inquired into the influence of its aponeuroses and compartments. Another approach to delve into the structure-function relationships of this muscle might be to create additional FEM with simpler 3D geometry. In early attempts to build a 3D model of the soleus, I created two geometries with the same shape and volume. The first was similar to soleus morphology and had an internal anterior aponeurosis that separated the muscle belly into compartments. The second had an external anterior aponeurosis and no median septum, resulting in a unipennate architecture that was similar to the medial gastrocnemius. I created fascicle tracts with similar pennation angles in each of these models and found that their lengths varied dramatically. In the posterior compartment of the model with an internal aponeurosis, fascicle lengths were significantly shorter and more uniform in length compared to the model with and external aponeurosis (Figure 7.5A). The physiological cross-sectional area (PCSA), calculated as average fascicle length divided by volume, was far greater with the internal aponeurosis. Although the soleus morphology seems complicated to us, it is likely the most economical way to increase its PCSA per its volume and therefor optimize force production in the distal leg without increasing mass.

I have envisioned a further "simple" modeling study to look more at how compartmental structure utilizes relationships between muscle fascicle lengths, volumes, and force production. Brian Jones has developed a soleus FEM with architecture that is much closer to the idealized architecture assumed in lumped parameter models (Jones et al., 2018, American Society of Biomechanics Meeting). Using a geometry similar to his models, I would create additional versions of the FEM that adds an internal aponeurosis to create two compartments, and a version with only the posterior compartment (Figure 7.5 B). These models could be used to simulate lengthening at different activation levels (described previously) in order to compare force production to muscle architecture. These models would allow for further inquiry into the structure-function of the soleus and expand our understanding of why muscles are arranged the way that they are.

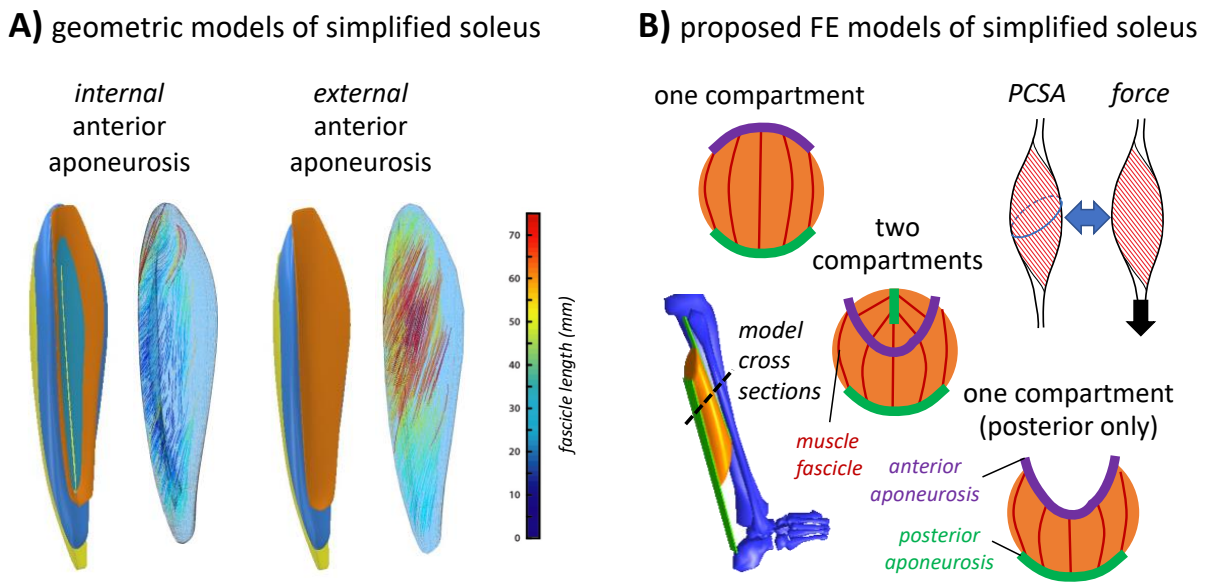

Figure 8.5: Simple models of the soleus muscle. A) Geometric models have the same volume and shape but different anterior aponeuroses. The model with an internal aponeurosis also included a median septum. Fascicles in the posterior compartment and muscle belly, respectively, of the two models are colored according to their length. **B)** The first two proposed simplified FE models would have the same shape and volume with different anterior aponeuroses. The anterior compartment volume would be removed from the second model to create the third. PCSA would be calculated for each geometry and compared to forces predicted in simulations.

Use of diffusion tensor imaging to improve FE simulations of complex muscle

A significant challenge of modeling complex muscles is first creating the model geometry and architecture. The next challenge is verifying that the model is accurately representing physiologic architecture and shape change. For the soleus model, I compared model fascicle tracts to soleus fascicles reconstructed from diffusion tensor imaging (DTI) in a previous study in the literature (Bolsterlee et al. 2018). DTI provides information about the fiber direction in the tissue volume and these data are used to construct architecture (Bolsterlee et al. 2017) with a method similar to how model architecture was reconstructed from computational fluid dynamics (CFD) simulations. A more direct comparison would therefore be between the spatially distributed vectors from the DTI and Laplacian flow results (Handsfield, Bolsterlee, et al. 2017). DTI of the same subject that was statically imaged to create model geometry might be used to directly map fiber directions to the model, replacing the need for the CFD method to determine fiber directions. DTI is subject to imaging noise especially near the muscle boundaries so it may not be possible to determine an accurate fiber direction for all model elements. Alternatively, DTI could be used in combination with CFD to determine model fiber directions. Tractography methods to reconstruct fascicles could use vectors fields from both DTI and CFD. DTI vectors could also be incorporated into CFD simulations as boundary conditions to direct flow, similar to how flow guides have been implemented in these simulations. Future work utilizing DTI has the potential to improve the development and verification of finite element models of muscle.

Experiments to characterize the mechanical properties of aponeuroses

Creating the soleus model illuminated how little is known about the mechanical properties of aponeuroses, especially in living humans. I compared the tuned properties in the soleus model to measurements made in aponeurosis tissue from elderly human cadavers (Shan et al. 2019), previously frozen turkeys (Azizi et al. 2009) and fresh rats (Holt et al. 2016). I also looked at estimates of *in vivo* stiffness determined from ultrasound and dynamometry methods (Magnusson et al. 2001); however this approach relies on the assumptions of lumped parameter models that may be ineffective at representing

the soleus. Future experiments that test biaxial properties of human aponeuroses in samples from younger adults would be a great asset to the biomechanics literature and improve 3D models of muscles. Further, no study has compared the properties of aponeuroses where muscle fascicles insert on a single side, like the soleus' posterior aponeurosis or the medial gastrocnemius' distal aponeurosis, to aponeuroses with fascicle insertions on both sides, like the soleus' anterior aponeurosis or tibialis anterior's central tendon. These differences in fascicle attachments likely lead to different in biaxially loading. These aponeuroses may adapt to the differences in loading patterns with differences in their collagen fiber arrangement. Experiments using animal models could be conducted to characterize the material properties of internal and external aponeuroses.

Combining Achilles tendon and soleus models into FEM of the entire triceps surae group

I have presented models here that explore the complexities of both the Achilles tendon and the soleus muscle. An exciting area for future work would be combining representations of these components with that of the gastrocnemius to create a multipart model of the triceps surae group. This model could expand on the work presented in this dissertation by examining the behaviors described here in the context of this complex muscle-tendon-unit. This full triceps surae model could help to answer further questions about the relative function of these different muscles and address how age-related tendon changes would impact the muscles.

Progressive changes with increasing age

The work presented in this dissertation was aimed to better understand what we defined as healthy muscle function which we assumed to apply to young adults in general. While there are clear differences in between people classified as "young" and "old", the age ranges that are appropriate for each group vary by circumstance. In age-related investigations of ambulatory function, "old" subjects are typically in their sixties or seventies, but investigations of the eye use younger "old" subjects as symptoms of presbyopia manifest when patients are in their fifties and even forties. In studying aging, there is an advantage to choosing subjects on the far ends of the spectrum to increase the possibility of

finding significant differences. While this approach improves statistical power, it leaves gaps in our knowledge of how function changes over time. In our own measurements of muscle volumes and tendon CSAs compared to age in Chapter 5, there are literal gaps in or data as we did not study individuals classified as "middle-aged". Without these measurements, we cannot conclude how muscles and tendons change over the decades; they could vary progressively over time or abruptly shift. All we know is that they are different by "old" age. Future work is needed in the study of aging to continue to characterize muscle and connective tissue anatomy, material properties, and function in people of different ages. The models presented in this work can help illuminate how changes in tissue structure may contribute to functional changes but rely on accurate characterization of how tissues change and at what time points to provide physiologically relevant predictions of age-related dysfunction.

Population disparities in age-related muscle dysfunction

A major assumption in this dissertation is that aging is a condition that affects all humans. While I believe that assumption is true in some ways there are many characteristics of humans besides age that might differentiate their biomechanics, including race, sex, disability, diet, socioeconomic status, and exercise habits. We have addressed aspects of human variability in the studies presented here, such as variations in anatomy and material property measurements. This variability was not compared to specific demographics beyond age. Nor were models designed to specifically represent a particular population. However, anatomical and material property data used to build the models either came from specific subjects (the soleus model was based on MR images of a white male) or from studies that either had relatively homogenous subject groups or did not report demographic information. In cases where these data are not available, we might guess that women and people of color were underrepresented as has been demonstrated throughout biological and medical literature. Though some studies have shown that specific mechanical changes with age may also vary with race (Grytz et al. 2014), most work into age-related biomechanical disparities associated with race have highlighted dysfunction that can be attributed to

differences in access to care (Allman et al. 2004; McCleary et al. 2014). Future work is needed to understand how the effects of age might vary across diverse groups.

8.5 Final Remarks

We use our muscles for many things and often do not recognize how wonderful their function is until we experience limits of that function. These limits are often met simply by the passing of time. As we push the boundaries of human health, the need will grow to stall the effects of age. To do this will require deeper inquiries into our own physiology. This pursuit has inspired the work in this dissertation.

George E.P. Box famously said: “All models are wrong, but some models are useful.” This quote has been shared in nearly every graduate course I have taken at UVA. While I recognize that the models I presented here are ‘wrong’ in many ways, I hope that their utility outweighs their shortcomings. These models have helped us to better understand the form and function relationships that govern the interactions of complex muscles and connective tissues. While I believe this work has raised as many (if not more) questions as it has answered, identifying these next questions moves us closer to being able to treat or prevent the muscle dysfunction that has been associated with aging.

"I'll say this to you, my friend, with all the love in my heart and all the wisdom of the universe. Take it sleazy."

– Michael, *The Good Place*

References

Abolmaali, A., R. A. Schachar, and T. Le. 2007. "Sensitivity Study of Human Crystalline Lens Accommodation." *Computer Methods and Programs in Biomedicine* 85(1):77–90.

Agur, Anne M., Victor Ng-Thow-Hing, Kevin A. Ball, Eugene Fiume, and Nancy Hunt McKee. 2003. "Documentation and Three-Dimensional Modelling of Human Soleus Muscle Architecture." *Clinical Anatomy* 16(4):285–93.

Albracht, K., A. Arampatzis, and V. Baltzopoulos. 2008. "Assessment of Muscle Volume and Physiological Cross-Sectional Area of the Human Triceps Surae Muscle in Vivo." *Journal of Biomechanics* 41(10):2211–18.

Aletras, Anthony H., Shujun Ding, Robert S. Balaban, and Han Wen. 1999. "DENSE: Displacement Encoding with Stimulated Echoes in Cardiac Functional MRI." *Journal of Magnetic Resonance* 137(1):247–52.

Alexander, R. Mc Neill. 2002. "Tendon Elasticity and Muscle Function." Pp. 1001–11 in *Comparative Biochemistry and Physiology - A Molecular and Integrative Physiology*. Vol. 133.

Allman, Richard M., Patricia Sawyer Baker, Richard M. Maisiak, Richard V. Sims, and Jeffrey M. Roseman. 2004. "Racial Similarities and Differences in Predictors of Mobility Change over Eighteen Months." *Journal of General Internal Medicine* 19(11):1118–26.

van Alphen, G. W. H. M., and W. P. Graebel. 1991. "Elasticity of Tissues Involved in Accommodation." *Vision Research* 31(7–8):1417–38.

An, K. N., K. Takahashi, T. P. Harrigan, and E. Y. Chao. 1984. "Determination of Muscle Orientations and Moment Arms." *Journal of Biomechanical Engineering* 106(3):280.

Anderson, Frank C., and Marcus G. Pandy. 2003. "Individual Muscle Contributions to Support in Normal Walking." *Gait and Posture* 17(2):159–69.

Arampatzis, Adamantios, Kiros Karamanidis, Gaspar Morey-Klapsing, Gianpiero De Monte, and Savvas Stafilidis. 2007. "Mechanical Properties of the Triceps Surae Tendon and Aponeurosis in Relation to Intensity of Sport Activity." *Journal of Biomechanics* 40(9):1946–52.

Arellano, Christopher J., Nicholas J. Gidmark, Nicolai Konow, Emanuel Azizi, and Thomas J. Roberts. 2016. "Determinants of Aponeurosis Shape Change during Muscle Contraction." *Journal of Biomechanics* 49(9):1812–17.

Arndt, A. N., P. V. Komi, G. P. Brüggemann, and J. Lukkariniemi. 1998. "Individual Muscle Contributions to the in Vivo Achilles Tendon Force." *Clinical Biomechanics* 13(7):532–41.

Arndt, Anton, Ann Sophie Bengtsson, Michael Peolsson, Alf Thorstensson, and Tomas Movin. 2012. "Non-Uniform Displacement within the Achilles Tendon during Passive Ankle Joint Motion." *Knee Surgery, Sports Traumatology, Arthroscopy* 20(9):1868–74.

Azizi, Emanuel, Elizabeth L. Brainerd, and Thomas J. Roberts. 2008. "Variable Gearing in Pennate Muscles." *Proceedings of the National Academy of Sciences* 105(5):1745–50.

Azizi, Emanuel, Gregory M. Halenda, and Thomas J. Roberts. 2009. "Mechanical Properties of the Gastrocnemius Aponeurosis in Wild Turkeys." *Integrative and Comparative Biology* 49(1):51–58.

Azizi, Emanuel, and Thomas J. Roberts. 2009. "Biaxial Strain and Variable Stiffness in Aponeuroses." *The Journal of Physiology* 587(Pt 17):4309–18.

Azizi, Emanuel, and Thomas J. Roberts. 2014. "Geared up to Stretch: Pennate Muscle Behavior during

Active Lengthening." *Journal of Experimental Biology* 217(3):376–81.

Barraquer, Rafael I., Ralph Michael, Rodrigo Abreu, Jose´ Lamarca, and Francisco Tresserra. 2006. "Human Lens Capsule Thickness as a Function of Age and Location along the Sagittal Lens Perimeter." *Investigative Opthalmology & Visual Science* 47(5):2053.

Baxter, Josh R., and Stephen J. Piazza. 2014. "Plantar Flexor Moment Arm and Muscle Volume Predict Torque-Generating Capacity in Young Men." *Journal of Applied Physiology* 116(5):538–44.

Baxter, Josh R., and Stephen J. Piazza. 2018. "Plantarflexor Moment Arms Estimated from Tendon Excursion in Vivo Are Not Strongly Correlated with Geometric Measurements." *Journal of Biomechanics* 77:201–5.

Blemker, Silvia S., and Scott L. Delp. 2005. "Three-Dimensional Representation of Complex Muscle Architectures and Geometries." *Annals of Biomedical Engineering* 33(5):661–73.

Blemker, Silvia S., and Scott L. Delp. 2006. "Rectus Femoris and Vastus Intermedius Fiber Excursions Predicted by Three-Dimensional Muscle Models." *Journal of Biomechanics* 39(8):1383–91.

Blemker, Silvia S., Peter M. Pinsky, and Scott L. Delp. 2005. "A 3D Model of Muscle Reveals the Causes of Nonuniform Strains in the Biceps Brachii." *Journal of Biomechanics* 38(4):657–65.

Bohm, Sebastian, Falk Mersmann, and Adamantios Arampatzis. 2015. "Human Tendon Adaptation in Response to Mechanical Loading: A Systematic Review and Meta-Analysis of Exercise Intervention Studies on Healthy Adults." *Sports Medicine - Open* 1(1):7.

Bolsterlee, Bart, Arkiev D'Souza, Simon C. Gandevia, and Robert D. Herbert. 2017. "How Does Passive Lengthening Change the Architecture of the Human Medial Gastrocnemius Muscle?" *Journal of Applied Physiology* 122(4):727–38.

Bolsterlee, Bart, Arkiev D'Souza, and Robert D. Herbert. 2019. "Reliability and Robustness of Muscle Architecture Measurements Obtained Using Diffusion Tensor Imaging with Anatomically Constrained Tractography." *Journal of Biomechanics* 86:71–78.

Bolsterlee, Bart, Taija Finni, Arkiev D'Souza, Junya Eguchi, Elizabeth C. Clarke, and Robert D. Herbert. 2018. "Three-Dimensional Architecture of the Whole Human Soleus Muscle *in Vivo*." *PeerJ* 6:e4610.

Bolsterlee, Bart, Simon C. Gandevia, and Robert D. Herbert. 2016. "Ultrasound Imaging of the Human Medial Gastrocnemius Muscle: How to Orient the Transducer so That Muscle Fascicles Lie in the Image Plane." *Journal of Biomechanics* 49(7):1002–8.

Boote, Craig, Ian A. Sigal, Rafael Grytz, Yi Hua, Thao D. Nguyen, and Michael J. A. Girard. 2020. "Scleral Structure and Biomechanics." *Progress in Retinal and Eye Research* 74:100773.

Boyer, Katherine A., Russell T. Johnson, Jacob J. Banks, Carl Jewell, and Jocelyn F. Hafer. 2017. "Systematic Review and Meta-Analysis of Gait Mechanics in Young and Older Adults." *Experimental Gerontology* 95:63–70.

Brooks, S. V, and J. A. Faulkner. 1994. "Skeletal Muscle Weakness in Old Age: Underlying Mechanisms." *Medicine and Science in Sports and Exercise* 26(4):432–39.

Brown, N. 1973. "The Change in Shape and Internal Form of the Lens of the Eye on Accommodation." *Experimental Eye Research* 15(4):441–59.

Burd, H. J., S. J. Judge, and J. A. Cross. 2002. "Numerical Modelling of the Accommodating Lens." *Vision Research* 42(18):2235–51.

Clark, William H., and Jason R. Franz. 2018. "Do Triceps Surae Muscle Dynamics Govern Non-Uniform Achilles Tendon Deformations?" *PeerJ* 2018(7).

Clark, William H., and Jason R. Franz. 2019. “Activation-Dependent Changes in Soleus Length-Tension Behavior Augment Ankle Joint Quasi-Stiffness.” *Journal of Applied Biomechanics* 35(3):182–89.

Clark, William H., and Jason R. Franz. 2020. “Triceps Surae Muscle–Subtendon Interaction Differs between Young and Older Adults.” *Connective Tissue Research* 61(1):104–13.

Clark, William H., Richard E. Pimentel, and Jason R. Franz. 2020. “Imaging and Simulation of Inter-Muscular Differences in Triceps Surae Contributions to Forward Propulsion During Walking.” *Annals of Biomedical Engineering* 1–13.

Criscione, John C., Andrew S. Douglas, and William C. Hunter. 2001. “Physically Based Strain Invariant Set for Materials Exhibiting Transversely Isotropic Behavior.” *Journal of the Mechanics and Physics of Solids* 49(4):871–97.

Croft, Mary Ann, A. Glasser, and P. L. Kaufman. 2001. “Accommodation and Presbyopia.” *International Ophthalmology Clinics* 41(2):33–46.

Croft, Mary Ann, Gregg Heatley, Jared P. McDonald, Alexander Katz, and Paul L. Kaufman. 2016. “Accommodative Movements of the Lens/Capsule and the Strand That Extends between the Posterior Vitreous Zonule Insertion Zone & the Lens Equator, in Relation to the Vitreous Face and Aging.” *Ophthalmic and Physiological Optics* 36(1):21–32.

Croft, Mary Ann, and Paul L. Kaufman. 2006. “Accommodation and Presbyopia: The Ciliary Neuromuscular View.” *Ophthalmology Clinics of North America* 19(1):13–24, v.

Croft, Mary Ann, Elke Lütjen-Drecoll, and Paul L. Kaufman. 2017. “Age-Related Posterior Ciliary Muscle Restriction – A Link between Trabecular Meshwork and Optic Nerve Head Pathophysiology.” *Experimental Eye Research* 158:187–89.

Croft, Mary Ann, Jared P. McDonald, Alexander Katz, Ting-Li Lin, Elke Lütjen-Drecoll, and Paul L. Kaufman. 2013. “Extralenticular and Lenticular Aspects of Accommodation and Presbyopia in Human Versus Monkey Eyes.” *Investigative Ophthalmology & Visual Science* 54(7):5035–48.

Croft, Mary Ann, T. Michael Nork, Jared P. McDonald, Alexander Katz, Elke Lütjen-Drecoll, and Paul L. Kaufman. 2013. “Accommodative Movements of the Vitreous Membrane, Choroid, and Sclera in Young and Presbyopic Human and Nonhuman Primate Eyes.” *Investigative Ophthalmology & Visual Science* 54(7):5049–58.

Cronin, Neil J., Janne Avela, Taija Finni, and Jussi Peltonen. 2013. “Differences in Contractile Behaviour between the Soleus and Medial Gastrocnemius Muscles during Human Walking.” *Journal of Experimental Biology* 216(5):909–14.

Cummins, E. J., and B. J. Anson. 1946. “The Structure of the Calcaneal Tendon (of Achilles) in Relation to Orthopedic Surgery, with Additional Observations on the Plantaris Muscle.” *Surgery, Gynecology & Obstetrics* 83:107–16.

Dalmau-Pastor, Miquel, Betlem Fargues-Polo, Daniel Casanova-Martínez, Jordi Vega, and Pau Golanó. 2014. “Anatomy of the Triceps Surae.” *Foot and Ankle Clinics* 19(4):603–35.

Dean, Mason N., Emanuel Azizi, and Adam P. Summers. 2007. “Uniform Strain in Broad Muscles: Active and Passive Effects of the Twisted Tendon of the Spotted Ratfish Hydrolagus Colliei.” *Journal of Experimental Biology* 210(19):3395–3406.

Delp, S. L., J. P. Loan, M. G. Hoy, F. E. Zajac, E. L. Topp, and J. M. Rosen. 1990. “An Interactive Graphics-Based Model of the Lower Extremity to Study Orthopaedic Surgical Procedures.” *IEEE Transactions on Biomedical Engineering* 37(8):757–67.

DeVita, Paul, and Tibor Hortobagyi. 2000. “Age Causes a Redistribution of Joint Torques and Powers during Gait.” *Journal of Applied Physiology* 88(5):1804–11.

Dorn, Tim W., Anthony G. Schache, and Marcus G. Pandy. 2012. “Muscular Strategy Shift in Human Running: Dependence of Running Speed on Hip and Ankle Muscle Performance.” *The Journal of Experimental Biology* 215(11):1944–56.

Dufour, Alyssa B., Marian T. Hannan, Joanne M. Murabito, Douglas P. Kiel, and Robert R. McLean. 2013. “Sarcopenia Definitions Considering Body Size and Fat Mass Are Associated with Mobility Limitations: The Framingham Study.” *Journals of Gerontology - Series A Biological Sciences and Medical Sciences* 68(2):168–74.

Ebrahimi, Anahid, Isaac F. Loegering, Jack A. Martin, Robin L. Pomeroy, Joshua D. Roth, and Darryl G. Thelen. 2020. “Achilles Tendon Loading Is Lower in Older Adults than Young Adults across a Broad Range of Walking Speeds.” *Experimental Gerontology* 137:110966.

Edama, M., M. Kubo, H. Onishi, T. Takabayashi, T. Inai, E. Yokoyama, W. Hiroshi, N. Satoshi, and I. Kageyama. 2015. “The Twisted Structure of the Human Achilles Tendon.” *Scandinavian Journal of Medicine & Science in Sports* 25(5):e497–503.

Eilaghi, Armin, John G. Flanagan, Inka Tertinegg, Craig A. Simmons, G. Wayne Brodland, and C. Ross Ethier. 2010. “Biaxial Mechanical Testing of Human Sclera.” *Journal of Biomechanics* 43(9):1696–1701.

Eng, Carolyn M., and Thomas J. Roberts. 2018. “Aponeurosis Influences the Relationship between Muscle Gearing and Force.” *Journal of Applied Physiology* 125(2):513–19.

Epstein, Marcelo, Max Wong, and Walter Herzog. 2006. “Should Tendon and Aponeurosis Be Considered in Series?” *Journal of Biomechanics* 39(11):2020–25.

Farnsworth, P. N., and S. E. Shyne. 1979. “Anterior Zonular Shifts with Age.” *Experimental Eye Research* 28(3):291–97.

Farris, Dominic James, Grant Trewartha, M. Polly McGuigan, and Glen A. Lichtwark. 2013. “Differential Strain Patterns of the Human Achilles Tendon Determined in Vivo with Freehand Three-Dimensional Ultrasound Imaging.” *Journal of Experimental Biology* 216(4):594–600.

Faulkner, John A., Lisa M. Larkin, Dennis R. Claflin, and Susan V. Brooks. 2007. “Age-Related Changes in the Structure and Function of Skeletal Muscles.” *Clinical and Experimental Pharmacology and Physiology* 34(11):1091–96.

Finni, Taija, John A. Hodgson, Alex M. Lai, V. Reggie Edgerton, and Shantanu Sinha. 2003a. “Mapping of Movement in the Isometrically Contracting Human Soleus Muscle Reveals Details of Its Structural and Functional Complexity.” *Https://Doi.Org/10.1152/Japplphysiol.00596.2003*.

Finni, Taija, John A. Hodgson, Alex M. Lai, V. Reggie Edgerton, and Shantanu Sinha. 2003b. “Nonuniform Strain of Human Soleus Aponeurosis-Tendon Complex during Submaximal Voluntary Contractions in Vivo.” *Journal of Applied Physiology* 95(2):829–37.

Fiorentino, Niccolo M., and Silvia S. Blemker. 2014. “Musculotendon Variability Influences Tissue Strains Experienced by the Biceps Femoris Long Head Muscle during High-Speed Running.” *Journal of Biomechanics* 47(13):3325–33.

Fiorentino, Niccolo M., Frederick H. Epstein, and Silvia S. Blemker. 2012. “Activation and Aponeurosis Morphology Affect in Vivo Muscle Tissue Strains near the Myotendinous Junction.” *Journal of Biomechanics* 45(4):647–52.

Fiorentino, Niccolo M., Michael R. Rehorn, Elizabeth S. Chumanov, Darryl G. Thelen, and Silvia S. Blemker. 2014. “Computational Models Predict Larger Muscle Tissue Strains at Faster Sprinting Speeds.” *Medicine & Science in Sports & Exercise* 46(4):776–86.

Fisher, R. F. 1969. “Elastic Constants of the Human Lens Capsule.” *The Journal of Physiology* 201(1):1–

19.

Fisher, R. F. 1971. “The Elastic Constants of the Human Lens.” *The Journal of Physiology* 212(1):147–80.

Flügel, C., E. H. Bárány, and E. Lütjen-Drecoll. 1990. “Histochemical Differences within the Ciliary Muscle and Its Function in Accommodation.” *Experimental Eye Research* 50(2):219–26.

Francis, Carrie A., Amy L. Lenz, Rachel L. Lenhart, and Darryl G. Thelen. 2013. “The Modulation of Forward Propulsion, Vertical Support, and Center of Pressure by the Plantarflexors during Human Walking.” *Gait & Posture* 38(4):993–97.

Franz, Jason R. 2016. “The Age-Associated Reduction in Propulsive Power Generation in Walking.” *Exercise and Sport Sciences Reviews* 44(4):129–36.

Franz, Jason R., and Rodger Kram. 2014. “Advanced Age and the Mechanics of Uphill Walking: A Joint-Level, Inverse Dynamic Analysis.” *Gait & Posture* 39(1):135–40.

Franz, Jason R., Michela Maletis, and Rodger Kram. 2014. “Real-Time Feedback Enhances Forward Propulsion during Walking in Old Adults.” *Clinical Biomechanics* 29(1):68–74.

Franz, Jason R., Laura C. Slane, Kristen Rasske, and Darryl G. Thelen. 2015. “Non-Uniform in Vivo Deformations of the Human Achilles Tendon during Walking.” *Gait & Posture* 41(1):192–97.

Franz, Jason R., and Darryl G. Thelen. 2015. “Depth-Dependent Variations in Achilles Tendon Deformations with Age Are Associated with Reduced Plantarflexor Performance during Walking.” *Journal of Applied Physiology* 119(3):242–49.

Franz, Jason R., and Darryl G. Thelen. 2016. “Imaging and Simulation of Achilles Tendon Dynamics: Implications for Walking Performance in the Elderly.” *Journal of Biomechanics* 49(9):1403–10.

Friberg, Thomas R., and John W. Lace. 1988. “A Comparison of the Elastic Properties of Human Choroid and Sclera.” *Experimental Eye Research* 47(3):429–36.

Fukunaga, T., M. Miyatani, M. Tachi, M. Kouzaki, Y. Kawakami, and H. Kanehisa. 2001. “Muscle Volume Is a Major Determinant of Joint Torque in Humans.” *Acta Physiologica Scandinavica* 172(4):249–55.

Geraghty, Brendan, Stephen W. Jones, Paolo Rama, Riaz Akhtar, and Ahmed Elsheikh. 2012. “Age-Related Variations in the Biomechanical Properties of Human Sclera.” *Journal of the Mechanical Behavior of Biomedical Materials* 16:181–91.

Glasser, A., and M. C. Campbell. 1999. “Biometric, Optical and Physical Changes in the Isolated Human Crystalline Lens with Age in Relation to Presbyopia.” *Vision Research* 39(11):1991–2015.

Glasser, Adrian. 2008. “Restoration of Accommodation: Surgical Options for Correction of Presbyopia.” *Clinical & Experimental Optometry : Journal of the Australian Optometrical Association* 91(3):279–95.

Goldberg, Daniel B. 2011. “Computer-Animated Model of Accommodation and Theory of Reciprocal Zonular Action.” *Clinical Ophthalmology (Auckland, N.Z.)* 5:1559–66.

Goldberg, Daniel B. 2015. “Computer-Animated Model of Accommodation and Presbyopia.” *Journal of Cataract and Refractive Surgery* 41(2):437–45.

Gordon, A. M., A. F. Huxley, and F. J. Julian. 1966. “The Variation in Isometric Tension with Sarcomere Length in Vertebrate Muscle Fibres.” *The Journal of Physiology* 184(1):170–92.

Grytz, Rafael, Massimo A. Fazio, Vincent Libertiaux, Luigi Bruno, Stuart Gardiner, Christopher A. Girkin, and J. Crawford Downs. 2014. “Age- and Race-Related Differences in Human Scleral

Material Properties." *Investigative Ophthalmology & Visual Science* 55(12):8163–72.

Hai, C. M., and R. A. Murphy. 1988. "Cross-Bridge Phosphorylation and Regulation of Latch State in Smooth Muscle." *American Journal of Physiology-Cell Physiology* 254(1):C99–106.

Hall, John E. 2010. *Guyton and Hall Textbook of Medical Physiology*. Elsevier Health Sciences.

Hamanaka, T. 1989. "Scleral Spur and Ciliary Muscle in Man and Monkey." *Japanese Journal of Ophthalmology* 33(2):221–36.

Handsfield, Geoffrey G., Bart Bolsterlee, Joshua M. Inouye, Robert D. Herbert, Thor F. Besier, and Justin W. Fernandez. 2017. "Determining Skeletal Muscle Architecture with Laplacian Simulations: A Comparison with Diffusion Tensor Imaging." *Biomechanics and Modeling in Mechanobiology* 1–11.

Handsfield, Geoffrey G., Joshua M. Inouye, Laura C. Slane, Darryl G. Thelen, G. Wilson Miller, and Silvia S. Blemker. 2017. "A 3D Model of the Achilles Tendon to Determine the Mechanisms Underlying Nonuniform Tendon Displacements." *Journal of Biomechanics* 51:17–25.

Handsfield, Geoffrey G., Craig H. Meyer, Mark F. Abel, and Silvia S. Blemker. 2016. "Heterogeneity of Muscle Sizes in the Lower Limbs of Children with Cerebral Palsy." *Muscle & Nerve* 53(6):933–45.

Handsfield, Geoffrey G., Craig H. Meyer, Joseph M. Hart, Mark F. Abel, and Silvia S. Blemker. 2014. "Relationships of 35 Lower Limb Muscles to Height and Body Mass Quantified Using MRI." *Journal of Biomechanics* 47(3):631–38.

Handsfield, Geoffrey G., Laura C. Slane, and Hazel R. C. Screen. 2016. "Nomenclature of the Tendon Hierarchy: An Overview of Inconsistent Terminology and a Proposed Size-Based Naming Scheme with Terminology for Multi-Muscle Tendons." *Journal of Biomechanics* 49(13):3122–24.

Helmholtz, H. 1855. "Ueber die Accommodation des Auges." *Archiv für Ophthalmologie* 2(2):1–74.

Herlihy, Jeremiah T., and Richard A. Murphy. 1973. "Length-Tension Relationship of Smooth Muscle of the Hog Carotid Artery." *Circulation Research* 33(3):275–83.

Herzog, Walter. 2017. "Skeletal Muscle Mechanics: Questions, Problems and Possible Solutions." *Journal of Neuroengineering and Rehabilitation* 14(1):98.

Heys, Karl Robert, Sandra Leigh Cram, and Roger John Willis Truscott. 2004. "Massive Increase in the Stiffness of the Human Lens Nucleus with Age: The Basis for Presbyopia?" *Molecular Vision* 10:956–63.

Hipsley, AnnMarie, Brad Hall, and Karolinne M Rocha. 2018. "Scleral Surgery for the Treatment of Presbyopia: Where Are We Today?" *Eye and Vision (London, England)* 5:4.

Hipsley, AnnMarie, Brad Hall, and Karolinne Maia Rocha. 2018. "Long-Term Visual Outcomes of Laser Anterior Ciliary Excision." *American Journal of Ophthalmology Case Reports* 10:38–47.

Hipsley, AnnMarie, David Hui-Kang Ma, Chi-Chin Sun, Mitchell A. Jackson, Daniel Goldberg, and Brad Hall. 2017. "Visual Outcomes 24 Months after LaserACE." *Eye and Vision (London, England)* 4:15.

Hirata, Kosuke, Hiroaki Kanehisa, Eri Miyamoto-Mikami, and Naokazu Miyamoto. 2015. "Evidence for Intermuscle Difference in Slack Angle in Human Triceps Surae." *Journal of Biomechanics* 48(6):1210–13.

Hodgson, John A., Taija Finni, Alex M. Lai, V. Reggie Edgerton, and Shantanu Sinha. 2006. "Influence of Structure on the Tissue Dynamics of the Human Soleus Muscle Observed in MRI Studies during Isometric Contractions." *Journal of Morphology* 267(5):584–601.

Hogan, Michael John, Jorge A. Alvarado, and Joan Esperson Weddell. 1971. *Histology of the Human*

Eye: An Atlas and Textbook [by] Michael J. Hogan, Jorge A. Alvarado [and] Joan Esperson Weddell. Saunders.

Holden BA, Fricke TR, Ho S, and et al. 2008. “Global Vision Impairment Due to Uncorrected Presbyopia.” *Archives of Ophthalmology* 126(12):1731–39.

Holt, Natalie C., Nicole Danos, Thomas J. Roberts, and Emanuel Azizi. 2016. “Stuck in Gear: Age-Related Loss of Variable Gearing in Skeletal Muscle.” *The Journal of Experimental Biology* 219(Pt 7):998–1003.

Holzbaur, Katherine R. S., Scott L. Delp, Garry E. Gold, and Wendy M. Murray. 2007. “Moment-Generating Capacity of Upper Limb Muscles in Healthy Adults.” *Journal of Biomechanics* 40(11):2442–49.

Hug, François, Lilian Lacourpaille, Olivier Maïsetti, and Antoine Nordez. 2013. “Slack Length of Gastrocnemius Medialis and Achilles Tendon Occurs at Different Ankle Angles.” *Journal of Biomechanics* 46(14):2534–38.

Inouye, Joshua M., Kant Y. Lin, Jamie L. Perry, and Silvia S. Blemker. 2016. “Contributions of the Musculus Uvulae to Velopharyngeal Closure Quantified With a 3-Dimensional Multimuscle Computational Model.” *Annals of Plastic Surgery* 77 Suppl 1(Suppl 1):S70-5.

Inouye, Joshua M., Jamie L. Perry, Kant Y. Lin, and Silvia S. Blemker. 2015. “A Computational Model Quantifies the Effect of Anatomical Variability on Velopharyngeal Function.” *Journal of Speech, Language, and Hearing Research : JSLHR* 58(4):1119–33.

Ishikawa, T. 1962. “Fine Structure of the Human Cillary Muscle.” *Investigative Ophthalmology* 1:587–608.

Janssen, Ian, Steven B. Heymsfield, Zi Mian Wang, and Robert Ross. 2000. “Skeletal Muscle Mass and Distribution in 468 Men and Women Aged 18-88 Yr.” *Journal of Applied Physiology* 89(1):81–88.

Johnson, M. A., J. Polgar, D. Weightman, and D. Appleton. 1973. “Data on the Distribution of Fibre Types in Thirty-Six Human Muscles: An Autopsy Study.” *Journal of the Neurological Sciences* 18(1):111–29.

Judge, S. J., and H. J. Burd. 2002. “Modelling the Mechanics of Accommodation and Presbyopia.” *Ophthalmic and Physiological Optics* 22(5):397–400.

Karamanidis, Kiros, and Adamantios Arampatzis. 2006. “Mechanical and Morphological Properties of Human Quadriceps Femoris and Triceps Surae Muscle-Tendon Unit in Relation to Aging and Running.” *Journal of Biomechanics* 39(3):406–17.

Karamanidis, Kiros, Gaspar Epro, Matthias König, Falk Mersmann, and Adamantios Arampatzis. 2019. “Simplified Triceps Surae Muscle Volume Assessment in Older Adults.” *Frontiers in Physiology* 10:1299.

Karatekin, Yavuz Selim, Bedri Karaismailoglu, Gokhan Kaynak, Tahir Ogut, Atilla Suleyman Dikici, Emel Ure Esmerer, Onder Aydingoz, and Huseyin Botanlioglu. 2018. “Does Elasticity of Achilles Tendon Change after Suture Applications? Evaluation of Repair Area by Acoustic Radiation Force Impulse Elastography.” *Journal of Orthopaedic Surgery and Research* 13(1).

Kaufman, Paul Leon, A. Alm, and Francis Heed Adler. 2003. *Adler’s Physiology of the Eye: Clinical Application*. Mosby.

Kawakami, Yasuo, Yoshiho Ichinose, and Tetsuo Fukunaga. 1998. “Architectural and Functional Features of Human Triceps Surae Muscles during Contraction.” *Journal of Applied Physiology* 85(2):398–404.

Ke, Bilian, Xinjie Mao, Hong Jiang, Jichang He, Che Liu, Min Li, Ying Yuan, and Jianhua Wang. 2017. "The Relationship Between High-Order Aberration and Anterior Ocular Biometry During Accommodation in Young Healthy Adults." *Investigative Opthalmology & Visual Science* 58(13):5628.

Kerrigan, D. Case., Mary K. Todd, Ugo Della Croce, Lewis A. Lipsitz, and James J. Collins. 1998. "Biomechanical Gait Alterations Independent of Speed in the Healthy Elderly: Evidence for Specific Limiting Impairments." *Archives of Physical Medicine and Rehabilitation* 79(3):317–22.

Keuler, Emily M., Isaac F. Loegering, Jack A. Martin, Joshua D. Roth, and Darryl G. Thelen. 2019. "Shear Wave Predictions of Achilles Tendon Loading during Human Walking." *Scientific Reports* 9(1):13419.

Knaus, Katherine R., Anahid Ebrahimi, Jack A. Martin, Isaac F. Loegering, Darryl G. Thelen, and Silvia S. Blemker. 2020. "Achilles Tendon Morphology Is Related to Triceps Surae Muscle Size and Peak Plantarflexion Torques During Walking in Young but Not Older Adults." *Frontiers in Sports and Active Living* 2:88.

Knaus, Katherine R., Ann Marie Hipsley, and Silvia S. Blemker. 2021. "The Action of Ciliary Muscle Contraction on Accommodation of the Lens Explored with a 3D Model." *Biomechanics and Modeling in Mechanobiology* 1–16.

Krag, S., T. Olsen, and T. T. Andreassen. 1997. "Biomechanical Characteristics of the Human Anterior Lens Capsule in Relation to Age." *Investigative Ophthalmology & Visual Science* 38(2):357–63.

Krag, Susanne, and Troels T. Andreassen. 2003. "Mechanical Properties of the Human Lens Capsule." *Progress in Retinal and Eye Research* 22(6):749–67.

Krupenevich, Rebecca L., William H. Clark, Gregory S. Sawicki, and Jason R. Franz. 2020. "Older Adults Overcome Reduced Triceps Surae Structural Stiffness to Preserve Ankle Joint Quasi-Stiffness During Walking." *Journal of Applied Biomechanics* 36(4):209–16.

Kubo, K., Y. Kawakami, H. Kanehisa, and T. Fukunaga. 2002. "Measurement of Viscoelastic Properties of Tendon Structures in Vivo." *Scandinavian Journal of Medicine & Science in Sports* 12(1):3–8.

LaCroix, Andrew S., Sarah E. Duenwald-Kuehl, Roderic S. Lakes, and Ray Vanderby. 2013. "Relationship between Tendon Stiffness and Failure: A Metaanalysis." *Journal of Applied Physiology* 115(1):43–51.

Lai, Adrian, Glen A. Lichtwark, Anthony G. Schache, Yi Chung Lin, Nicholas A. T. Brown, and Marcus G. Pandy. 2015. "In Vivo Behavior of the Human Soleus Muscle with Increasing Walking and Running Speeds." *Journal of Applied Physiology* 118(10):1266–75.

Lee, Hae-Dong, Taija Finni, John A. Hodgson, Alex M. Lai, V. Reggie Edgerton, and Shantanu Sinha. 2006. "Soleus Aponeurosis Strain Distribution Following Chronic Unloading in Humans: An in Vivo MR Phase-Contrast Study." *Journal of Applied Physiology* 100(6):2004–11.

Lichtwark, G. A., and A. M. Wilson. 2005. "In Vivo Mechanical Properties of the Human Achilles Tendon during One-Legged Hopping." *Journal of Experimental Biology* 208(24):4715–25.

Lichtwark, G. A., and A. M. Wilson. 2007. "Is Achilles Tendon Compliance Optimised for Maximum Muscle Efficiency during Locomotion?" *Journal of Biomechanics* 40(8):1768–75.

Lieber, Richard L., and Jan Fridén. 2000. "Functional and Clinical Significance of Skeletal Muscle Architecture." *Muscle & Nerve* 23(11):1647–66.

Lin, Theodore H. 2013. *Sefea: Strain-Enriched Finite Element Analysis-A New Generation of FEA, Theory and Benchmarks*. Pittsburgh, PA.

Liu, Zhuo, Boliang Wang, Xiuying Xu, and Cheng Wang. 2006. “A Study for Accommodating the Human Crystalline Lens by Finite Element Simulation.” *Computerized Medical Imaging and Graphics* 30(6–7):371–76.

Ljubimova, Darja, Anders Eriksson, and Svetlana Bauer. 2008. “Aspects of Eye Accommodation Evaluated by Finite Elements.” *Biomechanics and Modeling in Mechanobiology* 7(2):139–50.

Lossing, Laura Ashley, Loraine T. Sinnott, Chiu-Yen Kao, Kathryn Richdale, and Melissa D. Bailey. 2012. “Measuring Changes in Ciliary Muscle Thickness with Accommodation in Young Adults.” *Optometry and Vision Science* 89(5):719–26.

Lütjen-Drecoll, Elke, Paul L. Kaufman, Rainer Wasielewski, Lin Ting-Li, and Mary Ann Croft. 2010. “Morphology and Accommodative Function of the Vitreous Zonule in Human and Monkey Eyes.” *Investigative Ophthalmology & Visual Science* 51(3):1554–64.

Maas, Steve A., Benjamin J. Ellis, Gerard A. Ateshian, and Jeffrey A. Weiss. 2012. “FEBio: Finite Elements for Biomechanics.” *Journal of Biomechanical Engineering* 134(1).

Magnusson, S. Peter, Per Aagaard, Sofie Rosager, Poul Dyhre-Poulsen, and Michael Kjaer. 2001. “Load-displacement Properties of the Human Triceps Surae Aponeurosis in Vivo.” *The Journal of Physiology* 531(1):277–88.

Manjunath, Varsha, Mohammad Taha, James G. Fujimoto, and Jay S. Duker. 2010. “Choroidal Thickness in Normal Eyes Measured Using Cirrus-HD Optical Coherence Tomography.” *American Journal of Ophthalmology* 150(3):325-329.e1.

McCleary, Rachael, Eleanor M. Simonsick, Roland J. Thorpe, Thomas LaVeist, Jenny R. Smolen, and Keith E. Whitfield. 2014. “Racial Disparities in Disability Among Older Adults.” *Journal of Aging and Health* 26(8):1261–79.

McGibbon, Chris A. 2003. “Toward a Better Understanding of Gait Changes with Age and Disablement: Neuromuscular Adaptation.” *Exercise and Sport Sciences Reviews* 31(2):102–8.

McGowan, C. P., R. R. Neptune, and R. Kram. 2008. “Independent Effects of Weight and Mass on Plantar Flexor Activity during Walking: Implications for Their Contributions to Body Support and Forward Propulsion.” *Journal of Applied Physiology* 105(2):486–94.

Michael, Ralph, Marek Mikielewicz, Carlos Gordillo, Gustavo A. Montenegro, Laura Pinilla Cortés, and Rafael I. Barraquer. 2012. “Elastic Properties of Human Lens Zonules as a Function of Age in PresbyopesElasticity of Human Lens Zonules in Presbyopia.” *Investigative Ophthalmology & Visual Science* 53(10):6109–14.

Millard, Matthew, Thomas Uchida, Ajay Seth, and Scott L. Delp. 2013. “Flexing Computational Muscle: Modeling and Simulation of Musculotendon Dynamics.” *Journal of Biomechanical Engineering* 135(2).

Morrow, Duane A., Tammy L. Haut Donahue, Gregory M. Odegard, and Kenton R. Kaufman. 2010. “Transversely Isotropic Tensile Material Properties of Skeletal Muscle Tissue.” *Journal of the Mechanical Behavior of Biomedical Materials* 3(1):124–29.

Morse, C. I., J. M. Thom, K. M. Birch, and M. V. Narici. 2005. “Changes in Triceps Surae Muscle Architecture with Sarcopenia.” *Acta Physiologica Scandinavica* 183(3):291–98.

Morse, Christopher I., Jeanette M. Thom, Mark G. Davis, Ken R. Fox, Karen M. Birch, and Marco V. Narici. 2004. “Reduced Plantarflexor Specific Torque in the Elderly Is Associated with a Lower Activation Capacity.” *European Journal of Applied Physiology* 92(1–2):219–26.

Moses, R. A., and W. J. Grodzki. 1977. “The Scleral Spur and Scleral Roll.” *Investigative Ophthalmology & Visual Science* 16(10):925–31.

Moses, Robert A. 1965. “Detachment of Ciliary Body--Anatomical and Physical Considerations.” *Investigative Ophthalmology & Visual Science* 4(5):935–41.

Murray, Wendy M., Scott L. Delp, and Thomas S. Buchanan. 1995. “Variation of Muscle Moment Arms with Elbow and Forearm Position.” *Journal of Biomechanics* 28(5).

Nankivil, D., B. Maceo Heilman, H. Durkee, F. Manns, K. Ehrmann, S. Kelly, E. Arrieta-Quintero, and J. M. Parel. 2015. “The Zonules Selectively Alter the Shape of the Lens During Accommodation Based on the Location of Their Anchorage Points.” *Investigative Ophthalmology & Visual Science* 56(3):1751–60.

Narici, M. V., H. Hoppeler, B. Kayser, L. Landoni, H. Claassen, C. Gavardi, M. Conti, and P. Cerre^{TEL}li. 1996. “Human Quadriceps Cross-Sectional Area, Torque and Neural Activation during 6 Months Strength Training.” *Acta Physiologica Scandinavica* 157(2):175–186.

Narici, Marco V., and Constantinos N. Maganaris. 2007. “Plasticity of the Muscle-Tendon Complex with Disuse and Aging.” *Exercise and Sport Sciences Reviews* 35(3):126–34.

Neptune, R. R., S. A. Kautz, and F. E. Zajac. 2001. “Contributions of the Individual Ankle Plantar Flexors to Support, Forward Progression and Swing Initiation during Walking.” *Journal of Biomechanics* 34(11):1387–98.

Netter, Frank H. 2014. *Atlas of Human Anatomy*. Elsevier Health Sciences.

Nilwik, Rachel, Tim Snijders, Marika Leenders, Bart B. L. Groen, Janneau van Kranenburg, Lex B. Verdijk, and Luc J. C. van Loon. 2013. “The Decline in Skeletal Muscle Mass with Aging Is Mainly Attributed to a Reduction in Type II Muscle Fiber Size.” *Experimental Gerontology* 48(5):492–98.

Norman, Richard E., John G. Flanagan, Sophie M. K. Rausch, Ian A. Sigal, Inka Tertinegg, Armin Eilaghi, Sharon Portnoy, John G. Sled, and C. Ross Ethier. 2010. “Dimensions of the Human Sclera: Thickness Measurement and Regional Changes with Axial Length.” *Experimental Eye Research* 90(2):277–84.

Nuckols, R. W., T. J. M. Dick, O. N. Beck, and G. S. Sawicki. 2020. “Ultrasound Imaging Links Soleus Muscle Neuromechanics and Energetics during Human Walking with Elastic Ankle Exoskeletons.” *Scientific Reports* 10(1):1–15.

Obst, Steven J., Jean-Baptiste Renault, Richard Newsham-West, and Rod S. Barrett. 2014. “Three-Dimensional Deformation and Transverse Rotation of the Human Free Achilles Tendon in Vivo during Isometric Plantarflexion Contraction.” *Journal of Applied Physiology* 116(4).

Olewnik, Łukasz, Nicol Zielinska, Friedrich Paulsen, Michał Podgórski, Robert Haładaj, Piotr Karauda, and Michał Polguj. 2020. “A Proposal for a New Classification of Soleus Muscle Morphology.” *Annals of Anatomy - Anatomischer Anzeiger* 232:151584.

Onambele, Gladys L., Marco V. Narici, and Constantinos N. Maganaris. 2006. “Calf Muscle-Tendon Properties and Postural Balance in Old Age.” *Journal of Applied Physiology* 100(6):2048–56.

Orselli, Maria Isabel V., Jason R. Franz, and Darryl G. Thelen. 2017. “The Effects of Achilles Tendon Compliance on Triceps Surae Mechanics and Energetics in Walking.” *Journal of Biomechanics* 60(Supplement C):227–31.

Pappas, George P., Deanna S. Asakawa, Scott L. Delp, Felix E. Zajac, and John E. Drace. 2002. “Nonuniform Shortening in the Biceps Brachii during Elbow Flexion.” *Journal of Applied Physiology* 92(6):2381–89.

Pękala, P. A., B. M. Henry, A. Ochała, P. Kopacz, G. Tatoń, A. Młyniec, J. A. Walocha, and K. A. Tomaszewski. 2017. “The Twisted Structure of the Achilles Tendon Unraveled: A Detailed Quantitative and Qualitative Anatomical Investigation.” *Scandinavian Journal of Medicine &*

Science in Sports 27(12):1705–15.

Raiteri, Brent James. 2018. "Aponeurosis Behaviour during Muscular Contraction: A Narrative Review." *European Journal of Sport Science* 18(8):1128–38.

Raiteri, Brent James, Andrew Graham Cresswell, and Glen Anthony Lichtwark. 2018. "Muscle-Tendon Length and Force Affect Human Tibialis Anterior Central Aponeurosis Stiffness in Vivo." *Proceedings of the National Academy of Sciences of the United States of America* 115(14):E3097–3105.

Rana, Manku, Ghassan Hamarneh, and James M. Wakeling. 2013. "3D Fascicle Orientations in Triceps Surae." *Journal of Applied Physiology* 115(1):116–25.

Rana, Manku, Ghassan Hamarneh, and James M. Wakeling. 2014. "3D Curvature of Muscle Fascicles in Triceps Surae." *Journal of Applied Physiology* 117(11):1388–97.

Rasske, Kristen, and Jason R. Franz. 2018. "Aging Effects on the Achilles Tendon Moment Arm during Walking." *Journal of Biomechanics* 77:34–39.

Rasske, Kristen, Darryl G. Thelen, and Jason R. Franz. 2017. "Variation in the Human Achilles Tendon Moment Arm during Walking." *Computer Methods in Biomechanics and Biomedical Engineering* 20(2):201–5.

Reeder, Scott B., Charles A. McKenzie, Angel R. Pineda, Huanzhou Yu, Ann Shimakawa, Anja C. Brau, Brian A. Hargreaves, Garry E. Gold, and Jean H. Brittain. 2007. "Water–Fat Separation with IDEAL Gradient-Echo Imaging." *Journal of Magnetic Resonance Imaging* 25(3):644–52.

Rehorn, Michael R., and Silvia S. Blemker. 2010. "The Effects of Aponeurosis Geometry on Strain Injury Susceptibility Explored with a 3D Muscle Model." *Journal of Biomechanics* 43(13):2574–81.

Richdale, Kathryn, G. Lynn Mitchell, and Karla Zadnik. 2006. "Comparison of Multifocal and Monovision Soft Contact Lens Corrections in Patients With Low-Astigmatic Presbyopia." *Optometry and Vision Science* 83(5):266–73.

Richdale, Kathryn, Loraine T. Sinnott, Mark A. Bullimore, Peter A. Wassenaar, Petra Schmalbrock, Chiu-Yen Kao, Samuel Patz, Donald O. Mutti, Adrian Glasser, and Karla Zadnik. 2013. "Quantification of Age-Related and per Diopter Accommodative Changes of the Lens and Ciliary Muscle in the Emmetropic Human Eye." *Investigative Ophthalmology & Visual Science* 54(2):1095–1105.

Roberts, Thomas J., Carolyn M. Eng, David A. Sleboda, Natalie C. Holt, Elizabeth L. Brainerd, Kristin K. Stover, Richard L. Marsh, and Emanuel Azizi. 2019. "The Multi-Scale, Three-Dimensional Nature of Skeletal Muscle Contraction." *Physiology* 34(6):402–8.

Rohen, J. W. 1979. "Scanning Electron Microscopic Studies of the Zonular Apparatus in Human and Monkey Eyes." *Investigative Ophthalmology & Visual Science* 18(2):133–44.

Rubenson, Jonas, Neville J. Pires, Heok O. Loi, Gavin J. Pinniger, and Damian G. Shannon. 2012. "On the Ascent: The Soleus Operating Length Is Conserved to the Ascending Limb of the Force–Length Curve across Gait Mechanics in Humans." *Journal of Experimental Biology* 215(20):3539–51.

Ruggeri, Marco, Carolina de Freitas, Siobhan Williams, Victor M. Hernandez, Florence Cabot, Nilufer Yesilirmak, Karam Alawa, Yu-Cherng Chang, Sonia H. Yoo, Giovanni Gregori, Jean-Marie Parel, and Fabrice Manns. 2016. "Quantification of the Ciliary Muscle and Crystalline Lens Interaction during Accommodation with Synchronous OCT Imaging." *Biomedical Optics Express* 7(4):1351–64.

Schachar, R. A., A. Abolmaali, and T. Le. 2006. "Insights into the Age-Related Decline in the Amplitude of Accommodation of the Human Lens Using a Non-Linear Finite-Element Model." *The British*

Journal of Ophthalmology 90(10):1304–9.

Schachar, Ronald A. 2015. "Human Accommodative Ciliary Muscle Configuration Changes Are Consistent With Schachar's Mechanism of Accommodation." *Investigative Opthalmology & Visual Science* 56(10):6075.

Schmitz, André, and Markus Böl. 2011. "On a Phenomenological Model for Active Smooth Muscle Contraction." *Journal of Biomechanics* 44(11):2090–95.

Shan, Xiyao, Shun Otsuka, Tomiko Yakura, Munekazu Naito, Takashi Nakano, and Yasuo Kawakami. 2019. "Morphological and Mechanical Properties of the Human Triceps Surae Aponeuroses Taken from Elderly Cadavers: Implications for Muscle-Tendon Interactions" edited by J. H.-C. Wang. *PLOS ONE* 14(2):e0211485.

Shao, Yilei, Aizhu Tao, Hong Jiang, Meixiao Shen, Jianguang Zhong, Fan Lu, and Jianhua Wang. 2013. "Simultaneous Real-Time Imaging of the Ocular Anterior Segment Including the Ciliary Muscle during Accommodation." *Biomedical Optics Express* 4(3):466–80.

Sharif-Kashani, Pooria, Jean-Pierre Hubschman, Daniel Sassoon, and H. Pirouz Kavehpour. 2011. "Rheology of the Vitreous Gel: Effects of Macromolecule Organization on the Viscoelastic Properties." *Journal of Biomechanics* 44(3):419–23.

Sheppard, Amy L., and Leon N. Davies. 2010. "In Vivo Analysis of Ciliary Muscle Morphologic Changes with Accommodation and Axial Ametropia." *Investigative Ophthalmology & Visual Science* 51(12):6882–89.

Sherman, Michael A., Ajay Seth, and Scott L. Delp. 2013. "WHAT IS A MOMENT ARM? CALCULATING MUSCLE EFFECTIVENESS IN BIOMECHANICAL MODELS USING GENERALIZED COORDINATES." *Proceedings of the ... ASME Design Engineering Technical Conferences. ASME Design Engineering Technical Conferences* 2013.

Shim, Vickie B., Justin W. Fernandez, Prasad B. Gamage, Camille Regnery, David W. Smith, Bruce S. Gardiner, David G. Lloyd, and Thor F. Besier. 2014. "Subject-Specific Finite Element Analysis to Characterize the Influence of Geometry and Material Properties in Achilles Tendon Rupture." *Journal of Biomechanics* 47(15):3598–3604.

Shim, Vickie B., Geoff G. Handsfield, Justin W. Fernandez, David G. Lloyd, and Thor F. Besier. 2018. "Combining in Silico and in Vitro Experiments to Characterize the Role of Fascicle Twist in the Achilles Tendon." *Scientific Reports* 8(1):13856.

Silder, Amy, Christopher J. Westphal, and Darryl G. Thelen. 2009. "A Magnetic Resonance-Compatible Loading Device for Dynamically Imaging Shortening and Lengthening Muscle Contraction Mechanics." *Journal of Medical Devices, Transactions of the ASME* 3(3).

Sinha, Usha, Shantanu Sinha, John A. Hodgson, and Reggie V. Edgerton. 2011. "Human Soleus Muscle Architecture at Different Ankle Joint Angles from Magnetic Resonance Diffusion Tensor Imaging." *Journal of Applied Physiology* 110(3):807–19.

Siston, Robert A., Aaron C. Daub, Nicholas J. Giori, Stuart B. Goodman, and Scott L. Delp. 2005. "Evaluation of Methods That Locate the Center of the Ankle for Computer-Assisted Total Knee Arthroplasty." *Clinical Orthopaedics and Related Research* (439):129–35.

Slane, Laura Chernak, and Darryl G. Thelen. 2014. "Non-Uniform Displacements within the Achilles Tendon Observed during Passive and Eccentric Loading." *Journal of Biomechanics* 47(12):2831–35.

Slane, Laura Chernak, and Darryl G. Thelen. 2015. "Achilles Tendon Displacement Patterns during Passive Stretch and Eccentric Loading Are Altered in Middle-Aged Adults." *Medical Engineering*

and Physics 37(7):712–16.

Smigielski, Robert. 2008. “Management of Partial Tears of the Gastro-Soleus Complex.” *Clinics in Sports Medicine* 27(1):219–29, x.

Sopher, Ran S., Andrew A. Amis, D. Ceri Davies, and Jonathan Rt Jeffers. 2017. “The Influence of Muscle Pennation Angle and Cross-Sectional Area on Contact Forces in the Ankle Joint.” *The Journal of Strain Analysis for Engineering Design* 52(1):12–23.

Spottiswoode, B. S., X. Zhong, A. T. Hess, C. M. Kramer, E. M. Meintjes, B. M. Mayosi, and Frederick H. Epstein. 2007. “Tracking Myocardial Motion from Cine DENSE Images Using Spatiotemporal Phase Unwrapping and Temporal Fitting.” *IEEE Transactions on Medical Imaging* 26(1):15–30.

Stachs, Oliver, Heiner Martin, Detlef Behrend, Klaus-Peter Schmitz, and Rudolf Guthoff. 2006. “Three-Dimensional Ultrasound Biomicroscopy, Environmental and Conventional Scanning Electron Microscopy Investigations of the Human Zonula Ciliaris for Numerical Modelling of Accommodation.” *Graefe’s Archive for Clinical and Experimental Ophthalmology = Albrecht Von Graefes Archiv Für Klinische Und Experimentelle Ophthalmologie* 244(7):836–44.

Stenroth, Lauri, Jussi Peltonen, Neil J. Cronin, Sarianna Sipilä, and Taija Finni. 2012. “Age-Related Differences in Achilles Tendon Properties and Triceps Surae Muscle Architecture in Vivo.” *Journal of Applied Physiology* 113(10):1537–44.

Stitzel, Joel D., Stefan M. Duma, Joseph M. Cormier, and Ian P. Herring. 2002. “A Nonlinear Finite Element Model of the Eye with Experimental Validation for the Prediction of Globe Rupture.” *Stapp Car Crash Journal* 46:81–102.

Strenk, S. A., J. L. Semmlow, L. M. Strenk, P. Munoz, J. Gronlund-Jacob, and J. K. DeMarco. 1999. “Age-Related Changes in Human Ciliary Muscle and Lens: A Magnetic Resonance Imaging Study.” *Investigative Ophthalmology & Visual Science* 40(6):1162–69.

Studenski, Stephanie, Subashan Perera, Kushang Patel, Caterina Rosano, Kimberly Faulkner, Marco Inzitari, Jennifer Brach, Julie Chandler, Peggy Cawthon, Elizabeth Barrett Connor, Michael Nevitt, Marjolein Visser, Stephen Kritchevsky, Stefania Badinelli, Tamara Harris, Anne B. Newman, Jane Cauley, Luigi Ferrucci, and Jack Guralnik. 2011. “Gait Speed and Survival in Older Adults.” *JAMA : The Journal of the American Medical Association* 305(1):50–58.

Szaro, Paweł, Grzegorz Witkowski, Robert Śmigielski, Paweł Krajewski, and Bogdan Ciszek. 2009. “Fascicles of the Adult Human Achilles Tendon – An Anatomical Study.” *Annals of Anatomy - Anatomischer Anzeiger* 191(6):586–93.

Tamm, E., E. Lütjen-Drecoll, W. Jungkunz, and J. W. Rohen. 1991. “Posterior Attachment of Ciliary Muscle in Young, Accommodating Old, Presbyopic Monkeys.” *Investigative Ophthalmology & Visual Science* 32(5):1678–92.

Tamm, Ernst. 1992. “Age-Related Loss of Ciliary Muscle Mobility in the Rhesus Monkey.” *Archives of Ophthalmology* 110(6):871.

Tamm, Svenja, Ernst Tamm, and Johannes W. Rohen. 1992. “Age-Related Changes of the Human Ciliary Muscle. A Quantitative Morphometric Study.” *Mechanisms of Ageing and Development* 62(2):209–21.

Thorpe, Chavaunne T., Marta S. C. Godinho, Graham P. Riley, Helen L. Birch, Peter D. Clegg, and Hazel R. C. Screen. 2015. “The Interfascicular Matrix Enables Fascicle Sliding and Recovery in Tendon, and Behaves More Elastically in Energy Storing Tendons.” *Journal of the Mechanical Behavior of Biomedical Materials* 52:85–94.

Thorpe, Chavaunne T, Christian Klemt, Graham P. Riley, Helen L. Birch, Peter D. Clegg, and Hazel R.

C. Screen. 2013. “Helical Sub-Structures in Energy-Storing Tendons Provide a Possible Mechanism for Efficient Energy Storage and Return.” *Acta Biomaterialia* 9(8):7948–56.

Thorpe, Chavaunne T., C. P. Udeze, Helen L. Birch, Peter D. Clegg, and Hazel R. C. Screen. 2013. “Capacity for Sliding between Tendon Fascicles Decreases with Ageing in Injury Prone Equine Tendons: A Possible Mechanism for Age-Related Tendinopathy?” *European Cells & Materials* 25:48–60.

U.S. Department of Health and Human Services. 2018. *A Profile of Older Americans: 2018*.

Uchida, Thomas K., Jennifer L. Hicks, Christopher L. Dembia, and Scott L. Delp. 2016. “Stretching Your Energetic Budget: How Tendon Compliance Affects the Metabolic Cost of Running.” *PLOS ONE* 11(3):e0150378.

Ugarte, M., A. A. Hussain, and J. Marshall. 2006. “An Experimental Study of the Elastic Properties of the Human Bruch’s Membrane-Choroid Complex: Relevance to Ageing.” *British Journal of Ophthalmology* 90(5):621–26.

Urs, Raksha, Fabrice Manns, Arthur Ho, David Borja, Adriana Amelinckx, Jared Smith, Rakhi Jain, Robert Augusteyn, and Jean-Marie Parel. 2009. “Shape of the Isolated Ex-Vivo Human Crystalline Lens.” *Vision Research* 49(1):74–83.

Wade, Francesca E., Gregory S. Lewis, and Stephen J. Piazza. 2019. “Estimates of Achilles Tendon Moment Arm Differ When Axis of Ankle Rotation Is Derived from Ankle Motion.” *Journal of Biomechanics* 90:71–77.

Wang, Hsichun, Paul L. Prendiville, Peter J. McDonnell, and Wenji V. Chang. 1996. “An Ultrasonic Technique for the Measurement of the Elastic Moduli of Human Cornea.” *Journal of Biomechanics* 29(12):1633–36.

Wang, Kehao, Demetrios T. Venetsanos, Jian Wang, Andy T. Augousti, and Barbara K. Pierscionek. 2017. “The Importance of Parameter Choice in Modelling Dynamics of the Eye Lens.” *Scientific Reports* 7(1):16688.

Ward, Samuel R., Carolyn M. Eng, Laura H. Smallwood, and Richard L. Lieber. 2009. “Are Current Measurements of Lower Extremity Muscle Architecture Accurate?” *Clinical Orthopaedics and Related Research* 467(4):1074–82.

Wasilewski, Rainer, Jared P. McDonald, Gregg Heatley, Elke Lütjen-Drecoll, Paul L. Kaufman, and Mary Ann Croft. 2008. “Surgical Intervention and Accommodative Responses, II: Forward Ciliary Body Accommodative Movement Is Facilitated by Zonular Attachments to the Lens Capsule.” *Investigative Ophthalmology & Visual Science* 49(12):5495–5502.

Weiss, Jeffrey A., Bradley N. Maker, and Sanjay Govindjee. 1996. “Finite Element Implementation of Incompressible, Transversely Isotropic Hyperelasticity.” *Computer Methods in Applied Mechanics and Engineering* 135(1–2):107–28.

Wilde, G. S., H. J. Burd, and S. J. Judge. 2012. “Shear Modulus Data for the Human Lens Determined from a Spinning Lens Test.” *Experimental Eye Research* 97(1):36–48.

Wilkes, Robert P., and Matthew A. Reilly. 2016. “A Pre-Tensioned Finite Element Model of Ocular Accommodation and Presbyopia.” *International Journal of Advances in Engineering Sciences and Applied Mathematics* 8(1):25–38.

Winter, David A., Aftab E. Patla, James S. Frank, and Sharon E. Walt. 1990. “Biomechanical Walking Pattern Changes in the Fit and Healthy Elderly.” *Physical Therapy* 70(6):340–47.

Wolffsohn, James S., and Leon N. Davies. 2019. “Presbyopia: Effectiveness of Correction Strategies.” *Progress in Retinal and Eye Research* 68:124–43.

Worthington, Kristan S., Luke A. Wiley, Alexandra M. Bartlett, Edwin M. Stone, Robert F. Mullins, Aliasger K. Salem, C. Allan Guymon, and Budd A. Tucker. 2014. "Mechanical Properties of Murine and Porcine Ocular Tissues in Compression." *Experimental Eye Research* 121:194–99.

Zajac, F. E. 1989. "Muscle and Tendon: Properties, Models, Scaling, and Application to Biomechanics and Motor Control." *Critical Reviews in Biomedical Engineering* 17(4):359–411.

Zajac, F. E., and M. E. Gordon. 1989. "Determining Muscle's Force and Action in Multi-Articular Movement." *Exercise and Sport Sciences Reviews* 17:187–230.

Zajac, Felix E. 1993. "Muscle Coordination of Movement: A Perspective." *Journal of Biomechanics* 26:109–24.

Zelik, Karl E., and Jason R. Franz. 2017. "It's Positive to Be Negative: Achilles Tendon Work Loops during Human Locomotion." *PLOS ONE* 12(7):e0179976.

Zhong, Xiaodong, Frederick H. Epstein, Bruce S. Spottiswoode, Patrick A. Helm, and Silvia S. Blemker. 2008. "Imaging Two-Dimensional Displacements and Strains in Skeletal Muscle during Joint Motion by Cine DENSE MR." *Journal of Biomechanics* 41(3):532–40.

Citation Diversity Statement

Work in several fields of science has identified a bias in citation practices such that papers from women and other minority scholars are undercited relative to the number of papers in the field. Recognizing this bias, we have worked diligently to reference appropriate papers with fair gender and racial author inclusion that reflect the diversity of the field in thought, form of contribution, gender, race, ethnicity, and other factors. To understand the diversity represented by the citations in this dissertation we have quantified two measures of gender and race/ethnicity. First, we obtained or predicted the gender of the first and last author of each reference by using online databases. By this measure, our references contain 8% woman(first)/woman(last), 8% man/woman, 22% woman/man, and 61% man/man. This method is limited in that a) names, pronouns, and social media profiles used to construct the databases may not, in every case, be indicative of gender identity and b) it cannot account for intersex, non-binary, or transgender people. Second, we obtained or predicted racial/ethnic category of the first and last author of each reference using online databases. By this measure, our references contain 8% non-white author (first)/ non-white author (last), 9% white author/ non-white author, 10% non-white author/white author, and 72% white author/white author. This method is limited in that (a) names data used to make the predictions may not be indicative of racial/ethnic identity, and (b) it cannot account for Indigenous and

mixed-race authors, or those who may face differential biases due to the ambiguous racialization or ethnicization of their names. We look forward to future work that could help us to better understand how to support equitable practices in science.